First-principles investigation of inelastic magnetic excitations in nanostructures deposited on surfaces

Benedikt Johannes Schweflinghaus

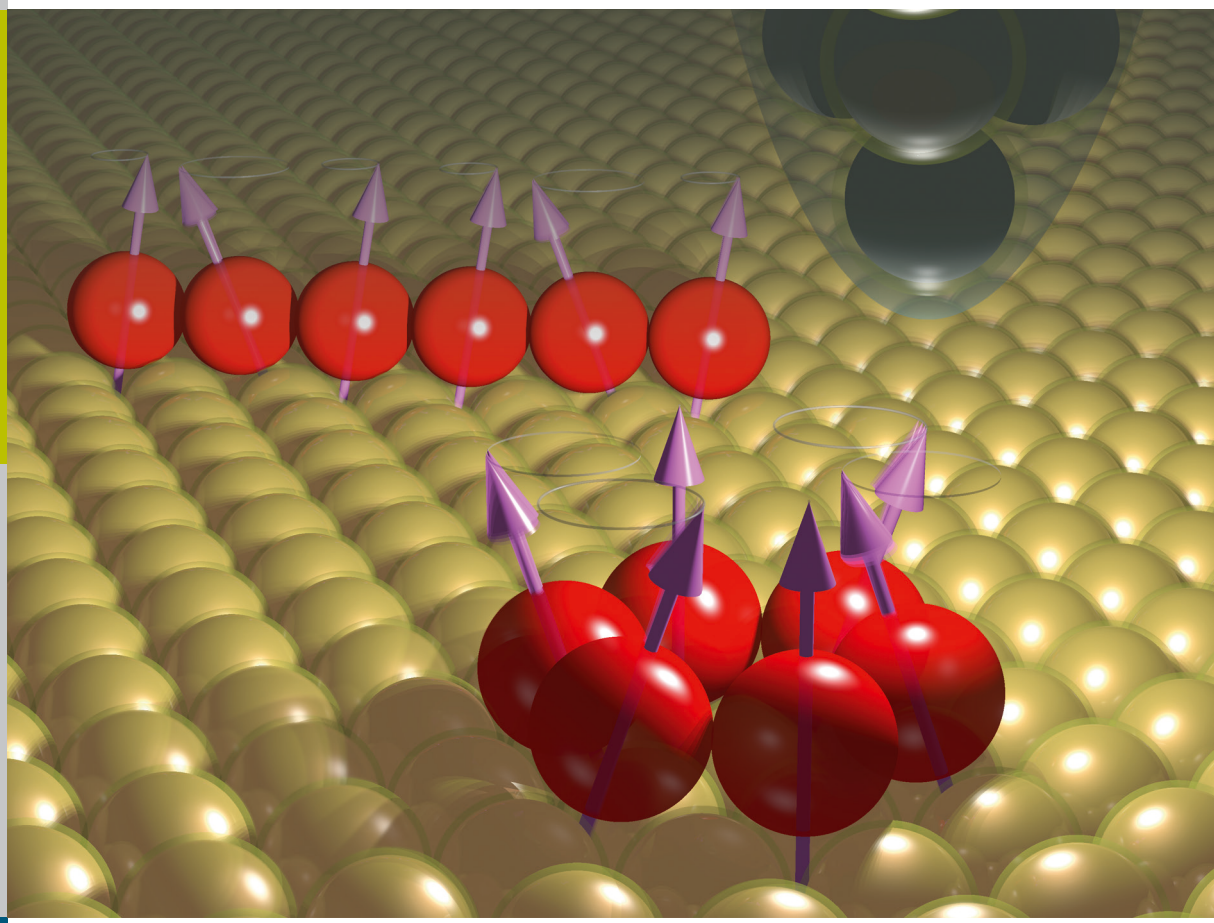

Schlüsseltechnologien / Key Technologies
Band / Volume 117
ISBN 978-3-95806-115-6

JÜLICH
FORSCHUNGSZENTRUM

Member of the Helmholtz Association

Schriften des Forschungszentrums Jülich
Reihe Schlüsseltechnologien / Key Technologies Band / Volume 117

Forschungszentrum Jülich GmbH
Peter Grünberg Institute (PGI)
Quantum Theory of Materials (PGI-1 / IAS-1)

First-principles investigation of inelastic magnetic excitations in nanostructures deposited on surfaces

Benedikt Johannes Schweflinghaus

Schriften des Forschungszentrums Jülich
Reihe Schlüsseltechnologien / Key Technologies Band / Volume 117

ISSN 1866-1807 ISBN 978-3-95806-115-6

Bibliographic information published by the Deutsche Nationalbibliothek.
The Deutsche Nationalbibliothek lists this publication in the Deutsche Nationalbibliografie; detailed bibliographic data are available in the Internet at http://dnb.d-nb.de.

Publisher and Distributor: Forschungszentrum Jülich GmbH
Zentralbibliothek
52425 Jülich
Tel: +49 2461 61-5368
Fax: +49 2461 61-6103
Email: zb-publikation@fz-juelich.de
www.fz-juelich.de/zb

Cover Design: Grafische Medien, Forschungszentrum Jülich GmbH

Printer: Grafische Medien, Forschungszentrum Jülich GmbH

Schriften des Forschungszentrums Jülich
Reihe Schlüsseltechnologien / Key Technologies, Band / Volume 117

D 82 (Diss. RWTH Aachen University, 2015)

ISSN 1866-1807
ISBN 978-3-95806-115-6

The complete volume is freely available on the Internet on the Jülicher Open Access Server at www.fz-juelich.de/zb/juwel

Abstract

This thesis provides a theoretical description of inelastic scanning tunneling spectroscopy (ISTS), using a newly developed first-principles approach, by combining time-dependent density functional theory and many-body perturbation theory. The Korringa-Kohn-Rostoker Green function method is utilized, since it affords a real-space description of nanostructures, well-suited to the ISTS context. The central quantity is the electron self-energy, containing the interactions between the tunneling electrons and the spin excitations of the nanostructure. This self-energy leads to a renormalized electronic structure in the vacuum region above the adsorbate, which can be directly compared with the experimental ISTS signal, in the spirit of the Tersoff-Hamann approximation.

As a first application, the developed method is applied to individual $3d$ transition-metal adatoms (Cr, Mn, Fe, and Co) deposited on metallic surfaces (Cu(111) and Pt(111)). The obtained magnetic excitation spectra for the regarded structures show differences in the excitation lifetime and the g shift, which can be attributed to the electronic structure of both, the adsorbate and the substrate. The calculated theoretical inelastic spectra reveal different non-trivial shapes of the excitation signatures, that vary with distance to the adsorbate. Observed asymmetries in these spectra could explain asymmetries in experimental findings. Furthermore, some spectra show additional bound states (satellites) that are not predictable by use of a simple Heisenberg model. For Fe and Co adatoms on Pt(111) the impact of hydrogen contamination on the excitation spectrum is investigated. In agreement to experimental findings, the presence or absence of hydrogen has a significant impact on the shape of the excitation spectrum.

In addition to the above analysis, we also consider clusters of two or more $3d$ transition-metal adatoms deposited on the Cu(111) surface, investigating the resulting magnetic excitation spectra. The magnetic moments are coupled by the exchange interaction which results in different excitation modes of acoustic and optical character. The obtained excitation spectra depend on the regarded adatom species, the interatomic distance, the alignment of the magnetic moments, the number of involved atoms, as well as the arrangement on the surface. A comparison of a ring and a chain structure reveals the impact of geometrical topology on magnetic excitations. The semiclassical Landau-Lifshitz-Gilbert model is used to provide an insightful interpretation of the first-principles spin-excitation modes.

Contents

Conventions and Abbreviations

Notation		Mathematical object
$\vec{a}$	arrow head	3-dim. vector (Roman letters for components, *e.g.*, a_i)
$\hat{a}$	hat	normalized 3-dim. vector
$\overleftrightarrow{a}$	double arrow head	(3×3)-dim. matrix
$\underline{b}$	underline	4-dim. vector (Greek letters for components, *e.g.*, b_α)
$\underline{\underline{b}}$	double underline	(4×4)-dim. matrix
$\boldsymbol{\phi}$	bold	vector in spin space (spinor)
$\boldsymbol{\sigma}$	bold	matrix in spin space
$\mathcal{S}$	calligraphic symbol	general operator (in basis independent form)
$\delta(\omega)$		Dirac δ-distribution, see Appendix C
$\Theta(\tau)$		Heaviside step function, see Appendix C
$f(\epsilon)$		Fermi-Dirac function, see Appendix C

Abbr.	Meaning	Abbr.	Meaning
AFM	antiferromagnetic	LDA	local-density approximation
ASA	atomic sphere approximation	LLG	Landau-Lifshitz-Gilbert
DFT	density functional theory	MBPT	many-body perturbation theory
DOS	density of states	SOC	spin-orbit coupling
fcc	face-centered cubic	STM	scanning tunneling microscope
FM	ferromagnetic	STS	scanning tunneling spectroscopy
FWHM	full-width at half maximum	TDDFT	time-dependent DFT
ISTS	inelastic STS	TM	transition metal
KKR	Korringa-Kohn-Rostoker	xc	exchange-correlation

1. Introduction

Storage and exchange of digital information are of ever-growing importance in modern society. Besides primary electronic devices such as laptops or smart phones, also domestic appliances (refrigerators *etc.*) and all kinds of vehicles are more and more linked together in the *Internet of Things*, enabling the synchronization of different areas of our daily life. This development would not have been possible without the tremendous advances in information technology. In 55 years, the Areal Density (AD) has increased by a factor of one billion from several kilobits per square inch up to almost one terabit per square inch, an AD value that for a long time was assumed to be the upper limit in data storage density [1]. This became possible through groundbreaking discoveries in fundamental research, such as the giant magneto-resistance (GMR) effect [2, 3], discovered by Albert Fert and by Peter Grünberg who were awarded the Nobel Prize in Physics in 2007.

However, the engineering of future electronic devices meets different challenges. On the one hand, the steady miniaturization of the bit size in conventional hard disk drives (HDD) eventually reaches a point at which stored binary information becomes vulnerable to thermal and electromagnetic fluctuations, leading to permanent loss of information. This barrier is known as the super-paramagnetic limit [4]. On the other hand, the transport of digital information using the electron charge implies power losses due to Joule heating, a well-known bottleneck for exascale computing. Novel concepts utilize the electron spin instead of its charge as information carrier. For this purpose, materials are needed that allow fast information transfer of huge data streams, *i.e.*, they should reach high switching rates, while other materials should be able to store information with a long-term stability within a small area of few atoms only. Therefore, the future development of novel electromagnetic devices will be mainly driven by their need for operating at low energy consumption to reduce the heat generation and by their ability to protect a binary unit against disturbing fields caused by switching processes in adjacent units. In order to meet these requirements, the understanding of magnetism dynamics in low-dimensional systems at the nanometer scale is of paramount importance.

Besides the mentioned request of industry towards research to continuously improve materials and develop novel ideas for binary information storage devices, it is of fundamental interest to understand the nature of magnetism at the nanometer scale. Such a task is far from being trivial, since, due to the atomic size of the problem, quantum-mechanical effects play a central role. In addition, the reduced dimension of surface structures results in atoms that usually exhibit different coordination numbers than in bulk, enhancing their spin and orbital magnetic moments. As a direct consequence, spin-orbit coupling induced effects, such as the magnetic anisotropy energy (MAE) or the Dzyaloshinskii-Moriya

interaction (DMI), are significantly enlarged by typically one or two orders of magnitude compared to the bulk value. Thus, they can lead to exotic spin textures beyond the collinear ferromagnetic (FM) or antiferromagnetic (AFM) alignments, *i.e.*, spin spirals of unique rotational sense [5–8] or skyrmions [9, 10], *i.e.*, twodimensional topologically protected vortex spin structures. Furthermore, magnetic properties of such systems are extremely sensitive to small manipulations in the structural arrangement [11, 12].

The understanding of magnetism at the atomic level was greatly boosted by the development of the scanning tunneling microscope (STM) by Gerd Binnig and Heinrich Rohrer [13]. Since the tunneling current from the STM tip to the analyzed sample decays exponentially with distance, this microscope produces an extremely precise topographical image of the surface structure with an accuracy in the sub-nanometer scale. By use of a spin-polarized tip, the image carries information about the magnetic texture of the structure in atomic resolution [14, 15]. In 1998 Stipe *et al.* [16] demonstrated for the first time how dynamical properties of the system can be studied, *i.e.*, excitations of the system. This is achieved by sweeping the applied bias voltage while the position of the tip is kept fixed. Then, these excitations are found in inelastic scanning tunneling spectroscopy (ISTS) measurements. For molecules or clusters deposited on surfaces, vibrational excitations can be found and are usually observed with excitation energies of several tenths electron volts [17]. In magnetic materials, spin-excitations may provide additional tunneling channels that allow the electrons to inelastically tunnel from tip to surface and *vice versa*, which results in a sudden change in the conductance spectrum at the corresponding excitation energy [12, 18–23].

These spin-excitation signatures are usually assumed to manifest as a step-like increase (or decrease for its counterpart at negative bias voltages) of the conductance spectrum. In fact, such spectra are usually interpreted in terms of quantum Heisenberg models [12, 18, 24–28] and beyond [29, 30]. By this procedure, however, certain characteristics of the measured excitation spectra are not accessible, for example asymmetries in the observed inelastic spectra or even the extinction of the spin-excitation signature. The lifetime of the excitation is often accounted for by means of an external parameter, however, within such a procedure its physical origin remains hidden. These models show good agreement to experiment as long as the adsorbate only couples weakly to the substrate [12, 18]. However, they do not properly account for cases where strong hybridization with the substrate electrons is present, leading to magnetic moments of the impurity atom which are far from integer or half-integer values. Furthermore, they rely on input parameters from experiment and therefore show a limited potential in exploring the behavior of designed chemical structures that have not been realized in experiment.

Parameter-free approaches to explore the spin-dynamics of a given system are rare. While density functional theory (DFT) shows tremendous success in describing ground-state properties of solids, the study of excitations is beyond its scope. Instead, two distinct concepts are established as reasonable extensions to the DFT formalism, capable to properly account for dynamical magnetic effects. On the one hand, time-dependent DFT

(TDDFT) allows the study of magnetization dynamics, as demonstrated for example by Buczek *et al.* [31] in an ultrathin Co(100) film exposed to a nonuniform magnetic field. The second approach utilizes many-body perturbation theory (MBPT), where magnetic scattering processes in a solid are accounted for by means of a so-called T-matrix [32–34]. In both approaches, the transverse dynamical magnetic susceptibility, χ, plays a central role, as it gives access to the magnetic response properties of a system [21, 35, 36]. For instance, when the hybridization between nanostructure and surface is not negligible, χ provides information on the intrinsic spectrum of spin excitations. Recently, this quantity has been evaluated in the context of adatoms on metallic surfaces by means of a fully first-principles approach [37, 38]. In this way, main characteristics, such as the excitation energy, the g shift, and the lifetime of the spin excitation can be obtained and compared to experimental findings [20, 23].

In this thesis we go beyond the description of the magnetic properties and describe theoretically the inelastic tunneling spectra as measured by an STM setup. This closes a gap between experiment and theory in the sense that the measured inelastic spectra contain the signature of the spin excitation as probed by an STM tip in the vacuum above the adsorbate, which is not captured by χ. Therefore, the main purpose of this novel approach is to directly access the inelastic tunneling spectra by means of a first-principles scheme. The coupling of the tunneling electrons to the spin excitation is described in terms of the electron self-energy, Σ. The applied method is based on the Korringa-Kohn-Rostoker (KKR) Green function method embedded in a TDDFT formalism in combination with MBPT. Thus, this method provides a realistic description of theoretical inelastic tunneling spectra. The advantage of such a scheme lies in the direct access to the Green function renormalized by the interaction of the spin-excitation with the electronic structure. Thus, one is able to predict the shapes of realistic excitation spectra in the vacuum region above the impurity or at any position next to it which represents a powerful tool to analyze and predict inelastic excitation spectra. In the spirit of the Tersoff-Hamann approximation [39] the renormalized electronic structure can be related to such measured spectra. With this method many aspects of these spectra can be observed and related to the electronic structure of the system.

With this novel method at hand we study the magnetization dynamics in nanostructures consisting of one or more $3d$ transition-metal (TM) adatoms (Cr, Mn, Fe and Co) deposited on Cu(111) as well as on Pt(111). This choice allows to compare to experimental ISTS studies [20, 23, 40] in order to demonstrate the ability of our scheme. On top of that, the predictive power of the presented approach is used to explore the spin-dynamics in nanostructures on surfaces that have not been measured in experiment so far, guiding experimentalists to promising candidates for ISTS studies in the future.

In the following the outline of the thesis is given: In Ch. 2 the fundamentals of DFT and TDDFT are presented, representing the theoretical basis of this work. The subsequent Ch. 3 is devoted to the KKR Green function method. Beyond the formalism that is found in the literature, the projected form of the KKR Green function is discussed, which is used

in the calculated dynamical properties. This is followed by Ch. 4, where the dynamical magnetic susceptibility in the framework of linear response DFT is introduced. The derivation of the self-energy in the framework of MBPT in Ch. 5 concludes the description of the theoretical background. It is shown how this object is mapped onto the TDDFT formalism used in the present thesis.

The subsequent Chs. 6, 7, and 8 present results obtained by use of the newly derived method: In Ch. 6 different transition-metal adatoms placed on the Cu(111) surface are considered and the resulting excitation spectra are described and analyzed in detail. First, the intrinsic spin-excitation spectra for the investigated adatoms are analyzed. A discussion of g shifts and lifetimes is given and connected to the electronic structure. Second, the self-energy for these systems and the renormalized spectra for the adatoms and the vacuum position above the adatoms are described.

The following Ch. 7 examines excitation spectra for TM adatoms on the Pt(111) surface. A comparison to the results obtained for the Cu(111) surface and to experimental findings are given. In addition, the impact on the obtained spectra is investigated when a hydrogen atom is positioned next to an Fe or a Co adatom on Pt(111).

Spin-excitation spectra for nanostructures of two or more magnetic adatoms on the Cu(111) surface are considered in Ch. 8. This analysis covers four different aspects: (i) an extensive study of spectra for ferromagnetic and antiferromagnetic spin alignments in dimers, (ii) trimer spectra for a linear or a triangular arrangement, (iii) how excitation spectra evolve in the process of building a chain of atoms, one by one, and (iv) the impact of topological arrangements by comparing spectra for rings or chains consisting of the same number of adatoms.

Finally in Ch. 9 we summarize the results that have been obtained within the thesis. A short outlook of possible improvements and further developments of the method as well as suggestions for future applications of the method conclude the thesis.

2. Density functional theory and its time-dependent extension

A typical condensed matter system consists of a very large number of interacting particles (a grain of sand already contains about 10^{15} to 10^{19} atoms). At a first sight, the theoretical investigation of such a system, in particular its ground state properties or even its low-energy collective excitations, is thus impossible due to the interacting nature of the problem. The impact of these collective excitations is crucial in determining several properties of materials, including those related to transport phenomena, magnetism, vibrations, and fluctuations. For instance, thermal expansion can be understood in terms of phonons (collective vibrations of the atoms in a solid), that behave like weakly interacting quasi-particles. Other examples of quasi-particles are magnons (collective spin-excitations) or plasmons (collective charge-excitations).

With this in mind, a reasonable description of such a complex system requires the following two steps: First, a proper characterization of the ground state is needed. For this purpose, density functional theory (DFT) has emerged to be the tool of choice. Then, the associated low-energy excitations are obtained from its dynamical extension, time-dependent DFT (TDDFT).

The structure of this chapter is as follows: After introducing the many-body problem in Sec. 2.1 we first consider a time-independent problem and discuss the formalism of DFT in Sec. 2.2. This is followed by Sec. 2.3 in which the main aspects of TDDFT are

presented. A connection to linear response is drawn paving the way to Ch. 4 in which the response function is discussed in more detail. The Chapter concludes with a brief summary in Sec. 2.4

2.1. The many-body problem

Suppose a system of N electrons in a solid is described by the quantum-mechanical state $|\Psi(t)\rangle$ which is solution to the Schrödinger equation

$$\mathrm{i}\frac{\partial}{\partial t}|\Psi(t)\rangle = \mathcal{H}(t)|\Psi(t)\rangle \ . \tag{2.1}$$

A first attempt to simplify the task of solving Eq. (2.1) is the Born-Oppenheimer approximation [41] in which the N_a nuclei are assumed to be at fixed positions $\{\vec{R}_I\}$ and enter the Hamiltonian in Eq. (2.1) as a set of parameters. Then, the corresponding time-dependent Hamiltonian $\mathcal{H}(t)$ in Eq. (2.1) decomposes into[1]

$$\mathcal{H}(t) = \mathcal{T} + \mathcal{W} + \mathcal{V}_{\mathrm{ext}}(t) \ , \tag{2.2}$$

with the kinetic energy

$$\mathcal{T} = -\sum_{i=1}^{N} \vec{\nabla}_i^2 \ , \tag{2.3}$$

the electron-electron interaction

$$\mathcal{W} = \frac{1}{2}\sum_{i=1}^{N}\sum_{j=1;j\neq i}^{N} \frac{2}{|\vec{r}_i - \vec{r}_j|} \ , \tag{2.4}$$

and the external potential

$$\mathcal{V}_{\mathrm{ext}}(t) = \sum_{i=1}^{N} \left[v_{\mathrm{nuc}}(\vec{r}_i) + v_{\mathrm{ext}}(\vec{r}_i, t)\right] \ , \tag{2.5}$$

where $\vec{r}_i$ is the position of the electron with label i. The external potential further splits into the (time-independent) external potential caused by the nuclei,

$$v_{\mathrm{nuc}}(\vec{r}_i) = -\sum_{I=1}^{N_a} \frac{2Z_I}{\left|\vec{r}_i - \vec{R}_I\right|} \ , \tag{2.6}$$

where Z_I is the charge number of the nucleus with label I, and $v_{\mathrm{ext}}(\vec{r}_i, t)$, which contains the coupling to time-dependent external fields. In principle, the Hamiltonian in Eq. (2.1) also

[1] Throughout this thesis formulas are given in Rydberg atomic units if not stated otherwise, see Appendix A.

contains higher-order terms that describe relativistic effects (such as spin-orbit coupling). In this thesis, however, such phenomena are not considered.

In the Schrödinger picture, the expectation value of an observable $A(t)$, *i.e.*, a quantity that could be measured in an experiment, is given by

$$\langle A(t)\rangle_{\Psi(t)} = \langle\Psi(t)|\mathcal{A}|\Psi(t)\rangle \;, \tag{2.7}$$

where $\mathcal{A}$ denotes the corresponding operator (an explicit time-dependency is possible, see for example Eq. (2.9)). If a complete and discrete set of eigenvectors $\{\phi_j(t)\}$ and eigenvalues $\{a_j(t)\}$ to this operator is known, Eq. (2.7) can be written as

$$\langle A(t)\rangle_{\Psi(t)} = \sum_j \langle\Psi(t)|\mathcal{A}|\phi_j(t)\rangle\langle\phi_j(t)|\Psi(t)\rangle = \sum_j a_j(t)\,|\langle\phi_j(t)|\Psi(t)\rangle|^2 \;, \tag{2.8}$$

which has an analogue integral form for operators with a continuous spectrum of eigenstates. The charge density of such a system is given by

$$n(\vec{r},t) = \langle\Psi(t)|\sum_{i=1}^{N}\delta(\vec{r}-\vec{r}_i)\mathcal{P}|\Psi(t)\rangle \;, \tag{2.9}$$

where $\vec{r}_i$ represents the position of particle i and

$$\mathcal{P} = |\vec{r}_1,\ldots,\vec{r}_N\rangle\langle\vec{r}_1,\ldots,\vec{r}_N| \tag{2.10}$$

is the projection operator onto the set of electronic positions $\{\vec{r}_i\}$. For the case that the investigated system is magnetic one defines the vector spin-density

$$\vec{m}(\vec{r},t) = \langle\Psi(t)|\sum_{i=1}^{N}\delta(\vec{r}-\vec{r}_i)\mathcal{P}\otimes\vec{\boldsymbol{\sigma}}|\Psi(t)\rangle \;, \tag{2.11}$$

where the vector

$$\vec{\boldsymbol{\sigma}} = \begin{pmatrix}\boldsymbol{\sigma}_x\\ \boldsymbol{\sigma}_y\\ \boldsymbol{\sigma}_z\end{pmatrix} \tag{2.12}$$

of Pauli matrices

$$\boldsymbol{\sigma}_x = \begin{pmatrix}0 & 1\\ 1 & 0\end{pmatrix} \quad , \quad \boldsymbol{\sigma}_y = \begin{pmatrix}0 & -\mathrm{i}\\ \mathrm{i} & 0\end{pmatrix} \quad , \quad \boldsymbol{\sigma}_z = \begin{pmatrix}1 & 0\\ 0 & -1\end{pmatrix} \tag{2.13}$$

has been introduced. Together with the unity matrix in spin space

$$\boldsymbol{\sigma}_0 = \begin{pmatrix}1 & 0\\ 0 & 1\end{pmatrix} = \mathbb{1}_{2\times2} \tag{2.14}$$

the Pauli matrices form a complete basis set for the spin space. With the definition of the four-vector density and the generalized projection operator,

$$\underline{n}(\vec{r},t) = \begin{pmatrix} n(\vec{r},t) \\ \vec{m}(\vec{r},t) \end{pmatrix} \quad \text{and} \quad \underline{\mathcal{P}} = \mathcal{P} \otimes \underline{\boldsymbol{\sigma}} \,, \quad \text{where} \quad \underline{\boldsymbol{\sigma}} = \begin{pmatrix} \boldsymbol{\sigma}_0 \\ \vec{\boldsymbol{\sigma}} \end{pmatrix} \tag{2.15}$$

one can write Eqs. (2.9) and (2.11) in a more compact way,

$$n_\alpha(\vec{r},t) = \langle \Psi(t)| \sum_{i=1}^{N} \delta(\vec{r}-\vec{r}_i) \mathcal{P}_\alpha |\Psi(t)\rangle \,, \tag{2.16}$$

where $\alpha \in \{0,x,y,z\}$.

The attempt to solve Eq. (2.1) directly requires to get access to the wave function in spatial representation,

$$\langle \vec{r}_1,\ldots,\vec{r}_N|\Psi(t)\rangle = \Psi(\vec{r}_1,\ldots,\vec{r}_N;t) \,, \tag{2.17}$$

an object that depends on $3N+1$ variables (the spin-degree of freedom is not even accounted for). It is already problematic if not impossible to store the information of such a wave function for a reasonable number of particles: For a given time argument, a relatively small number of $N = 100$ electrons, and a coarse grid point mesh of 10 points per degree of freedom in the spatial coordinates, one would have to store 10^{100} different numbers. Realizing that the estimated amount of information that the entire universe can register is of the same order of magnitude [42], a more efficient way to describe such many-body problems has to be utilized, *i.e.*, a method which avoids the determination of the wave function in Eq. (2.17). Such an alternative approach is provided by DFT in which the task of finding the full wave function is substituted by the search for the electronic density. The basic concepts of this method are presented in the next Sec. 2.2.

2.2. Ground-state DFT

Suppose that the Hamiltonian $\mathcal{H}$ does not depend on time. With the ansatz $|\Psi(t)\rangle = \mathrm{e}^{-\mathrm{i}Et}|\Psi\rangle$ Eq. (2.1) results in the eigenvalue problem

$$\mathcal{H}|\Psi_n\rangle = E_n|\Psi_n\rangle \quad , \quad E_0 \leq E_1 \leq \ldots \,. \tag{2.18}$$

The ground state is described by the lowest eigenenergy, $E_{\mathrm{GS}} = E_0$, and the corresponding eigenstate, $|\Psi_{\mathrm{GS}}\rangle = |\Psi_0\rangle$. Setting spin aside for the moment, the ground-state density is connected to the spatial representation of the ground-state wave function via

$$n_{\mathrm{GS}}(\vec{r}) = \sum_{i=1}^{N} \int \mathrm{d}^3 r_1 \cdots \int \mathrm{d}^3 r_N \Psi^*_{\mathrm{GS}}(\vec{r}_1,\ldots,\vec{r}_N) \delta(\vec{r}-\vec{r}_i) \Psi_{\mathrm{GS}}(\vec{r}_1,\ldots,\vec{r}_N) \,. \tag{2.19}$$

2.2.1. The theorems of Hohenberg and Kohn

In 1964 Hohenberg and Kohn [43] proved that the ground-state energy is a unique functional of the system's ground-state density, $n_{\mathrm{GS}}(\vec{r})$, provided that the ground state is non-degenerate, $E_0 < E_1$.[2] In a first theorem, they showed that there exists a one-to-one correspondence between the external potential $v_{\mathrm{ext}}(\vec{r})$ and the ground-state density (up to a constant shift in the potential),

$$v_{\mathrm{ext}}(\vec{r}) \leftrightarrow n_{\mathrm{GS}}(\vec{r}) \ . \tag{2.20}$$

In fact, the uniqueness of the ground-state density allows to represent the Hamiltonian and thus any other desired observable as a functional of the density (hence the name density functional theory). A second theorem states that the functional of the total energy get minimal for the ground-state density,

$$E_0 = E[n_{\mathrm{GS}}] = \min_n E[n] \ , \tag{2.21}$$

where the minimization condition accounts for densities that satisfy the condition $N = \int \mathrm{d}^3 r \ n(\vec{r})$. The formalism can be extended to magnetic systems, where instead of the density alone, a pair of density and magnetization serves as central basis, *e.g.*, $\mathcal{V}[n] \to \mathcal{V}[n, \vec{m}]$.

Although the theorems of Hohenberg and Kohn ensures that the ground-state density is sufficient to describe the system completely the task remains to find it. This can be achieved by means of the Kohn-Sham formalism [45] which will be presented in the next section.

2.2.2. The Kohn-Sham formalism

The central idea of the Kohn-Sham formalism is to introduce an auxiliary system of non-interacting particles that yields the same ground-state density as the one for the interacting electrons. By introducing the Kohn-Sham orbitals $\{\phi_j\}$ and accounting for the condition

$$n_{\mathrm{GS}}(\vec{r}) = \sum_{j=1}^{N} |\phi_j(\vec{r})|^2 \ , \tag{2.22}$$

one has to solve the Kohn-Sham equations,

$$\left(-\vec{\nabla}^2 + v_{\mathrm{eff}}[n_{\mathrm{GS}}](\vec{r})\right) \phi_j(\vec{r}) = \epsilon_j \phi_j(\vec{r}) \ , \tag{2.23}$$

which have the form of single-particle Schrödinger equations. The effective single-particle potential v_{eff} is an unknown functional of the ground-state density n_{GS}. The remaining

[2] The constraint of the original proof to be limited to systems with a non-degenerate ground state could be overcome by Levy [44] in 1979.

difficulty lies now in a clever way of splitting this potential into parts that are accessible and of dominant character and parts that are unknown yet and give only a small contribution. This is achieved by the Ansatz

$$v_{\text{eff}}(\vec{r}) = v_{\text{ext}}(\vec{r}) + v_{\text{H}}(\vec{r}) + v_{\text{xc}}(\vec{r}) \tag{2.24}$$

where besides the external potential (see Eq. (2.5)) and the Hartree potential

$$v_{\text{H}}(\vec{r}) = \int \mathrm{d}^3 r' \frac{2n(\vec{r}')}{|\vec{r} - \vec{r}'|} \tag{2.25}$$

the so-called *exchange-correlation* potential $v_{\text{xc}}(\vec{r})$ is introduced, collecting the remaining parts of v_{eff} that are not described by the $v_{\text{ext}}(\vec{r})$ or $v_{\text{H}}(\vec{r})$. The energy functional from Eq. (2.21) then reads

$$E[n] = T_s[n] + E_{\text{H}}[n] + E_{\text{xc}}[n] + E_{\text{ext}}[n] \ , \tag{2.26}$$

where

$$T_s[n] = -\int \mathrm{d}^3 r \sum_{j=1}^{\text{occ.}} \psi_j^*(\vec{r}) \nabla^2 \psi_j(\vec{r}) \tag{2.27}$$

is the kinetic energy of the Kohn-Sham orbitals,

$$E_{\text{H}}[n] = \int \mathrm{d}^3 r \int \mathrm{d}^3 r' \, \frac{n(\vec{r}) n(\vec{r}')}{|\vec{r} - \vec{r}'|} \tag{2.28}$$

is the Hartree energy, and $E_{\text{xc}}[n]$ is the exchange-correlation part of the energy functional and the remaining unknown. In fact, Eq. (2.26) defines E_{xc}. Its connection to the exchange-correlation potential (see Eq. (2.24)) is given by

$$v_{\text{xc}}[n_{\text{GS}}](\vec{r}) = \left. \frac{\delta E_{\text{xc}}[n]}{\delta n(\vec{r})} \right|_{n(\vec{r}) = n_{\text{GS}}(\vec{r})} \tag{2.29}$$

Note that the effective potential $v_{\text{eff}}(\vec{r})$ in Eq. (2.24) depends on the density and that this density, in return, is build by the solutions of Eq. (2.23), so the Kohn-Sham equations form a self-consistent problem. In fact, finding a self-consistent solution represents one of the most time-demanding tasks of any DFT-based code.

For the spin-dependent formulation the Kohn-Sham equation (2.23) takes the form

$$\left[\left(-\vec{\nabla}^2 + v_{\text{eff}}[n_{\text{GS}}, \vec{m}_{\text{GS}}](\vec{r}) \right) \boldsymbol{\sigma_0} + \vec{B}_{\text{eff}}[n_{\text{GS}}, \vec{m}_{\text{GS}}](\vec{r}) \cdot \vec{\boldsymbol{\sigma}} \right] \boldsymbol{\phi}_j(\vec{\mathrm{r}}) = \epsilon_j \boldsymbol{\phi}_j(\vec{r}) \ , \tag{2.30}$$

where

$$\boldsymbol{\phi}(\vec{r}) = \begin{pmatrix} \phi^{\uparrow}(\vec{r}) \\ \phi^{\downarrow}(\vec{r}) \end{pmatrix} = \sum_{\sigma = \uparrow, \downarrow} \phi^{\sigma}(\vec{r}) \boldsymbol{\chi}^{\sigma} \tag{2.31}$$

is a spinor of Kohn-Sham orbitals expressed in terms of the basis vectors in spin space,

$$|\uparrow\rangle \equiv \boldsymbol{\chi}^{\uparrow} \equiv \begin{pmatrix} 1 \\ 0 \end{pmatrix} \quad \text{and} \quad |\downarrow\rangle \equiv \boldsymbol{\chi}^{\downarrow} \equiv \begin{pmatrix} 0 \\ 1 \end{pmatrix} . \tag{2.32}$$

In Eq. (2.30) the previously introduced unity matrix in spin space and the vector of Pauli matrices ($\boldsymbol{\sigma_0}$ and $\vec{\boldsymbol{\sigma}}$, *cf.* Eqs. (2.13) and (2.14)) enter. The effective potential now depends on charge density and vector spin density of the ground state, $v_{\text{eff}} = v_{\text{eff}}[n_{\text{GS}}, \vec{m}_{\text{GS}}]$, where

$$n_{\text{GS}}(\vec{r}) = \sum_{j=1}^{N} \boldsymbol{\phi}_j(\vec{r})^{\dagger} \boldsymbol{\sigma}_0 \boldsymbol{\phi}_j(\vec{r}) \quad \text{and} \quad \vec{m}_{\text{GS}}(\vec{r}) = \sum_{j=1}^{N} \boldsymbol{\phi}_j(\vec{r})^{\dagger} \vec{\boldsymbol{\sigma}} \boldsymbol{\phi}_j(\vec{r}) , \tag{2.33}$$

and the dagger (†) denotes transposition of the spinor and complex conjugation of its components. Furthermore, in Eq. (2.30) the effective magnetic potential

$$\vec{B}_{\text{eff}}(\vec{r}) = \vec{B}_{\text{ext}}(\vec{r}) + \vec{B}_{\text{xc}}(\vec{r}) \tag{2.34}$$

was introduced, where $\vec{B}_{\text{ext}}$ is the external magnetic field and

$$\vec{B}_{\text{xc}}(\vec{r}) = \left. \frac{\delta\, E_{\text{xc}}[n, \vec{m}]}{\delta\, \vec{m}(\vec{r})} \right|_{n, \vec{m} = n_{\text{GS}}, \vec{m}_{\text{GS}}} \tag{2.35}$$

is the definition of the exchange-correlation magnetic potential. Thus, the effective magnetic potential is also a functional of charge and vector spin-density for the ground state, $\vec{B}_{\text{eff}} = \vec{B}_{\text{eff}}[n_{\text{GS}}, \vec{m}_{\text{GS}}]$.

For the case that the effective magnetic field points along the z direction, $\vec{B}_{\text{eff}} = B_{\text{eff}} \hat{\text{e}}_z$, one can write

$$n_{\text{GS}}(\vec{r}) = n^{\uparrow}_{\text{GS}}(\vec{r}) + n^{\downarrow}_{\text{GS}}(\vec{r}) \tag{2.36}$$

$$\text{and} \quad m_{\text{GS},z}(\vec{r}) = n^{\uparrow}_{\text{GS}}(\vec{r}) - n^{\downarrow}_{\text{GS}}(\vec{r}) , \tag{2.37}$$

where

$$n^{\sigma}_{\text{GS}}(\vec{r}) = \sum_{j=1}^{N} \left| \phi^{\sigma}_j(\vec{r}) \right|^2 \quad , \quad \sigma \in \{\uparrow, \downarrow\} \tag{2.38}$$

was introduced.

2.2.3. A practical approximation to the exchange-correlation energy

The functional dependence of the exchange-correlation energy $E_{\text{xc}}[n]$ on the density $n(\vec{r})$ is unknown. A central task in every DFT-based code is to approximate this quantity in a

way that satisfies the expected computational performance best. Over the years, different more or less involving approximations have been proposed suitable for all types of physical problems (see for example Refs. [46] and [47] for a review). The earliest and simplest approach is the local density approximation (LDA)

$$E_{\mathrm{xc}}^{\mathrm{LDA}}[n] = \int \mathrm{d}^3 r \; e_{\mathrm{xc}}^{\mathrm{hom}}(n(\vec{r})) \; , \tag{2.39}$$

where $e_{\mathrm{xc}}^{\mathrm{hom}}(n(\vec{r})) = e_{\mathrm{xc}}^{\mathrm{hom}}(\overline{n})|_{\overline{n}=n(\vec{r})}$ is the exchange-correlation energy for a homogeneous electron gas evaluated for the local density $\overline{n} = n(\vec{r})$. Due to its construction, the LDA is exact for the homogeneous electron gas and reasonable accurate when the density varies slowly with space. A decomposition of $e_{\mathrm{xc}}^{\mathrm{hom}}$ into an exchange part and a correlation part is possible, where the former is accessible through the Hartree-Fock formalism for a homogeneous electron gas [48]. In order to determine the correlation part one can use, *e.g.*, the Quantum Monte-Carlo method [49]. The extension to account for the spin degree of freedom is called local spin density approximation (LSDA),

$$E_{\mathrm{xc}}^{\mathrm{LDA}}[n, \vec{m}] = \int \mathrm{d}^3 r \; e_{\mathrm{xc}}^{\mathrm{hom}}(n(\vec{r}), \vec{m}(\vec{r})) \; . \tag{2.40}$$

The current work uses such a parametrization as proposed by Vosko, Wilk, and Nusair [50]. More involved approximations incorporate the gradient of the density (known as generalized gradient approximation, GGA) and beyond. For more information the reader is referred to the literature, *e.g.*, Refs. [46] and [47].

2.3. Time-dependent DFT

The fundamental task within density functional theory is to obtain the ground-state density $n_{\mathrm{GS}}(\vec{r})$ of a system. For its time-dependent counterpart there exists a similar theorem to the ones of Hohenberg and Kohn which connects the fundamental properties of a system that varies with time to its density at a given time t, $n(\vec{r}, t)$ (not necessarily the ground-state density).

However, the situation differs in two aspects to the one of conventional DFT: First, the variational minimum principle to obtain the system's total energy is not valid anymore, as its expectation value is not a conserved quantity anymore. Second, the corresponding time-dependent Schrödinger equation (and thus the corresponding time-dependent Kohn-Sham equations) represents an initial-value problem (unlike the stationary Schrödinger equation which is a boundary-value problem). This means that in addition to the time-dependent density any solution to the problem contains a dependence on $|\Psi(t_0)\rangle$, the initial state of the system for a given time t_0.

2.3.1. The theorem of Runge and Gross

In 1984 Runge and Gross [51] formulated a theorem analogous to the ones of Hohenberg and Kohn. They proved that – up to a time-dependent function $c(t)$ – there exists a one-to-one correspondence between the time-dependent external potential, $v_{\mathrm{ext}}(\vec{r},t)$ and the electronic one-body density, $n(\vec{r},t)$, for many-body systems evolving from a fixed initial state $|\Psi_0(t_0)\rangle$ with $t > t_0$,

$$v_{\mathrm{ext}}(\vec{r},t) + c(t) \leftrightarrow n(\vec{r},t) \; . \tag{2.41}$$

The original proof of Runge and Gross contains a restriction to external potentials that are Taylor-expandable about the initial time t_0,

$$v_{\mathrm{ext}}(\vec{r},t) = \sum_{k=0}^{\infty} \frac{v_{\mathrm{ext},k}(\vec{r})}{k!}(t-t_0)^k \; , \quad \text{where} \quad v_{\mathrm{ext},k}(\vec{r}) = \left.\frac{\partial^k v_{\mathrm{ext}}(\vec{r},t)}{\partial t^k}\right|_{t=t_0} \; . \tag{2.42}$$

An alternative proof by van Leeuwen [52] lifts this constraint.

2.3.2. Time-dependent Kohn-Sham formalism

The stationary Kohn-Sham equations (see Eq. (2.23)) have also a TDDFT counterpart. Again, an auxiliary system with non-interacting particles is introduced, the Kohn-Sham orbitals $\phi_j(\vec{r},t)$, which satisfy the condition to reproduce the density for the interacting system at a given time t,

$$n(\vec{r},t) = \sum_{j=1}^{N} |\phi_j(\vec{r},t)|^2 \; . \tag{2.43}$$

These orbitals $\phi_j(\vec{r},t)$ are solutions to the time-dependent Kohn-Sham equations

$$\mathrm{i}\frac{\partial}{\partial t}\phi_j(\vec{r},t) = \left(-\vec{\nabla}^2 + v_{\mathrm{eff}}[n,\Psi_0,\Phi_0](\vec{r},t)\right)\phi_j(\vec{r},t) \; . \tag{2.44}$$

Now the effective potential becomes a functional of the density as well as the initial states of interacting and non-interacting system, Ψ_0 and Φ_0, respectively. As it is done for the time-independent analogue one splits it into time-dependent external potential v_{ext}, Hartree potential v_{H}, and the exchange-correlation potential v_{xc}, where the functional dependence gets transferred to the latter:

$$v_{\mathrm{eff}}[n,\Psi_0,\Phi_0](\vec{r},t) = v_{\mathrm{ext}}(\vec{r},t) + v_{\mathrm{H}}(\vec{r},t) + v_{\mathrm{xc}}[n,\Psi_0,\Phi_0](\vec{r},t) \; . \tag{2.45}$$

Thus, the task of finding a reasonable expression for the exchange and correlation part of the effective potential becomes even more difficult as it was the case for DFT. In most situations, however, the density history stored in the exchange-correlation part can be

dropped, making it local in time. This is known as adiabatic approximation, which can be combined with the LDA (see Eq. (2.39)) to give the adiabatic LDA (ALDA)

$$v_{\mathrm{xc}}^{\mathrm{ALDA}}(\vec{r},t) = v_{\mathrm{xc}}^{\mathrm{LDA}}(n(\vec{r}))\big|_{n(\vec{r})=n(\vec{r},t)} \ . \tag{2.46}$$

The vast majority of TDDFT-based calculations employ this approximation, see for example Ref. [47] for a review.

The time-dependent Kohn-Sham equation (2.44) can be formulated in a spin-polarized form (analogue to Eq. (2.30)), where a time-dependent effective magnetic potential

$$\vec{B}_{\mathrm{eff}}(\vec{r},t) = \vec{B}_{\mathrm{ext}}(\vec{r},t) + \vec{B}_{\mathrm{xc}}(\vec{r},t) \tag{2.47}$$

enters, that is a sum of external field $\vec{B}_{\mathrm{ext}}$ and exchange-correlation field $\vec{B}_{\mathrm{xc}}$. The latter quantity can be expressed by introducing the spin in the adiabatic version of the LSDA (ALSDA).

2.3.3. Charge linear response and TDDFT

In most applications of spectroscopy a small perturbation (*e.g.*, a probing laser pulse or a low-energy electron beam) is used to analyze the spectral properties of a system. In such cases, the system occupies states that do not deviate much from the ground state $|\Psi_{\mathrm{GS}}\rangle$. Although for this type of problems the application of the full formalism of TDDFT leads to the correct description, one can avoid the overhead by treating the system in linear response theory.

Consider that the external potential is described by a time-independent potential coming from the nuclei (*cf.* Eq. (2.6)) and a small time-dependent contribution that is switched on at a given time t_0,

$$v_{\mathrm{ext}}(\vec{r},t) = \begin{cases} v_{\mathrm{nuc}}(\vec{r}) & , \quad t < t_0 \\ v_{\mathrm{nuc}}(\vec{r}) + \delta v_{\mathrm{ext}}(\vec{r},t) & , \quad t \geq t_0 \end{cases} \ . \tag{2.48}$$

As a direct consequence of switching on the time-dependent perturbation in the external potential for $t > t_0$, the system will deviate from its ground state and the ansatz

$$n(\vec{r},t) = \begin{cases} n_{\mathrm{GS}}(\vec{r}) & , \quad t < t_0 \\ n_{\mathrm{GS}}(\vec{r}) + \delta n(\vec{r},t) & , \quad t \geq t_0 \end{cases} \tag{2.49}$$

becomes reasonable. The central idea in linear response is that one can relate the induced change in the density, $\delta n(\vec{r},t)$, to the small variation of the external potential, $\delta v_{\mathrm{ext}}(\vec{r},t)$, in a linear fashion,

$$\delta n(\vec{r},t) = \int \mathrm{d}^3 r' \int \mathrm{d}t' \ \chi(\vec{r},t;\vec{r}',t') \delta v_{\mathrm{ext}}(\vec{r}',t') \ . \tag{2.50}$$

The connecting element in Eq. (2.50) is the full or enhanced susceptibility $\chi(\vec{r},t;\vec{r}\,',t')$.

In the corresponding Kohn-Sham system the formalism is a bit more involving: the induced change in the density leads to a change in the effective potential, as it is a functional of the density.[3] One finds the expression

$$\delta v_{\mathrm{eff}}[n](\vec{r},t) \;=\; \underbrace{\delta v_{\mathrm{H}}(\vec{r},t)+\delta v_{\mathrm{xc}}[n](\vec{r},t)}_{\text{induced}}+\underbrace{\delta v_{\mathrm{ext}}(\vec{r},t)}_{\text{direct}}\;. \tag{2.51}$$

In Eq. (2.51) it is stressed that the change in the external potential is direct whereas the changes in the Hartree and the exchange-correlation potential are induced. The latter two are of the form

$$\delta v_{\mathrm{H}}(\vec{r},t)=\int \mathrm{d}^3r'\frac{2}{|\vec{r}-\vec{r}\,'|}\delta n(\vec{r}\,',t) \tag{2.52}$$

and

$$\delta v_{\mathrm{xc}}[n](\vec{r},t)=\int \mathrm{d}^3r'\int \mathrm{d}t' f_{\mathrm{xc}}[n](\vec{r},t;\vec{r}\,',t')\delta n(\vec{r}\,',t')\;, \tag{2.53}$$

where the exchange-correlation kernel

$$f_{\mathrm{xc}}[n](\vec{r},t;\vec{r}\,',t')=\frac{\delta v_{\mathrm{xc}}(\vec{r},t)}{\delta n(\vec{r}\,',t')} \tag{2.54}$$

has been introduced. The change in the density is directly related to the variation of the effective potential via the Kohn-Sham susceptibility $\chi_{\mathrm{KS}}(\vec{r},t;\vec{r}\,',t')$

$$\delta n(\vec{r},t)=\int \mathrm{d}^3r'\int \mathrm{d}t'\;\chi_{\mathrm{KS}}(\vec{r},t;\vec{r}\,',t')\delta v_{\mathrm{eff}}[n](\vec{r}\,',t')\;. \tag{2.55}$$

The Kohn-Sham susceptibility is explicitly given in terms of the ground-state Kohn-Sham eigenenergies and eigenorbitals, which will be demonstrated in Ch. 4.

A connection of the Kohn-Sham susceptibility χ_{KS} to the full susceptibility χ is given by use of Eq. (2.51) and by comparing Eqs. (2.50) and (2.55), and reads

$$\begin{aligned}\chi(\vec{r},t;\vec{r}\,',t') \;=\;& \chi_{\mathrm{KS}}(\vec{r},t;\vec{r}\,',t')+\int \mathrm{d}^3r_1\int \mathrm{d}t_1\int \mathrm{d}^3r_2\int \mathrm{d}t_2\\ & \chi_{\mathrm{KS}}(\vec{r},t;\vec{r}_2,t_2)\left(\frac{2\delta(t_2-t_1)}{|\vec{r}_2-\vec{r}_1|}+f_{\mathrm{xc}}[n](\vec{r}_2,t_2;\vec{r}_1,t_1)\right)\chi(\vec{r}_1,t_1;\vec{r}\,',t')\;.\end{aligned} \tag{2.56}$$

Due to its form, Eq. (2.56) is referred to as Dyson-like equation. Note that the presented formalism can naturally be extended to spin polarized systems. Such an extension will be shown in detail in Ch. 4.

[3] For simplicity the dependence on the initial states of interacting and non-interacting system, Ψ_0 and Φ_0, respectively, is dropped here.

2.4. Summary

In this chapter the concepts of density functional theory (DFT) and its time-dependent extension (TDDFT) have been introduced as suitable methods to study ground-state properties as well as time-dependent phenomena in solids. For the regime of low-energy excitations a TDDFT approach involving linear response theory has been presented in which the enhanced susceptibility χ is connected to the one of the Kohn-Sham system, χ_{KS}, via a Hartree kernel and the exchange-correlation kernel f_{xc}. However, it turns out that the correct description of the excitations of the system requires a careful and consistent treatment of the pair of Kohn-Sham susceptibility and exchange-correlation kernel. This issue will be addressed in Ch. 4 where a connection of the kernel to the density via a sum rule is made.

Furthermore, besides the DFT-based approach there exists another powerful route towards low-energy excitations based on many-body perturbation theory (MBPT), see Ch. 5. There, the central quantity is the self-energy Σ, which corrects the non-interacting quasi-particle states by modifying their energy and giving them a finite lifetime, and leads to a renormalization of the electronic structure. At the core of this thesis lies the attempt to combine these two concepts and thus to provide a means of studying magnetic excitations in a solid.

3. The Korringa-Kohn-Rostoker (KKR) Green function method

This chapter introduces to the Korringa-Kohn-Rostoker (KKR) Green function (GF) method. Most of the preformed calculations that are presented within this thesis are based on this scheme. Initially formulated within multiple-scattering theory by Korringa [53] in 1947 and by Kohn and Rostoker [54] in 1954 its main idea is to divide the approach to the correct description of the electronic structure of a solid into two tasks:

(a) Solve the problem for a single scattering center and

(b) incorporate the structural environment of this particular scatterer by use of a multiple-scattering ansatz.

Formally the second request is fulfilled by the condition that the outgoing wave function from one scattering center equals the sum of all incoming wave functions to this scatterer.

A significant improvement of the method was its reformulation as a Green function method [55, 56]. By use of the so-called Dyson equation, this enables to connect the physical properties of two different systems in an efficient way, *e.g.*, a localized impurity structure in an elsewise perfectly clean crystal to the same host structure without impurity. Such an embedding scheme in its real space version avoids computationally expensive supercell structures as they would become necessary in wave function methods. This feature makes a Green function technique well-suited for nanostructures on surfaces, the type of system that is investigated within this thesis.

3.1. Definition and general properties of a Green function

Suppose a system is described by the time-independent Hamiltonian $\mathcal{H}$ for which a complete basis set of eigenfunctions $\{|\psi_n\rangle\}$ with eigenvalues $\{E_n\}$ exists, satisfying

$$\mathcal{H}|\psi_n\rangle = E_n|\psi_n\rangle \ . \tag{3.1}$$

The Green function $\mathcal{G}(z)$ is defined as an operator that solves the equation

$$(z\mathcal{I} - \mathcal{H})\,\mathcal{G}(z) = \mathcal{I} \ , \tag{3.2}$$

where z is a complex number with a finite imaginary part and $\mathcal{I}$ is the identity operator. The Green function is also called resolvent of the Hamiltonian and can be characterized as its inverse, $\mathcal{G}(z) = (z\mathcal{I} - \mathcal{H})^{-1}$. Formally, one can define the derivative of a Green function with respect to its argument,

$$\frac{\mathrm{d}}{\mathrm{d}z}\mathcal{G}(z) = \frac{\mathrm{d}}{\mathrm{d}z}\,(z\mathcal{I} - \mathcal{H})^{-1} = -\,(z\mathcal{I} - \mathcal{H})^{-2} = -\,(\mathcal{G}(z))^2 \ . \tag{3.3}$$

By use of the set of eigenvalues and eigenfunctions the Green function can be represented in a spectral representation, often referred to as Lehmann representation,

$$\mathcal{G}(z) = \sum_n \frac{|\psi_n\rangle\langle\psi_n|}{z - E_n} \ . \tag{3.4}$$

Its adjoint $\mathcal{G}(z)^\dagger$ satisfies the equation $\mathcal{G}(z)^\dagger\,(z\mathcal{I} - \mathcal{H}) = \mathcal{I}$. Together with Eq. (3.4) this leads to the identity

$$\mathcal{G}(z)^\dagger = \mathcal{G}(z^*) \tag{3.5}$$

with z^* being the conjugate complex of z. For two complex numbers z_1 and z_2 with nonvanishing imaginary parts one easily verifies the identity

$$\mathcal{G}(z_2) = \mathcal{G}(z_1) + \mathcal{G}(z_1)(z_1 - z_2)\mathcal{G}(z_2) = \mathcal{G}(z_1)\,(\mathcal{I} - (z_1 - z_2)\mathcal{G}(z_1))^{-1} \ . \tag{3.6}$$

Furthermore, for two different Hamiltonians, $\mathcal{H}_1$ and $\mathcal{H}_2$, the two corresponding resolvents, $\mathcal{G}_1(z) = (z\mathcal{I} - \mathcal{H}_1)^{-1}$ and $\mathcal{G}_2(z) = (z\mathcal{I} - \mathcal{H}_2)^{-1}$, connect via the form

$$\mathcal{G}_2(z) = \mathcal{G}_1(z) + \mathcal{G}_1(z)\,(\mathcal{H}_2 - \mathcal{H}_1)\,\mathcal{G}_2(z) = \mathcal{G}_1(z)\,(\mathcal{I} - (\mathcal{H}_2 - \mathcal{H}_1)\mathcal{G}_1(z))^{-1} \ . \tag{3.7}$$

Eq. (3.7) already illustrates the form of the Dyson equation that is topic of Sec. 3.1.1. For $z = E + \mathrm{i}\eta$ the side limits of the Green function are defined by

$$\lim_{|\eta|\to 0} \mathcal{G}(E + \mathrm{i}\eta) = \begin{cases} \mathcal{G}^+(E) \ , & \eta > 0 \\ \mathcal{G}^-(E) \ , & \eta < 0 \end{cases} \tag{3.8}$$

Using Eq. (3.5) one sees that $\mathcal{G}^-$ is the adjoint of $\mathcal{G}^+$ and *vice versa*, $\mathcal{G}^{\pm}(E)^\dagger = \mathcal{G}^{\mp}(E)$. Often one refers to these Green functions as retarded ($\mathcal{G}^+$) and advanced ($\mathcal{G}^-$) Green functions. The reason for this will become apparent at a later stage. Formally, one can define an expression for the imaginary part of the Green function[1] by use of the side limits as given in Eq. (3.8),

$$\mathrm{Im}\mathcal{G}(E) = \frac{1}{2\mathrm{i}}\left[\mathcal{G}^+(E) - \mathcal{G}^-(E)\right] \ . \tag{3.9}$$

The Green function is very useful, since it allows to determine the expectation value of any ground-state observable. However, the reader may ask why one would use the Green function for it (see Eq. (3.4)), to compute it where the Green function is a function of eigenstates and eigenfunctions of the system, while one can calculate it directly.

After some general features of Green functions in perturbed systems are discussed, a formula will be presented that connects the expectation value of an observable to the Green function (*cf.* Eq. (3.29)).

3.1.1. Dyson equation, T-matrix, and the Lippmann-Schwinger equation

Some of the most practical features of Green functions come to light when a perturbed system is considered. Say, a Hamiltonian $\mathcal{H}$ for a system of interest can be written as

$$\mathcal{H} = \mathcal{H}_0 + \mathcal{V} \ , \tag{3.10}$$

where $\mathcal{H}_0$ corresponds to an unperturbed solvable physical problem and $\mathcal{V}$ states its difference to the desired full system with perturbation. The Green functions of the full Hamiltonian and reference Hamiltonian then read

$$\mathcal{G}(z) \ = (z\mathcal{I} - \mathcal{H} \ )^{-1} \quad , \quad \mathcal{G}_0(z) = (z\mathcal{I} - \mathcal{H}_0)^{-1} \ . \tag{3.11}$$

The Dyson equation

Using the operator identity from Eq. (3.7) one finds the connection

$$\begin{aligned} \mathcal{G}(z) &= \mathcal{G}_0(z) + \mathcal{G}_0(z)\mathcal{V}\mathcal{G}(z) = \mathcal{G}_0(z)\left(\mathcal{I} - \mathcal{V}\mathcal{G}_0(z)\right)^{-1} \\ &= \mathcal{G}_0(z) + \mathcal{G}(z)\mathcal{V}\mathcal{G}_0(z) = \left(\mathcal{I} - \mathcal{G}_0(z)\mathcal{V}\right)^{-1}\mathcal{G}_0(z) \ . \end{aligned} \tag{3.12}$$

[1] This definition of an imaginary part is an extension of the usual definition $\mathrm{Im}\, z = \frac{1}{2\mathrm{i}}\left(z - z^*\right)$ (for a complex number z) to operators. Depending on the chosen basis set, the matrix elements of the Green function operator's imaginary part can still be complex. The eigenvalues and therefore the trace, however, are always real.

Any of these formulas represents the famous Dyson equation. By iteratively inserting this expression into itself one arrives at

$$\begin{aligned}\mathcal{G}(z) &= \mathcal{G}_0(z) + \mathcal{G}_0(z)\mathcal{V}\mathcal{G}(z) \\ &= \mathcal{G}_0(z) + \mathcal{G}_0(z)\mathcal{V}\mathcal{G}_0(z) + \mathcal{G}_0(z)\mathcal{V}\mathcal{G}_0(z)\mathcal{V}\mathcal{G}(z) \\ &= \mathcal{G}_0(z) + \mathcal{G}_0(z)\mathcal{V}\mathcal{G}_0(z) + \mathcal{G}_0(z)\mathcal{V}\mathcal{G}_0(z)\mathcal{V}\mathcal{G}_0(z) + \dots \ . \end{aligned} \tag{3.13}$$

Such a series allows to express the requested Green function $\mathcal{G}$ exclusively by the two operators $\mathcal{G}_0$ and $\mathcal{V}$. For the case that the potential $\mathcal{V}$ represents a small perturbation the series in Eq. (3.13) converges. Thus, by applying Eq. (3.13) up to a certain order in $\mathcal{V}$ one possesses a means to access $\mathcal{G}$ up to a desired accuracy without having to calculate the matrix inversion in Eq. (3.12).

The T-matrix

Eq. (3.13) can be written as

$$\mathcal{G}(z) = \mathcal{G}_0(z) + \mathcal{G}_0(z)\mathcal{T}(z)\mathcal{G}_0(z) \ , \tag{3.14}$$

where $\mathcal{T}(z)$ is the transition matrix or T-matrix. One easily verifies that

$$\mathcal{T}(z) = \mathcal{V} + \mathcal{V}\mathcal{G}_0(z)\mathcal{V} + \mathcal{V}\mathcal{G}_0(z)\mathcal{V}\mathcal{G}_0(z)\mathcal{V} + \dots \tag{3.15}$$

or

$$\mathcal{T}(z) = \mathcal{V} + \mathcal{V}\mathcal{G}_0(z)\mathcal{T}(z) \ . \tag{3.16}$$

Thus, the problem of finding the full Green function $\mathcal{G}(z)$ can be transferred to a problem of finding the T-matrix $\mathcal{T}(z)$.

The Lippmann-Schwinger equation

Suppose the Hamilton operators from Eq. (3.10), $\mathcal{H}$ and $\mathcal{H}_0$, solve the equations

$$(z\mathcal{I} - \mathcal{H}_0)|\psi_0\rangle = 0 \tag{3.17}$$

$$\text{and} \quad (z\mathcal{I} - \mathcal{H}\ )|\psi\rangle = (z\mathcal{I} - \mathcal{H}_0)|\psi\rangle - \mathcal{V}|\psi\rangle = 0 \ , \tag{3.18}$$

with their respective wave functions $|\psi\rangle$ and $|\psi_0\rangle$ and a complex argument z. Employing the ansatz

$$|\psi\rangle = |\psi_0\rangle + \delta|\psi\rangle \tag{3.19}$$

leads to

$$\begin{aligned} 0 &\stackrel{!}{=} (z\mathcal{I} - \mathcal{H}_0)|\psi\rangle - \mathcal{V}|\psi\rangle \\ &= \underbrace{(z\mathcal{I} - \mathcal{H}_0)|\psi_0\rangle}_{=0} + (z\mathcal{I} - \mathcal{H}_0)\delta|\psi\rangle - \mathcal{V}|\psi\rangle \ . \end{aligned} \tag{3.20}$$

Multiplication with $\mathcal{G}(z) = (z\mathcal{I} - \mathcal{H}_0)^{-1}$ yields

$$|\psi\rangle = |\psi_0\rangle + \mathcal{G}_0(z)\mathcal{V}|\psi\rangle \ . \tag{3.21}$$

Eq. (3.21) is known as the Lippmann-Schwinger equation. Its importance lies in the connection between a wave function of the perturbed system to a wave function of the unperturbed system. Again, by iteratively inserting the expression of the wave function into itself one arrives at a series of the form

$$|\psi\rangle = |\psi_0\rangle + \mathcal{G}_0\mathcal{V}|\psi_0\rangle + \mathcal{G}_0\mathcal{V}\mathcal{G}_0\mathcal{V}|\psi_0\rangle + \dots \ . \tag{3.22}$$

This is the so-called Born series. By use of the T-matrix (see Eq. (3.16)) one finds

$$|\psi\rangle = |\psi_0\rangle + \mathcal{G}_0(z)\mathcal{T}(z)|\psi_0\rangle \ , \tag{3.23}$$

which allows the association

$$\delta|\psi\rangle = \mathcal{G}(z)\mathcal{V}|\psi_0\rangle = \mathcal{G}_0(z)\mathcal{V}|\psi\rangle = \mathcal{G}_0(z)\mathcal{T}(E_n)|\psi_0\rangle \ . \tag{3.24}$$

3.1.2. Access to physical observables through the Green function

For a system of fermionic particles the statistical average of a physical observable A is given by

$$\langle A\rangle = \sum_n f(E_n)\langle n|\mathcal{A}|n\rangle \ , \tag{3.25}$$

where $\mathcal{A}$ is the corresponding Hermitian operator and the Fermi-Dirac distribution $f(E)$ reads

$$f(E) = \frac{1}{\mathrm{e}^{\beta(E-\mu)}+1} \ , \tag{3.26}$$

where $\beta = 1/k_\mathrm{B}T$, k_B the Boltzmann constant, T the system's temperature, and μ the chemical potential. By forming the expression

$$f(z)\mathrm{Tr}\,[\mathcal{A}\mathcal{G}(z)] = \sum_n \frac{f(z)\langle n|\mathcal{A}|n\rangle}{z-E_n} \ , \tag{3.27}$$

where $\mathrm{Tr}\,[.]$ denotes the trace of an operator, and by applying Cauchy's theorem one obtains (see for example Ref. [57], Ch. 18)

$$\langle A\rangle = \mp\frac{1}{\pi}\mathrm{Im}\int \mathrm{d}E\ f(E)\mathrm{Tr}\left[\mathcal{A}\mathcal{G}^{\pm}(E)\right] \ . \tag{3.28}$$

In the zero temperature limit the Fermi-Dirac distribution turns into the step-function $\Theta(E_{\mathrm{F}} - E)$, where E_{F} is the Fermi energy, and one finds

$$\langle A \rangle = \mp \frac{1}{\pi} \mathrm{Im} \int_{-\infty}^{E_{\mathrm{F}}} \mathrm{d}E \ \mathrm{Tr} \left[\mathcal{A} \mathcal{G}^{\pm}(E) \right] \ . \tag{3.29}$$

With this formula at hand one gains access to the statistical average of any desired ground state property.

For the remaining part of this chapter most formulas involve only the positive side limit, $\mathcal{G}^{+}(E)$, which is why the index $(+)$ is dropped in the following whereas the index $(-)$ appears explicitly when $\mathcal{G}^{-}(E)$ is meant.

Charge and magnetization density via the Green function

The charge and the magnetization density, $n(\vec{r})$ and $\vec{m}(\vec{r})$, play a crucial role in the density functional formalism. Therefore, Eq. (3.29) is used to express these important quantities by means of the Green function. For this purpose it is useful to project the abstract Green function operator onto a spin- and space-dependent basis set,

$$G^{\sigma\sigma'}(\vec{r}, \vec{r}\,'; E) = \langle \vec{r}\sigma | \mathcal{G}(E) | \vec{r}\,'\sigma' \rangle = \sum_{n} \frac{\psi_n^{\sigma}(\vec{r}) \psi_n^{\sigma'}(\vec{r}\,')^*}{E - E_n + \mathrm{i}0^+} \ . \tag{3.30}$$

The asterisk denotes complex conjugation for the wave function and 0^+ is a positive infinitesimal. In spin-space the Green function takes the form of a (2×2) matrix (indicated by a bold symbol)

$$\boldsymbol{G}(\vec{r}, \vec{r}\,'; E) = \begin{pmatrix} G^{\uparrow\uparrow}(\vec{r}, \vec{r}\,'; E) & G^{\uparrow\downarrow}(\vec{r}, \vec{r}\,'; E) \\ G^{\downarrow\uparrow}(\vec{r}, \vec{r}\,'; E) & G^{\downarrow\downarrow}(\vec{r}, \vec{r}\,'; E) \end{pmatrix} = \sum_{n} \frac{\boldsymbol{\psi}_n(\vec{r}) \boldsymbol{\psi}_n(\vec{r}\,')^{\dagger}}{E - E_n + \mathrm{i}0^+} \ , \tag{3.31}$$

with the two-dimensional spinor in spin-space, $\boldsymbol{\psi}_n = \left(\psi_n^{\uparrow}, \psi_n^{\downarrow}\right)^{\mathrm{T}}$. By use of the real-space projector

$$\mathcal{P}_{\vec{r},\alpha} = |\vec{r}\rangle\langle\vec{r}| \otimes \boldsymbol{\sigma}_{\alpha} = \begin{cases} |\vec{r}\rangle\langle\vec{r}| \otimes \boldsymbol{\sigma}_0 & , \quad \alpha = 0 \\ |\vec{r}\rangle\langle\vec{r}| \otimes \boldsymbol{\sigma}_i & , \quad \alpha = i \in \{x, y, z\} \end{cases} \ , \tag{3.32}$$

where $\alpha \in \{0, x, y, z\}$ and σ_{α} is a component of the four-vector consisting of identity operator in spin-space, $\boldsymbol{\sigma}_0 = \mathbb{1}_{2\times2}$, and the three Pauli matrices, σ_x, σ_y, σ_z (*cf.* Eq. (2.13)), one arrives at

$$n_{\alpha}(\vec{r}) = -\frac{1}{\pi} \mathrm{Im} \int_{-\infty}^{E_{\mathrm{F}}} \mathrm{d}E \ \mathrm{Tr} \left[\boldsymbol{\sigma}_{\alpha} \boldsymbol{G}(\vec{r}, \vec{r}; E) \right] \ , \tag{3.33}$$

where the four-component vector n_{α} contains charge and magnetization density,

$$n_{\alpha}(\vec{r}) = \begin{cases} n(\vec{r}) & , \quad \alpha = 0 \\ m_i(\vec{r}) & , \quad \alpha = i \in \{x, y, z\} \end{cases} \ . \tag{3.34}$$

Rewritten in terms of charge density and magnetization density vector, this leads to

$$\alpha = 0: \quad n(\vec{r}) = -\frac{1}{\pi}\mathrm{Im}\int_{-\infty}^{E_\mathrm{F}} \mathrm{d}E\ \mathrm{Tr}\left[\boldsymbol{\sigma}_0 \boldsymbol{G}(\vec{r},\vec{r};E)\right] \tag{3.35}$$

$$\alpha = i: \quad \vec{m}(\vec{r}) = -\frac{1}{\pi}\mathrm{Im}\int_{-\infty}^{E_\mathrm{F}} \mathrm{d}E\ \mathrm{Tr}\left[\vec{\boldsymbol{\sigma}} \boldsymbol{G}(\vec{r},\vec{r};E)\right]\ . \tag{3.36}$$

By introducing the spin-resolved densities

$$n^\sigma(\vec{r}) = -\frac{1}{\pi}\mathrm{Im}\int_{-\infty}^{E_\mathrm{F}} \mathrm{d}E\ G^{\sigma\sigma}(\vec{r},\vec{r};E)\ , \tag{3.37}$$

with $\sigma \in \{\uparrow,\downarrow\}$ one finds

$$n(\vec{r}) = n^\uparrow(\vec{r}) + n^\downarrow(\vec{r}) \tag{3.38}$$

$$\text{and} \quad m_z(\vec{r}) = n^\uparrow(\vec{r}) - n^\downarrow(\vec{r})\ . \tag{3.39}$$

Instead of integrating over energy one can use the definition of the spin- and space-resolved local density of states,

$$n^\sigma(\vec{r},E) = -\frac{1}{\pi}\mathrm{Im}G^{\sigma\sigma}(\vec{r},\vec{r};E)\ , \tag{3.40}$$

to obtain the density of states integrated over the volume of the unit cell, V. This results in the density of states as function of the energy,

$$n(E) = \underbrace{\int_V \mathrm{d}^3r\ n^\uparrow(\vec{r},E)}_{=n^\uparrow(E)} + \underbrace{\int_V \mathrm{d}^3r\ n^\downarrow(\vec{r},E)}_{=n^\downarrow(E)}\ , \tag{3.41}$$

an important quantity that is studied within this thesis.

3.2. KKR Green function in the atomic sphere approximation (ASA)

In the KKR formalism space is divided into Voronoi cells such that each cell contains a scattering center and all the points in space that are closest to it. Usually these scattering centers represent atoms within a crystal. In special cases, however, such a scatterer can represent a mixture of two different atoms (coherent potential approximation, see Ref. [58]) or a vacuum site.

The KKR Green function accounts for such a Voronoi cell division of space and takes the form

$$\begin{aligned}\boldsymbol{G}(\vec{x}\,,\vec{x}';E) &= \boldsymbol{G}(\vec{r}+\vec{R}_i,\vec{r}'+\vec{R}_j;E)\\ &= \boldsymbol{G}_{ij}(\vec{r},\vec{r}';E)\\ &= \delta_{ij}\mathring{\boldsymbol{G}}_{ii}(\vec{r},\vec{r}';E) + \boldsymbol{G}^{\mathrm{str}}_{ij}(\vec{r},\vec{r}';E)\ ,\end{aligned} \tag{3.42}$$

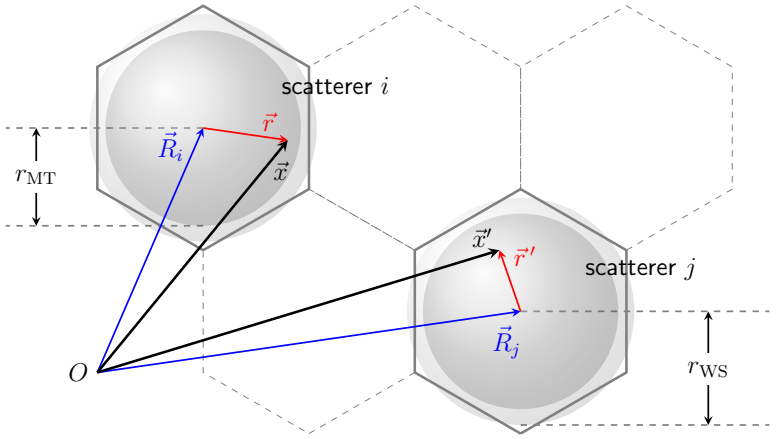

Figure 3.1.: This figure illustrates the nomenclature for spatial coordinates with respect to two scatterers, labeled i and j. The globally defined vectors $\vec{x}$ and $\vec{x}'$ are given by $\vec{R}_i + \vec{r}$ and $\vec{R}_j + \vec{r}'$, respectively, where $\vec{r}$ and $\vec{r}'$ are defined with respect to their corresponding scattering centers located at $\vec{R}_i$ and $\vec{R}_j$, see Eq. (3.42). In addition the muffin tin radius r_{MT} and the Wigner-Seitz radius r_{WS} are indicated.

where $\vec{x}$ and $\vec{x}'$ are defined as global spatial coordinates, while $\vec{r}$ and $\vec{r}'$ are locally given with respect to their respective scattering centers at $\vec{R}_i$ and $\vec{R}_j$, see Fig. 3.1 for nomenclature. The single-site problem is accounted for by $\mathring{\boldsymbol{G}}_{ii}$, whereas the back-scattering part is captured by $\boldsymbol{G}^{\mathrm{str}}_{ij}$, the structural Green function. Throughout this thesis the atomic sphere approximation (ASA) incorporating the full charge density is assumed, *i.e.*, the potentials for the scattering sites take a radial symmetric form. Furthermore, spin-orbit coupling is not considered in this work and only collinear magnetic states are studied, such that the Green function becomes diagonal in spin space. Thus, for the rest of this Chapter a single spin-label $\sigma \in \{\uparrow, \downarrow\}$ is used to distinguish Green functions for the two different spin-channels. The (spin-polarized) potential is then given as a sum of contributions from each Voronoi cell and reads

$$V^{\sigma}(\vec{x}) = \langle \vec{x} | \, \mathcal{V}^{\sigma} \, | \vec{x} \rangle = \sum_{i=1}^{N} v_i^{\sigma}(\vec{r}) \quad , \quad \vec{r} = \vec{x} - \vec{R}_i \, , \tag{3.43}$$

where

$$v_i^{\sigma}(\vec{r}) = \begin{cases} v^{\sigma}(r) & , \quad r < r_{\mathrm{MT}} \\ 0 & , \quad \text{else} \end{cases} \tag{3.44}$$

and r_{MT} is called muffin-tin (MT) radius (see Fig. 3.1). In the ASA, however, one uses the Wigner-Seitz (WS) radius r_{WS} instead, which is defined such, that the volume of all

spheres adds up to the total volume of space. Since the WS cells are not spherical, the WS spheres overlap, see Fig. 3.1.

In conclusion, we seek to find for each spin channel a Green function $G^\sigma(\vec{x}, \vec{x}'; E)$ that satisfies

$$(E - H^\sigma(\vec{x}))\, G^\sigma(\vec{x}, \vec{x}'; E) = \delta(\vec{x} - \vec{x}') \;, \tag{3.45}$$

where $H^\sigma(\vec{x}) = -\nabla^2 + V^\sigma(\vec{x})$. As will be shown in the next paragraphs the Green function can be constructed out of the wave functions $R^\sigma_{i,\ell}(r, E)$ and $H^\sigma_{i,\ell}(r, E)$, the regular and irregular solution to the radial Schrödinger equation, *i.e.*,

$$\left(-\frac{1}{r}\frac{\partial^2}{\partial r^2} r + \frac{\ell(\ell+1)}{r^2} + v^\sigma(\vec{r}) - E\right) R^\sigma_{i,\ell}(\vec{r}, E) = 0 \tag{3.46}$$

and

$$\left(-\frac{1}{r}\frac{\partial^2}{\partial r^2} r + \frac{\ell(\ell+1)}{r^2} + v^\sigma(\vec{r}) - E\right) H^\sigma_{i,\ell}(\vec{r}, E) = 0 \tag{3.47}$$

for each Wigner-Seitz sphere and each spin channel. In the following the spin label will be dropped.

3.2.1. Single-site term

In this section a single spherically symmetric scattering center at the origin is assumed, such that the (localized) potential is given by[2]

$$V(\vec{x}) = V(\vec{r}) = \langle \vec{r} | \mathcal{V} | \vec{r} \rangle = \begin{cases} v(r) & , \quad r < r_{\mathrm{WS}} \\ 0 & , \quad \text{else} \end{cases} \;. \tag{3.48}$$

For such a spherically symmetric problem an expansion of the Green function and other spatially dependent quantities in spherical harmonics becomes convenient.

Single-site term for the free electron

The expansion of a plane wave (the solution of the free-electron problem, $v(r) \equiv 0$) in spherical functions reads

$$\psi_{\vec{k}}(\vec{r}) = \mathrm{e}^{\mathrm{i}\vec{k}\cdot\vec{r}} = \sum_L a_L(\hat{k})\; j_\ell(kr)\; Y_L(\hat{r}) \;, \tag{3.49}$$

[2] In a more general case (*i.e.*, when spin-orbit coupling is considered) the spatial representation of the potential is non-local in space and shows non-vanishing offdiagonals in spin space, see for example Ref. [59]. This, however, is beyond the scope of this thesis and shall not be considered.

with the expansion coefficients $a_L(\hat{k}) = 4\pi\,\mathrm{i}^\ell\,Y_L(\hat{k})$, where $r = |\vec{r}|$ and $\hat{r} = \vec{r}/r$, as well as $k = |\vec{k}| = \sqrt{E}$ and $\hat{k} = \vec{k}/k$. Furthermore the multi-index $L = (\ell, m)$ of angular momentum ℓ and magnetic quantum number m, the spherical Bessel function $j_\ell(x)$, and the real spherical harmonics $Y_L(\hat{x})$ have been introduced.

For a free electron the Green function is given by

$$g(\vec{r}, \vec{r}\,'; E) = -\frac{1}{4\pi}\,\frac{\mathrm{e}^{\mathrm{i}k|\vec{r}-\vec{r}\,'|}}{|\vec{r}-\vec{r}\,'|}\;, \tag{3.50}$$

which in angular momentum representation reads

$$g(\vec{r}, \vec{r}\,'; E) = \sum_L Y_L(\hat{r})\,g_\ell(r, r'; E)\,Y_L(\hat{r}')\;. \tag{3.51}$$

The expansion coefficients read

$$g_\ell(r, r'; E) = -\mathrm{i}k\,j_\ell(kr_<)\,h_\ell(kr_>)\;, \tag{3.52}$$

where $r_< = \min\{r, r'\}$, $r_> = \max\{r, r'\}$. The spherical Hankel function $h_\ell(x)$ is connected to the spherical Bessel function via $h_\ell(x) = j_\ell(x) + \mathrm{i}n_\ell(x)$, where $n_\ell(x)$ denotes the spherical Neumann function (also called spherical Bessel function of second kind). Due to the fact that $h_\ell(x) \xrightarrow[x\to 0]{} \infty$ while $j_\ell(x)$ remains finite at the origin, the expression in Eq. (3.52) is well-defined except for the singularity $r = r' = 0$. Both, $j_\ell(kr)$ and $n_\ell(kr)$, are solution to the radial Schrödinger equation for free particles which is also true for $h_\ell(kr)$ and any other linear combination.

Single-site term for a spherical potential of finite range

For the general case of a spherical potential $v(r)$ that is different from zero inside a finite spherical region an analytical expression for the Green function is not possible anymore. However, the Lippmann-Schwinger equation (*cf.* Eq. (3.21)) allows a means to determine the single-site Green function nonetheless. The form of such a Green function reads

$$\mathring{G}(\vec{r}, \vec{r}\,'; E) = \sum_L Y_L(\hat{r})\,\mathring{G}_\ell(r, r'; E)\,Y_L(\hat{r}')\;, \tag{3.53}$$

where the expansion coefficients read

$$\mathring{G}_\ell(r, r'; E) = -\mathrm{i}kR_\ell(r_<; E)H_\ell(r_>; E)\;. \tag{3.54}$$

The functions $R_\ell(r; E)$ and $H_\ell(r; E)$ are solutions to the Lippmann-Schwinger equations

$$R_\ell(r; E) \;=\; j_\ell(kr) + \int_0^{r_{\mathrm{WS}}} \mathrm{d}r' r'^2\,g_\ell(r, r'; E)\,v(r')\,R_\ell(r'; E) \tag{3.55}$$

$$\text{and}\quad H_\ell(r; E) \;=\; h_\ell(kr) + \int_0^{r_{\mathrm{WS}}} \mathrm{d}r' r'^2\,g_\ell(r, r'; E)\,v(r')\,H_\ell(r'; E)\;. \tag{3.56}$$

When $r > r_{\mathrm{WS}}$ one can simplify these expressions to [60, 61]

$$R_\ell(r;E) = j_\ell(kr) - \mathrm{i}kt_\ell(E)h_\ell(r';E) \quad (r > r_{\mathrm{WS}}) \tag{3.57}$$

$$\text{and} \quad H_\ell(r;E) = h_\ell(kr) \quad (r > r_{\mathrm{WS}}) \,, \tag{3.58}$$

where the single-site t-matrix

$$t_\ell(E) = \int_0^{r_{\mathrm{WS}}} \mathrm{d}r' r'^2 j_\ell(kr) v(r) R_\ell(r;E) \tag{3.59}$$

was introduced.

3.2.2. Structural part

Now we divide the space into WS cells, even for the free electron gas, and evaluate the Green function connecting two lattice sites i and j.

Structural part for free electrons

Again, the free electron is considered first, *i.e.*, $V(\vec{r}) \equiv 0$. The free electron's Green function can be written in the form

$$g(\vec{x},\vec{x}';E) = g(\vec{r}+\vec{R}_i,\vec{r}'+\vec{R}_j;E) = g_{ij}(\vec{r},\vec{r}';E) \,. \tag{3.60}$$

By applying an addition theorem for the Hankel function [60]

$$h_L(\vec{r}'+\vec{R}_j-\vec{R}_i;E) = \frac{\mathrm{i}}{k}\sum_{L'} g^{\mathrm{str}}_{iL,jL'}(E) j_\ell(kr') Y_L(\hat{r}') \tag{3.61}$$

with the expansion coefficients (the so-called structural Green functions)

$$g^{\mathrm{str}}_{iL,jL'}(E) = -(1-\delta_{ij})\,4\pi\mathrm{i}\sqrt{E}\sum_{L''} \mathrm{i}^{\ell-\ell'+\ell''} C_{LL'L''}\, h_{L''}(\vec{R}_i-\vec{R}_j;E) \tag{3.62}$$

and the Gaunt coefficients $C_{LL'L''} = \int \mathrm{d}\Omega Y_L(\hat{r}) Y_{L'}(\hat{r}) Y_{L''}(\hat{r})$ one can prove that [56]

$$\begin{aligned} g_{ij}(\vec{x},\vec{x}';E) &= -\frac{1}{4\pi}\frac{e^{\mathrm{i}k|\vec{r}+\vec{R}_i-\vec{r}'-\vec{R}_j|}}{|\vec{r}+\vec{R}_i-\vec{r}'-\vec{R}_j|} \\ &= -\mathrm{i}k\sum_L j_L(\vec{r}_<;E)\, h_L(\vec{r}_>;E)\delta_{ij} + \sum_{LL'} j_L(\vec{r};E)\, g^{\mathrm{str}}_{iL,jL'}(E)\, j_{L'}(\vec{r}';E) \,, \end{aligned} \tag{3.63}$$

Due to the fact that the Gaunt coefficients vanish for $\ell'' > \ell + \ell'$ the sum in Eq. (3.62) is finite.

Structural part for spherical potentials

In this section the potential is considered to be a superposition of scattering centers which are spherically symmetric with respect to their center (*cf.* Eq. (3.43)). This leads to the general form of the KKR Green function in ASA, consisting of the single-site term and the structural scattering part. Accounting for the spin with the label $\sigma \in \{\uparrow, \downarrow\}$ the KKR Green function reads $G^{\sigma}_{ij}(\vec{x}\,, \vec{x}\,'; E) = \delta_{ij} \mathring{G}^{\sigma}_{ii}(\vec{r}, \vec{r}\,'; E) + G^{\mathrm{str},\sigma}_{ij}(\vec{r}, \vec{r}\,'; E)$ (*cf.* Eq. (3.42), for nomenclature of the spatial coordinates, see Fig. 3.1), where

$$\mathring{G}^{\sigma}_{ii}(\vec{r}, \vec{r}\,'; E) = -\mathrm{i}k \sum_{L} R^{\sigma}_{iL}(\vec{r}_{<}; E)\, H^{\sigma}_{iL}(\vec{r}_{>}; E) \tag{3.64}$$

and

$$G^{\mathrm{str},\sigma}_{ij}(\vec{r}, \vec{r}\,'; E) = \sum_{LL'} R^{\sigma}_{iL}(\vec{r}; E)\, G^{\mathrm{str},\sigma}_{iL,jL'}(E)\, R^{\sigma}_{iL}(\vec{r}\,'; E)\ . \tag{3.65}$$

Here the abbreviations

$$R^{\sigma}_{iL}(\vec{r}; E) = Y_L(\hat{r}) R^{\sigma}_{iL}(r; E) \quad \text{and} \quad H^{\sigma}_{iL}(\vec{r}; E) = Y_L(\hat{r}) H^{\sigma}_{iL}(r; E) \tag{3.66}$$

have been used. The energy dependent structural part of the Green function, $G^{\mathrm{str},\sigma}_{iL,jL'}(E)$, describes the backscattering effects and is given by

$$G^{\mathrm{str},\sigma}_{iL,jL'}(E) = g^{\mathrm{str},\sigma}_{iL,jL'}(E) + \sum_{kL''} g^{\mathrm{str},\sigma}_{iL,kL''}(E) t^{\sigma}_{\ell''}(E) G^{\mathrm{str},\sigma}_{kL'',jL'}(E) \tag{3.67}$$

where $t^{\sigma}_{\ell}(E)$ is the single-site t-matrix as given in Eq. (3.59) but now for a spin-dependent potential $v^{\sigma}(r)$. The same holds for the spin-dependent regular and irregular radial wave function, which were introduced in Eqs. (3.57) and (3.58).

3.2.3. Computational details of the KKR GF code

In practice the energy integration in Eq. (3.29) is performed by splitting it into two parts,

$$\int_{-\infty}^{E_{\mathrm{F}}} \mathrm{d}E = \sum_{\text{core states}} + \int_{E_{\mathrm{B}}}^{E_{\mathrm{F}}} \mathrm{d}E \tag{3.68}$$

with a well-chosen boundary energy E_{B} (higher than the core states in energy, lower than the valence state energies). This is for reducing the computational demand on solving this integral. Furthermore the analytic properties of the Green function above the real axis are used to use a contour integration, rather than to integral along the real axis. This usually reduces the computational costs due to the fact that the Green function is much smoother for energies with a larger imaginary part.

3.3. The projected form of the KKR Green function

Many performed calculations within this thesis involve numerical integrations over space and energy, for which, in principle, the knowledge of the KKR Green functions is requested/would be required. Recalling the form of the KKR Green function in ASA (*cf.* Eq. (3.42)),

$$G_{ij}(\vec{r},\vec{r}\,';E) = \sum_{LL'} Y_L(\hat{r}) G_{iL,jL'}(r\,,r\,';E) Y_{L'}(\hat{r}') \tag{3.69}$$

with

$$\begin{aligned} G_{iL,jL'}(r\,,r\,';E) &= \delta_{ij}\delta_{LL'} R_{i\ell}(r_<;E) H_{i\ell}(r_>;E) \\ &\quad + R_{i\ell}(r\,;E) G^{\mathrm{str}}_{iL,jL'}(E) R_{j\ell'}(r\,';E)\;, \end{aligned} \tag{3.70}$$

one realizes that besides the structural part, $G^{\mathrm{str}}_{iL,jL'}(E)$, also $R_{i\ell}(r\,;E)$ and $H_{i\ell}(r\,;E)$, the regular and irregular radial wave functions, carry an energy dependency. Thus, the calculation of the KKR Green function for various different energies becomes time-consuming and computationally demanding. An alternative more efficient approach is presented in the following which uses the knowledge stored in a few KKR Green function to extrapolate the energetic landscape in the surrounding area. Only by this procedure, many of the shown results have been made achievable in the first place. However, where there is light, there is also shadow: The drawback utilizing the shown concept comes along with a loss in accuracy that has to be accounted for carefully by checking the resulting fit functions in the used energy domain.

In the following it is demonstrated how the energy and spatial dependency can be disentangled by means of a new basis set $\{|\phi_{i\ell b}\rangle\}$, accounting for lattice site i, orbital ℓ, evaluated at energy E_b for $b \in \{1,2,\dots\}$. The task of this new basis set is to allow for a definition of the projected Green function that shows a remaining dependency on the energy, but is independent of the spatial coordinates, *i.e.*,

$$G^{\mathrm{proj}}_{iLb;jL'b'}(E) = \int_0^{r_{MT}} \mathrm{d}r r^2 \int_0^{r_{MT}} \mathrm{d}r' r'^2 Y_L(\hat{r}) \phi_{i\ell b}(r) G_{iL;jL'}(r,r\,';E) Y_{L'}(\hat{r}') \phi_{i\ell' b'}(r')\;. \tag{3.71}$$

This separation enables, in a second step, to approximate the projected Green function in terms of a rational fit. For most of the calculations carried out for this thesis, this efficient technique was used, that allows a drastic reduction of the computational costs.

Such a projection technique has been successfully applied in different flavors. For instance, within the GT approximation [34], where the projection onto a basis set of Wannier functions was done. Furthermore, Buczek [62] used such an approach to calculate the susceptibility employing Chebyshev polynomials.

The two-step approach to the fit functions used within this thesis is demonstrated in the following two sections.

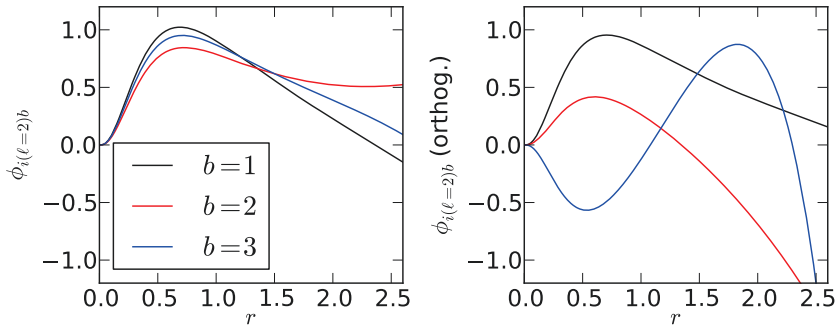

Figure 3.2.: In the left panel of this figure, regular radial wave functions for the d orbital and the majority spin channel of Fe adatoms on the Cu(111) (as discussed in more detail in Ch. 6), where the energies (E_b) are set to $E_1 = 0.6401\ \mathrm{Ry} = E_\mathrm{F}$, $E_2 = 0.3\ \mathrm{Ry}$, and $E_3 = 0\ \mathrm{Ry}$. The shape of the three resulting basis functions is similar. By use of the Gram–Schmidt process (see Eqs. (3.75) and (3.76)) one obtains orthonormal basis functions to the problem, as visualized in the right panel. Due to the fact that already the first basis function (black curve in the left figure) seems to represent the Green function for a large energy window, this thesis incorporates only one basis function per orbital and spin channel.

Spatial dependence

In this work, the radial wave functions, evaluated at a set of different energies E_b (b counts the basis function; a reasonable choice for $b = 1$ is the Fermi energy) serves as basis functions. On the one hand, they are available due to the computational scheme without any effort, and on the other hand, the basis set is well-suited to the problem, such that typically only one or two basis functions become necessary to describe the problem sufficiently accurate. Thus, as basis function one defines

$$\phi_{i\ell b}(r) = \frac{R_{i\ell}(r; E_b)}{\sqrt{\int_0^{r_{MT}} \mathrm{d}r' r'^2 \left(R_{i\ell}(r'; E_b)\right)^2}} \,. \tag{3.72}$$

By use of the overlap matrix

$$\mathcal{O}_{i\ell,bb'} = \int \mathrm{d}r' r'^2 \phi_{i\ell b}(r') \phi_{i\ell b'}(r') \,. \tag{3.73}$$

one can apply the Gram–Schmidt process to obtain orthonormalized basis functions (see Fig. 3.2, right panel): First, one defines basis functions that are orthogonal,

$$(b = 1) \quad \phi^{\mathrm{new}}_{i\ell b}(r) = \phi^{\mathrm{old}}_{i\ell b}(r) \tag{3.74}$$

$$(b > 1) \quad \phi^{\mathrm{new}}_{i\ell b}(r) = \phi^{\mathrm{old}}_{i\ell b}(r) - \sum_{b'=1}^{b-1} \frac{\mathcal{O}_{i\ell,bb'}}{\mathcal{O}_{i\ell,b'b'}} \phi^{\mathrm{new}}_{i\ell b'}(r) \,, \tag{3.75}$$

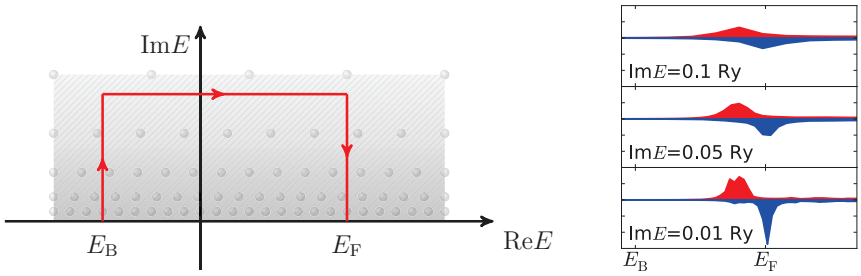

Figure 3.3.: The left figure schematically illustrates the distribution of energy points in the complex energy plane used for the panels (grey circles) compared to the ones used for the KKR energy contour (red line). For each of the panel energy points the projected Green function is calculated and the fit incorporates all of these points. The right figure exemplifies how the imaginary part of the KKR Green function smoothens out when the imaginary part of the energy is increased. The regarded system (Fe adatom on the Cu(111) surface) is discussed in Ch. 6 in more detail.

where in $\mathcal{O}_{i\ell,bb'}$ and $\mathcal{O}_{i\ell,b'b'}$ the old basis function is used for b and the new basis function for b'. Second, the orthonormality is achieved by renormalizing the new basis functions,

$$\phi_{i\ell b}(r) \to \frac{\phi_{i\ell b}(r)}{\sqrt{\int_0^{r_{MT}} \mathrm{d}r' r'^2 \left(\phi_{i\ell b}(r')\right)^2}} \,. \tag{3.76}$$

Typically one or two basis functions are already sufficient to capture most of the behavior of the radial functions, even for a larger range of energies on which the KKR Green functions depend. Within this thesis only one basis function per orbital and spin-channel are considered. Note also that the basis set is chosen such that E_b is the same energy value for both spin channels.

Energy dependence

The projected form of the KKR Green function reads

$$G_{ij}(\vec{r}_i, \vec{r}'_j; E) = \sum_{LL'} Y_L(\hat{r}_i) \left[\sum_{bb'} \phi_{i\ell b}(r_i) G^{\mathrm{proj}}_{iLb,jL'b'}(E) \phi_{j\ell' b'}(r'_j) \right] Y_{L'}(\hat{r}'_j) \tag{3.77}$$

Since the Green function is required in the upper complex plane in an area which is close to the Fermi energy, a compact representation in the upper complex energy plane is necessary.

The handling of the energy dependence is realized by a rational fit to the Green function,

such that

$$G^{\mathrm{fit},\sigma}_{iLb,jL'b'}(E) = \frac{\sum_{p=0}^{P} a^{\sigma(p)}_{iLb,jL'b'} E^p}{1 + \sum_{q=1}^{Q} b^{\sigma(q)}_{iLb,jL'b'} E^q} \tag{3.78}$$

The Green function is analytic in the upper complex plane and behaves like $1/z$ for $z \to \infty$, so $Q = P + 1$. Reasonable parameters for this approximation are $P = 19$ and $Q = 20$. The projected form of the KKR Green function is calculated for an upper complex energy area, where usually five panels (line segments) with different fixed imaginary energy values are considered. In Fig. 3.3 schematically illustrates the panels in the complex plane with respect to the KKR energy contour. Due to the fact that five panels are used, one normally avoids numerically artificial poles such as poles in the upper complex plane in the requested energy area. The parameters $a^{(p)}_{iLb,jL'b'}$ and $b^{(q)}_{iLb,jL'b'}$ are chosen such that the squared difference between the Green function fit and the projected Green function, incorporating all energy points in the five panels (possibly weighted differently depending on criteria such as distance to the real axis of the Fermi energy), reaches a minimal value for any combination of P and Q values that are below their maximal values (in our example 19 and 20).

Within this thesis we assume no spin-orbit coupling (*i.e.*, the Green function is diagonal in spin space), just one basis function per orbital and spin channel, where the projection is done with respect to wave functions at the Fermi energy (E_{F}), in other words this work builds upon the assumption $R^{\sigma}_{i\ell}(r;E) \approx R^{\sigma}_{i\ell}(r;E_{\mathrm{F}})$. In addition, the projection is performed only with respect to the d-orbital subspace, which carries the main contribution to the magnetic spin moment. Test calculations for magnetic adatoms have revealed that the quantities describing the magnetic excitation spectrum remain nearly unchanged when the performed calculations also include the projection of s and p orbitals. The reason is that the magnetic moment in these systems is mainly carried out by the d-states. Furthermore, given that the states of interest are the d orbitals of a single magnetic adatom, one may drop the site label i and keep only $\ell = 2$, projecting on the regular scattering solutions computed at E_{F}:

$$\begin{aligned} G^{\sigma}_{d,mm'}(E) \;&=\; \int \mathrm{d}\vec{r} \int \mathrm{d}\vec{r}\,' \phi^{\sigma}_{d}(r;E_{\mathsf{F}})\, Y_{2m}(\hat{r}) \times \\ &\quad \times G^{\sigma}(\vec{r},\vec{r}\,';E)\, \phi^{\sigma}_{d}(r';E_{\mathsf{F}})\, Y_{2m'}(\hat{r}') \end{aligned} \tag{3.79}$$

This defines the projection on the d orbitals of the adatom of the KKR Green function, upon suitable normalization. The general form accounting for different lattice sites i and j reads

$$G^{\sigma}_{iLjL'}(E) = \int \mathrm{d}\vec{r} \int \mathrm{d}\vec{r}\,' \phi^{\sigma}_{i\ell}(r;E_{\mathrm{F}})\, Y_{L}(\hat{r}) G^{\sigma}_{ij}(\vec{r},\vec{r}\,';E)\, \phi^{\sigma}_{j\ell'}(r';E_{\mathrm{F}})\, Y_{L'}(\hat{r}') \tag{3.80}$$

We conclude by demonstrating in Fig. 3.4 the quality of the presented procedure in terms of a d-DOS calculation for the Fe adatom on Cu(111) (for more details see Ch. 6). In this

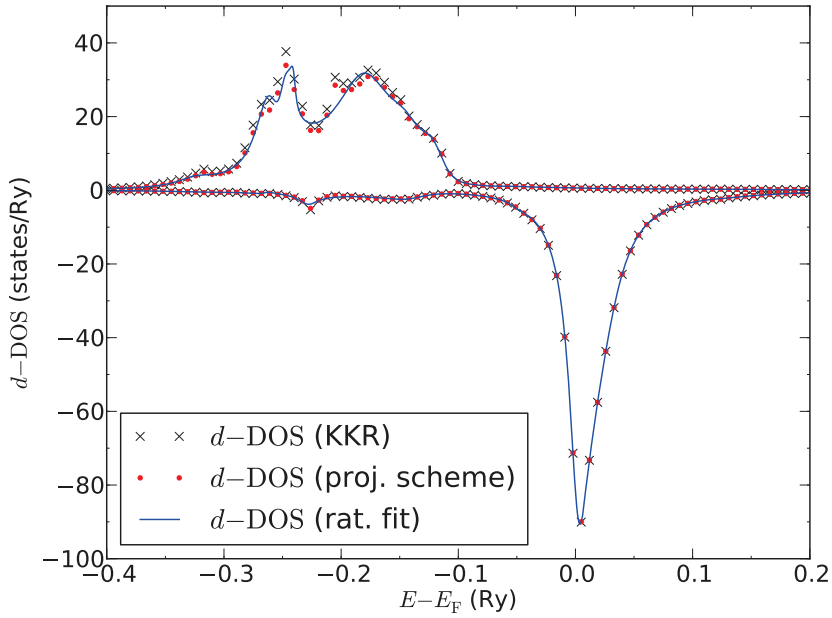

Figure 3.4.: This figure compares the density of states for the d orbitals of an Fe adatom on Cu(111) for both spin channels (d-DOS) calculations utilizing three different quantities: The KKR Green function (black crosses), the projected Green function (red dots), and the rational fit to the projected Green function (blue line). Around the Fermi energy E_F the three different expressions are nearly identical whereas for the majority spin channel deviations are observable.

figure we compare the KKR Green function's DOS to the one using the projected Green function and show the rational fit to the projected Green function. Around the Fermi energy E_F the three Green functions behave in good agreement. In regions far of E_F, however, the value can deviate and numerically errors are made. This is a disadvantage of the presented method. On the other hand, the presented procedure comes along with the advantage of being very efficient: Where as the KKR Green function for a certain energy value requires the calculation of regular and irregular wave function, onsite and structural Green function, the value for the rational fit function is calculated instantaneously. Numerical integrations over expressions that involve Green functions (as many presented quantities within this thesis rely on such a computational challenge) are therefore even possible.

3.4. Summary

This Chapter introduced the Korringa-Kohn-Rostoker (KKR) Green function formalism as a flexible first-principles method that is based on the density functional formalism and is capable of describing impurity structures of finite size placed on otherwise perfect crystal surfaces by means of an embedded scheme. Therefore this method is well-suited for nanostructures deposited on metallic substrates, representing the type of structure that is studied within this thesis. In a second part of this Chapter the projected form of the KKR Green function was discussed, enabling the disentanglement of spatial and energy dependencies. Many of the subsequent calculated quantities are depending on the projected form.

We proceed in the next Chapter to introduce to the concept of linear response, where the response of a system to an external perturbation is described in terms of the susceptibility.

4. Magnetic excitations within linear response theory

All information about a quantum mechanical system is gained through either analyzing its effects on other physical systems (*i.e.*, measuring instruments) or studying its reaction to a controllable external perturbation. Since one of the principal laws of thermodynamics says that a closed system aspires to reach its thermal equilibrium state with time, it seems fair to assume that the system maintains close to its ground state if such a probing perturbation is of small character. For such type of physical problems the concept of linear response theory is well established. The core of this theory assumes a linear dependency of a probed operator, say $\mathcal{A}$, with respect to the perturbation $\delta\mathcal{B}$. The change of the expectation value, $\delta\langle\mathcal{A}\rangle$, is described by

$$\delta\langle\mathcal{A}\rangle(t) = \int \mathrm{d}t' \chi_{AB}(t-t')\delta\mathcal{B}(t') \tag{4.1}$$

where χ_{AB} describes the reaction in first order and is called response function or susceptibility. In order to preserve causality the response function is retarded, which means that it vanishes for $t - t' < 0$.

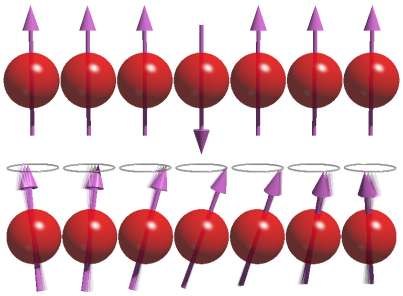

Figure 4.1.: Schematic sketch of a single spin-flip excitation (top) and a collective excitation (bottom) depicted for a chain of ferromagnetically coupled magnetic moments indicated by arrows. Whereas the excitation of a spin-flip process requires a certain energy, a spin wave, in principle, can be realized already for vanishing excitation energy, when, *e.g.*, the wave length of the spin excitation is approaching infinity and all moments are rotating in phase (acoustic mode).

4.1. Magnetic excitations in solids

A magnetic excitation generally describes a particle-conserving process in which the system reaches an excited state by pushing one or more magnetic moments out of their energetically preferred orientations. As the present thesis investigates structures that contain $3d$ transition metal atoms as magnetic impurities, their localized d shell electrons play the role of these excited magnetic moments. One distinguishes single-particle excitations and those of collective character, as schematically illustrated in Fig. 4.1. Magnetic (or spin) excitations are particle conserving which increase or decrease the total spin of the system by one. Thus, they are of bosonic character and obey the Bose-Einstein distribution. In the Appendix E the formalism will be demonstrated by use of the Matsubara formalism.

Magnetic excitations which are extended throughout the solid are classified as quasi particles with momentum $\vec{q}$ and energy ω. A Stoner excitation is the simplest possible magnetic excitation, a single spin-flip process that involves an electron-hole pair of opposite spin. Although this picture suggests a localized process, such Stoner excitations can also come to existence in a metallic environment with itinerant electrons. Then, the excited electron-hole pair is described by two Bloch states of opposite spin character.

One the other hand, when more than one atom is part of the excitation more complex response can be observed. These collective excitations are called magnons or spin waves. They are not eigenstates to the unperturbed Hamiltonian. Suitable models to describe such spectra are given by the linear response formalism where the single spin flip susceptibility gets renormalized by the exchange and correlation kernel to be the enhanced susceptibility.

The present study focuses on excitations in a localized impurity in form of a nanostructure

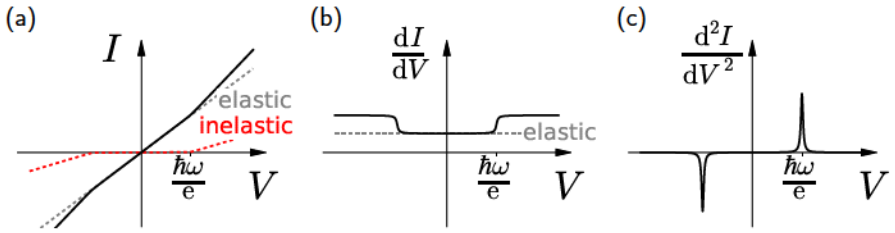

Figure 4.2.: Inelastic scanning tunneling spectroscopy: An additional inelastic excitation channel for the tunneling electrons usually manifests in a sudden change of slope in the I-V spectrum (a). The corresponding signature appears as step in the conductance or $\mathrm{d}I/\mathrm{d}V$ spectrum (b) or as peak or dip in the derivative of the conductance or $\mathrm{d}^2I/\mathrm{d}V^2$ spectrum (c).

of one or more magnetic $3d$ transition metal atoms. Despite the interaction with the electron sea of the substrate atoms, such an excitation is of local character. Therefore the usual formalism involving a $\vec{q}$-vector dependence does not hold anymore.

4.1.1. Experimental techniques

Nowadays a variety of excellent experimental techniques are available to study magnetic excitations in solids. The choice of the best suited method depends on the target system, the external parameters (like, *e.g.*, the temperature or the possibility of applying magnetic fields) and the desired aspect of research.

Spatially averaging experimental techniques

The majority of these techniques are averaging techniques, which means that a large area or volume of the sample is involved in the measuring process, allowing to put aside unwanted effects that originate from defects and similar local deviations from a perfect crystal environment. Prominent representatives of such methods are inelastic neutron scattering (INS) [63], ferromagnetic resonance (FMR) [64], angle-resolved photoemission spectroscopy (ARPES) [65–67] or spin-polarized electron energy loss spectroscopy (SPEELS) [68], just to name a few. Common to all these techniques is that the resulting spectra are obtained when probing a surface area that is much larger than the atomic spacing.

Spatially resolved experimental technique: Inelastic scanning tunneling spectroscopy

On the other hand the study of magnetic excitations in a non-averaging approach has emerged to be a well-established experimental technique. This method is called inelastic scanning tunneling spectroscopy (ISTS). It allows to study the response of nanostructures down to the single atom. The key to the excitation spectra lies here in the variation of the applied bias voltage (V) while the tip position above the regarded nanostructure is fixed. This variation is accompanied by a variation of the tunneling current (I). If the energy for the tunneling electrons becomes large enough additional tunneling channels may become available that allow the electrons to tunnel inelastically. In the I-V spectrum such additional tunneling channels manifest in a sudden change of the slope of the curve. In the conductance spectrum ($\mathrm{d}I/\mathrm{d}V$) these excitation processes lead to steps in the else wise flat conductance curve. In the derivative of the conductance one observes peaks or dips at the corresponding energies. This is shown schematically in Fig. 4.2. By use of the Tersoff-Hamann approximation [39] one can relate the conductance spectrum to the local density of states. This connection will be picked up again in Ch. 6.

4.2. The dynamical magnetic response function

The linear response of the magnetic moment due to an external time-dependent magnetic perturbation is a particular form of the linear response theory. Before the magnetic response function is considered, the general concept of the linear response formalism is presented.

4.2.1. General form of a linear response function

Suppose a quantum-mechanical system is described by the time-dependent Schrödinger equation

$$\mathrm{i}\frac{\partial}{\partial t}|\psi(t)\rangle = \mathcal{H}(t)|\psi(t)\rangle \quad , \text{ with } \quad \mathcal{H}(t) = \mathcal{H}_0 + \delta v_{\mathrm{ext}}(t) \; . \tag{4.2}$$

The Hamiltonian $\mathcal{H}(t)$ contains a time-independent part, $\mathcal{H}_0$, and a small time-dependent external perturbation $\delta v_{\mathrm{ext}}(t)$ that is switched on at $t = t_0$ and couples to the observable $\mathcal{B}$ via an external force δF,

$$\delta v_{\mathrm{ext}}(t) = \begin{cases} 0 & , \quad t < t_0 \\ \mathcal{B}\, \delta F(t) & , \quad t \geq t_0 \end{cases} \; . \tag{4.3}$$

By use of the Ansatz

$$|\psi(t)\rangle = \mathrm{e}^{-\mathrm{i}\mathcal{H}_0(t-t_0)}\mathcal{U}(t)|\psi_0(0)\rangle \; , \tag{4.4}$$

where $\mathcal{U}(t) = 1 \; \forall \; t \leq t_0$, the expectation value of an observable $\mathcal{A}$ takes the form

$$\begin{aligned} \langle \mathcal{A} \rangle (t) &= \langle \psi(t) | \mathcal{A} | \psi(t) \rangle \\ &= \langle \psi_0(t_0) | \mathcal{U}(t)^\dagger \mathrm{e}^{\mathrm{i}\mathcal{H}(t-t_0)} \mathcal{A} \mathrm{e}^{-\mathrm{i}\mathcal{H}(t-t_0)} \mathcal{U}(t) | \psi_0(t_0) \rangle \; . \end{aligned} \tag{4.5}$$

Up to linear order in δv_{ext} this results in [69]

$$\langle \mathcal{A} \rangle (t) = \langle \psi_0(t_0) | \mathcal{A}^{\mathsf{H}}(t) | \psi_0(t_0) \rangle - \mathrm{i} \int_{t_0}^{t} \mathrm{d}t' \, \langle \psi_0(t_0) | \left[\mathcal{A}^{\mathsf{H}}(t), \delta v^{\mathsf{H}}(t') \right] | \psi_0(t_0) \rangle \; , \tag{4.6}$$

where $\mathcal{A}^{\mathsf{H}}(t) = \mathrm{e}^{\mathrm{i}\mathcal{H}_0(t-t_0)} \mathcal{A} \mathrm{e}^{-\mathrm{i}\mathcal{H}_0(t-t_0)}$ denotes the representation of an operator in the Heisenberg picture. Then, the induced change in the expectation value (the *response* of the system) is given by

$$\begin{aligned} \delta \langle \mathcal{A} \rangle (t) &= \langle \mathcal{A} \rangle (t) - \langle \psi_0(t_0) | \mathcal{A}^{\mathsf{H}}(t) | \psi_0(t_0) \rangle \\ &= \int \mathrm{d}t' \, \chi^{AB}(t,t') \, \delta F_{\mathrm{ext}}(t') \; , \end{aligned} \tag{4.7}$$

where

$$\chi^{AB}(t,t') = -\mathrm{i} \langle \psi_0(t_0) | \left[\mathcal{A}^{\mathsf{H}}(t), \mathcal{B}^{\mathsf{H}}(t') \right] | \psi_0(t_0) \rangle \Theta(t-t') \tag{4.8}$$

is the general form of the susceptibility or response function. Through the response function $\chi^{AB}(t,t')$ in Eq. (4.8), $\delta \langle \mathcal{A} \rangle (t)$ reflects in principle the change of the system due to all forces $\delta F_{\mathrm{ext}}(t')$ of all past times ($t' < t$). Using Eq. (4.8) directly it follows that the susceptibility can be expressed as a functional derivative,

$$\chi^{AB}(t,t') = \left. \frac{\delta \langle \mathcal{A} \rangle (t)}{\delta F(t')} \right|_{F=0,\mathrm{GS}} \; . \tag{4.9}$$

Introducing a complete set of states ($\mathcal{H}_0 |\psi_{0n}\rangle = E_n |\psi_{0n}\rangle$ and $\sum_n |\psi_{0n}\rangle\langle\psi_{0n}| = 1$) one arrives at

$$\begin{aligned} \chi^{AB}(t-t') &= -\mathrm{i} \sum_n \Big[\mathrm{e}^{-\mathrm{i}(E_n - E_0)(t-t')} \, \langle \psi_0 | \mathcal{A} | \psi_{0n} \rangle \langle \psi_{0n} | \mathcal{B} | \psi_0 \rangle \\ &\qquad - \mathrm{e}^{\mathrm{i}(E_n - E_0)(t-t')} \, \langle \psi_0 | \mathcal{B} | \psi_{0n} \rangle \langle \psi_{0n} | \mathcal{A} | \psi_0 \rangle \Big] \, \Theta(t-t') \; , \end{aligned} \tag{4.10}$$

where the ground state, *i.e.*, the state of lowest energy E_0, is denoted by $|\psi_0\rangle$. Note that due to the assumption that $\mathcal{H}_0$ is time-independent, the susceptibility only depends on the difference in time, $t - t_0$. In frequency space the response is described by

$$\delta \langle \mathcal{A} \rangle (\omega) = \chi^{AB}(\omega) \, \delta F(\omega) \; , \tag{4.11}$$

where the response function is given by the Lehmann representation

$$\chi^{AB}(\omega) = \sum_n f_n \left[\frac{\langle \psi_0 | \mathcal{A} | \psi_n \rangle \langle \psi_n | \mathcal{B} | \psi_0 \rangle}{\omega - (E_n - E_0) + \mathrm{i}0^+} - \frac{\langle \psi_0 | \mathcal{B} | \psi_n \rangle \langle \psi_n | \mathcal{A} | \psi_0 \rangle}{\omega + (E_n - E_0) + \mathrm{i}0^+} \right] \; , \tag{4.12}$$

where $f_n = f(E_n)$ is the occupation number of state with energy E_n. The response function has poles when the frequency of the external perturbation matches the energy difference between two eigenstates (unless the matrix element vanishes).

By use of the spectral representation of the Green function $\mathcal{G}(z) = \sum_n |\psi_n\rangle\langle\psi_n|/(z - E_n)$ (see Eq. (3.4)) one can show that

$$\begin{aligned}\chi^{AB}(\omega + \mathrm{i}0^+) &= -\frac{1}{\pi}\int \mathrm{d}E f(E)\Big[\mathrm{Tr}\,\left[\mathcal{A}\,\mathcal{G}(E+\omega+\mathrm{i}0^+)\,\mathcal{B}\,\mathrm{Im}\mathcal{G}(E)\right] \\ &\qquad +\mathrm{Tr}\,\left[\mathcal{A}\,\mathrm{Im}\mathcal{G}(E)\,\mathcal{B}\,\mathcal{G}(E-\omega-\mathrm{i}0^+)\right]\Big]\,, \quad (4.13)\end{aligned}$$

which in the real space representation leads to

$$\begin{aligned}&\chi^{AB}(\vec{x}\,,\vec{x}\,';\omega+\mathrm{i}0^+) \\ &\quad = -\frac{1}{\pi}\int \mathrm{d}E f(E)\Big[\mathrm{Tr}\,\left[\mathcal{A}\,G(\vec{x}\,,\vec{x}\,';E+\omega+\mathrm{i}0^+)\,\mathcal{B}\,\mathrm{Im}G(\vec{x}\,',\vec{x}\,;E)\right] \\ &\qquad +\mathrm{Tr}\,\left[\mathcal{A}\,\mathrm{Im}G(\vec{x}\,,\vec{x}\,';E)\,\mathcal{B}\,G(\vec{x}\,',\vec{x}\,;E-\omega-\mathrm{i}0^+)\right]\Big]\,. \quad (4.14)\end{aligned}$$

The form of the general susceptibility in the Lehmann representation allows for the symmetry relations

$$\begin{aligned}&\chi^{AB}(\vec{x}\,,\vec{x}\,';-\omega+\mathrm{i}0^+) \\ &= \sum_{n,m}(f_n - f_m)\frac{A_{nm}(\vec{x})B_{mn}(\vec{x}\,')}{-\omega-(E_m-E_n)+\mathrm{i}0^+} \quad (4.15)\\ &= \sum_{n,m}(f_m - f_n)\frac{B_{mn}(\vec{x}\,')A_{nm}(\vec{x}\,)}{\omega-(E_n-E_m)-\mathrm{i}0^+} = \chi^{BA}(\vec{x}\,',\vec{x}\,;\omega-\mathrm{i}0^+) \quad (4.16)\\ &= \sum_{n,m}(f_m - f_n)\left[\frac{A_{mn}(\vec{x})B_{nm}(\vec{x}\,')}{\omega-(E_n-E_m)+\mathrm{i}0^+}\right]^* = \chi^{AB}(\vec{x}\,,\vec{x}\,';\omega+\mathrm{i}0^+)^* \quad (4.17)\\ &= \sum_{n,m}(f_n - f_m)\left[\frac{B_{nm}(\vec{x}\,')A_{mn}(\vec{x}\,)}{-\omega-(E_m-E_n)-\mathrm{i}0^+}\right]^* = \chi^{BA}(\vec{x}\,',\vec{x}\,;-\omega-\mathrm{i}0^+)^*\,, \quad (4.18)\end{aligned}$$

where the asterisk $(*)$ denotes complex conjugation.

4.2.2. Charge and magnetization response

As the present thesis deals with magnetic excitations, Eq. (4.8), the general form of the linear response function, can be specified in terms of an electromagnetic external perturbation. It will be introduced as a four-component vector leading to a 4×4 susceptibility tensor. However, as we concentrate on spin-flip processes while at the same time spin-orbit

coupling (SOC) is neglected, a number of symmetries and vanishing components of the susceptibility tensor will be revealed. The driving force of the external perturbation reads

$$\delta \underline{V}_{\text{ext}}(\vec{x}\,,t) = \begin{pmatrix} \delta V(\vec{x}\,,t) \\ \delta \vec{B}(\vec{x}\,,t) \end{pmatrix} \,, \tag{4.19}$$

with the external electrostatic potential δV and the external magnetic field $\delta \vec{B}$. Then the induced change in the expectation value of charge and magnetic moment is described by

$$\delta \underline{n}(\vec{x}\,,t) = \int \mathrm{d}^3x' \int \mathrm{d}t' \underline{\underline{\chi}}(\vec{x}\,,\vec{x}\,',t-t') \delta \underline{V}_{\text{ext}}(\vec{x}\,',t') \,, \tag{4.20}$$

where

$$\delta \underline{n}(\vec{x}\,,t) = \begin{pmatrix} \delta n(\vec{x}\,,t) \\ \delta \vec{m}(\vec{x}\,,t) \end{pmatrix} \tag{4.21}$$

is the four-vector of the induced charge $\delta n = n_1 - n_0$ and magnetization $\delta \vec{m} = \vec{m}_1 - \vec{m}_0$, caused by the presence of the external perturbation $\delta \underline{V}_{\text{ext}}$. The response function in Eq. (4.20) is a (4×4)-matrix and reads

$$\underline{\underline{\chi}}(\vec{x}\,,\vec{x}\,';t-t') = \begin{pmatrix} \chi_{00} & \chi_{0x} & \chi_{0y} & \chi_{0z} \\ \chi_{x0} & \chi_{xx} & \chi_{xy} & \chi_{xz} \\ \chi_{y0} & \chi_{yx} & \chi_{yy} & \chi_{yz} \\ \chi_{z0} & \chi_{zx} & \chi_{zy} & \chi_{zz} \end{pmatrix} \,, \tag{4.22}$$

where its components have the same spatial and time dependence, $\chi_{\alpha\beta} = \chi_{\alpha\beta}(\vec{x}\,,\vec{x}\,';t-t')$ for $\alpha,\beta \in \{0,x,y,z\}$ and can be expressed as

$$\chi_{\alpha\beta}(\vec{x}\,,t;\vec{x}\,',t') = -\mathrm{i}\langle [S_\alpha(\vec{x}\,,t), S_\beta(\vec{x}\,',t')] \rangle \Theta(t-t') \,, \tag{4.23}$$

where $S_\alpha(\vec{x}\,,t) = \mathrm{e}^{\mathrm{i}\mathcal{H}_0(t-t_0)} S_\alpha(\vec{x}) \mathrm{e}^{-\mathrm{i}\mathcal{H}_0(t-t_0)}$ and $S_\alpha(\vec{x}\,) = \sum_{i=1}^N \frac{\boldsymbol{\sigma}_\alpha}{2} \delta(\vec{x}-\vec{x}_i)$ is the four-vector spin density for a system of N electrons located at positions $\{\vec{x}_i\}$ (see the analogue definition in Eq. (2.16)). The form of the matrix $\underline{\underline{\chi}}$ in Eq. (4.22) gets simplified for the case that a ferromagnetic ground state is considered, spin-orbit coupling is set aside and the magnetization points in z direction. Then, the Green function is of the form

$$\begin{aligned} \boldsymbol{G}(\vec{x}\,,\vec{x}\,';z) &= \begin{pmatrix} G^{\uparrow\uparrow}(\vec{x}\,,\vec{x}\,';z) & G^{\uparrow\downarrow}(\vec{x}\,,\vec{x}\,';z) \\ G^{\downarrow\uparrow}(\vec{x}\,,\vec{x}\,';z) & G^{\downarrow\downarrow}(\vec{x}\,,\vec{x}\,';z) \end{pmatrix} = \begin{pmatrix} G^{\uparrow}(\vec{x}\,,\vec{x}\,';z) & 0 \\ 0 & G^{\downarrow}(\vec{x}\,,\vec{x}\,';z) \end{pmatrix} \\ &= \frac{G^{\uparrow}(\vec{x}\,,\vec{x}\,';z) + G^{\downarrow}(\vec{x}\,,\vec{x}\,';z)}{2} \boldsymbol{\sigma}_0 + \frac{G^{\uparrow}(\vec{x}\,,\vec{x}\,';z) - G^{\downarrow}(\vec{x}\,,\vec{x}\,';z)}{2} \boldsymbol{\sigma}_z \end{aligned} \tag{4.24}$$

and one arrives at

$$\underline{\underline{\chi}}(\vec{x}\,,\vec{x}\,';t-t') = \begin{pmatrix} P & 0 & 0 & \chi_{0z} \\ 0 & \chi_{xx} & \chi_{xy} & 0 \\ 0 & -\chi_{xy} & \chi_{xx} & 0 \\ \chi_{0z} & 0 & 0 & \chi_{zz} \end{pmatrix} , \tag{4.25}$$

where the polarization P was introduced. Together with χ_{0z} and χ_{zz} it forms the longitudinal part of the susceptibility, *i.e.*, the part which describes changes in the charge density and the length of the magnetic moment. Since throughout the thesis we are interested in describing spin-flip processes our focus is the transversal part of the susceptibility, described by the matrix elements χ_{xx} and χ_{xy}. By defining the operators

$$S^{\pm} = \frac{1}{2}\boldsymbol{\sigma}^{\pm} = \frac{1}{2}\left(\boldsymbol{\sigma}_x \pm \mathrm{i}\boldsymbol{\sigma}_y\right) = \begin{cases} \begin{pmatrix} 0 & 1 \\ 0 & 0 \end{pmatrix} & , \quad + \\ \begin{pmatrix} 0 & 0 \\ 1 & 0 \end{pmatrix} & , \quad - \end{cases} \tag{4.26}$$

and inserting them into Eq. (4.8) one can identify

$$\chi^{+-} = 2\left(\chi_{xx} - \mathrm{i}\chi_{xy}\right) \tag{4.27}$$

$$\chi^{-+} = 2\left(\chi_{xx} + \mathrm{i}\chi_{xy}\right) \tag{4.28}$$

4.3. Magnetic linear response within TDDFT

In general, the response of a system to an external perturbation is formulated in Eq. (4.20). However, the formalism within time-dependent density functional theory (TDDFT) leads to a modification of the effective potential, which besides the external contribution contains a Hartree potential and an exchange-correlation potential. In Sec. 2.3.3 the charge response was discussed. Here, the formalism is extended to spin polarized systems and a focus is set on the magnetic response of the system.

The comprehensive form of the Kohn-Sham susceptibility, describing the four-vector charge response to a four-vector effective potential is defined via the equation

$$\delta n_\alpha(\vec{x}\,,t) = \sum_\beta \int \mathrm{d}^3x' \int \mathrm{d}t' \chi_{\mathrm{KS},\alpha\beta}(\vec{x},t;\vec{x}\,',t')\delta v_{\mathrm{eff},\beta}(\vec{x}\,',t') \tag{4.29}$$

with $\alpha,\beta \in \{0,x,y,z\}$ and

$$\delta v_{\mathrm{eff},\alpha}(\vec{x}\,,t) = \delta v_{\mathrm{ext},\alpha}(\vec{x}\,,t) + 2\delta_{0,\alpha}\int \mathrm{d}^3x' \frac{\delta n_0(\vec{x}\,',t)}{|\vec{x}-\vec{x}\,'|} + \delta v^\alpha_{\mathrm{xc}}(\vec{x}\,,t)\ . \tag{4.30}$$

Thus, the Kohn-Sham susceptibility is given in terms of a functional derivative,

$$\chi_{\mathrm{KS},\alpha\beta}(\vec{x}\,,t;\vec{x}\,',t') = \left.\frac{\delta n_\alpha[\delta \underline{v}_{\mathrm{eff}}](\vec{x}\,,t)}{\delta v_{\mathrm{eff},\beta}(\vec{x}\,',t')}\right|_{\delta v_{\mathrm{eff},\beta}=0,\mathrm{GS}} . \tag{4.31}$$

The second term of Eq. (4.30) is the time-dependent Hartree response to the perturbation. The third term represents a response due to the exchange and correlation potential and is given by

$$\delta v_{\mathrm{xc},\alpha}(\vec{x}\,,t) = \sum_\beta \int \mathrm{d}^3x' \int \mathrm{d}t' f_{\mathrm{xc},\alpha\beta}(\vec{x}\,,t,\vec{x}\,',t')\delta n_\beta(\vec{x}\,',t') \tag{4.32}$$

The exchange-correlation kernel is a functional of the ground state density, n_{GS}, and takes the form

$$f_{\mathrm{xc},\alpha\beta}[n_{\mathrm{GS}}](\vec{x}\,,t;\vec{x}\,',t') = \left.\frac{\delta v_{\mathrm{xc},\alpha}(\vec{x}\,,t)}{\delta n_\beta(\vec{x}\,',t')}\right|_{F=0,n=n_{\mathrm{GS}}} \tag{4.33}$$

Similar to Eq. (2.56) one finds a Dyson-like equation that connects the Kohn-Sham susceptibility to the enhanced susceptibility,

$$\begin{aligned}\chi^{+-}(\vec{x}\,,t;\vec{x}\,',t') &= \chi^{+-}_{\mathrm{KS}}(\vec{x}\,,t;\vec{x}\,',t') + \int \mathrm{d}^3x_1 \int \mathrm{d}t_1 \int \mathrm{d}^3x_2 \int \mathrm{d}t_2 \\ &\quad \chi^{+-}_{\mathrm{KS}}(\vec{x}\,,t;\vec{x}_2,t_2)\left(f_{\mathrm{xc}}[n](\vec{x}_2,t_2;\vec{x}_1,t_1)\right)\chi^{+-}(\vec{x}_1,t_1;\vec{x}\,',t') .\end{aligned} \tag{4.34}$$

4.4. The susceptibility within the KKR Green function formalism

The KKR formalism (see Ch. 3 and especially Eq. (3.42)) utilized retarded Green functions of the form

$$G(\vec{x}\,,\vec{x}\,';z) = G(\vec{R}_i+\vec{r}\,,\vec{R}_j+\vec{r}\,';z) = G_{ij}(\vec{r}\,,\vec{r}\,';z) . \tag{4.35}$$

These Green functions arise from a DFT based method and therefore describe Kohn-Sham particles in an effective potential. The transverse Kohn-Sham susceptibility in frequency space is given in terms of a convolution of two KKR Green functions and reads

$$\begin{aligned}\chi^{\sigma\bar{\sigma}}_{\mathrm{KS},ij}(\vec{r}\,,\vec{r}\,';\omega) &= -\frac{1}{\pi}\int \mathrm{d}E f(E)\Big[G^{\bar{\sigma}}_{ij}(\vec{r}\,,\vec{r}\,';E+\omega+\mathrm{i}0^+)\mathrm{Im}G^{\sigma}_{ji}(\vec{r}\,',\vec{r}\,';E) \\ &\quad +\mathrm{Im}G^{\bar{\sigma}}_{ij}(\vec{r}\,,\vec{r}\,';E)G^{\sigma}_{ji}(\vec{r}\,',\vec{r}\,';E-\omega-\mathrm{i}0^+)\Big] ,\end{aligned} \tag{4.36}$$

where $\sigma \in \{\uparrow, \downarrow\}$ and $\mathrm{Im}G_{ij} = -\mathrm{i}(G_{ij} - G^{-}_{ji})/2$, as defined in Eq. (3.9). This quantity is numerically difficult to tackle since the integration in principle requests knowledge of the Green function along the real axis. In practice, however, the integration is performed for the zero-temperature limit, $\int \mathrm{d}E f(E) \to \int^{E_\mathrm{F}} \mathrm{d}E$. Additionally, one can separate the integral in Eq. (4.36) into two parts [37, 38],

$$\chi^{\sigma\overline{\sigma}}_{\mathrm{KS},ij}(\vec{r}, \vec{r}\,'; \omega) = \mathcal{I}^{\sigma\overline{\sigma}}_{1,ij}(\vec{r}, \vec{r}\,'; \omega) + \mathcal{I}^{\sigma\overline{\sigma}}_{2,ij}(\vec{r}, \vec{r}\,'; \omega) \; , \tag{4.37}$$

where

$$\begin{aligned} \mathcal{I}^{\sigma\overline{\sigma}}_{1,ij}(\vec{r}, \vec{r}\,'; \omega) &= \frac{\mathrm{i}}{2\pi} \int_{-\infty}^{E_\mathrm{F}} \mathrm{d}E \Big[G^{\overline{\sigma}}_{ij}(\vec{r}, \vec{r}\,'; E + \omega + \mathrm{i}0^+) G^{\sigma}_{ji}(\vec{r}\,', \vec{r}; E + \mathrm{i}0^+) \\ &\qquad - G^{\overline{\sigma}}_{ij}(\vec{r}, \vec{r}\,'; E - \mathrm{i}0^+) G^{\sigma}_{ji}(\vec{r}\,', \vec{r}; E - \omega - \mathrm{i}0^+) \Big] \end{aligned} \tag{4.38}$$

and

$$\begin{aligned} \mathcal{I}^{\sigma\overline{\sigma}}_{2,ij}(\vec{r}, \vec{r}\,'; \omega) &= \frac{\mathrm{i}}{2\pi} \int_{E_\mathrm{F}}^{E_\mathrm{F}-\omega} \mathrm{d}E G^{\overline{\sigma}}_{ij}(\vec{r}, \vec{r}\,'; E + \omega + \mathrm{i}0^+) G^{\sigma}_{ji}(\vec{r}\,', \vec{r}; E - \mathrm{i}0^+) \\ &\quad . \end{aligned} \tag{4.39}$$

The first part $\mathcal{I}_1$ involves an integration from $-\infty$ to E_F, while the integrand is analytical above the real axis (use Eq. (3.5) to see). Thus, one can benefit from the KKR contour (see Ch. 3.2.3) when solving this integral. The integrand in $\mathcal{I}_2$, however, contains a product of Green functions which have poles on opposite sides of the real axis. A distortion of the integration into the complex plane is therefore not possible. On the other hand, the integration interval is of length ω and therefore finite.

As pointed out by Lounis *et al.* [38] another separation of the expression for the Kohn-Sham susceptibility is possible. In Eq. (4.38), more precisely for the integrand that contains the first product of the two Green functions, $G(E + \omega + \mathrm{i}0^+)G(E + \mathrm{i}0^+)$, the integration up to the Fermi energy is replaced by $\int_{-\infty}^{E_\mathrm{F}-\omega} + \int_{E_\mathrm{F}-\omega}^{E_\mathrm{F}}$ and distributes the latter term to the expression that is defined in Eq. (4.39). In contrast to Ref. [38] a distinction between positive and negative frequencies is not considered. After a variable substitution of the first integrand (such that the upper integration boundary is identical to the Fermi energy, $\int_{-\infty}^{E_\mathrm{F}-\omega} \to \int_{-\infty}^{E_\mathrm{F}}$) one arrives at a partition of the form $\chi = \overline{\mathcal{I}}_1 + \overline{\mathcal{I}}_2$, where

$$\begin{aligned} \overline{\mathcal{I}}^{\sigma\overline{\sigma}}_{1,ij}(\vec{r}, \vec{r}\,'; \omega) &= \frac{\mathrm{i}}{2\pi} \int_{-\infty}^{E_\mathrm{F}} \mathrm{d}E \Big[G^{\overline{\sigma}}_{ij}(\vec{r}, \vec{r}\,'; E + \mathrm{i}0^+) G^{\sigma}_{ji}(\vec{r}\,', \vec{r}; E - \omega + \mathrm{i}0^+) \\ &\qquad - G^{\overline{\sigma}}_{ij}(\vec{r}, \vec{r}\,'; E - \mathrm{i}0^+) G^{\sigma}_{ji}(\vec{r}\,', \vec{r}; E - \omega - \mathrm{i}0^+) \Big] \end{aligned} \tag{4.40}$$

and

$$\overline{\mathcal{I}}^{\sigma\overline{\sigma}}_{2,ij}(\vec{r},\vec{r}\,';\omega) = \frac{\mathrm{i}}{2\pi}\int_{E_\mathrm{F}}^{E_\mathrm{F}-\omega}\mathrm{d}E G^{\overline{\sigma}}_{ij}(\vec{r},\vec{r}\,';E+\omega+\mathrm{i}0^+) \left(G^{\sigma}_{ji}(\vec{r}\,',\vec{r};E-\mathrm{i}0^+) - G^{\sigma}_{ji}(\vec{r}\,',\vec{r};E+\mathrm{i}0^+)\right) \tag{4.41}$$

Here $\chi^{\uparrow\downarrow}$ and $\chi^{\downarrow\uparrow}$ correspond to χ^{+-} and χ^{-+}, respectively.

The two contributions to the Kohn-Sham susceptibility either take the form as given by Eqs. (4.38) and (4.39) or separate in a way as provided by Eqs. (4.40) and (4.41). Both forms are mathematically identical. Numerically they lead to the exact same values for $\omega = 0$ and show insignificant deviations for small frequency values (in the region of a few meV). Thus, all presented results within Chs. 6 and 7 utilize the first separation (*cf.* Eqs. (4.38) and (4.39)). However, for a larger frequency window and when the susceptibility is required for more than one atom, in some susceptibility spectra small numerical instabilities were found, whereas the second separation (*cf.* Eqs. (4.40) and (4.41)) has proven to be more robust against such shortcomings. Therefore, in Ch. 8, where nanostructures beyond the single atom impurity are considered, the second separation is used. Finally, note that the calculated susceptibilities shown in Chs. 6, 7 and 8 are utilizing a rational fit of the projected Green function, see Sec. 3.3. Thus, the spatial dependency in Eqs. (4.38), (4.39), (4.40), and (4.41) is dropped and one finds

$$\chi^{\sigma\overline{\sigma}}_{\mathrm{KS},ij}(\omega) = \mathcal{I}^{\sigma\overline{\sigma}}_{1,ij}(\omega) + \mathcal{I}^{\sigma\overline{\sigma}}_{2,ij}(\omega) = \overline{\mathcal{I}}^{\sigma\overline{\sigma}}_{1,ij}(\omega) + \overline{\mathcal{I}}^{\sigma\overline{\sigma}}_{2,ij}(\omega)\ , \tag{4.42}$$

where $\mathcal{I}^{\sigma\overline{\sigma}}_{1,ij}(\omega)$ and $\mathcal{I}^{\sigma\overline{\sigma}}_{2,ij}(\omega)$ are given by Eqs. (4.38) and (4.39) by replacing the Green function with the rational fit and the same for the separation into $\overline{\mathcal{I}}^{\sigma\overline{\sigma}}_{1,ij}(\omega)$ and $\overline{\mathcal{I}}^{\sigma\overline{\sigma}}_{2,ij}(\omega)$.

4.4.1. Approximation of the exchange-correlation kernel

The connection between enhanced and Kohn-Sham susceptibility is given by Eq. (4.34), an equation of the following schematic structure,

$$\chi = \chi_0\left(1 - U\chi_0\right)^{-1}\ , \tag{4.43}$$

where U is the exchange-correlation kernel. Since relativistic effects are not considered within this thesis, spin-orbit coupling is neglected and therefore magnetic anisotropy does not appear. This implies that a rotation of the magnetic moments in spin space is energetically invariant, as long as no external magnetic field breaks this symmetry. The response of the system is then infinite for zero frequency, which leads to the so-called Goldstone mode. It turns out, however, that in DFT based methods this condition is not fulfilled exactly [31] due to a violation of the Ward identity [38]. One possibility is to enforce the Goldstone mode by an ad hoc correction [33], *i.e.*, the exchange-correlation

kernel is scaled by a factor. In this thesis we use a sum rule that enforces the Goldstone mode by construction. The sum rule reads [38]

$$\sum_j \int \mathrm{d}\vec{r}\,' \, \chi^{+-}_{\mathrm{KS},ij}(\vec{r},\vec{r}\,';0) B^{\mathrm{eff}}_{j,z}(\vec{r}\,') = m_{i,z}(\vec{r}\,) \;, \tag{4.44}$$

where

$$\chi^{+-}_{\mathrm{KS},ij}(\vec{r},\vec{r}\,';0) = \mathcal{I}^{+-}_{1,ij}(\vec{r},\vec{r}\,';\omega) = \overline{\mathcal{I}}^{+-}_{1,ij}(\vec{r},\vec{r}\,';0) \;, \tag{4.45}$$

as well as $B^{\mathrm{eff}}_{i,z}(\vec{r}\,) = V^{\downarrow}_i(\vec{r}\,) - V^{\uparrow}_i(\vec{r}\,)$, the difference between the potentials of the two spin channels for atom i, and

$$m_{i,z}(\vec{r}\,) = -\frac{1}{\pi}\mathrm{Im}\int_{-\infty}^{E_{\mathrm{F}}} \mathrm{d}E \left[G^{\uparrow}_{ii}(\vec{r},\vec{r};E) - G^{\downarrow}_{ii}(\vec{r},\vec{r};E) \right] \;. \tag{4.46}$$

Expanding the susceptibility in real spherical harmonics, *i.e.*,

$$\chi^{+-}_{\mathrm{KS},ij}(\vec{r},\vec{r}\,';\omega) = \sum_{L,L',L'',L'''} \chi^{+-}_{\mathrm{KS},iLL',jL''L'''}(r\,,r\,';\omega) Y_L(\hat{\vec{r}}) Y_{L'}(\hat{\vec{r}}\,') Y_{L''}(\hat{\vec{r}}\,') Y_{L'''}(\hat{\vec{r}}) \;, \tag{4.47}$$

and assuming a spherical symmetric problem with $\vec{m}_i(\vec{r}\,,t) = \vec{m}_i(r\,,t)$ and $\vec{B}^{\mathrm{ext}}_i(\vec{r}\,,t) = \vec{B}^{\mathrm{ext}}_i(r\,,t)$ (as it is the case within the atomic-sphere approximation, see Ch. 3), one arrives at

$$\sum_j \int \mathrm{d}r\,' \, \Gamma_{ij}(r\,,r\,') U_j(r\,') = m_{i,z}(r\,) \;, \tag{4.48}$$

where

$$\Gamma_{ij}(r\,,r\,') = \sum_{L,L'} \chi^{+-}_{\mathrm{KS},iLL',jL'L}(r\,,r\,';0) m_{j,z}(r\,') \tag{4.49}$$

and

$$U_j(r\,') = \frac{B^{\mathrm{eff}}_{j,z}(r\,')}{4\pi m_{j,z}(r\,')} \;, \tag{4.50}$$

which is the form of the exchange-correlation kernel within the adiabatic local-density approximation, *i.e.*, it is local in space and frequency independent. The elements within Eq. (4.48) can be understood as vectors and matrices, depending on whether they carry one or two site labels, respectively. Then, an inverse of the Γ-matrix gives rise to the definition of the exchange-correlation kernel of the form

$$U_i(r\,) = \sum_j \int \mathrm{d}r\,' \left((\Gamma(r\,,r\,'))^{-1} \right)_{ij} m_{j,z}(r\,') \;. \tag{4.51}$$

Within this thesis all derived expressions are written in terms of the projected Green functions of the subspace of d-orbitals, such that the spatial dependency is captured by the utilized basis set. Thus, the used exchange-correlation kernel within this thesis reduces to a single (real) number per magnetic atom. For one atom one identifies

$$U = \left(\chi_{\mathrm{KS}}^{+-}(\omega=0)\right)^{-1}\Big|_{B^{\mathrm{ext}}=0} \tag{4.52}$$

and for two or more atoms the expression reads

$$U_i = \sum_j \left((\Gamma)^{-1}\right)_{ij}\Big|_{B^{\mathrm{ext}}=0} m_{d,j} \ , \tag{4.53}$$

where $m_{d,j}$ is the projected form of the magnetic moment for atom j and Γ the projected form of the matrix given in Eq. (4.49).

4.4.2. Linearization of the susceptibility

In practice, the dynamical transverse magnetic Kohn-Sham susceptibility shows a fairly linear behavior for small frequencies. This can be used to formulate an expansion in form of a Taylor series [70, 71] or a Padé series up to first order in frequency. The advantage of such a scheme is that main characteristics of magnetic excitations, such as its lifetime or the g shift, become accessible already by applying a static DFT formalism.

By making the ansatz $\chi_{\mathrm{KS}}^{+-}(\omega) = \chi_{\mathrm{KS}}^{+-}(0) + S^{+-}\omega + \mathcal{O}(\omega^2)$ one arrives at [71]

$$\begin{aligned} S_{ij}^{+-}(\vec{r},\vec{r}\,') \\ = \ & \frac{\mathrm{i}}{2\pi}\Bigg[\int^{E_{\mathrm{F}}} \mathrm{d}z \left(\frac{\mathrm{d}G_{ij}^{\downarrow}(\vec{r},\vec{r}\,';z)}{\mathrm{d}z} G_{ji}^{\uparrow}(\vec{r}\,',\vec{r};z) + G_{ji}^{*\downarrow}(\vec{r}\,',\vec{r};z)\frac{\mathrm{d}G_{ij}^{*\uparrow}(\vec{r},\vec{r}\,';z)}{\mathrm{d}z}\right) \\ & + G_{ij}^{\downarrow}(\vec{r},\vec{r}\,';E_{\mathrm{F}}) G_{ij}^{*\uparrow}(\vec{r},\vec{r}\,';E_{\mathrm{F}})\Bigg] \ . \end{aligned} \tag{4.54}$$

For small frequencies one can describe the imaginary part of the Kohn-Sham susceptibility by dropping contribution beyond the linear term in ω. Thus, one arrives at the handy form

$$\mathrm{Im}\chi_{\mathrm{KS},ij}(\vec{r},\vec{r}\,';\omega+\mathrm{i}0^+) = -\pi n_{ij}^{\uparrow}(\vec{r},\vec{r}\,';E_{\mathrm{F}}) n_{ij}^{\downarrow}(\vec{r},\vec{r}\,';E_{\mathrm{F}}) \cdot \omega \ , \tag{4.55}$$

where

$$n_{ij}^{\sigma}(\vec{r},\vec{r}\,';E) = -\frac{1}{2\pi\mathrm{i}}\left(G_{ij}^{\sigma}(\vec{r},\vec{r}\,';E) - G_{ij}^{*\sigma}(\vec{r},\vec{r}\,';E)\right) \quad , \quad \sigma \in \{\uparrow,\downarrow\} \ . \tag{4.56}$$

Such a linear description of the susceptibility is quite useful and demonstrates reasonable accuracy in the low-frequency regime [71]. In Ch. 6 the linear dependence in frequency will be considered in more detail.

4.5. Summary

In this Chapter the dynamical transverse magnetic susceptibility was introduced as a tool to describe the induced change in the magnetic moment due to an external time-dependent magnetic perturbation. Following a scheme proposed by Lounis *et al.* [38] we presented the formulas for the Kohn-Sham susceptibility and the exchange-correlation kernel that will later be used to describe the intrinsic excitation spectra, see Chs. 6, 7, and 8. However, the goal of this thesis is to go one step further by evaluating the signature of the spin-excitation in the electronic structure, for instance the electronic structure in vacuum, which is the quantity probed by STM experiments. To achieve this connection an electron self-energy is to be determined playing the major role of the next Chapter and serves as the heart of the present thesis. This quantity, Σ, is accessible through many-body perturbation theory (MBPT) and allows via the Dyson equation the renormalization of the vacuum DOS that incorporates the spin excitation.

5. Approach to the self-energy via many-body perturbation theory

The central goal of this thesis is to provide an approach from first principles to inelastic magnetic excitation spectra as they are obtained in inelastic scanning tunneling spectroscopy (ISTS) measurements. In Ch. 4 the linear response of a system with respect to an external perturbation was analyzed and the transverse magnetic susceptibility χ^{+-} was discussed. It contains the intrinsic spin-excitation spectrum of a system and can be compared to experimentally obtained $\mathrm{d}^2I/\mathrm{d}V^2$ spectra (see the sketch in Fig. 4.2(c)) providing a theoretical means to analyze characteristics of the spin-excitation, such as the lifetime and the g shift [20]. The inelastic spectra from experiment, however, include the interaction of the probing electron with the spin excitation, which is not included in the spectrum of χ^{+-}. To account for this interaction, this Chapter presents a newly developed approach to spin-excitation spectra that allows to evaluate the signature of the spin-excitation in the vacuum site above the adatom which is related to the inelastic excitation spectra measured in experiment. This method uses the framework of many-body perturbation theory (MBPT). By means of the electron self-energy Σ it provides a systematic formalism that describes scattering processes in a solid driven out of its equilibrium state. Since spin-flip processes are of primary importance in the description of magnetic excitations in ISTS experiments, the focus of this Chapter lies on such processes which are represented by a certain Feynman diagram.

The structure of this Chapter is as follows: In Sec. 5.1 we introduce in a schematic picture the basic processes that occur in inelastic scanning tunneling experiments to motivate the subsequent approach. This is followed by Sec. 5.2 where the central idea behind MBPT is presented and the overall structure of the self-energy that is used to describe spin-flip

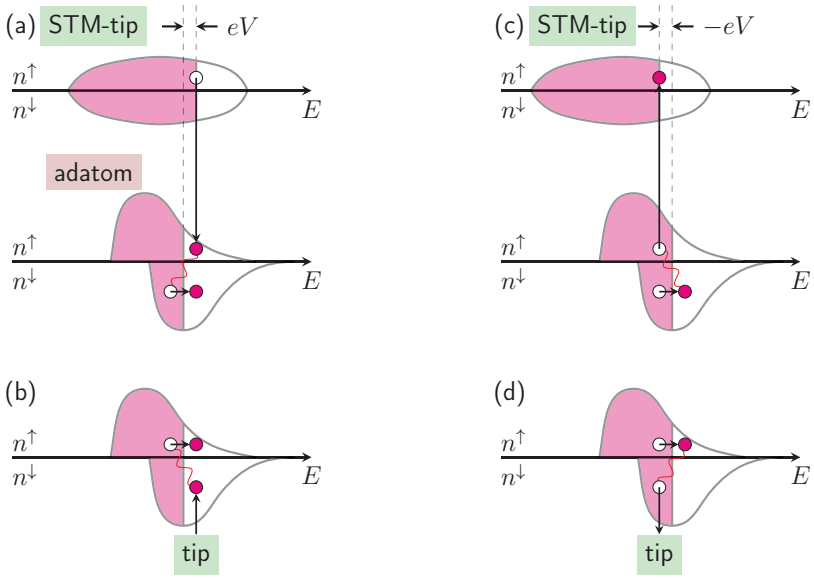

Figure 5.1.: This figure illustrates the four basic spin-flip processes that occur in inelastic tunneling experiments ((a)-(d)). The electrons are indicated by red circles, the holes by empty white circles. The wiggly lines represent electron-hole pair interactions. The probability for such processes to appear depends on the sign of the applied bias voltage V as well as its strength.

processes is shown. A connection to time-dependent density functional theory (TDDFT) and to the Korringa-Kohn-Rostoker (KKR) Green function formalism is given in Sec. 5.3. In Sec. 5.4 it is demonstrated how the electronic structure renormalized via the self-energy can be related to measured inelastic excitation spectra by means of the Tersoff-Hamann (TH) approximation. Finally, we draw the main conclusions in Sec. 5.5 and summarize the theoretical framework of the thesis.

5.1. Inelastic spin-flip scattering – the four basic processes

In this Section we introduce to the basic inelastic tunneling processes that occur in ISTS measurements of magnetic systems. By inelastic processes we mean scattering events that involve a gain or loss of energy of the tunneling electron exciting a magnetic state in the nanostructure. We seek to describe these processes in terms of a MBPT approach, where the spin-flip scattering events are described by the spin-dependent self-energy Σ^σ with $\sigma \in \{\uparrow, \downarrow\}$.

In Fig. 5.1 the four basic spin-flip processes are visualized in a schematic way. Higher-order terms in the interaction are not considered and will be included later by renormalization of the electron-hole pair. In the first process (see Fig. 5.1(a)) an electron with spin up tunnels from the tip to the surface where it excites an electron in the minority band. The hole created in the minority-spin channel and the *tunneling* electron can form a bound electron-hole pair of opposite spins. The other processes are obtained by swapping the spin labels (see Fig. 5.1(b)), the role of electrons and holes (see Fig. 5.1(c)), or both (see Fig. 5.1(d)). The electron-hole pairs after renormalization via the mediating screened interactions (indicated by wiggly red lines) lead to correlated spin-flip excitations, *i.e.*, magnons in extended systems. Processes in Figs. 5.1(a) and 5.1(c) mainly contribute to $\Sigma^{\uparrow}$ while $\Sigma^{\downarrow}$ is dominated by processes in Figs. 5.1(b) and 5.1(d). As exemplified in Fig. 5.1, some processes can be dominant depending on the electronic structure. This is related to the density of states (DOS) for electrons and holes available for the different processes. In Fig. 5.1(b), for example, the amplitude of the electron-hole pair defined by the unoccupied minority-spin states and occupied majority-spin states is much larger than the amplitude of the electron-hole pair defined by the occupied minority-spin states and unoccupied majority-spin states shown in Fig. 5.1(d). Thus, one expects the self-energy for the majority-spin channel to be mainly shaped by the process in Fig. 5.1(c) while the minority-spin channel would be mainly shaped by the process in Fig. 5.1(b). This is in agreement with explanations intuitively proposed in Ref. [72].

5.2. Basic concepts of many-body perturbation theory

Many-body perturbation theory (MBPT) is designed to study how systems with a large number of electrons react to small perturbations, such as the ejection or injection of electrons (*e.g.*, as it happens in many probing experimental techniques). The probability amplitude for the propagation of a particle with spin σ from $2 = (\vec{r}_2, t_2)$ to $1 = (\vec{r}_1, t_1)$ in a reference system is given by the time-ordered Green function or *propagator*

$$G_0^{\sigma}(1,2) = -\mathrm{i}\langle \mathcal{T}\left[\hat{\psi}^{\sigma}(1)\hat{\psi}^{\sigma}(2)^{\dagger}\right]\rangle = \begin{cases} -\mathrm{i}\langle \hat{\psi}^{\sigma}(1)\hat{\psi}^{\sigma}(2)^{\dagger}\rangle & , \; t_1 - t_2 > 0 \\ +\mathrm{i}\langle \hat{\psi}^{\sigma}(2)^{\dagger}\hat{\psi}^{\sigma}(1)\rangle & , \; t_1 - t_2 < 0 \end{cases} , \tag{5.1}$$

where $\hat{\psi}^{\sigma}(1)$ and $\hat{\psi}^{\sigma}(1)^{\dagger}$ are the field operators annihilating and creating a particle, respectively. The time-ordering operator $\mathcal{T}$ ensures that the field operators are ordered with respect to their time argument, *i.e.*, depending on the sign of $t_1 - t_2$, the particle is interpreted as electron or hole.

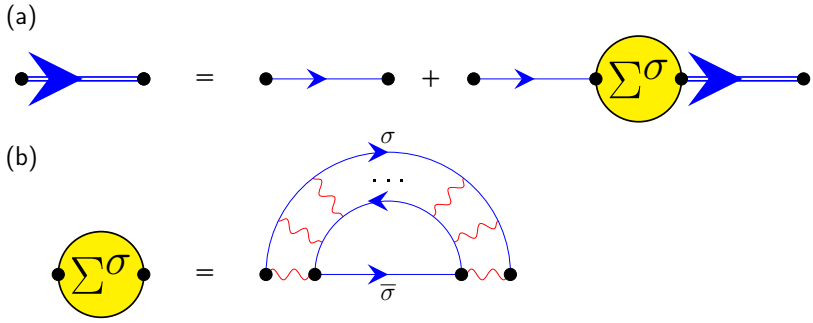

Figure 5.2.: (a) The Feynman diagram of the Dyson equation (see Eq. (5.2)) is shown. The Green function that describes the full interaction of a particle with spin σ (G^σ, double-lined blue arrow on the left) depends on the reference Green function (G_0^σ, single-lined blue arrow) and the electron self-energy (Σ^σ, yellow bubble) up to infinite order. (b) The self-energy as used in this thesis is shown, where $\overline{\sigma}$ corresponds to the opposite spin channel. The double arc is identified with the susceptibility, describing the renormalized electron-hole pair interaction. The diagram is a compact way of writing the infinite sum over different orders in the interaction (U, wiggly red lines).

5.2.1. Dyson equation and self-energy

Of crucial importance in the MBPT formalism is the Dyson equation

$$G^\sigma(1,2) = G_0^\sigma(1,2) + \int \mathrm{d}3 \int \mathrm{d}4\; G_0^\sigma(1,3)\Sigma^\sigma(3,4)G^\sigma(4,2)\;, \tag{5.2}$$

which describes the renormalization of the reference Green function G_0^σ via the self-energy Σ^σ. In Fig. 5.2(a) the corresponding Feynman diagram is shown. While $G_0^\sigma(1,2)$ describes the free propagation, $G^\sigma(1,2)$ describes the full propagation, *i.e.*, it accounts for all higher orders of interaction with the surrounding particles of the reference system described by Σ^σ. It is important to keep in mind, though, that G_0^σ may contain already exchange and correlation effects if constructed out of a mean-field Hamiltonian, as it is the case in Hartree-Fock or DFT-based methods. Thus, the difference between free and full propagation is given by those interactions that go beyond these mean-field interactions.

The explicit form of the self-energy Σ^σ given in Eq. (5.2) is not known. Instead, it represents an infinite series of scattering events of different orders and the art is to find a reasonable approximation instead. We focus here on spin-flip processes that represent the relevant events to describe the interaction of the electrons to the spin-excitation. By use of the description of four basic processes the form of the self-energy is given by a convolution of the susceptibility and the reference Green function. We do not include spin-conserving processes which give rise to excitons, *i.e.*, excited electron-hole pairs of the

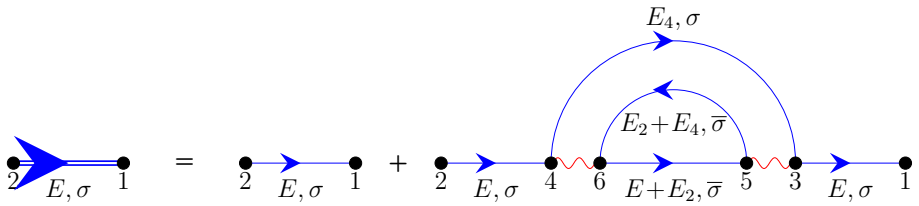

Figure 5.3.: In this figure we illustrate Eq. (5.3), which represents the lowest order term of the series of diagrams that result from the Dyson Equation (5.2). The term on the right-hand side is the lowest order diagram that is capable of describing spin-flip processes.

same spin, as they are connected to the longitudinal susceptibility which describes charge response processes.

In Fig. 5.2(b) the self-energy is shown that incorporates the spin-flip processes. It contains a particle of spin σ (upper blue half-circle) and an particle-antiparticle pair of opposite spin $\overline{\sigma}$ (blue bubble in the center), which exists for a characteristic lifetime before annihilation. During its existence an electron-hole pair of opposite spins is created which interacts via the screened interaction U (wiggly red lines). Note that for several decades different approaches to the self-energy have been proposed, starting from simple models [73–77] or a tight-binding scheme [78]. The diagram shown in Fig. 5.2(b) appears as one constituent of the T-matrix that is used in the GT-approximation [79–81]. There, the T-matrix is used to describe electron-electron, hole-hole, or electron-hole interactions and gives rise to the self-energy $\Sigma = GT$ and can be used to compensate for shortcomings that appear in the GW approximation [82] for low-electron densities [83]. Such a formalism can be embedded in a density functional approach [32, 34, 84] and applied to bulk materials.

5.2.2. Lowest order self-energy and ladder sum

Rewriting Eq. (5.2) in terms of a series one finds an infinite number of diagrams out of which we consider those that describe spin-flip processes and discuss the one of lowest order in the following. If one substitutes $G^\sigma(4,2)$ by $G_0^\sigma(4,2)$ on the right-hand side of Eq. (5.2) and accounts for the creation and annihilation of a single electron-hole pair only, one arrives at the Dyson equation as depicted in terms of the Feynman diagram in Fig. 5.3. The corresponding equation to solve reads

$$\begin{aligned} G^\sigma(1,2) \;=\; & G_0^\sigma(1,2) + \int \mathrm{d}3 \int \mathrm{d}4 \int \mathrm{d}5 \int \mathrm{d}6 \\ & G_0^\sigma(1,3) U(3,5) G_0^{\overline{\sigma}}(5,6) U(6,4) G_0^\sigma(4,2) G_0^\sigma(3,4) G_0^{\overline{\sigma}}(6,5)\,, \end{aligned} \tag{5.3}$$

where $\overline{\sigma}$ accounts for the opposite spin-channel. In Appendix D Eq. (5.3) is solved in the frequency domain, where we define $G_{1,2}^{\sigma,0}(E) = \int \mathrm{d}t\, G_{1,2}^{\sigma,0}(E)\, \mathrm{e}^{\mathrm{i}Et}$ and $G_{1,2}^{\sigma,0}(t) =$

$G^{\sigma,0}_{1,2}(t_1 - t_2) = G^{\sigma}_0(1,2)$ and use that the interactions are local in time and isotropic, $U_{12} = U(\vec{\mathrm{r}}_1, \vec{\mathrm{r}}_2; t_1 - t_2) = U_{1,2}\delta(t_1 - t_2) = U_{2,1}\delta(t_2 - t_1)$. After this reformulation one arrives at

$$G^{\sigma}_{1,2}(E) = G^{\sigma,0}_{1,2}(E) + \int \mathrm{d}^3 r_3 \int \mathrm{d}^3 r_4 G^{\sigma,0}_{1,3}(E)\Sigma^{\sigma,0}_{3,4}(E)G^{\sigma,0}_{4,2}(E) \; , \tag{5.4}$$

where $\Sigma^{\sigma,0}_{3,4}(E)$ represents the lowest order term that enters the self-energy. It reads (see Appendix D for a derivation)

$$\Sigma^{\sigma,0}_{3,4}(E) = \int \mathrm{d}^3 r_5 \int \mathrm{d}^3 r_6 U_{3,5} S^{\sigma,0}_{53;46}(E) U_{6,4} \; , \tag{5.5}$$

where

$$S^{\sigma,0}_{53;46}(E) = \mathrm{i} \int \frac{\mathrm{d}E_2}{2\pi} G^{\sigma,0}_{5,6}(E + E_2)\chi^{\sigma\bar{\sigma},0}_{36;54}(E_2) \; . \tag{5.6}$$

and

$$\chi^{\sigma\bar{\sigma},0}_{36;54}(E_2) = -\mathrm{i} \int \frac{\mathrm{d}E_4}{2\pi} G^{\sigma,0}_{3,4}(E_4) G^{\bar{\sigma},0}_{6,5}(E_2 + E_4) \; . \tag{5.7}$$

Note that this expression represents the lowest order of the self-energy diagram shown in Fig. 5.2(b). In a last step one renormalizes the electron-hole excitation described by $\chi^0_{36;54}$, in order to account for higher order terms. This is done by means of a so-called ladder diagram. In the random-phase approximation (RPA) [33, 35, 36] one can relate the susceptibility of the reference system to the interacting system via a Dyson-like equation of the form

$$\chi^{\sigma\bar{\sigma}}_{36;54}(E_2) = \chi^{\sigma\bar{\sigma},0}_{36;54}(E_2) + \int \mathrm{d}^3 r_7 \int \mathrm{d}^3 r_8 \; \chi^{\sigma\bar{\sigma},0}_{86;74}(E_2) U_{7,8} \chi^{\sigma\bar{\sigma}}_{37;58}(E_2) \; . \tag{5.8}$$

5.3. Connection to TDDFT and the KKR Green function formalism

It was already shown that a mapping between the approach via MBPT and the TDDFT formalism is possible by identifying U with the exchange-correlation kernel [37, 38]. A similar connection in the spirit of the Bethe-Salpeter equation was proposed for the case of charge excitations [85] or for spin-excitations [86]. In the following the objects that appear in MBPT (Green function or propagator, screened interaction, susceptibility, self-energy) are associated with the corresponding objects that are used in the TDDFT formalism.

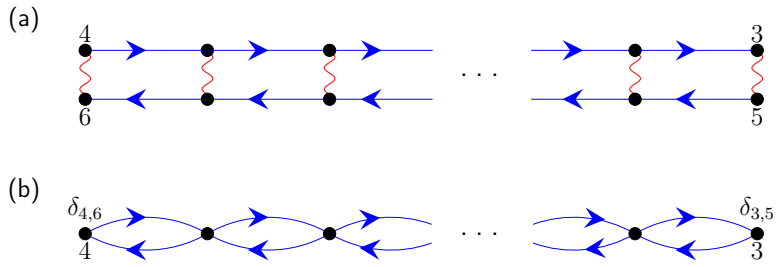

Figure 5.4.: Comparison of expressions for the susceptibility as they occur in MBPT and TDDFT. The Feynman diagrams are shown for the Nth order term of (a) $U(3,5)\chi_{36;54}U(4,6)$ in the MBPT formalism (ladder diagram) and (b) $U_3\delta_{3,5}\chi_{3;4}U_4\delta_{4,6}$ in the TDDFT formalism (bubble diagram), where the interaction is mediated by the local exchange-correlation kernel.

Connection to KKR Green function

In the previous Sec. 5.2 the time-ordered Green function was introduced. Using the definition for the field operators the Green function from Eq. (5.1) reads

$$G_0^\sigma(1,2) = -\mathrm{i}\sum_n \phi_n^\sigma(\vec{\mathrm{r}}_1)\phi_n^{\sigma*}(\vec{\mathrm{r}}_2)\,\mathrm{e}^{-\mathrm{i}E_n(t_1-t_2)}\cdot\begin{cases}(1-f_n) & ,\ t_1-t_2>0\\ (-f_n) & ,\ t_1-t_2<0\end{cases}, \tag{5.9}$$

where f_n is the Fermi-Dirac function (see Appendix D for details). In the KKR formalism, however, the retarded Green function is used. Retarded and time-ordered Green functions are discussed in Appendix D. One can show that they are connected via

$$G_{12}^{[t]}(E) = \mathrm{Re}G_{12}^{[R]}(E) + \mathrm{i}\,\mathrm{sgn}(E-E_\mathrm{F})\,\mathrm{Im}G_{12}^{[R]}(E)\,, \tag{5.10}$$

where E_F is the Fermi energy. In addition the KKR Green function does not include the occupation number f_n, being the resolvent of the Kohn-Sham Hamiltonian which describes the reference system.

Connection to KKR susceptibility

The connection between time-ordered (MBPT) and retarded susceptibility (KKR) is given by (see Appendix D for details)

$$\chi_{36;54}^{[t]}(E) = \mathrm{Re}\chi_{36;54}^{[R]}(E) + \mathrm{i}\,\mathrm{sgn}(E)\,\mathrm{Im}\chi_{36;54}^{[R]}(E)\,. \tag{5.11}$$

As it is also shown in Appendix D the resulting expression for the retarded susceptibility is identical to the one discussed in Ch. 4.

The renormalization of the single-particle susceptibility with the interaction U is connected to the form of the exchange-correlation kernel in TDDFT which is local, $U_3\delta_{3,5}$. Therefore the ladder diagram as it appears in the RPA corresponds to a bubble diagram in the TDDFT formalism. A comparison of the susceptibility in TDDFT to the one in MBPT is given in Fig. 5.4. This form then replaces the one shown in the diagram in Fig. 5.2(b).

Connection to KKR self-energy

The self-energy in the KKR formalism is build out of retarded Green functions, therefore it is a retarded self-energy. In Appendix D it is shown that the relation between time-ordered and retarded self-energy is given by

$$\Sigma_{34}^{[t]}(E) = \mathrm{Re}\Sigma_{34}^{[R]}(E) + \mathrm{i}\,\mathrm{sgn}(E - E_\mathrm{F})\,\mathrm{Im}\Sigma_{34}^{[R]}(E)\ . \tag{5.12}$$

In the following we use this connection (a detailed derivation is given in Appendix D) to formulate the (retarded) self-energy in terms of the KKR Green functions and in terms of the projected Green functions (see Sec. 3.3). For this we also adjust the notation style such that it fits the one used in the KKR formalism (*i.e.*, the spatial dependency in given in terms of site labels i and j as well as radial vectors $\vec{r}$ and $\vec{r}\,'$). This results in

$$\Sigma_{ij}^{\sigma}(\vec{r},\vec{r}\,';E) = \mathcal{I}_{1,ij}^{\sigma}(\vec{r},\vec{r}\,';E) + \mathcal{I}_{2,ij}^{\sigma}(\vec{r},\vec{r}\,';E)\ , \tag{5.13}$$

where

$$\mathcal{I}_{1,ij}^{\sigma}(\vec{r},\vec{r}\,';E) = -\frac{U_i(\vec{r})U_j(\vec{r}\,')}{\pi}\int_0^\infty \mathrm{d}\Omega\ \mathrm{Im}\left[G_{ij}^{\overline{\sigma}}(\vec{r},\vec{r}\,';\Omega+E)\overline{\chi}_{ij}^{\sigma\overline{\sigma}}(\vec{r},\vec{r}\,';\Omega)\right] \tag{5.14}$$

and

$$\mathcal{I}_{2,ij}^{\sigma}(\vec{r},\vec{r}\,';E) = +\frac{U_i(\vec{r})U_j(\vec{r}\,')}{\pi}\int_0^{E_\mathrm{F}-E} \mathrm{d}\Omega\ \mathrm{Im}\left[G_{ij}^{\overline{\sigma}}(\vec{r},\vec{r}\,';\Omega+E)\right]\overline{\chi}_{ji}^{\sigma\overline{\sigma}}(\vec{r}\,',\vec{r};\Omega)^*\ . \tag{5.15}$$

The asterisk ($*$) in Eq. (5.15) represents complex conjugation. Furthermore,

$$\overline{\chi}_{ij}^{\sigma\overline{\sigma}}(\vec{r},\vec{r}\,';\Omega) = \sum_{LL'}\chi_{iL;jL'}^{\sigma\overline{\sigma}}(\vec{r},\vec{r}\,';\Omega) \tag{5.16}$$

defines the spherical component of the transverse susceptibility, where L and L' sum over all orbitals and $\chi^{\sigma\overline{\sigma}}$ is associated with χ^{+-} for $\sigma =\uparrow$ and with χ^{-+} for $\sigma =\downarrow$. Note that $\mathcal{I}_{1,ij}^{\sigma}(\vec{r},\vec{r}\,';E)$ is purely real (see Eq. (5.14)). Therefore, the imaginary part of the self-energy only depends on the imaginary part of $\mathcal{I}_{2,ij}^{\sigma}(\vec{r},\vec{r}\,';E)$, which represents a convolution of the density matrix $n_{ij}^{\overline{\sigma}}(\vec{r},\vec{r}\,';E) = -\frac{1}{\pi}G_{ij}^{\overline{\sigma}}(\vec{r},\vec{r}\,';E)$ of the opposite spin channel $\overline{\sigma}$ with the transverse susceptibility,

$$\mathrm{Im}\,\Sigma_{ij}^{\sigma}(\vec{r},\vec{r}\,';E) = -U_i(\vec{r})U_j(\vec{r}\,')\int_0^{E_\mathrm{F}-E} \mathrm{d}\Omega\ n_{ij}^{\overline{\sigma}}(\vec{r},\vec{r}\,';\Omega+E)\mathrm{Im}\left[\overline{\chi}_{ji}^{\sigma\overline{\sigma}}(\vec{r}\,',\vec{r};\Omega)^*\right]\ . \tag{5.17}$$

Using the projected Green function (see Sec. 3.3) and the corresponding expression for the susceptibility we arrive at

$$\Sigma_{ij}^{\sigma}(E) = -\frac{U_i U_j}{\pi}\left[\int_0^{\infty} \mathrm{d}\Omega\ \mathrm{Im}\left[G_{ij}^{\overline{\sigma}}(\Omega+E)\overline{\chi}_{ij}^{\sigma\overline{\sigma}}(\Omega)\right] - \int_0^{E_\mathrm{F}-E} \mathrm{d}\Omega\ \mathrm{Im}\left[G_{ij}^{\overline{\sigma}}(\Omega+E)\right]\overline{\chi}_{ji}^{\sigma\overline{\sigma}}(\Omega)^*\right] , \quad (5.18)$$

where the site labels i and j can be dropped in case of a single magnetic adatom.

5.4. Connection to ISTS measurements via Tersoff-Hamann model

Once the retarded self-energy as given by Eq. (5.18) is known, it allows to renormalize the projected form of the KKR Green function by use of the Dyson equation (see Eq. (5.2)). The resulting renormalized Green function then contains the interaction of the electronic structure with the spin-excitation providing access to n_vac, the density of states in the vacuum above the adatom. By use of the Tersoff-Hamann approximation [39] one can relate the resulting density of states to the inelastic excitation spectrum as measured by ISTS experiments.

The key statement of the Tersoff-Hamann approximation is that there exists a proportionality between the conductance ($\frac{\mathrm{d}I}{\mathrm{d}V}(V)$) as measured in ISTS experiments and the product of density of states (DOS) from the tip, n_tip, as well as from the probed adatom, n_vac, measured at distance $\vec{R}$ above the adatom,

$$\frac{\mathrm{d}I}{\mathrm{d}V}(V) \propto \left[n_\mathrm{tip}^{\uparrow}\cdot n_\mathrm{vac}^{\uparrow}(E_\mathrm{F}+V,\vec{R}) + n_\mathrm{tip}^{\downarrow}\cdot n_\mathrm{vac}^{\downarrow}(E_\mathrm{F}+V,\vec{R})\right] . \quad (5.19)$$

The form of Eq. (5.19) is given such that it accounts for the two spin channels, $\uparrow$ and $\downarrow$. For a nonmagnetic tip, one has $n_\mathrm{tip}^{\uparrow} = n_\mathrm{tip}^{\downarrow} = \frac{N}{2}$, with N the local density of states of the tip, which leads to

$$\frac{\mathrm{d}I}{\mathrm{d}V} \propto \left[n_\mathrm{vac}^{\uparrow} + n_\mathrm{vac}^{\downarrow}\right] . \quad (5.20)$$

One can also account for a possible magnetization of the STM tip, *i.e.*, when a different weighting of the two spin channels in the total renormalized DOS is used: For a magnetic tip one finds a nonvanishing polarization:

$$P = \frac{n_\mathrm{tip}^{\uparrow} - n_\mathrm{tip}^{\downarrow}}{N} . \quad (5.21)$$

Thus, we have

$$n_\mathrm{tip}^{\uparrow} = \frac{N}{2}(1+P) \quad \text{and} \quad n_\mathrm{tip}^{\downarrow} = \frac{N}{2}(1-P) . \quad (5.22)$$

Depending on the sign of P, one spin channel gives a larger contribution to the spectrum than the other,

$$\frac{\mathrm{d}I}{\mathrm{d}V} \propto \left[(1+P)\cdot n^{\uparrow}_{\mathrm{vac}} + (1-P)\cdot n^{\downarrow}_{\mathrm{vac}}\right] \ . \tag{5.23}$$

In order to capture the impact of the spin excitation on the electronic structure in the vacuum, $n^{\sigma}_{\mathrm{vac}}$ in Eq. (5.19) is renormalized by the self-energy and takes the form

$$n^{\sigma}_{\mathrm{vac}}(E_{\mathrm{F}}+V) = -\frac{1}{\pi}\mathrm{Im}\ \left[G^{\sigma}_{\mathrm{vac,vac}}(E_{\mathrm{F}}+V)\right] \ , \tag{5.24}$$

with

$$G^{\sigma}_{\mathrm{vac,vac}} = G^{\sigma,0}_{\mathrm{vac,vac}} + G^{\sigma,0}_{\mathrm{vac,ad}}\Delta T^{\sigma}_{\mathrm{ad}} G^{\sigma,0}_{\mathrm{ad,vac}} \tag{5.25}$$

and

$$\Delta T^{\sigma}_{\mathrm{ad}} = \left(1 - \Sigma^{\sigma}_{\mathrm{ad}} G^{\sigma,0}_{\mathrm{ad,ad}}\right)^{-1} \Sigma^{\sigma}_{\mathrm{ad}} \ . \tag{5.26}$$

This marks the connection to the previous paragraph and provides the renormalization of the electronic structure through updating the Green function via the Dyson Equation (5.2) such that it contains the interaction of the spin-excitation with the electronic structure.

5.5. Summary

This Chapter presents a novel first-principles approach to magnetic excitation spectra as measured in inelastic scanning tunneling spectroscopy (ISTS) experiments. The central quantity is the self-energy Σ that describes the interaction of magnetic excitation with the electronic structure of the regarded system. In the framework of many-body perturbation theory (MBPT) a systematic formulation of Σ becomes possible by means of a special Feynman diagram that can be used to describe four basic spin-flip processes. Once the structure of Σ is found a connection to the time-dependent density functional theory (TDDFT) is made. Via a comparison of the time-ordered Green function (used in MBPT) and the retarded Green function (used in the Korringa-Kohn-Rostoker (KKR) Green function formalism) one finds an expression for the (retarded) self-energy. This expression renormalizes the reference KKR Green function via the Dyson equation. Finally, the renormalized density of states can be related to the inelastic spectra as measured in ISTS experiments by use of the Tersoff-Hamann approximation.

This Chapter concludes the presentation of the theoretical framework of the thesis. The subsequent Chapters focus on the application of the formalism to magnetic adatoms and clusters on metallic surfaces and compare the obtained results to experimental findings if accessible.

6. Spin-excitations in transition-metal adatoms on Cu(111)

The previous Chapters have been used to present the theoretical framework of our first-principles approach to magnetic excitations in solids and to introduce to the underlying computational method. With this formalism at hand, excitation spectra of realistic nanostructures measured by inelastic scanning tunneling spectroscopy (ISTS) become accessible in a real-space approach. It allows to identify and spin-characterize experimentally observed magnetic excitation signatures and to analyze describing features, such as the position in the spectrum, linewidths, or shapes, by connecting them to system-specific features of the underlying electronic structure. On top of that, the predictive power of such a first-principles method enables to systematically study excitation spectra of structures that have not been yet analyzed experimentally.

As a first application, magnetic excitation spectra in transition-metal (TM) atoms placed as adsorbed atoms (adatoms) on the Cu(111) surface in an fcc hollow side are considered.

In Sec. 6.1, we point out characteristics of the Cu(111) surface and what has been found employing ISTS measurements. In Sec. 6.2 characteristics of the electronic structure are pointed out and connected to the form of the intrinsic magnetic excitation spectrum. This is followed by Sec. 6.3, where the newly developed approach to the excitation spectrum is presented, a method that takes into account the interaction of the magnetic excitation to the electronic structure leading to a renormalization of the density of states (DOS). A summary in Sec. 6.4 concludes the Chapter.

6.1. Adatoms on Cu(111): State of the art

One of the prime examples for studying spin-excitations in single magnetic adatoms on a metallic surface is Cu(111) [20, 87]. For the surface atoms the local density of states near the Fermi energy shows a linear behavior in the I/U characteristic near the Fermi energy [88], and therefore this system is a suitable playground for first studies of the underlying mechanisms. Through atomic manipulation these adatoms can be arranged within perfectly designed nanostructures and their magnetic properties measured via STM spectroscopy. For instance, nanostructures such as nanowires, nanorings, nano-Kagome [87] can be constructed and analyzed, even logic-devices at the nanometer scale, where the magnetic state of the adatoms and their mutual interactions are the principal working mechanism, have been realized [89].

In a simplified picture, the driving mechanisms come from two types of involved electrons. On the one hand the adatom contains localized d-electrons and on the other hand the Cu surface exhibits electrons in delocalized states, itinerant sp-electrons. In the underlying substrate the latter form a sea of electrons to which the localized electrons of the adatom couple, *i.e.*, their states hybridize. Such hybridization effects have a significant impact on the magnetization dynamics of magnetic impurity structure. In contrast to weakly hybridized systems [90], magnetic excitations on the Cu(111) surface are strongly damped and show a significant decay into excited electron-hole pairs, *i.e.*, Stoner excitations, involving the itinerant electrons from the substrate [35].

Such a decay reduces the lifetime of the magnetic excitation in the impurity and this is reflected in a broadening of the excitation resonance in the inelastic spectrum. For Fe adatoms on the Cu(111) surface, for example, a lifetime of $200\ \mathrm{fs}$ was reported [20]. The hybridization affects also the g value, which deviates from 2, the value for an isolated electron. Also asymmetries in the measured spectra have been noticed [20]. All these observations are difficult to tackle in terms of isolated spin models and more involving methods have to be applied in order to analyze and spin-characterize the experimentally observed spectra. The method presented within this thesis accounts for these hybridization effects via the electronic structure of the system in a real-space approach.

6.2. The intrinsic magnetic-excitation spectrum

In Ch. 4 the transverse dynamical magnetic susceptibility χ^{+-} was introduced as a quantity that describes the induced transverse magnetization as response of a small external transverse dynamical magnetic field within linear response. The following analysis only considers the spherical average of the susceptibility,

$$\chi^{+-}(\omega) = \sum_{m,m'=-\ell}^{+\ell} \chi^{+-}_{mm';m'm}(\omega) \quad , \ \ell = 2 \, , \tag{6.1}$$

where m and m' sum over the d orbitals, and $\chi_{mm';m'm}(\omega)$ is the onsite ($i = j = 1$) projected form of the enhanced susceptibility as given in Ch. 4. Written in this form, χ^{+-} is simply a complex number rather than a matrix expression. In this Section we analyze this object by considering four different TM impurities (Cr, Mn, Fe, Co) placed as adatoms on the Cu(111) surface. It will be demonstrated that differences in their excitation spectra can be understood by means of characteristics in the electronic structure [71].

6.2.1. Electronic structure for different TM adatoms

A detailed description of the performed calculations and the computational details can be found in Appendix B. Here, it is sufficient to briefly introduce the structure of the considered real-space impurity cluster to which the following calculations will refer to. In Fig. 6.1 the Cu(111) surface and the adatom with the surrounding impurity cluster are visualized. If not stated differently the impurity cluster contains the adatom, the twelve nearest fcc scattering sites (including vacuum scattering sites), and an additional vacuum scattering site 6.3 Å above the adatom. The latter is necessary to investigate the impact of the calculated spin-excitations onto the vacuum site that may be probed by an STM tip in experiment. Test calculations have revealed that a larger real-space cluster with twice the diameter does not lead to significantly different results. A relaxation of 14 % of the impurity towards the surface is considered [91, 92].

Density of states and magnetic moments

In Fig. 6.2 the adatom-projected spin-resolved total density of states for Cr, Mn, Fe, and Co adatoms on the Cu(111) surface are shown. In all four cases the orbitals of the majority-spin states (↑) are almost fully occupied, *i.e.*, their resonance is below the Fermi energy E_{F} (indicated by a dotted black line). The resonances for the orbitals of the minority-spin states, on the other hand, show a trend of being shifted downwards in energy due to increased filling of the d-states when the series of $3d$ adatoms in the periodic table is followed: For Cr and Mn the resonance is above E_{F}, such that the minority-spin orbitals are nearly unoccupied, whereas for Fe and Co the resonance appears at E_{F}, *i.e.*,

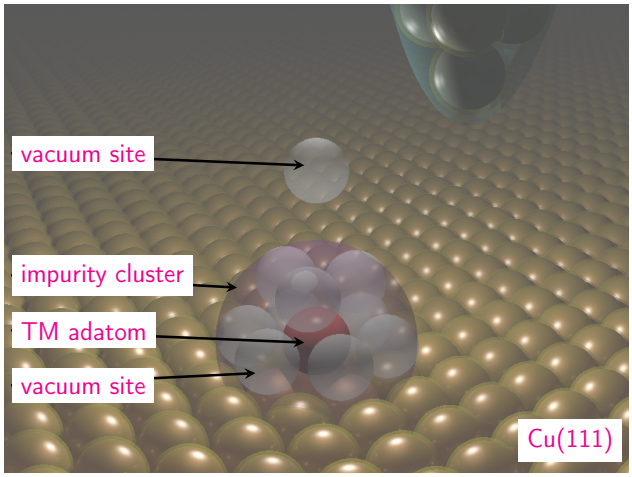

Figure 6.1.: An artist's view of the Cu(111) surface and the impurity cluster. The impurity atom (red sphere) is surrounded by three Cu atoms (underneath), six nearest-neighbor vacuum sites in the same layer and three more in the layer above (semitransparent white spheres). To account for the vacuum site that is probed by an STM tip (object in the upper right part of the figure, not accounted for in this thesis) an additional vacuum site three layers above the impurity is part of the cluster as well, corresponding to a center-to-center distance of about 6.3 Å with respect to the impurity atom.

the minority spin d orbitals are half-filled. This implies that the magnetic moments of the Cr adatom and the Mn adatom are larger than the ones of Fe and Co.

In Table 6.1 ground-state properties for Cr, Mn, Fe, and Co adatoms on the Cu(111) surface are shown. For all four systems, the number of d-electrons is non-integer. This is due to the hybridization of these d-electrons with the electrons from the metallic surface, which is reflected in Fig. 6.2, where the majority-spin states are partially filled and show a tail that reaches above the Fermi energy. In addition the hybridization leads to a loss of the pure d-states character of these states. As already mentioned in the previous paragraph, the magnetic moments of Cr and Mn are larger than those of Fe and Co due to the increased minority d-band filling (see Fig. 6.2).

Note that albeit the values for the magnetic moments when using the projected scheme (m_d) are a bit smaller than the ones calculated using the original KKR Green functions (m^{total}), the main contribution is captured. Already the projection on the d orbitals alone provides the major part of the magnetic moment. Therefore, the presented calculations utilize the projected Green function onto the d orbitals only. This could be verified by test calculations in which also the projection onto s and p states were included and no significant changes in the obtained data was observable.

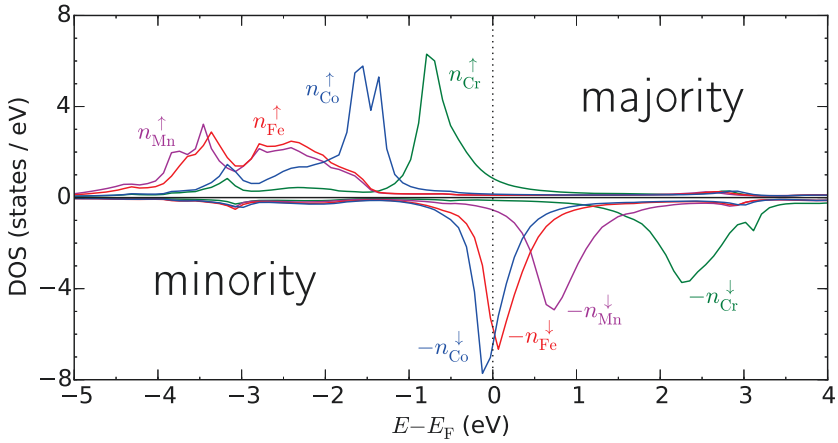

Figure 6.2.: The spin-resolved total density of states (DOS) are shown for the four adatoms (Cr, Mn, Fe, and Co) placed on the Cu(111) surface. For the majority spin channel (↑) the orbitals are almost filled, whereas for the minority spin channel (↓) the resonance is above (Cr and Mn) or at (Fe and Co) the Fermi energy (dotted black line). Thus, the local density of states at the Fermi energy can differ a lot from adatom to adatom and lead to different properties for the magnetic excitations, as explained in the text.

adatom	N_d	$n_d^{\uparrow}(E_{\mathrm{F}})$ $(\frac{\text{states}}{\text{eV}})$	$n_d^{\downarrow}(E_{\mathrm{F}})$ $(\frac{\text{states}}{\text{eV}})$	m_d (μ_{B})	m^{total} (μ_{B})
Cr	4.30	0.740	0.0629	3.86	3.98
Mn	4.84	0.0402	0.436	3.88	4.29
Fe	5.90	0.0377	6.88	2.86	3.25
Co	7.22	0.0744	6.71	1.78	1.98

Table 6.1.: Ground-state properties for the four adatoms: N_d is the number of d-electrons, $n_d^{\downarrow}(E_{\mathrm{F}})$ and $n_d^{\uparrow}(E_{\mathrm{F}})$ describe the local density of states at the Fermi energy E_{F} for both spin-channels, and m_d is the magnetic moment when only the d-orbitals are considered. All these quantities are calculated using the projected Green function, see Sec. 3.3, and considering the adatom's contribution only. A comparison to m^{total}, the magnetic moment without projection and by taking into account all orbitals, shows that the main part of the moment is captured by m_d.

6.2.2. The transverse dynamical magnetic susceptibility

In the previous section, the electronic structure of different TM adatoms on Cu(111) has been analyzed and compared. Before the resulting magnetic excitation spectra are presented, we discuss in which way the electronic structure affects characteristics of the excitation spectra, such as the g shift and damping (which is connected to the lifetime of the excitation).

The origin of the damping and the possibility of a g shift can be directly related to the local density of states at the Fermi energy (see Sec. 4.4.2 and Ref. [71]). For the imaginary part of the enhanced susceptibility χ (only possible for the spherical form, see Eq. (6.1)) one can identify

$$\mathrm{Im}\chi^{+-}(\omega) = \frac{\mathrm{Im}\chi^{+-}_{\mathrm{KS}}(\omega)}{\left[1 - U\mathrm{Re}\chi^{+-}_{\mathrm{KS}}(\omega)\right]^2 + \left[U\mathrm{Im}\chi^{+-}_{\mathrm{KS}}(\omega)\right]^2} , \tag{6.2}$$

where U is the exchange-correlation kernel and χ_{KS} is the Kohn-Sham susceptibility. Note, that in Eq. (6.2) the imaginary part of χ_{KS} plays the role of damping. A linearization of $\mathrm{Im}\chi_{\mathrm{KS}}(\omega)$ up to the first order in its argument ω (see Eq. (4.55)), leads to [71]

$$\mathrm{Im}\chi^{+-}_{\mathrm{KS}}(\omega) \approx -\pi \sum_{m,m'=-2}^{+2} n^{\uparrow}_{mm'}(E_{\mathrm{F}})\, n^{\downarrow}_{mm'}(E_{\mathrm{F}})\, \omega , \tag{6.3}$$

where $n^{\sigma}_{mm'}(E) = -\frac{1}{\pi}\mathrm{Im}G^{\sigma}_{mm'}(E)$ for $\sigma \in \{\uparrow,\downarrow\}$ are the spin-resolved density-matrix elements. This shows the important connection of damping to the electronic structure. If no states close to the Fermi energy are available, the coupling to the surrounding electron bath plays only a minor role and the lifetime of the excitation can be large. In contrast to this, a short lifetime corresponds to strong damping, *i.e.*, when the density of states around the Fermi energy is nonzero and the decay into Stoner excitation in the substrate becomes possible. The intersection of the real part of the susceptibility with the z-axis is given by (see Appendix F)

$$\mathrm{Re}\chi^{+-}_{\mathrm{KS}}(0) = -\frac{m}{2\left(B^{\mathrm{xc}} + B^{\mathrm{ext}}\right)} \approx \frac{1}{U} + \frac{2B^{\mathrm{ext}}}{U^2 m_d} \tag{6.4}$$

where in the last step an expansion up to first order in ω and $\frac{1}{U} = -\frac{m}{2B^{\mathrm{xc}}}$ was used. Within this formalism one can define an effective g value (see Appendix F)

$$g_{\mathrm{eff}} = \frac{1}{\mu_{\mathrm{B}} B^{\mathrm{ext}}} \frac{\left|\frac{1}{U} - \mathrm{Re}\chi^{+-}_{\mathrm{KS}}(0)\right|}{\left|\frac{\partial}{\partial\omega}\chi^{+-}_{\mathrm{KS}}(\omega)\big|_{\omega=0}\right|} \approx 2\frac{\left|\frac{1}{\mu_{\mathrm{B}} U^2 m_d}\right|}{\left|\frac{\partial}{\partial\omega}\chi^{+-}_{\mathrm{KS}}(\omega)\big|_{\omega=0}\right|} , \tag{6.5}$$

where in the last step Eq. (6.4) was inserted. The form of Eq. (6.5) implies that the electronic structure leads to a renormalization of the g value.

When a rotation of the magnetization can be achieved without energetical costs, an infinitesimal perturbation leads to a gigantic response in the induced magnetization. Then,

$\mathrm{Im}\chi^{+-}$, describing the excitation spectrum, shows an infinite response at $\omega = 0$. This is the Goldstone mode. In Sec. 4.4.1 it was demonstrated that the present method computes an exchange-correlation kernel that is consistent with the Goldstone mode, *e.g.*, the condition for the appearance of a resonance at $\omega = 0$ for no applied magnetic field is fulfilled by construction.

In the presence of spin-orbit coupling (SOC), however, breaking of spin-rotation symmetry occurs and an in-plane or out-of-plane orientation of the atom's spin normally is preferred energetically. As a consequence the resonance position shifts to a finite value in the frequency spectrum, which reflects the costs in energy for a rotation of the spin moment away from its easy direction. The same behavior would appear in the presence of an external magnetic field applied along the z-direction, *i.e.*, perpendicular to the surface plane. The method discussed within this thesis does not include SOC.[1] If the SOC-induced gap in the spectrum is known, however, one can mimic this effect by applying an auxiliary external magnetic field. For the Fe adatom on the Cu(111) surface the SOC-induced gap is known [20] and results in an auxiliary magnetic field of $\mu_\mathrm{B} B_0 = 0.55\ \mathrm{meV}$. Thus, a gap in the excitation spectra at the Larmor resonance frequency, $\omega_\mathrm{res} = \mu_\mathrm{B} g B_0$ ($g \sim 2$ is the Landé factor) is induced, which therefore matches the experimental data for the Fe adatom [20] by construction. For the sake of comparison, the same auxiliary field is used for all adatoms.

In Fig. 6.3 the magnetic excitation spectra for the four different TM adatoms (Cr, Mn, Fe, Co) on the Cu(111) surface are shown. The imaginary and real part of the spherical component of the Kohn-Sham susceptibility are given in Fig. 6.3(a) and Fig. 6.3(b), while the spherical component of the imaginary part for the enhanced susceptibility is presented in Fig. 6.3(c). The curves describing the imaginary part of the Kohn-Sham susceptibility in Fig. 6.3(a) show a fair linear behavior and the steepness of the (negative) slope increases

[1] It should be noted, however, that the formalism can be extended to include SOC directly [70].

adatom	U (eV)	g_eff	ω_res (meV)	Γ (meV)	τ_χ (fs)
Cr	-0.904	1.89	1.05	0.163	2020
Mn	-0.987	2.17	1.20	0.109	3020
Fe	-0.990	1.95	1.07	0.558	590
Co	-0.979	2.15	1.18	1.37	239

Table 6.2.: This table shows characteristic properties of the susceptibility for the four adatoms: The exchange-correlation kernel U as well as the effective g value $g_\mathrm{eff} = \omega_\mathrm{res}/B_0$ is shown. For an applied field of $B_0 = 0.55\ \mathrm{meV}$ the resulting resonance position ω_res, the full-width at half-maximum Γ, and the lifetime τ_χ of the excitation is shown (see Eq. (6.6)).

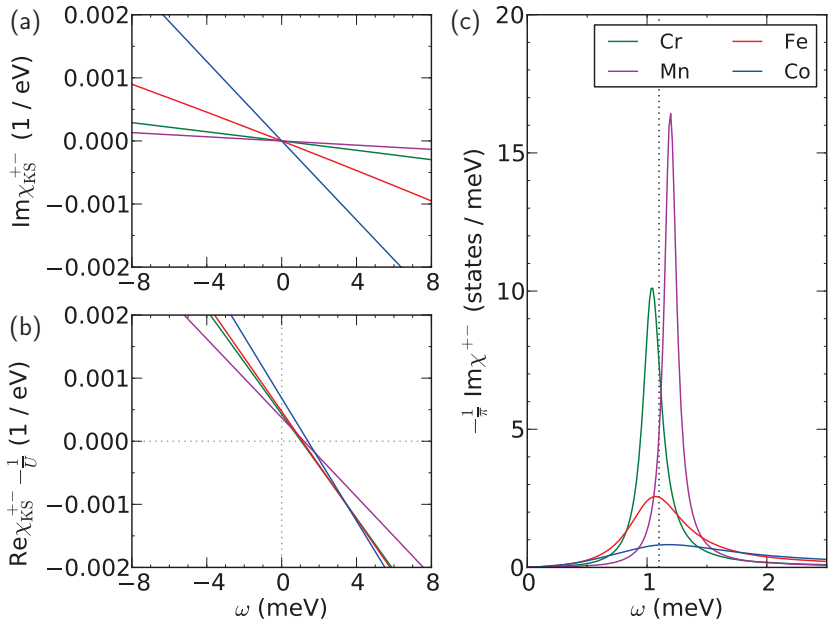

Figure 6.3.: For different TM adatoms on the Cu(111) surface the spherical part of the Kohn-Sham susceptibility and the enhanced susceptibility are shown, see Eq. (6.1). The applied magnetic field is the same for all systems to allow for a better comparison. The lower panel shows a dotted vertical line the resonance position for a g-factor of exactly 2.

from Mn and Cr to Fe and reaches it highest (absolute) value for Co. The trend can already be obtained using Eq. (6.3) with spin-resolved local densities at the Fermi energy ($n_d^{\uparrow}(E_\mathrm{F})$ and $n_d^{\downarrow}(E_\mathrm{F})$) as given in Table 6.1. More accurate, however, is the use of the density matrix with elements $n_{mm}^{\sigma}(E_\mathrm{F}), \sigma \in \{\uparrow,\downarrow\}$, see also the slope of the imaginary part in Table I of Ref. [71]. For Cr one obtains the slope of $-0.038\ \mathrm{eV}^{-2}$ when using Eq. (6.3) which is in nice agreement with the actual slope of the shown curve in Fig. 6.3(a), $-0.037\ \mathrm{eV}^{-2}$. The same is true for Mn (Eq. (6.3): $-0.014\ \mathrm{eV}^{-2}$, slope in Fig. 6.3(a): $-0.017\ \mathrm{eV}^{-2}$), Fe (Eq. (6.3): $-0.132\ \mathrm{eV}^{-2}$, slope in Fig. 6.3(a): $-0.120\ \mathrm{eV}^{-2}$) and Co (Eq. (6.3): $-0.333\ \mathrm{eV}^{-2}$, slope in Fig. 6.3(a): $-0.314\ \mathrm{eV}^{-2}$).

For the corresponding real parts (see Fig. 6.3(b)) we compare the expected values for the Kohn-Sham susceptibility at zero frequency minus the exchange-correlation kernel to the values obtained using Eq. (6.4). For Cr, we read the offset of $3.49 \cdot 10^{-4}\ \mathrm{eV}^{-1}$ from Fig. 6.3(b) which is in good agreement to $4.31 \cdot 10^{-4}\ \mathrm{eV}^{-1}$ which is the value obtained using Eq. (6.4). For Mn the respective pair reads $2.91 \cdot 10^{-4}\ \mathrm{eV}^{-1}$ and $3.74 \cdot 10^{-4}\ \mathrm{eV}^{-1}$, for Fe we have $3.92 \cdot 10^{-4}\ \mathrm{eV}^{-1}$ and $4.73 \cdot 10^{-4}\ \mathrm{eV}^{-1}$, and for Co we have $6.45 \cdot 10^{-4}\ \mathrm{eV}^{-1}$

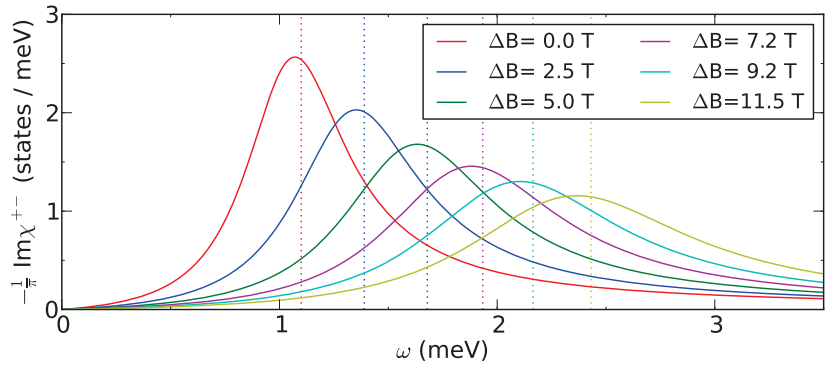

Figure 6.4.: Fe adatoms on Cu(111): The enhanced susceptibility as function of external magnetic field, where ΔB is the difference to the auxiliary B-field $\mu_\mathrm{B}\, B_0 = 0.55\ \mathrm{meV}$. The dotted vertical lines mark the resonance position for the case that the g-factor of exactly 2.

and $6.83 \cdot 10^{-4}\ \mathrm{eV}^{-1}$. Also here the comparison provides a good agreement in all four cases.

The knowledge gain from the analysis of real and imaginary part of the Kohn-Sham susceptibility can be used to understand the obtained intrinsic excitation spectra, described by the imaginary of the enhanced susceptibility χ^{+-}, see Fig. 6.3(c). Whereas the spectra of Cr and Mn adatoms show a relatively sharp resonance, the corresponding resonance for Fe and Co adatoms is broader. This allows for the interpretation that the excited state shows a short lifetime when states are available around the Fermi energy, allowing for the excitation to couple to Stoner excitations in the surface. In Table 6.2 some characterizing properties of the spin-excitation spectrum are shown. As explained in Ch. 4 the exchange-correlation kernel U reduces to a single number, see Eq. (4.52). The effective g value g_eff, the resonance position ω_res, the full-width at half-maximum (FWHM) Γ, and the lifetime

$$\tau_\chi = \frac{\hbar}{2\Gamma} \tag{6.6}$$

are extracted from the curves shown in Fig. 6.3(c). The values for g shift and lifetime are in reasonable agreement to experimentally observed values in Ref. [20], where $g = 2.1$ and $\tau = 200\ \mathrm{fs}$ was found.

Variation of the external magnetic field

Due to the magnetic nature of the excitation, the corresponding spectra are sensitive towards variation of the external applied magnetic field. For different applied magnetic

fields $\mu_{\mathrm{B}}\, B_z^{\mathrm{ext}} = \mu_{\mathrm{B}}\, B_0 + \Delta B$ Fig. 6.4 shows the response function for the Fe impurity. As before, the auxiliary B-field for this system is chosen to be $\mu_{\mathrm{B}} B_0 = 0.55\ \mathrm{meV}$.

The enhanced susceptibility is dominated by a resonance around twice the value of the applied magnetic field, corresponding to the Larmor frequency. The deviation of the actual value can be drawn back to the effect of the broadening of the resonance. Without damping the resonance position would be exactly coincide with the dashed lines in Fig. 6.4. By plotting the resonance position against the applied magnetic field one can extract from a linear fit the slope which reveals the g value as performed in the previous Section.

As will become important at a later stage of the thesis, one can compare the obtained results to the susceptibility that comes from the Landau-Lifshitz-Gilbert (LLG) model [93, 94],

$$\frac{\mathrm{d}\vec{m}}{\mathrm{d}t} = -\gamma\vec{m} \times \vec{B}^{\mathrm{eff}} + \eta\frac{\vec{m}}{m} \times \frac{\mathrm{d}\vec{m}}{\mathrm{d}t}\ , \tag{6.7}$$

with the effective magnetic field $\vec{B}^{\mathrm{eff}} = -\frac{\partial E}{\partial \vec{m}}$ acting on the magnetic moment, $E(\vec{m}) = -\vec{B}^{\mathrm{ext}}(t) \cdot \vec{m}$, the gyromagnetic ratio γ, and a phenomenological damping factor η. A detailed analysis of the LLG model is given in Appendix G. Within the LLG model for a single magnetic moment the response function is of the form

$$\mathrm{Im}\,\chi^{\mathrm{LLG}}(\omega) = \frac{\gamma m_z}{1+\eta^2}\frac{\eta\omega}{\left(\omega-\omega_0\right)^2 + \left(\eta\omega_0\right)^2}\ , \tag{6.8}$$

where $\omega_0 = \gamma B^{\mathrm{eff}}/\left(1+\eta^2\right)$. Note that $\eta\omega_0$ enters the denominator of χ^{LLG} as a constant and is responsible for the resonance linewidth (*i.e.*, the damping) and thus that the resonance width increases linearly with the strength of the effective magnetic field. Since one can identify $B^{\mathrm{eff}} = B_0 + B^{\mathrm{ext}}$ this means that the damping in Fig. 6.4 increases linearly with applied external magnetic field. Furthermore the resonance position is expected at $\omega_{\mathrm{res}} = \sqrt{1+\eta^2}\omega_0 = \frac{\gamma B^{\mathrm{eff}}}{\sqrt{1+\eta^2}}$ (see Appendix G) so that the resonance energy should increase linearly with external applied magnetic field. This effect can be observed in Fig. 6.4 as well. This means that in conclusion one can use the LLG model in the context of spin excitations of our interest, using parameters obtained from DFT or TDDFT. Note that for more complex systems (beyond single atom impurities) the LLG model turns out to be a useful tool to interpret the obtained excitation spectra, see Ch. 8.

6.2.3. Interim resume

The focus of this section was the susceptibility that describes the spectrum of magnetic excitation in the impurity. It was demonstrated that a comparison to excitation spectra obtained via ISTS measurements leads to a reasonable agreement on features such as g shift and damping [20]. It should be pointed out, however, that the STM spectra contain more information than that captured by the intrinsic magnetic excitation spectra. Experimentally one measures the signature of the spin excitation in the electronic structure decaying into vacuum, rather than the intrinsic spin excitation in the adatom. Therefore,

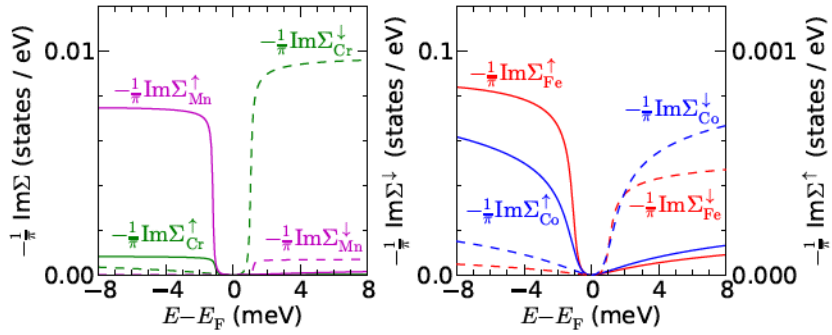

Figure 6.5.: For the four investigated systems, the imaginary part of the self-energy is shown, where the curves represent sums over the diagonals in the d orbitals. Whereas for Cr and Mn adatoms the self-energy step heights for the two spin channels are of the same order; they differ by a factor of 100 for Fe and Co adatoms.

the following section goes beyond state of the art, presenting a novel approach on studying magnetic excitation spectra from first principles which provides a deeper understanding of the nature of spin excitations.

6.3. Access to the magnetic-excitation spectrum via the renormalized density of states

Our strategy is to evaluate the interactions among the electrons and the spin-excitation in terms of the self-energy as discussed in Ch. 5. Then, we have direct access to the renormalization of the electronic structure at the adatom or at the surface or even more important for our STM discussion in the vacuum. This is important because this allows the comparison of the DOS in the vacuum to the $\frac{\mathrm{d}I}{\mathrm{d}V}$-curves measured experimentally using the Tersoff-Hamann approximation [39], as discussed in Sec. 5.4.

6.3.1. The electron self-energy

In Fig. 6.5 the imaginary part of the self-energy for the four investigated systems is shown, where

$$\Sigma^{\sigma}(E) = \sum_{m=-\ell}^{+\ell} \Sigma^{\sigma}_{mm}(E)\,, \tag{6.9}$$

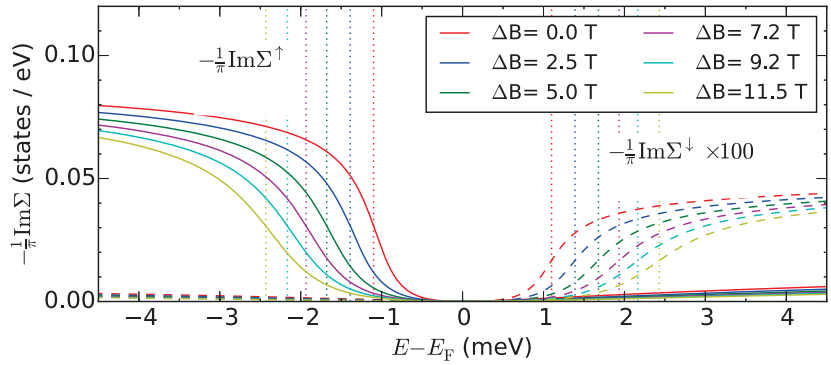

Figure 6.6.: Fe adatoms on Cu(111): The self-energy for different applied magnetic fields is shown. Also here, we observe that the width of the step indicates an increased damping, indicating that the lifetime decreases.

with $\ell = 2$ and $\sigma \in \{\uparrow, \downarrow\}$. As described in Ch. 5, the form of the imaginary part of the self-energy reads

$$\mathrm{Im}\,[\Sigma^{\sigma}_{mm'}(E)] = -U^2 \int_0^{E_\mathrm{F}-E} \mathrm{d}\Omega\; n^{\overline{\sigma}}_{mm'}(E+\Omega)\mathrm{Im}\left[\chi^{\sigma\overline{\sigma}}(\Omega)^*\right] \;, \tag{6.10}$$

where $n^{\sigma}(E) = -1/\pi \cdot \mathrm{Im}\,[G^{\sigma}_0(E)]$ is the local DOS obtained for the initial Green function, $\chi^{\sigma\overline{\sigma}}$ is the spherical part of the susceptibility, see Eq. (6.1).

The origin of the spin asymmetry observed in the step height of $\mathrm{Im}\Sigma$, visible in Fig. 6.5, is the different local density of states near the Fermi energy, see Fig. 6.2. Contrary to Mn, Fe, and Co adatoms, Cr adatom is the only case where $n^{\uparrow}(E_\mathrm{F}) > n^{\downarrow}(E_\mathrm{F})$ leading to $\mathrm{Im}\Sigma^{\uparrow}(E_\mathrm{F}) < \mathrm{Im}\Sigma^{\downarrow}(E_\mathrm{F})$. Since the spin asymmetry is large for the DOS of Fe and Co adatoms, the spin-dependent step heights of $\mathrm{Im}\Sigma$ differ by two orders of magnitude.

Naturally, one expects a steplike function as soon as the integration goes over a bias voltage V equal to ω_res. The resulting spin-resolved imaginary parts of the self-energy for the Fe adatom on Cu(111) for different applied external magnetic fields (see Fig. 6.4) is shown in Fig. 6.6, where the traces of $\Sigma^{\uparrow}$ and $\Sigma^{\downarrow}$ are indicated by solid and dashed lines, respectively. Because of the relation between the step positions and ω_res, the gap between them increases with ΔB. Whereas the resonances in $\chi^{\sigma\overline{\sigma}}$ are equal in height with respect to the two spin channels, the step height in the self-energy differs by a factor of about 100. This can be understood as the resonance being weighted by the DOS of the opposite spin channel, *cf.* Eq. (6.10): if there is only a small number of $\overline{\sigma}$-states available, the scattering is unlikely to happen. In contrast to the extremely small $n^{\uparrow}_\mathrm{Fe}$, the $n^{\downarrow}_\mathrm{Fe}$ displays a large resonance. Since the step widths are related to the line widths extracted from the susceptibility peaks, they increase when the excitation energy ω_res increases.

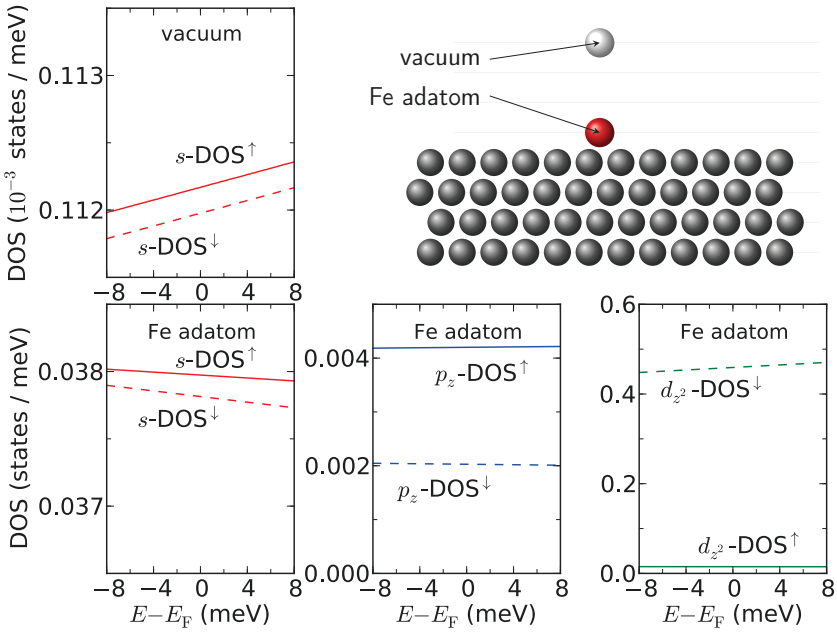

Figure 6.7.: An orbital-resolved analysis of the DOS for Fe adatoms on the Cu(111) surface are shown (s, p_z, and d_{z^2} orbitals) and compared to the DOS of the vacuum site 6.3 Å above the impurity (just considering the s channel of the Green function at the vacuum site). The solid and dashed lines refer to spin up and spin down DOS, respectively. Only for the s and the p_z orbitals of the adatom the DOS for majority spin is larger than the one for the minority spin, which matches the weighting obtained for the vacuum site.

6.3.2. Density of states: A spin- and orbital-resolved analysis

At this point we take a closer look at the spin-resolved behavior of the DOS for the Fe adatom as well as the vacuum position three layers above. In Fig. 6.7 the orbital-resolved DOS without including the spin-excitation is shown (connected the elastic spectrum). Only states extending farthest into vacuum above the adatom are displayed (s, p_z, and d_{z^2}). Contrary to the d_{z^2}-resolved DOS, for the s and p_z states the majority-spin contribution is larger than the minority-spin contribution. This spin asymmetry in the magnitude of the DOS seem to be maintained in vacuum. Whereas the d_{z^2} state is dominant at the adatom it decays fast into vacuum due to its more localized character than the p_z and the s states. This is even more remarkable since the latter orbitals do only show a difference in the spin-resolved terms by a factor of 2 and are by more than two orders of magnitude smaller than those of the d_{z^2} orbitals at the adatom. Such an observation does not

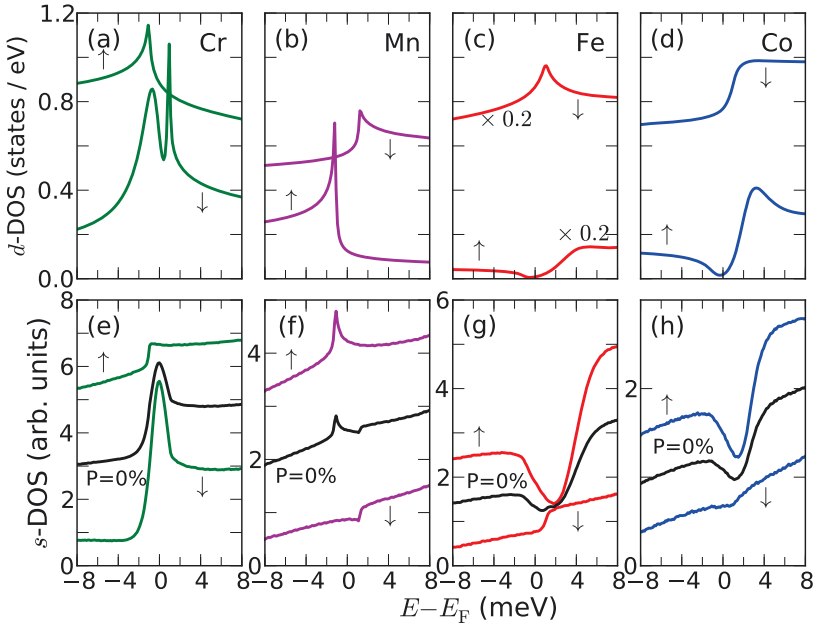

Figure 6.8.: This figure shows the density of states for the investigated $3d$ TM adatoms, renormalized by spin excitations, where the d orbitals of the impurity atom (top row) and s orbitals in the vacuum, 6.3 Å above the adatoms (bottom row) are considered. In each plot two curves are shown, one per spin channel. For the renormalized vacuum DOS (bottom row) the spin-averaged DOS for a non-polarized tip ($P = 0\%$, *i.e.*, $\frac{\uparrow+\downarrow}{2}$) is indicated by black curves.

necessarily remain true for all systems but indicates that the position of the STM tip plays an important role when investigating the spin asymmetry of the elastic and inelastic spectra.

6.3.3. The renormalized spectrum for different TM adatoms

The excitation spectra of Cr, Mn, Fe, and Co adatoms are given in Fig. 6.8. The top row (*cf.* Figs. 6.8(a)-6.8(d)) shows the DOS for the spin-resolved d orbitals of the adatoms and the bottom row (*cf.* Figs. 6.8(e)-6.8(h)) shows the spin-resolved and the spin-averaged (dashed lines) vacuum s orbitals above the impurity. For the Cr adatom, peaklike structures are observed in the d-DOS, which transform in vacuum into a reversed step for the majority-spin channel, while in the minority-spin channel the spin excitation and an additional bound state, a satellite, overlap at E_F. The renormalized spectra for Fe and Co adatoms show similar shapes for both, the DOS at the atom and in the vacuum. For the majority-spin

their spectra include an additional bound state, a satellite. For the minority-spin channel of the Co adatom, the spin-excitation feature almost vanishes in vacuum. In contrast to Fe and Co, the renormalized DOS for the Mn adatom does not show additional states (satellites). However, the excitation signatures are steplike functions with a peaklike resonance at the edges. This analysis of excitation spectra has an important outcome that needs to be emphasized: The general belief that a spin-excitation shows up as step in the inelastic spectrum does not hold. Instead, by including the electronic structure our method predicts a higher variety of excitation signatures (steps, reversed steps, peaks) up to the extinction of the signature.

We note that Co adatoms on Cu(111) is a traditional Kondo system and that processes leading to Kondo behavior are not accessible through the scheme that is utilized in this thesis. However, spin excitations and Kondo can coexist, see for example Ref. [95]. In contrast to Co, Fe shows no Kondo signature down to 0.3 K [20]. This is strengthened by the measurements of magnetic exchange interactions among Fe adatoms [87]. Also, Cr and Mn adatoms placed on Cu(111) are expected to behave as on Au(111) [96], where no Kondo behavior was observed.

The lifetime of the spin-excitation, τ_χ, is given by the line width of $\mathrm{Im}\chi$, which is different from the lifetime extracted from the inelastic spectra, τ_{DOS}. Both lifetimes are calculated from $\tau = \hbar/(2\Gamma)$, where Γ is the full-width half-maximum of the signature of the spin excitations. Because of the convolution with the reference Green function, more information is encoded in τ_{DOS}, which is the only quantity reachable experimentally. Contrary to τ_χ, τ_{DOS} is spin-dependent and the difference between the spin channels can reach a factor 5. Indeed, $\tau_\chi = \{2.0, 3.0, 0.6, 0.2\}$ ps for, respectively, {Cr, Mn, Fe, and Co} (see Table 6.2), while the sequence changes to $\{1.1, 0.5, 0.1, 0.3\}$ ps for $\tau^{\uparrow}_{\mathrm{DOS}}$ and $\{0.4, 0.8, 0.5, 0.1\}$ ps for $\tau^{\downarrow}_{\mathrm{DOS}}$. In the literature asymmetries have been observed in inelastic spectra [12, 20]. By use of the method presented in this thesis such asymmetries are accessible from first-principles and can be related to the interaction of the spin excitation with the electronic structure. Furthermore, for some systems an additional satellite contribute to the effective lifetime of the excitation signature (Cr is the extreme case). The lifetimes of Co and Fe adatoms are up to one order of magnitude smaller than those of Mn and Cr adatoms when the resonance of the susceptibility is used. This is due to the relatively small minority-DOS at E_{F} for the latter two systems: the excited electron cannot easily find an unoccupied state to deexcite to leading to an increased excitation lifetime.

6.3.4. Fe/Cu(111): Comparison to experimental spectrum

In this Section we take a closer look to the resulting renormalized spectra for the d orbitals of the Fe adatom and for the s orbitals of the vacuum site, shown in Figs. 6.9(a) and 6.9(b), respectively. Whereas the self-energy shows a height difference between the two spin channels of about two orders of magnitude, the resulting DOS magnitudes do not differ much anymore. Although in the adatom, the d-DOS for the minority-spin channel is larger than the one for the majority-spin channel (because of the large minority-spin

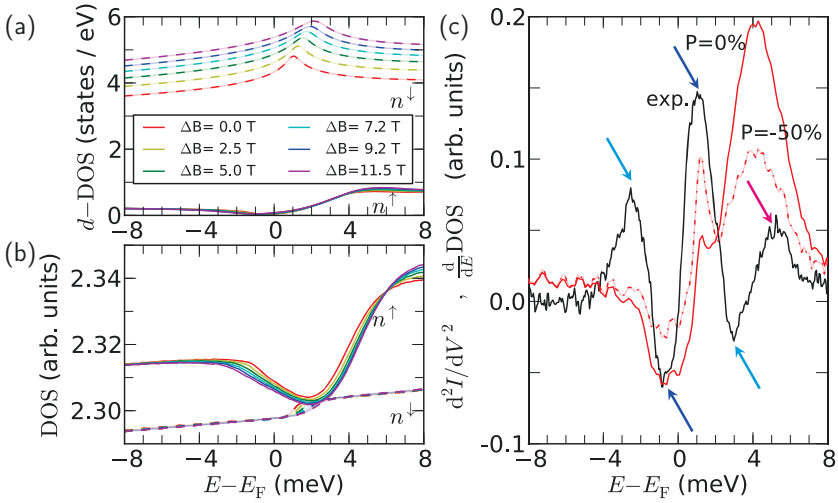

Figure 6.9.: Fe adatoms on Cu(111): The renormalized spectrum is shown for (a) the d-DOS of the adatom and (b) the s-DOS in vacuum above the impurity. All quantities are plotted for spin-up (solid lines, $\uparrow$) and spin-down (dashed lines, $\downarrow$). (c) A comparison to the derivative of the conductance spectra obtained in experiment [20]. The agreement improves when instead of a nonpolarized tip (solid red curve) a polarization of $P = -50\ \%$ is assumed (dashed red curve).

resonance), the opposite is found in vacuum for the s-DOS. Hybridization, interferences effects, and decays of orbitals shape the final form of the vacuum DOS. For example, the peaklike feature in the minority-spin channel of the d orbital at the Fe adatom (see dashed lines) can evolve into a steplike feature for the s states at the vacuum site, which in the presented calculations is about 6.3 Å above the adatom.

In Fig. 6.9(c), we show a comparison of the experimental $\mathrm{d}^2I/\mathrm{d}V^2$ data for an Fe adatom from Ref. [20] with the energy derivative of the calculated renormalized s-DOS in vacuum, *cf.* Fig. 6.9(b). The experimental spectrum is not perfectly symmetric with respect to the origin. The most dominant peak is observed at $+1\ \mathrm{meV}$, which is accompanied by a dip at $-1\ \mathrm{meV}$ (see blue arrows in Fig. 6.9(c)). The origin of these features can be attributed to the spin-excitation, as they match the resonance position of the imaginary part of the transverse magnetic susceptibility, discussed in Sec. 6.2.2. However, the experimental spectrum is much richer since, for example, another peak and dip pair is found in the region of about $\pm 3\ \mathrm{meV}$ (see cyan arrows in Fig. 6.9(c)). The origin for this could be that in the conductance spectrum the excitation signature is not a perfect step. Instead, a more complicated shape (possibly a combination of a peak and a step signature) causes such shapes. But most importantly, there is an additional peak in the experimental spectrum at $+5\ \mathrm{meV}$ that has no matching dip at $-5\ \mathrm{meV}$ (see magenta arrow in Fig. 6.9(c)).

This clearly leads to an asymmetry in the observed spectrum that cannot be understood from the symmetric excitation spectrum, provided by the susceptibility, alone. This extra feature, however, is in good agreement with our simulations (*e.g.*, by identifying it with the satellite at $+4\ \mathrm{meV}$ in the shown excitation spectra, see the red curves in Fig. 6.9(c)). The origin of this extra feature can be traced back to $\mathrm{Re}\Sigma$. In the expression for G, the denominator $(1 - G_0\Sigma)$ causes a resonance when $\mathrm{Im}(G_0\Sigma) \ll 1$ and $\mathrm{Re}(G_0\Sigma)$ is close to 1. This condition seems to be satisfied in the majority-spin channel around E_F. The self-energy thus is acting as an additional potential on the electrons, which can lead to satellites very similar to split-off states observed when adatoms interact with surface states [24, 97].

Finally, Fig. 6.9(c) shows an improved agreement between theory and experiment, when a polarization of the STM tip is taken into account, see Eq. (5.23). By comparing the curves for $P = 0\ \%$ and $P = -50\ \%$, one observes that the overall shape of the spectrum can be modified by changing the weight of the spin-resolved spin-excitation signature [*cf.* solid versus dashed red line in Fig. 6.9(c)]. This can improve the agreement with the experiment and indicates that the shape of the inelastic spectra is not only a function of the adsorbate but also of the polarization of the tip.

6.3.5. Fe/Cu(111): Spectrum for a larger energy window

Up to this point, the excitation spectrum was analyzed for the energy window of a few meV above and below the Fermi energy. In this section, however, the Fe adatom on the Cu(111) surface is considered for a larger energy window of several eV.

The renormalization of the electronic structure for the d orbitals in the adatom is shown in the top panel of Fig. 6.10. Around the Fermi energy the resonance in the minority spin channel gets slightly damped and shifts by around $0.2\ \mathrm{eV}$ up in energy. Also the majority spin channel shows a strong impact on the renormalized electronic structure.

In the lower panel of Fig. 6.10 the renormalized DOS in the vacuum above the adatom is shown for the same energy window. In order to notice the small corrections we show here the difference to the DOS without the impact of the self-energy. Clearly, one sees that most of the change takes place nearby the Fermi energy. At the Fermi energy the curve shows a sharp signature that is a combination of the spin-excitation steps and the satellite that has been discussed in Sec. 6.3.3.

6.3.6. Fe/Cu(111): The excitation spectrum as function of distance

Due to the fact that the present analysis is based on a real-space method, it is possible to investigate the renormalized DOS at different vacuum sites nearby the adatom. Thus, one is able to simulate ISTS spectra measured at different positions above or next to the

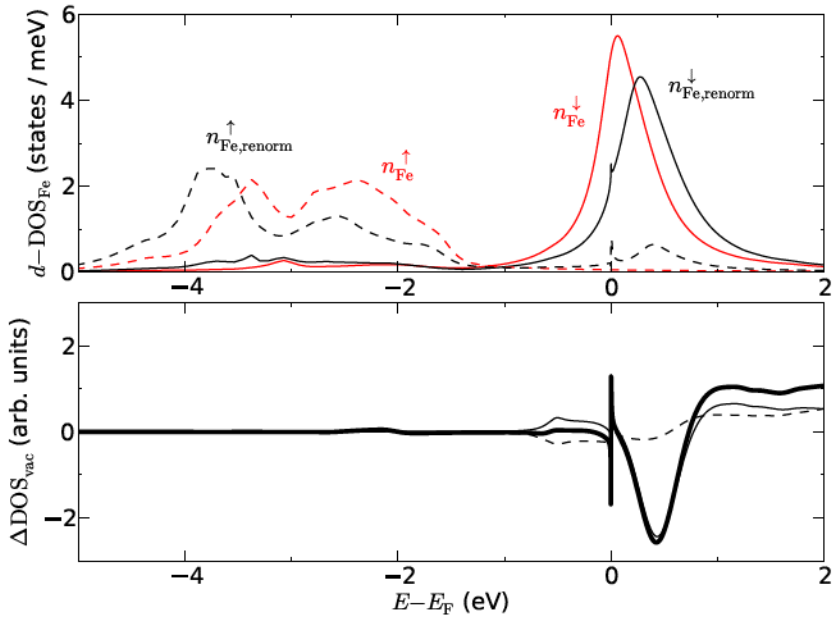

Figure 6.10.: Fe adatom on Cu(111): For a larger energy window, this figure illustrates how the electronic structure get affected by the renormalization via the self-energy. Whereas the d orbitals of Fe (top figure) show remarkable changes for both spin channels and throughout the entire spectrum, the variation in the DOS at the vacuum above the adatom (bottom figure, the thick black curve represents the sum over spins) mainly varies in the region nearby the Fermi energy.

magnetic impurity. In general, the impact of the inelastic signal on the DOS is expected to decrease with distance. Also, the shape of the spin-excitation signature may show a dependence on the probed vacuum site. In the following, these aspects are addressed.

In Fig. 6.11 we show the signature of the spin-excitation for different vacuum sites and the dependence of the inelastic signal on the distance for an Fe adatom on the Cu(111) surface. We probe $\Delta\mathrm{DOS}(E) = n^{\mathrm{ren}}(E) - n^{0}(E)$, the change in the DOS due to renormalization, for different vacuum sites three layers (labeled vc3, see Fig. 6.11(a)) and two layers (labeled vc2, see Fig. 6.11(b)) above the adatom. Since the vacuum positions in the data set vc3 are farther away from the surface their DOS is smaller. If following the path away from the adatom (following the labels $1, 2, \ldots, 8$) a drastic reduction of the inelastic signal in the DOS is observed as well. In Fig. 6.11(c) the strength of the inelastic signal is plotted as function of the distance (projected on the xy plane)

$$d = \sqrt{(\Delta x)^2 + (\Delta y)^2}\,, \tag{6.11}$$

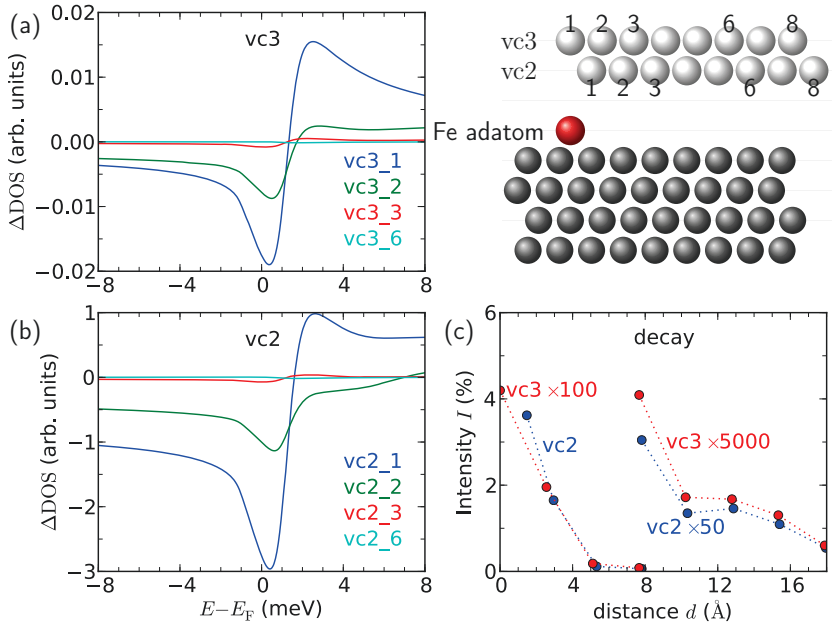

Figure 6.11.: This figure illustrates how the presence of the spin excitation in the Fe adatom affects the density of states for different vacuum sites, three layers (a) or two layers (b) above the one of the impurity. The decay with distance is quantified in terms of the intensity I (see Eq. (6.14)) and plotted versus the projected in-plane distance d (see Eq. (6.11)) to the Fe atom (c). Note, that for each data series $I(d)$ is plotted twice, each time with a suitable scaling factor, such that one can follow and compare their decays for a larger range in distance (*i.e.*, from 0 Å to 8 Å and from 8 Å to 18 Å).

where

$$\Delta x = (i-1)a_{\mathrm{Lat}}\frac{1}{\sqrt{2}} = (i-1)2.556\ \text{Å}\,, \tag{6.12}$$

$$\Delta y = \begin{cases} 0\ \text{Å} & ,\ \text{vc3} \\ a_{\mathrm{Lat}}\frac{1}{\sqrt{6}} = 1.476\ \text{Å} & ,\ \text{vc2} \end{cases}, \tag{6.13}$$

and $a_{\mathrm{Lat}} = 3.615$ Å is the Cu lattice constant. The vacuum sites are labeled by i (see sketch, upper right of Fig. 6.11). By defining the intensity

$$I = \max_E\{|\Delta_{\mathrm{rel}}(E)|\} \quad ,\ \text{with}\ \Delta_{\mathrm{rel}}(E) = \frac{n^{\mathrm{ren}}(E) - n^0(E)}{n^{\mathrm{ren}}(E) + n^0(E)} \tag{6.14}$$

one can obtain the expected behavior as demonstrated in Fig. 6.11(c). A significant part

of the inelastic signal is visible up to about 5 Å. For even larger distances the inelastic signal is still observable, although the order of magnitude is much smaller.

In the shape of the spectra we also notice a slight modification of the signature as can be seen when comparing the spectra for the two vacuum sites with labels 1 and 2 in the vc2 data series: For the vacuum at site 1 the left shoulder of the excitation signature is less pronounced than the right shoulder, which in addition has a spread hill around $+2.5\ \mathrm{meV}$, whereas for the vacuum site 2, the strengths of both shoulders is more balanced and the a hill around $+2.5\ \mathrm{meV}$ is not visible. Although the difference in their shapes is marginal, it shows, however, that a different placement of the probing STM tip (rather than on top of the impurity) can lead to a variation of the spin signature with respect to both, its strength and its shape.

6.4. Summary

Within this Chapter the study of magnetic excitation spectra from first principles was presented for $3d$ transition-metal adatoms placed on a Cu(111) surface. It was shown by use of the dynamical susceptibility that their intrinsic magnetic excitation spectra differ in terms of excitation energies (different g values) and excitation lifetime (different linewidths). The density of states, renormalized by the self-energy, could be connected to the inelastic excitation spectra as measured in ISTS experiments. It showed that different adatoms with different electronic structure can have tremendously different footprints in the renormalized DOS spectra.

The discussion of the imaginary part of the self-energy revealed that characteristic features regarding the steps of the obtained imaginary parts of the spin-resolved self-energies, $\mathrm{Im}\,\Sigma^{\uparrow}$ and $\mathrm{Im}\,\Sigma^{\downarrow}$, can already be concluded from a brief analysis of the spin-resolved density of states (DOS), $n^{\uparrow}(E)$ and $n^{\downarrow}(E)$. The step heights of the imaginary part of the self-energy for a given spin channel are weighted by the density of states of the opposite spin channel near the Fermi energy.

A focus was set on the Fe adatom on the Cu(111) surface where also the impact on the excitation spectra was analyzed when different vacuum sites above the adatoms are considered which showed a reasonable decay of the excitation signature as one naively would expected it. This last instance is one of the great advantages of such a real space approach that allows the study of excitation spectra at different sites next to the excited magnetic structure.

7. Spin-excitations in transition-metal adatoms on Pt(111)

In the previous Ch. 6 spin-excitations in transition-metal (TM) adatoms on the Cu(111) surface have been analyzed and discussed as a first touchstone of the newly developed method that is presented within this thesis. Besides the access to characteristics of the spin-excitation, such as the g shift and the excitation lifetime, it allows to spin-characterize experimentally observed inelastic scanning tunneling spectra (ISTS) and to connect asymmetries in the obtained spectra to the interaction between the excitation and the electronic structure of the system. The focus of this Chapter is the analysis of spin-excitations in TM adatoms on the Pt(111) surface. In contrast to the Cu(111) surface (electronic configuration of Cu: [Ar]$3d^{10}4s^1$) that exhibits s-like surface states near the Fermi energy, the Pt(111) surface (electronic configuration of Pt: [Xe]$4f^{14}5d^96s^1$) is characterized by a large density of states including localized d-orbitals around the Fermi energy. Thus, naively, one would expect a larger damping of the excitations compared to the Cu(111) surface. As we will see later this picture does not necessarily hold because not only the pure surface electronic structure matters but the one of the adatom after considering hybridization effects defines the damping properties which then impact on the spin-excitations lifetimes. Besides the possibility of comparing the calculated spectra to those of adatoms on the Cu(111) surface (see Ch. 6), some new aspects become subject of research, namely in which way the spectra depend on the regarded stacking site of the

adatom (fcc or hcp stacking) and how they change due to the presence of hydrogen (H) in the vicinity of the nanostructure.

The structure of the Chapter is as follows: In Sec. 7.1 the current understanding of excitations for this type of structure is summarized. The presentation of the calculated magnetic spectra is done in two steps: First, in Sec. 7.2 the calculated magnetic excitation spectra are presented for pure TM adatoms (Cr, Mn, Fe, and Co). Second, in Sec. 7.3 the contamination of Fe and Co adatoms with H is analyzed and how this affects the obtained excitation spectra. The results are summarized in Sec. 7.4.

7.1. Adatoms on Pt(111): State of the art

High magnetic anisotropies at the atomic scale are of great importance for the steady miniaturization of future data storage devices, as they are mandatory to stabilize spins against external magnetic or electric forces or thermal fluctuations. Therefore, Gambardella *et al.* [11] caused a stir when they reported in 2003 about a large magnetic anisotropy energy (MAE) of $9\ \mathrm{meV}$ per atom for single Co adatoms on Pt(111) with an easy axis perpendicular to the surface. These findings were substantiated by calculations using the relativistic screened Korringa-Kohn-Rostoker (KKR) method including orbital polarization (OP) leading to more than $18\ \mathrm{meV}$ per Co atom [11]. Using the conventional fully relativistic version of the KKR Green function method Etz *et al.* [98] found a smaller out-of-plane MAE of around $5\ \mathrm{meV}$ per Co atom and about the same value when considering single Fe adatoms on Pt(111).

Several groups have tried to shed light onto the magnetic dynamics of Fe and Co adatoms on the Pt(111) surface by means of ISTS measurements. Balashov *et al.* [19] studied excitation spectra for Co and Fe single adatoms and find resonances of more than $10\ \mathrm{meV}$ for the Co adatom and around $6\ \mathrm{meV}$ for the Fe adatom. They could not verify the nature of a magnetic excitation by applying an external magnetic field but they claimed that this excitation is of magnetic origin by comparison of the excitation position to the expected one considering the magnetic anisotropy energy measured by Gambardella *et al.* [11].

Khajetoorians *et al.* [23] investigated Fe adatoms on Pt(111) and come to a different conclusion. They find values for the anisotropy that are one order of magnitude smaller than those reported in Refs. [11] and [98]. But more remarkable, a strong dependency on the stacking site was found for the magnetic properties of the Fe adatom. The fcc stacking site shows an out-of-plane MAE while for the hcp stacking it is in-plane. By applying the KKR method, we could verify this observation by accounting for its high magnetic polarizability [23]: When the MAE is extracted using a large number of surrounding Pt atoms, *i.e.*, a large polarization cloud, indeed, the MAE show the experimentally observed dependency on the stacking site of the adatom. In addition, the values for the MAE are about one order of magnitude smaller than the ones given in Refs. [11] and [98].

Also, Dubout *et al.* [40] examined this system and found that the contamination of the

nanostructure with hydrogen (H) or deuterium (D) strongly affects the observed spectra. A magnetic excitation was not observed for the pure Co system, in contradiction to Ref. [19], while clear excitation signatures occur as soon as the surface is exposed to one or two H or D atoms. For the fcc absorbed CoH_2 nanostructures they even observe a peak at the Fermi energy that they associate with a Kondo peak.

All these findings reveal that there are different understandings of this system and many aspects are still open for discussion. For the description of the spin-excitations, in the present work SOC is not included. Instead, the main focus is set on the discussion of g shift and lifetimes as well as an analysis of the shape of the spin-excitation signatures in absence and presence of H atoms.

7.2. Pure adatom spectra

This Section considers pure $3d$ TM adatoms (Cr, Mn, Fe, Co) placed on the fcc and the hcp stacking site on Pt(111). As it was done for the Cu(111) surface (see Ch. 6) the analysis is threefold: First the ground-state properties are analyzed, second the intrinsic excitation spectra (given by the transverse dynamical magnetic susceptibility) is given. Finally the renormalized spectra, incorporating the interaction of spin-excitation and electronic structure, is presented and discussed.

7.2.1. Ground-state properties: fcc *vs.* hcp stacking

The spin-resolved density of states (DOS) projected onto the adatom is shown in Fig. 7.1. The top and the bottom figures correspond to fcc and hcp stacking of the adatoms,

adatom	N_d		$n_d^{\uparrow}(E_\mathrm{F})$ $(\frac{\text{states}}{\text{eV}})$		$n_d^{\downarrow}(E_\mathrm{F})$ $(\frac{\text{states}}{\text{eV}})$		m_d (μ_B)	
	fcc	hcp	fcc	hcp	fcc	hcp	fcc	hcp
Cr	4.26	4.30	1.42	2.19	0.152	0.142	3.19	3.17
Mn	4.97	4.99	0.470	0.469	0.199	0.177	3.75	3.78
Fe	5.53	5.51	0.190	0.169	1.26	0.888	2.79	2.78
Co	6.91	6.80	0.264	0.207	4.85	4.64	1.77	1.80

Table 7.1.: Ground-state properties for the four adatoms: N_d is the number of d-electrons, $n_d^{\downarrow}(E_\mathrm{F})$ and $n_d^{\uparrow}(E_\mathrm{F})$ describe the local density of states at the Fermi energy E_F for both spin-channels, and m_d is the magnetic moment when only the d-orbitals are considered. All these quantities are calculated using the projected Green function, see Sec. 3.3, and considering the adatom's contribution only.

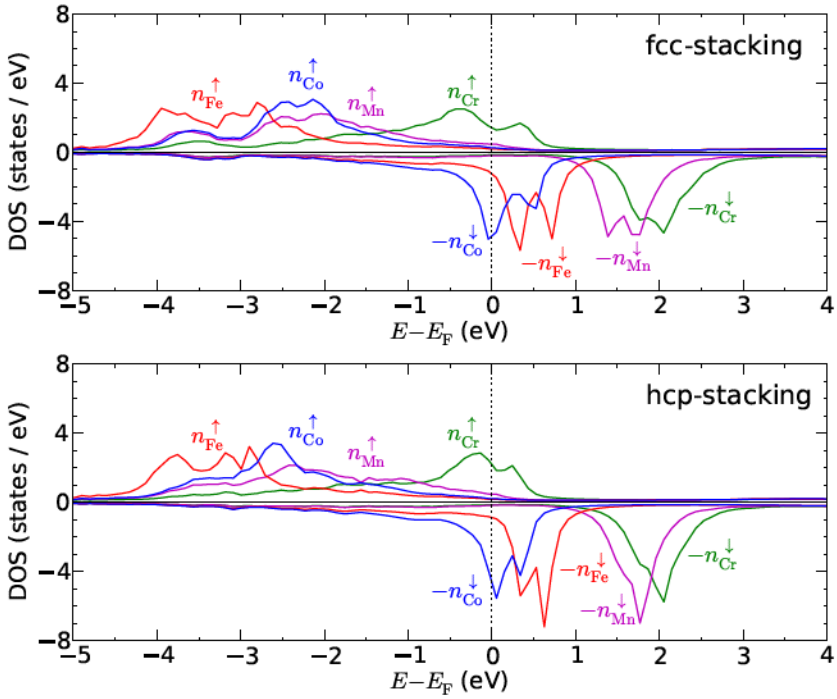

Figure 7.1.: The spin-resolved total density of states (DOS) are shown for the four adatoms (Cr, Mn, Fe, and Co) placed on the Pt(111) surface. The upper figure considers the fcc stacking of the adatoms, while the lower figure considers the hcp stacking. The Fermi energy is indicated by a dotted vertical line.

respectively. A first observation is that the difference of the two types of stacking is not very striking. A comparison to the DOS analysis for the adatoms place on the Cu(111) surface (see Fig. 6.2) reveals that the resonances show a stronger splitting. This is due to the hybridization with the d-orbitals of the Pt substrate the five d-orbitals of the adatoms split into 3 symmetry groups (according to the point group symmetry C_{3V} one has E_2 for $d_{x^2-y^2}$ and d_{xy}, E_1 for d_{xy} and d_{xz}, and A_1 for the remaining $d_{3z^2-r^2}$). As pointed out earlier the observed excitation mainly is determined by the local DOS at the Fermi energy E_F. In Table 7.1 some system-specific ground-state properties are listed. Also here, the differences between fcc and hcp stacking are small. Compared to the values for the Cu(111) surface (see Table 6.1) the local DOS at the Fermi energy, $n_d^{\downarrow}(E_F)$ and $n_d^{\uparrow}(E_F)$, show the tendency to be larger, such that a larger damping of the spin-excitation is expected.

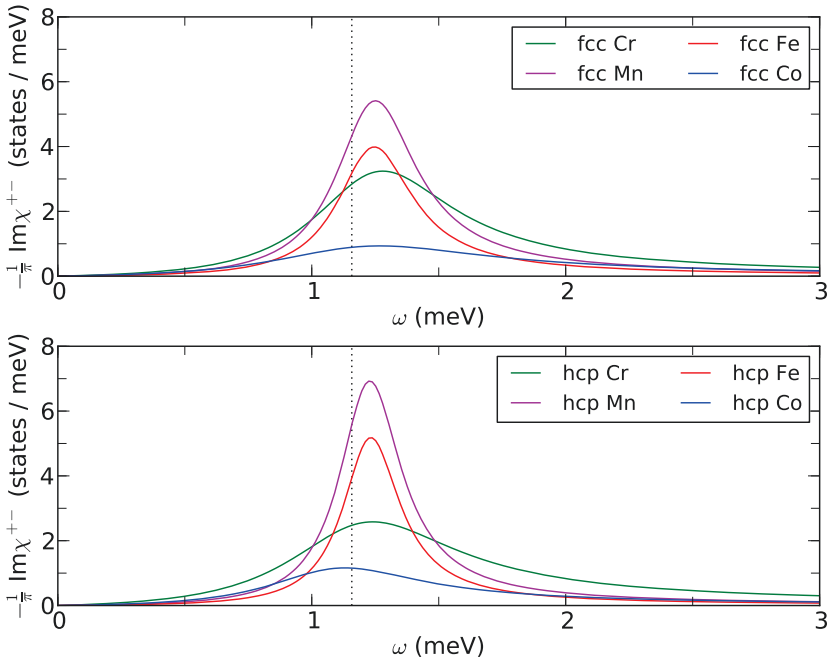

Figure 7.2.: The imaginary part of the dynamical enhanced susceptibility for the four TM adatoms are shown, describing the intrinsic excitation spectrum. The upper and lower panel show the excitation spectra for an fcc and an hcp stacking, respectively. The applied B-field is set to 10 Tesla in order to compare among the different systems.

7.2.2. Intrinsic magnetic excitation spectra

The intrinsic magnetic excitation spectra, given by $\mathrm{Im}\chi^{+-}$, the imaginary part of the enhanced susceptibility, is shown in Fig. 7.2 for the investigated TM adatoms on the Pt substrate at the fcc stacking site (top figure) and the hcp stacking site (bottom figure). Extracted from these curves, the resonance frequency as well as for the g shift and the lifetime are given in Table 7.2. Generally, the fcc stacking results in a higher g shift which is largest for Co ($g_{\mathrm{eff}} = 2.19$ and $g_{\mathrm{eff}} = 1.95$ for fcc and hcp stacking, respectively) which was found experimentally for the Fe adatom [23]. The largest damping is found for Cr and Co adatoms causing their excitation life times to be three times smaller than those for Mn and Fe adatoms. Compared to the excitation spectra for the Cu(111) surface (*cf.* Fig. 6.3 and Table 6.2) the differences of resonance heights and linewidths among the TM adatoms are smaller on the Pt surface (*e.g.*, the excitation life time for Cr adatoms on Cu(111) was 10 times larger than the one for Co). This reflects the different kinds hybridizations on these two surfaces, see discussion in Sec. 7.2.1.

7.2.3. Renormalized density of states via the self-energy

In Fig. 7.3 the self-energies for the four adatoms on the Pt substrate are shown. The upper panels show the spectra for the fcc stacking of the adatom on the Pt(111) surface. The lower two panels show the spectra for hcp stacking. On the left the spin-up components are shown, on the right the spin-down components are plotted.

As already found in the analysis of DOS and intrinsic excitation spectra (see Figs. 7.1 and 7.2) the impact of the stacking position of the adatom is little. The largest difference in the step height is found for the Cr adatom, where the self-energy reaches in the minority spin channel a step height that is larger by $50\ \%$ for the hcp stacking compared to the fcc stacking. This can be understood by looking at the spin-resolved DOS of the Cr adatom (see Fig. 7.1): For the hcp stacking the DOS of the majority spin channel around the Fermi energy is slightly larger (compared to the DOS for the fcc stacking) providing a higher number of states that can be excited. Furthermore, the step height ratio for the two spin channels is $\mathrm{Im}\left[\Sigma^{\downarrow}(+8\ \mathrm{meV}+E_{\mathrm{F}})\right]/\mathrm{Im}\left[\Sigma^{\uparrow}(-8\ \mathrm{meV}+E_{\mathrm{F}})\right] \approx 10$ (for both stacking sites). This is in nice agreement with the ratio of spin resolved DOS at the Fermi energy, $n_d^{\uparrow}(E_{\mathrm{F}})/n_d^{\downarrow}(E_{\mathrm{F}})$, see Table 7.1 and reflects the fact that the step height is connected to the DOS of opposite spin channel (hence the swap of spin labels in the ratio). For the Mn adatom the step heights for the two spin channels are in the same order of magnitude. Due to the low DOS in both spin channels (see Fig. 7.1) the possibility for magnetic excitations is reduced when compared to the other adatoms. As a consequence the impact on the DOS due to the renormalization (see Fig. 7.4 and corresponding discussion in next paragraph) turns out to be the smallest. For the Fe adatom the step widths are relatively sharp and the difference between the step heights of both spin channels is only a factor of about $1/10$ (compared to the factor of $1/100$ for the Cu(111) surface, see Ch. 6). Finally the Co adatom shows the broadest steps compared to the other three adatoms, *i.e.*, the largest damping. This matches with the observation that only for the Co adatom the

adatom	g_{eff}		ω_{res} (meV)		τ_χ (fs)	
	fcc	hcp	fcc	hcp	fcc	hcp
Cr	2.21	2.14	1.28	1.24	494	403
Mn	2.16	2.12	1.25	1.23	864	1210
Fe	2.16	2.14	1.25	1.24	968	1270
Co	2.19	1.95	1.27	1.13	310	440

Table 7.2.: This table shows characteristic properties of the susceptibility for the four adatoms, considering fcc and hcp stackings of the adatoms. For an applied field of $B_0 = 10\ T$ the resulting effective g value $g_{\mathrm{eff}} = \omega_{\mathrm{res}}/B_0$, the resonance position ω_{res}, and the lifetime $\tau_\chi = \hbar/(2\Gamma)$ of the excitation is shown, where Γ is the full-width at half-maximum.

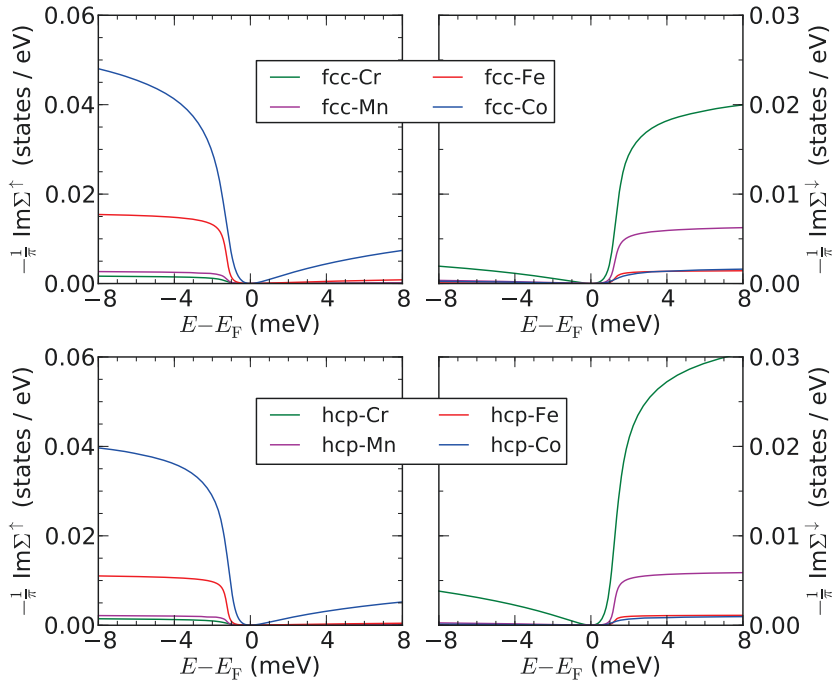

Figure 7.3.: The imaginary part of the self-energy for four different $3d$ transition-metal adatom impurities is shown. The upper and lower panel show this quantity for an fcc and an hcp stacking, respectively. The applied magnetic field is always set to 10 Tesla in order to compare among the different systems.

minority resonance in the DOS is located at E_{F}, allowing the most efficient decay into Stoner excitations among all studied adatoms.

As demonstrated in Sec. 5.4, the renormalized DOS can be related to the experimental measured excitation spectra via the Tersoff-Hamann approximation. A collection of renormalized DOS for the four investigated adatoms on Pt(111) are shown in Fig. 7.4. The first two rows of panels represent fcc stackings and the second two rows show the spectra for adatoms at the hcp stacking site. As already discussed in Ch. 6 (see Fig. 6.8) the shapes of the calculated spin-excitation signatures reveal a great variety. Similar to the Cr adatom on Cu(111) (see Figs. 6.8(a) and 6.8(e)) the minority spin channel exhibits a satellite around $-2\ \mathrm{meV}$, while for the Mn adatom only the excitation signatures are found. At the vacuum site above the Fe adatom (for both, fcc and hcp stacking) an additional excitation, a bound state or satellite, appears in the majority spin channel, nearby the Fermi energy. Such a satellite was already found for the Fe adatom on Cu(111) (see Figs. 6.8(g)). Finally, the renormalized spectrum for the Co adatom shows a satellite for the majority spin channel, that, however, does not affect the shape of the excitation

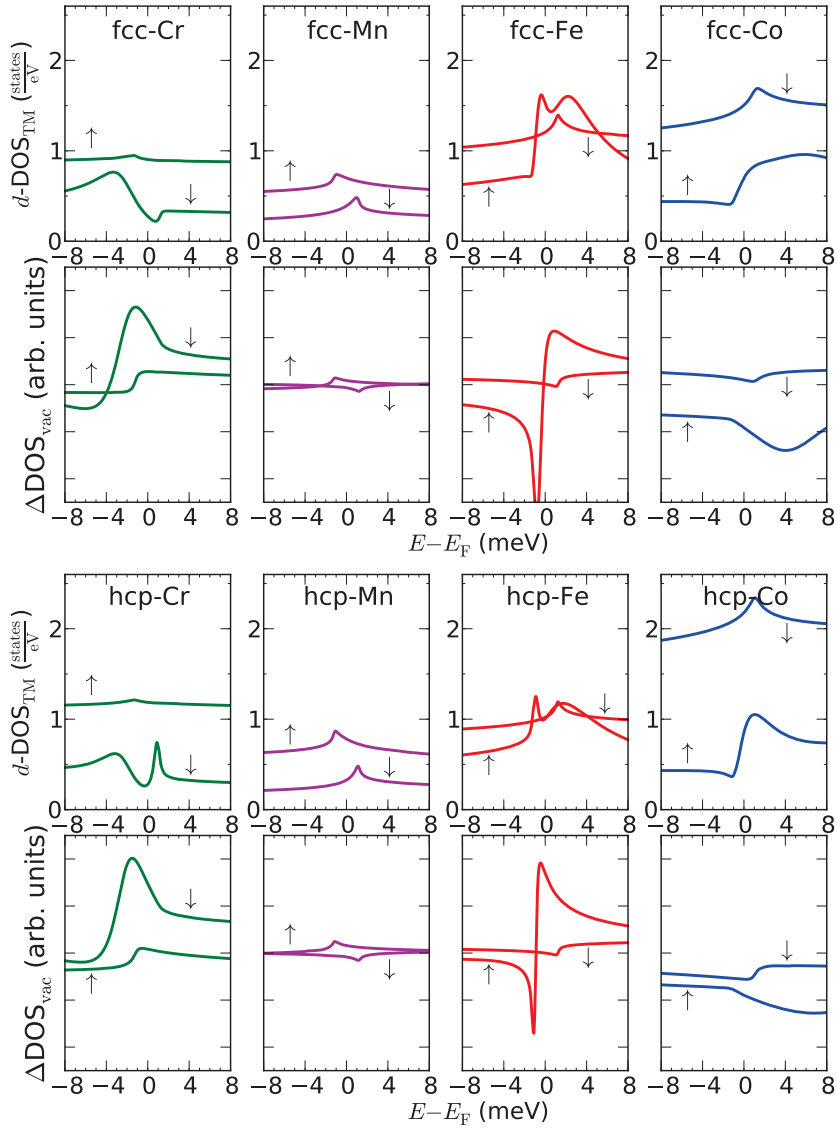

Figure 7.4.: Renormalized DOS for TM adatoms (from left to right: Cr, Mn, Fe, Co) on Pt(111): Top row: Renormalized d-DOS in the adatom for the fcc stacking. Second row: For the same systems the renormalized DOS in the vacuum site above the adatom. Third row: Renormalized d-DOS in the adatom for the hcp stacking. Bottom row: For the same systems the renormalized DOS in the vacuum site above the adatom.

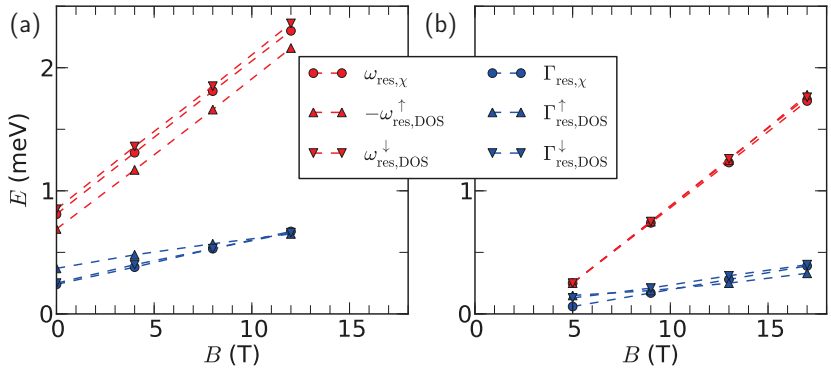

Figure 7.5.: Fe adatoms on Pt(111): The resonance frequency, $\omega_{\mathrm{res},\chi}$, as well as the full width at half maximum, $\Gamma_{\mathrm{res},\chi}$, using the intrinsic excitation spectra (given by the susceptibility χ) are compared to the spin-resolved values when using the renormalized DOS. A distinction is made between (a) fcc stacking and (b) hcp stacking of the Fe adatom. Note that $\omega^{\uparrow}_{\mathrm{res,DOS}}$ corresponds to the step at negative energy and is plotted with a minus sign which allows a comparison among all three resonances. In order to mimic the SOC-induced gap found in Ref. [23] an auxiliary magnetic field of $B_0 = 0.375\ \mathrm{meV}/\mu_{\mathrm{B}}$ is assumed for the fcc stacking, while for the hcp stacking the in-plane magnetization is accounted for by an offset of $+3\ T$, the field that has to be applied to overcome the in-plane magnetization, see Fig. 4 of Ref. [23].

signature much at the vacuum site. We return to the excitation signatures of Fe and Co adatoms in Sec. 7.3 where the change in the shapes is analyzed due to the adsorption of hydrogen.

The analysis of the magnetic excitation spectra for pure TM adatoms on Pt(111) is concluded with an analysis of resonance position and line width as function of an applied magnetic field. In Fig. 7.5 we show for fcc and hcp stacked Fe adatoms on Pt(111) a comparison between resonances and linewidths as they result from analyzing the intrinsic excitation spectra (given by the imaginary part of the susceptibility) and the renormalized spectra (given by the renormalization of the DOS via the self-energy). For the fcc stacking (see Fig. 7.5(a)) an auxiliary magnetic field of $B_0 = 0.375\ \mathrm{meV}/\mu_{\mathrm{B}}$ mimics the SOC-induced gap in the ISTS measurements from Ref. [23]. For the hcp stacking (see Fig. 7.5(b)) the Fe adatom was found to have an in-plane magnetization [23] which is accounted for by shifting the curves in Fig. 7.5(b) by $+3\ T$ which corresponds to the field that has to be applied to overcome the in-plane magnetization. For both cases, the fcc and the hcp stacking, the values for resonance frequency and linewidth increase linearly with applied magnetic field. For the fcc stacking the lifetime of the resonance in the intrinsic excitation spectrum drops from about $1370\ \mathrm{fs}$ (for zero B-field) to $491\ \mathrm{fs}$ (for $12\ T$) and

for the hcp stacking from 5490 fs (for $5\ T$) to 844 fs (for $17\ T$). The higher lifetime for the hcp stacking, of course, reflects the assumption of an in-plane magnetization that first has to be overcome by the applied magnetic field. We notice that the presence of the satellite in the spin up channel is located near the Fermi energy and therefore strongly affects the shape of the calculated inelastic spectra which leads to a stark distortion of resonance and linewidth of the spin down channel when the renormalized spectra of the two spin channels are superimposed with equal weights.

7.3. Hydrogenized adatom spectra

This Section analyzes in which way the magnetic excitation spectra change when the presence of an additional hydrogen (H) atom is assumed. Such contamination of metallic surfaces is a known aspect of STM measurements even when the sample is placed in ultra-high vacuum chambers. We only consider Fe and Co adatoms placed at fcc or hcp stacking sites on the Pt(111) surface and consider one additional H atom next to the adatom. The analysis is twofold: In a first step, we perform structure optimization calculations where different configurations of the FeH dimer are considered. A comparison of the resulting total energies allows to conclude in which way the H atom attaches to the adatom. Based on this analysis, the second step analyzes excitation spectra for different FeH and CoH dimers where the presence of H next to the adatom is varied. Two arrangements, H on top and H at the side of the TM adatom, are considered.

7.3.1. Structure optimization: Position of hydrogen

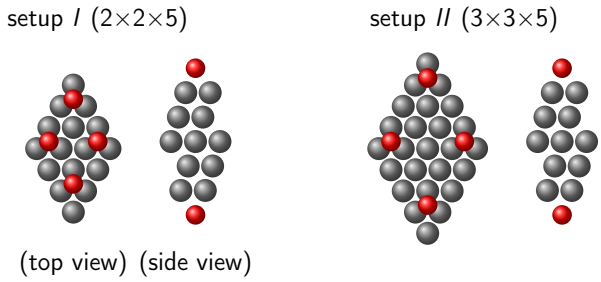

Figure 7.6.: The different supercell setups used for the relaxation are shown schematically. The gray and red circles denote Pt and Fe atoms, respectively. For clarity the H atoms are not visualized.

When performing STM measurements of transition-metal adatoms on the Pt(111) surface the presence of one or more hydrogen atoms that contaminate the nanostructure can play a crucial role [40]. However, experimentally it is difficult to extract the position of the

H atom by topography measurements with an STM tip. Therefore the following analysis considers different FeH dimer structures with the goal to predict the most probable position taken by the H atom.

These structural optimization calculations are carried out by use of the projector augmented wave method (PAW) as implemented in the Vienna *Ab initio* Simulation Package (VASP) [99] utilizing the PBE exchange-correlation potential. The supercell is inversion symmetric and consists of 5 Pt layers as well as two H-Fe dimers that are placed in the layers above and below the slab, see Fig. 7.6. The size within the xy plane is such that neighboring impurities are separated by 2 or 3 lattice constants. The use of two different unit cell sizes (labeled setup *I* and *II*, see Fig.7.6) allows for an analysis in which way the influence of neighboring impurities decays with distance. The distance to the neighboring slab is 28 Å, so that the thickness of the vacuum region in between is about 15 Å. The two-dimensional Brillouin zone is sampled for the 2×2 and 3×3 supercells, by 11×11×1 and 7×7×1 $\vec{k}$-point meshes, respectively. An energy cutoff parameter of $500\ \mathrm{eV}$ is chosen and the tolerance for the forces is set to $0.01\ \mathrm{eV/Å}$. The lattice constant is $a = 3.924$ Å. For all steps the size and the shape of the unit cell is kept fixed.[1] The calculations cover both, the fcc and the hcp stacking of the Fe adatom, each with eight different initial FeH dimers as starting configurations, where the positions are labeled from *a* to *h*, *cf.* Fig. 7.7. Whereas for the 2×2 supercell the H-Fe dimer is constrained to vary along the axis perpendicular to the surface only, the relaxations for the 3×3 supercell include all spatial directions for the impurity and the top-most Pt layer. Furthermore, we discuss the modification of m_{Fe}, the magnetic moment of Fe, when H is attached, *e.g.*, on top of Fe or at the side of it in the same layer.

In Fig. 7.7 the total energies are plotted with respect to the initial position of the H atom, for both, the fcc stacking (top figure) and the hcp stacking (bottom figure) of the Fe atom. In each figure the total energies are given with respect to the minimal value, such that their relative values can be compared directly. Each figure shows one energy comparison for the 2×2 supercell (setup *I*) and two for the 3×3 supercell (setup *II*). The colors of the curves correspond to different constraints in the performed relaxations: a black curve indicates that the impurity atoms are relaxed along the z-direction only while the Pt atoms are kept fixed in bulk-like positions, a blue curve allows more degrees of freedom, where the impurity atoms and Pt atoms of the surface layer nearby are relaxed in all three directions. In addition to the curves each figure contains a small top view sketch of the corresponding supercells, including the position of the H atoms with their respective label, all in one image and indicated by small white circles. The Pt atoms in the surface layer are indicated by gray circles, the Fe atoms by red circles. Note, that the label color matches the color code used for the energy curves (*e.g.*, black/blue labels refer to the black/blue curve).

Already the smallest supercell structure (setup *I*, the 2×2 supercell) affords an important outcome: The sampled energy landscapes for fcc and hcp stackings are qualitatively very

[1] Test calculations showed that the lattice parameter increases by less than 1 % when the volume of the unit cell is relaxed as well. This is in accordance with the common observation that GGA functionals slightly overestimate the lattice constant of Pt.

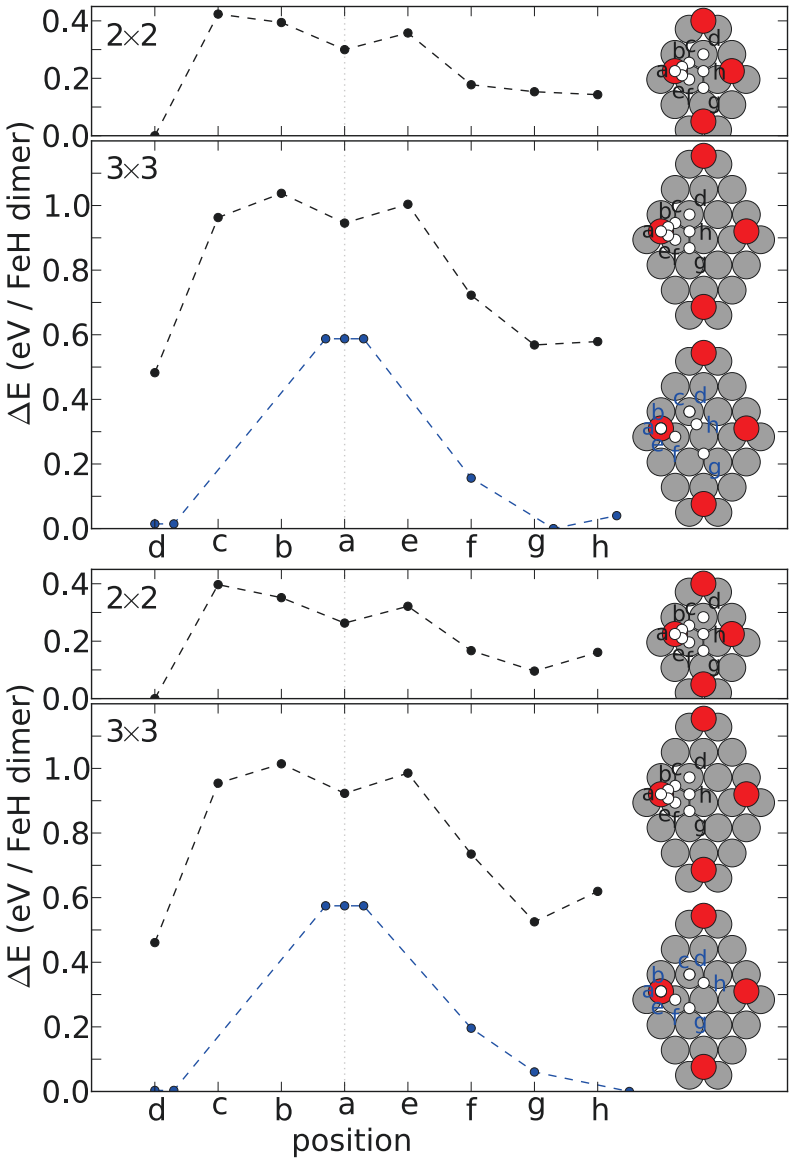

Figure 7.7.: The total energies for the 2×2 and the 3×3 supercell are shown with respect to eight different starting positions for H. The top and bottom figures analyze the fcc and the hcp stacking of the Fe adatom, respectively. The different colors refer to different constraints in the performed relaxations: Black indicates relaxation of the FeH dimer along the z-direction, while blue means a full relaxation of the dimer and the surface Pt layer.

similar. Only for position *h* it seems that the presence (or absence) of a Pt atom in the layer below the surface has a small effect. A closer look to the energy curve reveals a second important result: The H atom shows the tendency to nestle at the side of Fe rather than on top of it. Whereas H on top of Fe (position *a*) exhibits a local minimum (position *b* and *e* are nearby but higher in energy) the total minimum of the investigated structures appears for position *d*, the structural arrangement where H is on top of a Pt atom and as far as possible separated from the neighboring Fe impurities.

Although the calculations using setup *I* only contain a small supercell and have a limited degree of freedom in the performed relaxations, the main conclusions presented in the previous paragraph also hold for the more comprehensive analysis of the calculations performed for setup *II* we will be able to confirm the obtained tendencies. In the black curve of the 3×3 supercell (fcc and hcp similarly) we rediscover the local minimum for the H atom on top of Fe. Small quantitative differences between the 2×2 and the 3×3 supercells only show up for larger distances between Fe and H, namely positions *d*, *g*, and *h*. Here the impact of neighboring Fe impurities on the H atom is manifested where the energy differences with respect to the other positions increase by about $0.2\ \mathrm{eV}$ to $0.3\ \mathrm{eV}$ per FeH dimer. All in all it underlines the observation that those positions that contain a large distance between Fe and H usually are energetically the most favorable ones.

By relaxing the impurity atoms as well as the Pt surface layer in all three directions (blue curve) we notice that for some arrangements the H atom travels some distance within the supercell (usually not more than 2 Å) whereas the Fe atom's position remains unchanged (below 1 %). The H atoms located in position *b* and *e* relax into the local minimum on top of Fe (position *a*). Thus, the relaxation calculations for position *a*, *b*, and *e* lead to the same structural arrangement which explains the equal value for their total energies (see plateau in blue curves in Fig. 7.7). For position *c* we obtain a large energy gain (above $0.4\ \mathrm{eV}$ per FeH dimer) compared to the value for the black curve. In fact the structure now matches the one from position *d*, an indication that the H atom prefers to be located on top of a Pt atom rather than at a hollow position. This gets confirmed by the fact that the H atom at position *f* does not move away from its position on top of Pt even though it starts with the same distance to the Fe atom as it is the case for position *c*. For position *g* and *h* we notice a difference for the corresponding fcc and hcp setups. The positions that the H atoms relax to are slightly distinct leading to a small dissimilarity for their total energies. However, the resulting energy differences are too small to allow for extracting a tendency out of this. Finally, we state that the largest energy gain for all investigated structures (with respect to the black curve) is achieved through the relaxations of the Pt atoms of the topmost layer, as could be verified by exclusively relaxing these atoms alone. Especially a simultaneous translation of the surface Pt layer and the impurities on top by about 7 % away from the slab (the percentage value is given with respect to the bulk-like interlayer distance) indicates a slight overestimation of the lattice constant.

It total two main conclusions can be formulated as results of the performed structural relaxation analysis:

- In the examined energy landscape of positioning the FeH dimer, one observes a local minimum for having the H atom located on top of the Fe atom.
- A global minimum is found when the H atom is in contact with the Pt surface layer. It is however driven away from the Fe atom.

These two outcomes hold for both stacking sites.

Magnetic moment of Fe and Co adatoms in the presence of H

The analysis of the structural optimization is concluded with a comparison of the corresponding total charge and magnetic moments of the Fe and the Co adatom. Depending on where the H atom is located, the adatom may experience different strengths of hybridization with the substrate, leading to a change in the magnetic moment and thus a change in the excitation spectrum, discussed in the subsequent Section.

Table 7.3 presents a collection of values for total charge and magnetic moments of Fe and Co adatoms, where only the contribution from the d orbitals is considered (the total charge and total magnetic moments are a few percent larger). A comparison of fcc and hcp stacking of the adatom reveals no significant difference. It turns out that for both stacking sites, the presence of hydrogen does not affect the values of total charge and magnetic moment in a noticeable way. The magnetic moment of the Fe atoms are in the range of $3.1\ \mu_{\mathrm{B}}$ and $3.3\ \mu_{\mathrm{B}}$. When the distance between H and Fe is beyond the nearest

adatom	position of H	N_d		m_d (μ_{B})	
		fcc	hcp	fcc	hcp
Fe	(no H)	6.10	6.11	3.27	3.28
	a	5.97	5.97	3.30	3.32
	f	6.18	6.17	3.09	3.11
	h	6.10	6.11	3.27	3.28
Co	(no H)	7.24	7.24	2.12	2.14
	a	7.11	7.10	2.17	2.20

Table 7.3.: Total charge N_d and magnetic moment m_d projected on the d-orbital of the considered adatom, Fe and Co. The positions of the H atom are labeled in accordance with Fig. 7.7. Note that charge and magnetic moments of the adatom are not affected much by the presence of hydrogen.

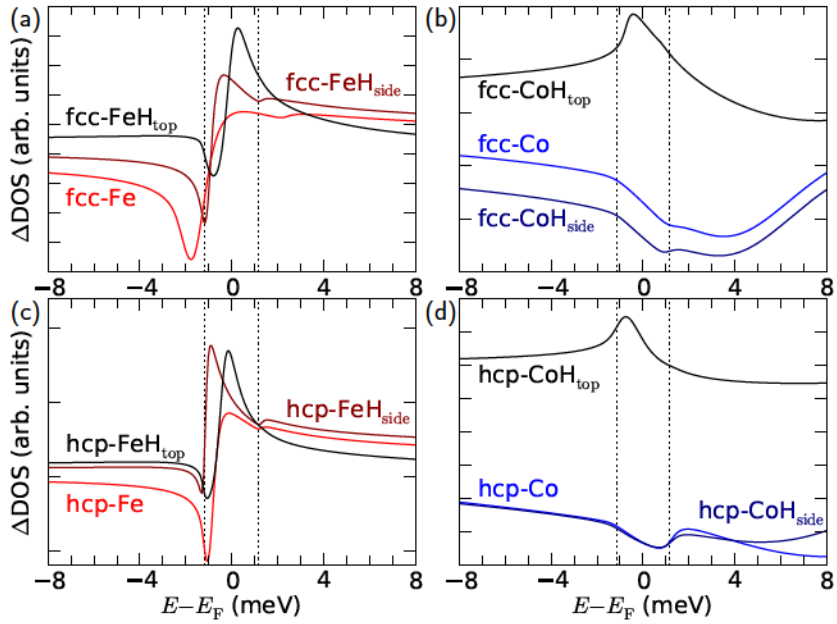

Figure 7.8.: Impact of hydrogen on the magnetic excitation spectra of (a) Fe and (b) Co adatoms at the fcc stacking site on Pt(111) and (c) Fe and (d) Co adatoms at the hcp stacking site. For each case the shape of the spectrum for the pure adatom is compared to those for adatoms that are contaminated by one H atom at the side (H_{side}) or an top of it (H_{top}). $\Delta\,\text{DOS}$ corresponds to the difference in the density of states with and without including the self-energy and has been scaled by an arbitrary factor in order to allow a comparison of the shapes. The dotted vertical lines indicate the expected positions of the magnetic resonance positions for the case that $g = 2$.

neighbor distance (see values in Table 7.3 for pure Fe adatom and those for position *h* of the H atom) hydrogen shows no effect on charge and moment of the adatom.

This concludes the structure optimization analysis that utilizes the VASP code. In the light of the presented findings we turn in the next Section to the exploration of spin-excitation spectra for hydrogenized adatoms on Pt(111), using the KKR-based method that was developed within this thesis.

7.3.2. Spin-excitations in the presence of hydrogen

Following the previously presented structure optimization analysis (see Sec. 7.3.1) one can think of two possible scenarios: Either the H is adsorbed on top of the adatom in a local energy minimum, or it directly sits on the Pt surface next to the adatom. Although the latter is lower in energy it is still reasonable to account for both scenarios in the analysis of spin-excitation spectra of adatoms that are contaminated by hydrogen. Due to the KKR formalism space is divided into Voronoi cells (see Sec. 3.2) and the two chosen sites for H are (i) position *h* in the same layer as the Fe adatom (in the following referred to as $\mathrm{FeH_{side}}$) and (ii) position *f* in the layer above the Fe adatom (referred to as $\mathrm{FeH_{top}}$), where positions *h* and *f* are as given in Fig. 7.7.

Since experimentally a focus is set on Fe and Co adatoms we concentrate on how a side position or a top position of hydrogen changes the excitation spectra [40]. At this stage of the Chapter we fill confident to skip the presentation and analysis of intrinsic excitation spectra (*i.e.*, the susceptibility) and self-energy and move directly to the analysis of the renormalized DOS in the vacuum above the adatom. A distinction is made between the fcc and the hcp stacking to allow a comparison between these two setups. As it was done in the comparison among the different TM adatoms (see Sec. 7.2) a universal auxiliary magnetic field of $10\ T$ mimics a SOC-induced gap in the excitation spectra, albeit in general they may differ from system to system.

In Fig. 7.8 the impact on the excitation spectra of Fe adatoms and Co adatoms in the presence of H contamination is shown. These plots show the difference in the DOS when including the self-energy (both spin channels are weighted equally). In addition, the curves of each subplot are normalized by individual factors that enable to compare their shapes directly. For the Fe systems (see Fig. 7.8(a) and Fig. 7.8(c)) the presence of H at the side of Fe seems to sharpen the resonance widths meaning that the lifetime of the excitation is enlarged. For the top position of the H atom, the satellite (coming from the spin up channel) moves to the Fermi energy and interfere with the excitation signature originating from the spin down channel (expected at about $+1.1\ \mathrm{meV}$). For the Co adatom (see Fig. 7.8(b) and Fig. 7.8(d)) the side position of the H atom does not affect the excitation spectra in a remarkable way. When putting it on top of the Co adatom, however, an interesting change in the renormalized spectra for fcc and for hcp stacking is observed: Near the Fermi energy a resonance appears and dominates the shape of the spectra completely compared to the spectrum of the Co adatom alone. This is a strong indication that the presence of H can affect measured inelastic excitation spectra substantially, a conclusion that was also found in ISTS experiments [40].

7.4. Summary

In this Chapter we studied spin-excitations in TM adatoms on the Pt(111) surface utilizing the newly developed method that accounts for the interaction of the spin-excitation with the electronic structure via the self-energy. The presented analysis was twofold:

In a first part, the calculated excitation spectra for Cr, Mn, Fe, and Co adatoms were analyzed, considering both, fcc and hcp stacking. The analysis incorporated the presentation and discussion of intrinsic excitation spectra (provided by the susceptibility), the self-energy, and the signature of the spin-excitation in the electronic structure in the adatom and the vacuum above the adatom, the quantity that is proportional to the experimentally measured inelastic spectra. Although the obtained values for g shift and lifetimes are in accordance with our previously published results [23] we notice that the shape of the calculated excitation spectra may deviate from expected step-like shapes and the presence of bound states (satellite) can occur, as it was already found for the Cu(111) surface (see Ch. 6).

In a second part, the impact of hydrogen (H) on the obtained excitation spectra of Fe and Co adatoms were studied. A structural optimization analysis revealed two possible scenarios: Either H is positioned on top of the adatom in a local minimum, or it is adsorbed on the Pt surface next to the adatom. Accounting for both absorption scenarios of the H atom as well as the fcc and hcp stacking sites for the adatom, the excitation spectra for Fe and Co adatoms were calculated and compared to the shape of the spectra obtained for the same systems without H. In accordance to previously reported ISTS measurements [40] the shape can show a strong dependence on the hydrogenization of the structure.

8. Spin-excitations in transition-metal clusters on Cu(111)

Up to this point of the thesis, the focus was set on the analysis of magnetic excitation spectra of single transition-metal (TM) adatoms (*i.e.*, monomers) placed on metallic surfaces (Cu(111) and Pt(111), see Chs. 6 and 7, respectively). In this Chapter we revisit the Cu(111) surface as utilized in Ch. 6 and investigate magnetic excitation spectra for impurity clusters, *i.e.*, structures that consist of more than one magnetic impurity atom. Similar to the discussion of monomer impurities one expects a rich variety of the obtained spectra, depending on the TM type and on how strong the localized d-electrons hybridize with the itinerant electrons of the substrate. Instead of comparing excitation spectra for different TM adatoms, however, this Chapter mainly concentrates on Fe adatoms on Cu(111) and a new aspect is of central interest, namely the exchange coupling among the respective magnetic moments.

For a system of two or more magnetic adatoms the potential energy as function of magnetic

moments can be expressed in terms of a Heisenberg model,[1]

$$E(\{\vec{m}_i\}) = -\frac{1}{2}\sum_{i,j|i\neq j} J_{ij}\vec{m}_i \cdot \vec{m}_j - \vec{B}^{\text{ext}} \cdot \sum_i \vec{m}_i \ , \tag{8.1}$$

where J_{ij} is the coupling constant between magnetic moments $\vec{m}_i$ and $\vec{m}_j$. As a consequence, systems with coupled moments may have two or more excitation states at different energies (similar to a system of two mass points coupled via a spring that shows two eigenmodes at different oscillation frequencies, an acoustic and an optical mode, *i.e.*, the masses oscillate synchronously and in opposite directions). These excitation energies should manifest as resonances at the respective frequency in the excitation spectrum and characteristics such as the width of these resonances hold information about the excitation, *i.e.*, the g shift when applying an external magnetic field or the lifetime of the excitation.

In the literature, only a few cluster structures have become subject of research in terms of inelastic scanning tunneling spectroscopy (ISTS). Among them is an analysis of Mn chains on the semi-metallic CuN surface [12]. An even-odd effect of the excitation spectra was observed, *i.e.*, the spectra for an even or an odd number of Mn atoms within the chain differ qualitatively. The authors mention a nonsymmetric behavior of their measured spectra and propose that first-principle calculations could help to gain a better insight into the reason for such an asymmetry. Balashov *et al.* [19] investigate structures of two and three Fe atoms on the Pt(111) surface and present the magnetic excitation spectrum for an Fe dimer where Gaussian fits are used to visualize acoustic and optical mode of the system. A theoretical approach to excitation spectra for different dimers on Cu(001) including also mixed dimers is presented by Lounis *et al.* [38], forming the basis of the presented method within this thesis.

The chapter is organized as follows: In Sec. 8.1 the smallest cluster structure is analyzed, *i.e.*, a dimer consisting of two impurity adatoms. In this discussion a distinction is made between the regime of strong and weak exchange coupling and how this affects the obtained spin-excitation spectra. This is followed in Sec. 8.2 by an analysis of trimer clusters, *i.e.*, a structure that contains three impurity adatoms. The focus here is the comparison of two trimer structures that only differ in their arrangements on the surface and how this reflects in the obtained spin-excitation spectra. In Sec. 8.3 clusters of up to six Fe atoms arranged along a straight chain are considered and their spin-excitation spectra are compared. The effect of boundary conditions for such a chain is the topic of Sec. 8.4 where the spin-excitation spectra of a six-atomic Fe chain is compared to the one of a six-atomic Fe ring. A connection to impurity structures of infinite length is sketched by analyzing chain and ring structures consisting of up to twelve Fe atoms. Finally, in Sec. 8.5 the results are summarized and the main conclusions are drawn.

[1] Usually the energy of such a Heisenberg model is a function of the spin vectors $\{\vec{S}_i\}$ instead of being a function of the magnetic moments $\{\vec{m}_i\}$. Due to the proportionality $\vec{m}_i = -\frac{g\mu_B}{\hbar}\vec{S}_i$, however, magnetic moment and spin differ by a (negative) constant, that can be accounted for by a modification of the coupling constant J_{ij} without changing the physics.

8.1. Dimers

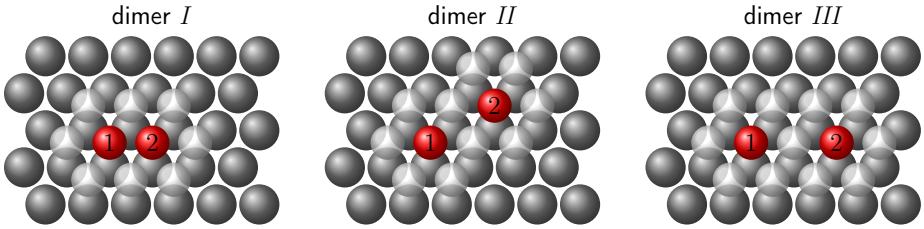

Figure 8.1.: Top view of the three different investigated dimer structures. The gray spheres represent the surface layer of the Cu(111) surface. The two impurity atoms forming the dimer are indicated by red spheres. The white semitransparent spheres represent the vacuum sites that are included in the impurity cluster. Dimer I describes the nearest-neighbor dimer. Within dimer II the atoms are further apart by a factor of $\sqrt{3}$, compared to dimer I. Finally dimer III contains two atoms that are separated by twice the nearest-neighbor distance.

In this Section magnetic excitation spectra for different dimer structures, *i.e.*, different pairs of magnetic atoms, placed on the Cu(111) surface are analyzed. Depending on the atoms that form the dimer and depending on the distance that separates them, their magnetic moments couple ferromagnetically (FM) or antiferromagnetically (AFM), *i.e.*, the ground state is reached when they are aligned in a parallel or an antiparallel fashion, respectively. Such an exchange coupling can be described in terms of a Heisenberg model $\mathcal{H} = -J\vec{m}_1 \cdot \vec{m}_2$, where the coupling constant J enters the Hamiltonian $\mathcal{H}$ and describes the coupling between moments $\vec{m}_1$ and $\vec{m}_2$ of the two dimer atoms. Such a Hamiltonian is used in Appendix G forming a basis to the analysis of a dimer within the Landau-Lifshitz-Gilbert (LLG) model. It shows that the obtained excitation spectra strongly depends on the exchange coupling.

The presented analysis incorporates four different dimers that cover the whole range of possible magnetic couplings, strong and weak FM and AFM coupling. Similar to the discussion of single adatoms on Cu(111), see Ch. 6, a relaxation of the impurity structure by 14 % towards the surface is assumed and the adatoms are positioned in fcc hollow sites. As illustrated in Fig. 8.1 three different impurity clusters are considered, in the following referred to as dimer I, dimer II, and dimer III. The essential difference among the three investigated structures is the distance that separates the two adatoms: For dimer I it is the nearest neighbor distance a_{nn}, for dimer II it is $\sqrt{3}a_{\mathrm{nn}}$, and for dimer III it is $2a_{\mathrm{nn}}$. The analysis incorporates three Fe-Fe dimers of type I, II, and III and a Mn-Mn dimer of type I (in the following referred to as Fe I dimer *etc.*).

In Table 8.1 the total energy difference among a ferromagnetic and an antiferromagnetic alignment of the magnetic moments of the two impurity adatoms, $\Delta E = E^{\mathrm{FM}} - E^{\mathrm{AFM}}$, and the value of the magnetic moments for atom 1 are given, m_1^{total}. Note that $|m_2^{\mathrm{total}}| =$

$|m_1^{\text{total}}|$ in both cases, the ferromagnetic and antiferromagnetic alignment. Under the assumption that the total energy can be approximated by a Heisenberg energy, one can make the ansatz

$$\Delta E = E^{\text{FM}} - E^{\text{AFM}} = -J^{\Delta E}\left(m_1^{\text{total,FM}} m_2^{\text{total,FM}} - m_1^{\text{total,AFM}} m_2^{\text{total,AFM}}\right) , \quad (8.2)$$

where

$$J^{\Delta E} \approx -\frac{\Delta E}{\left(m_1^{\text{total,FM}}\right)^2 + \left(m_1^{\text{total,AFM}}\right)^2} \quad (8.3)$$

was defined. With this approach we find a strong FM coupling for the Fe I dimer and a weak AFM coupling for the other two Fe dimers. Furthermore, the Mn I dimer shows an AFM coupling.

The strength and the sign of the exchange coupling strongly affects the spin-excitation spectrum of a dimer. It can be used to predict the excitation frequencies of the different modes of such a system. It turn out, however, that the method that is used to extract the coupling constant has to be consistent with the dynamical spin-excitation formalism in order to single out the impact of the dynamical effects. The coupling constant extracted

dimer		ΔE (meV)	m_1^{total} (μ_{B})	$m_{d,1}$ (μ_{B})	$J^{\Delta E}\left(\frac{\text{meV}}{\mu_{\text{B}}^2}\right)$	$J\left(\frac{\text{meV}}{\mu_{\text{B}}^2}\right)$
Fe I	(FM)	-415.6	3.13	2.79	21.4	22.3
	(AFM)		3.10	2.73		38.0
Fe II	(FM)	29.1	3.25	2.85	-1.37	0.03
	(AFM)		3.26	2.87		-0.02
Fe III	(FM)	6.1	3.25	2.86	-0.29	-0.14
	(AFM)		3.25	2.86		-0.28
Mn I	(FM)	84.9	4.12	3.76	-2.52	-7.0
	(AFM)		4.09	3.69		-5.4

Table 8.1.: Ground-state properties for the four investigated dimer structures: Self-consistent impurity calculations are used to extract $\Delta E = E^{\text{FM}} - E^{\text{AFM}}$, the difference of the total energy for a FM and an AFM alignment of the magnetic moments, and m_1^{total}, the total magnetic moment of atom 1. The projection of the magnetic moment on the d-orbital for atom 1 is given by $m_{d,1}$. Utilizing Eq. (8.3) provides $J^{\Delta E}$, a first approach to the value of the exchange coupling constant. However, by use of Eq. (8.5) the exchange coupling J is determined consistently with the formalism of calculating the spin-excitation spectra.

from Eq. (8.3) assumes that it is not affected by the rotation angle between the two magnetic moments, which in practice is not always a reasonable assumption. Another method is based on the infinitesimal rotation of the moments [100].

The method used in this thesis is similar to the latter one and represents a mapping of the calculated susceptibilities to those obtained from the LLG model (see Appendix G), evaluated at zero frequency. Applying this adiabatic approach one finds

$$J = -A_{12}^{\mathrm{LLG}}(\omega = 0) = -\left(\left(\chi^{\mathrm{LLG}}(\omega = 0)\right)^{-1}\right)_{12} = +\frac{1}{2}\left(\left(\chi_{\mathrm{KS}}^{+-}(\omega = 0)\right)^{-1}\right)_{12} , \quad (8.4)$$

where 1 and 2 label two magnetic moments for which the coupling constant is determined. For a dimer consisting of two atoms of the same type this results in

$$J = -\frac{1}{2}\frac{\chi_{\mathrm{KS},12}^{+-}}{\left(\chi_{\mathrm{KS},11}^{+-} + \chi_{\mathrm{KS},12}^{+-}\right)\left(\chi_{\mathrm{KS},11}^{+-} - \chi_{\mathrm{KS},12}^{+-}\right)} , \quad (8.5)$$

where all Kohn-Sham susceptibility elements represent the spherical average (*cf.* Eq. (6.1)) and are evaluated at zero frequency and therefore represent real numbers.

The definition of J as proposed in Eq. (8.5) can be related to the expression for the exchange coupling as proposed by Lichtenstein *et al.* [100], where the exchange coupling is derived via infinitesimal rotation of the (normalized) magnetic moments based on the magnetic force theorem. This formula can be written as [101]

$$J_0 = -\frac{1}{2}U_1\chi_{\mathrm{KS},12}^{+-}U_2 = -\frac{1}{2}\frac{\chi_{\mathrm{KS},12}^{+-}}{\left(\chi_{\mathrm{KS},11}^{+-} + \chi_{\mathrm{KS},12}^{+-}\right)^2} , \quad (8.6)$$

where $U_1 = U_2 = \left(\chi_{\mathrm{KS},11}^{+-} + \chi_{\mathrm{KS},12}^{+-}\right)^{-1}$ represent the exchange-correlation kernels for atoms 1 and 2. The expressions for the exchange coupling in Eqs. (8.5) and (8.6) differ in the denominator. A comparison of Eqs. (8.5) and (8.6) reveals

$$\begin{aligned} J &= -\frac{1}{2}\frac{\chi_{\mathrm{KS},12}^{+-}}{\left(\chi_{\mathrm{KS},11}^{+-} + \chi_{\mathrm{KS},12}^{+-}\right)^2}\frac{\chi_{\mathrm{KS},11}^{+-} + \chi_{\mathrm{KS},12}^{+-}}{\chi_{\mathrm{KS},11}^{+-} - \chi_{\mathrm{KS},12}^{+-}} = J_0\frac{1}{1 - 2\frac{\chi_{\mathrm{KS},12}^{+-}}{\chi_{\mathrm{KS},11}^{+-} + \chi_{\mathrm{KS},12}^{+-}}} \\ &= J_0\left(1 + 4U^{-1}J_0\right)^{-1} , \end{aligned} \quad (8.7)$$

where $U = U_1 = U_2$. The form of Eq. (8.7) has been discussed in the literature [102, 103]. Analogue to the connection between χ and χ_{KS} via U, the exchange coupling constant J can be seen as a renormalization of J_0 by U^{-1}, the inverse exchange-correlation kernel. Although originally derived for a FM structure as starting configuration, Eq. (8.6) can also be utilized starting from an AFM structure. There, the exchange-correlation kernel for both atoms reads $U_1 = U_2 = \left(\chi_{\mathrm{KS},11}^{+-} - \chi_{\mathrm{KS},12}^{+-}\right)^{-1}$, and Eq. (8.7) exhibits the more general form $J = J_0\left(1 \pm 4U^{-1}J_0\right)^{-1}$, where $+$ and $-$ account for a FM and an AFM alignment of the two involved magnetic moments, respectively.

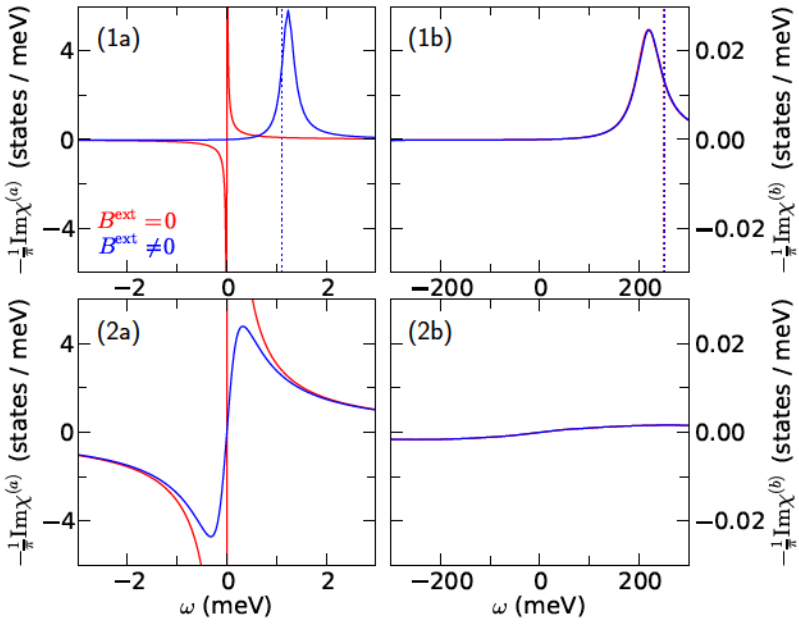

Figure 8.2.: The eigenmodes of the magnetic excitation spectra for the Fe I dimer are shown. The top row presents the two eigenmodes when a FM alignment of the magnetic moments is considered (cases (1a) and (1b)), whereas in the bottom row the two modes for an AFM alignment are explored (cases (2a) and (2b)). All spectra are shown twice, without applied external magnetic field (red curves) and with a field of $B^{\text{ext}} = 0.55\ \text{meV}/\mu_{\text{B}}$ (blue curves). Dotted vertical lines indicate the resonance positions when applying the adiabatic approach, see Eqs. (8.11) and (8.12) for $\gamma = 2$, $\eta = 0$, and J and m_d as given in Table 8.1.

In the following the definition of J via Eq. (8.5) is used. Given that the exchange coupling shows a different order of magnitude depending on the dimer (see Table 8.1), we will separately analyze the regimes of strong (Fe I and Mn I) and weak coupling (Fe II and Fe III). For each dimer the eigenmodes of the spin-excitation spectra are evaluated for both, a FM and an AFM alignment of the moments. Since one configuration represents the ground state while the other is an excited state, this study allows to determine whether the nature of the initial state (ground state or excited state) affects the signature of the spin-excitation spectrum.

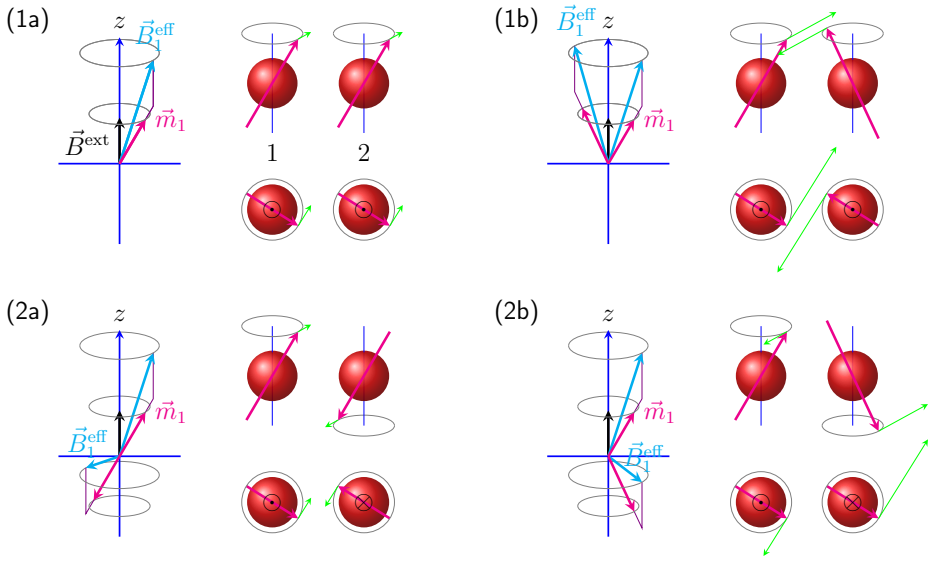

Figure 8.3.: LLG model for a dimer of identical atoms (labeled 1 and 2) with magnetic moments $\vec{m}_1$ and $\vec{m}_2$ (magenta arrows) that couple ferromagnetically ($J > 0$). This figure illustrates four different cases, for which Eq. (8.8) is solved (green arrows) without damping ($\eta_1 = \eta_2 = 0$), and by use of the effective magnetic fields $\vec{B}_1$ and $\vec{B}_2$ (blue arrows) as given by Eqs. (8.9) and (8.10): In case (1a) both magnetic moments are deflected out of their equilibrium direction, *i.e.*, the alignment along the positive z-axis, such that they remain parallel to each other. In case (1b) they are deflected in opposite directions. For cases (2a) and (2b) an antiparallel alignment is assumed with a deflection in the same or opposite directions, respectively. The first three cases represent eigenmodes of the system, two acoustic (cases (1a) and (2a)) and one optical mode (case (1b)). In contrast to this, case (2b) does not represent an eigenmode of the system, since the rotational sense of $\vec{m}_2$ is opposite to the one of $\vec{m}_1$ (see clockwise and anticlockwise precession direction of green arrows).

8.1.1. Strong coupling

In Fig. 8.2 the eigenmodes of the Fe I dimer are shown for a FM and for an AFM spin alignment. The first row (cases (1a) and (1b)) shows a distribution into eigenspectra for the case of a FM alignment of the magnetic moments, while the second row (cases (2a) and (2b)) represents the same for an AFM alignment. In all four cases two curves are shown, one without (red curves) and one with external magnetic field (blue curves) of strength $B^{\text{ext}} = 0.55\ \text{meV}/\mu_\text{B}$, in order to match the SOC-induced gap for single Fe adatoms on Cu(111) [20]. Here and in the following the applied field is always of the

same strength which allows a comparison among the different cases. Note that the use of an auxiliary applied magnetic field is in line with the procedure that has been utilized already in Ch. 6. However, it is important to point out that for the AFM alignment the interpretation of the applied magnetic field being an auxiliary field that mimics a SOC induced gap in the excitation spectrum does not hold anymore. Since it couples in form of a Zeeman term to the magnetic moments, it stabilizes one moment (the one that is oriented in the same direction) while it destabilizes the other, leading to a broken symmetry between the two moments. In contrast to this, a SOC induced gap stabilizes both moments at the same time to be aligned along the direction of lowest energy cost, the easy axis, and no break in the symmetry occurs. An analysis of resonances in antiferromagnets that incorporates anisotropy effects has been proposed by Keffer and Kittel [104, 105].

Our goal is to analyze in detail the properties of the spin-excitations and detect their signatures as functions of the initial state, the ground state (FM alignment for the Fe I dimer, cases (1a) and (1b)) and an excited state (AFM alignment, cases (2a) and (2b)). In the following we discuss the obtained spectra for all four cases that are shown in Fig. 8.2 and connect the interpretation to four different modes described in terms of the LLG model for dimer, see Appendix G. In the LLG model, the time derivative of $\vec{m}_i$, the magnetic moment of atom $i \in \{1, 2\}$ reads

$$\frac{\mathrm{d}\vec{m}_i}{\mathrm{d}t} = -\gamma_i \vec{m}_i \times \vec{B}_i^{\mathrm{eff}} + \eta_i \frac{\vec{m}_i}{m_i} \times \frac{\mathrm{d}\vec{m}_i}{\mathrm{d}t} \,, \tag{8.8}$$

where γ_i is the gyromagnetic ratio for atom i and η_i is a site-dependent phenomenological damping factor. The effective magnetic fields acting on moments $\vec{m}_1$ and $\vec{m}_2$ take the form

$$\vec{B}_1^{\mathrm{eff}} = J\vec{m}_2 + \vec{B}^{\mathrm{ext}} \tag{8.9}$$

$$\text{and} \quad \vec{B}_2^{\mathrm{eff}} = J\vec{m}_1 + \vec{B}^{\mathrm{ext}} \,. \tag{8.10}$$

In Fig. 8.3 four cases with four different starting configurations of the two magnetic moments are distinguished:

(1) The dominant z components of the magnetic moments of atom 1 and 2 point along the positive z component.

   (a) The x and y components of both magnetic moments are the same.

   (b) The x and y components of the magnetic moments are opposite to each other.

(2) The z components of the magnetic moments of atom 1 and 2 are opposite to each other, pointing along the positive and negative z axis.

   (a) The x and y components of the magnetic moments are opposite to each other.

   (b) The x and y components of both magnetic moments are the same.

For each of the four cases Eq. (8.8) is solved for a FM coupling ($J > 0$) and using always the same external magnetic field $\vec{B}^{\mathrm{ext}}$ pointing along the positive z axis. The resulting

time-derivative expression is indicated by a green arrow. Note that within these figures the damping term is neglected for simplicity ($\eta = 0$). Each of these figure subplots carries information in form of a visualization of the vectors of magnetic moments and magnetic fields. In addition the precession of the magnetic moments is visualized from the side and from the top. In the latter, the dominant component of the magnetic moment along the z axis can be positive or negative, which is indicated by a $\odot$ (positive) or a $\otimes$ (negative). It should be stressed that direction and strength of $\frac{\mathrm{d}\vec{m}_i}{\mathrm{d}t}$ (green arrows in Fig. 8.3) are globally defined (by solving Eq. (8.8) without the damping term) which allows to compare the resulting vectors throughout the entire figure. For example, the same length for two different green arrows (take for example moment 1 for cases (1a) and (2a)) means that the precession frequency for the corresponding excited atoms is the same, which then is also true for the resulting resonance frequency at which the resonance appears in the excitation spectrum. In Table 8.2 the four eigenmodes (see Fig. 8.2) are characterized in terms of the frequency at which the curves reach their maxima and the lifetimes related to Γ, the full-width at half maximum (FWHM).

Let us turn to the first eigenmode, case (1a): In Fig. 8.2(1a) eigenmode (a) for a ferromagnetic alignment of the magnetic moments is shown, where two curves describe the excitation spectrum for no applied magnetic field (red curve) and an applied field of the strength $B^{\mathrm{ext}} = 0.55\ \mathrm{meV}/\mu_{\mathrm{B}}$ (blue curve). The red curve exhibits a resonance at zero frequency corresponding to an infinite response of the system to an external perturbation. Therefore, this mode represents the Goldstone mode. In the presence of an external field (blue curve) the rotational symmetry of the magnetic moments is broken and the resonance shifts to a positive value for the frequency (see Table 8.2) with a finite lifetime. This observation is analogue to the discussion of a single Fe adatom on the Cu(111) surface, see Ch. 6. The reason is that this eigenmode represents the acoustic mode of the system where both atoms respond to the external perturbation synchronously. The strong coupling also affects the excitation energy that is slightly enlarged compared to

dimer		g^{eff}	$\omega^{(a)}$ (meV)	$\tau^{(a)}$ (fs)	$\omega^{(b)}$ (meV)	$\tau^{(b)}$ (fs)
Fe I	(FM)	2.25	1.23	1330.	219.	5.44
	(AFM)	–	0.33	299.	255.	0.72
Mn I	(FM)	2.19	1.20	1640.	−79.8	28.4
	(AFM)	–	0.48	329.	45.0	1.74

Table 8.2.: Spin-excitation spectra for Fe I and Mn I dimers: For each system the effective g value, $g^{\mathrm{eff}} = \omega^{(a)}/B^{\mathrm{ext}}$, is given. The two eigenmodes are characterized by their maxima, $\omega^{(a)}$ and $\omega^{(b)}$, as well as the corresponding lifetimes, $\tau^{(a)}$ and $\tau^{(b)}$. The lifetimes are given by $\tau = \hbar/(2\ \Gamma)$, where Γ is the full-width at half maximum. All values are obtained when applying a magnetic field $B^{\mathrm{ext}} = 0.55\ \mathrm{meV}/\mu_{\mathrm{B}}$.

the single Fe adatom, where an effective g value of $g^{\text{eff}} = 1.95$ was found (*cf.* Table 6.2). Utilizing the LLG model this mode is described in Fig. 8.3(1a), where the two magnetic moments are aligned parallel to each other along the positive z axis. If no field was applied ($B^{\text{ext}} = 0$) all magnetic moments and effective fields would be parallel and no torque would be observed. In the presence of a field, however, the moments experience a torque that leads to a uniform precession in phase with a small but finite frequency. Due to the fact that the moments are parallel to each other at any time, this excitation is lowest in energy and one finds (see Appendix G)

$$\omega_{\text{LLG}}^{(\text{a})} = \frac{\gamma}{\sqrt{1+\eta^2}} B_z^{\text{ext}} \,, \tag{8.11}$$

in accordance with the resonance shift shown in Fig. 8.2(1a).

For the second eigenmode, case (1b), a different behavior is observed: In Fig. 8.2(1b) the two curves for no applied (red curve) and finite applied field (blue curve) are shown. Note that the absence of an applied field still leads to a resonance at finite frequency and width. When a field is applied the resonance position shifts to a higher frequency value in a similar manner as in case (1a), where their maximum positions differ by about $0.6\ \text{meV}$. Due to the large range for which the frequency dependence is shown these two curves appear on top of each other. This behavior can be understood utilizing the LLG model, represented by Fig. 8.3(1b). Case (1b) represents the optical mode of the system, *i.e.*, the two moments precess with a phase shift of π (leading to the factor $\mathrm{e}^{\mathrm{i}\pi} = -1$) around the z-axis. Within the LLG model one finds the frequency of the optical resonance at

$$\omega_{\text{LLG}}^{(\text{b})} = \frac{\gamma}{\sqrt{1+\eta^2}} \left(B_z^{\text{ext}} + 2Jm_d \right) \,. \tag{8.12}$$

Inserting the exchange coupling J and the magnetic moment m_d from Table 8.1 one finds a resonance at $\omega_{\text{LLG}}^{(\text{b})} = 250\ \text{meV}$, where no damping was assumed ($\eta = 0$). This value is larger than the one obtained from the obtained spectra (see Fig. 8.2 and Table 8.2) and to make these values match a relatively strong damping of $\eta = 0.5$ would become necessary. This shows the strong impact of dynamical effects on the effective magnetic interactions. Once more this demonstrates that electron-hole excitations can strongly renormalize the interactions predicted from the adiabatic approach.

The first eigenmode of the AFM alignment of the magnetic moments, case (2a), is similar to case (1a): In Fig. 8.2(2a) red and blue curves respectively correspond to the first eigenmode without and with applied magnetic field. The red curve shows a resonance at zero frequency, where the moments exhibit an infinite response. Applying a field along the z-axis breaks this symmetry and shifts the resonance position to a finite frequency value. This is a similar behavior as in case (1a), albeit the resonance here is much broader. Note that besides the resonance at positive frequency ($\omega = 0.33\ \text{meV}$) one obtains a resonance at negative frequency ($\omega = -0.33\ \text{meV}$). This is because the applied field acts on the AFM aligned moments in an opposite manner: While the moment pointing along the z-axis gets stabilized, the moment pointing opposite to it gets destabilized. For

the interpretation the LLG model in form of Fig. 8.3(2a) is used. It shows the acoustic mode for the case of having the magnetic moments aligned opposite to each other. For no applied external field magnetic moments and effective magnetic fields are aligned within the same axis, so that no torque is found. As soon as a finite field is applied the effective magnetic fields get tilted away from this axis and a finite torque is observed, in accordance with the observed spectra in Fig. 8.2(2a). Note that an effective g value cannot be given since the resonance position of this frequency is not expected to shift linearly with the applied field, see Appendix G.

Finally, the second eigenmode of the AFM alignment is discussed, case (2b): In Fig. 8.2(2a) the mode is strongly damped for both, the red curve (no applied field) and the blue curve (applied field). Again this observation can be understood by analyzing the LLG model (see Appendix G). In Fig. 8.3(2b) a phase shift between atom 1 and atom 2 leads to a state which is no eigenstate to the system. The rotational sense of the two atoms are in opposite direction, clockwise and anti-clockwise. In addition the strength of the velocity is different for both atoms. Thus, their relative angle will change with time which is in contradiction to the assumption of energy conservation (no driving force in form of an external transverse time-dependent magnetic field).

After the discussion of the intrinsic spin-excitation modes of the Fe I dimer, we turn to the Mn I dimer. In this nearest-neighbor configuration, the two Mn atoms show an AFM coupling, *i.e.*, the parallel alignment of the magnetic moments is higher in energy than the antiparallel alignment, see Table 8.1. In Fig. 8.4 the eigenmodes of the magnetic excitation spectra are shown, distributed in four cases. These cases represent the two eigenmodes for a parallel (labeled (1a) and (1b)) and an antiparallel (labeled (2a) and (2b)) alignment of the two magnetic moments, where now the latter alignment represents the ground state of the system. The presentation of the four eigenmodes is analogue to the eigenmode distribution for the Fe I dimer, see Fig. 8.2. Again, the interpretation of the four cases is accompanied by considering four cases in terms of the LLG model, see Fig. 8.5. The only difference to the dimer modes as shown in Fig. 8.3 is that here, an AFM coupling between the two atoms is assumed ($J < 0$), which affects the direction of the effective magnetic fields for both atoms.

Again, we start with the discussion of case (1a), shown in Fig. 8.4(1a), for which the magnetic moments are aligned parallel to each other. The red curve shows a resonance at zero frequency and for an applied field of $B^{\mathrm{ext}} = 0.55\ \mathrm{meV}/\mu_{\mathrm{B}}$, the resonance shifts to a positive value. Analogue to the analysis of eigenmode (1a) of the Fe I dimer, this mode obeys the Goldstone theorem and represents the acoustic mode of the system. In Fig. 8.5 the effective magnetic fields (given by Eqs. (8.9) and (8.10)) are aligned antiparallel to the magnetic moments as long as no external field is applied ($B^{\mathrm{ext}} = 0$). Only when $B^{\mathrm{ext}} > 0$ their vector product does not vanish and a torque on the magnetic moments is found (indicated by the green arrows in Fig. 8.5, see also Eq. (8.8)). This mode represents the acoustic mode, *i.e.*, the two moments remain always parallel to each other. Note that this state does not relax to the ground state which would be an AFM alignment of spins. Instead, both moments show a synchronized damped precession towards the orientation

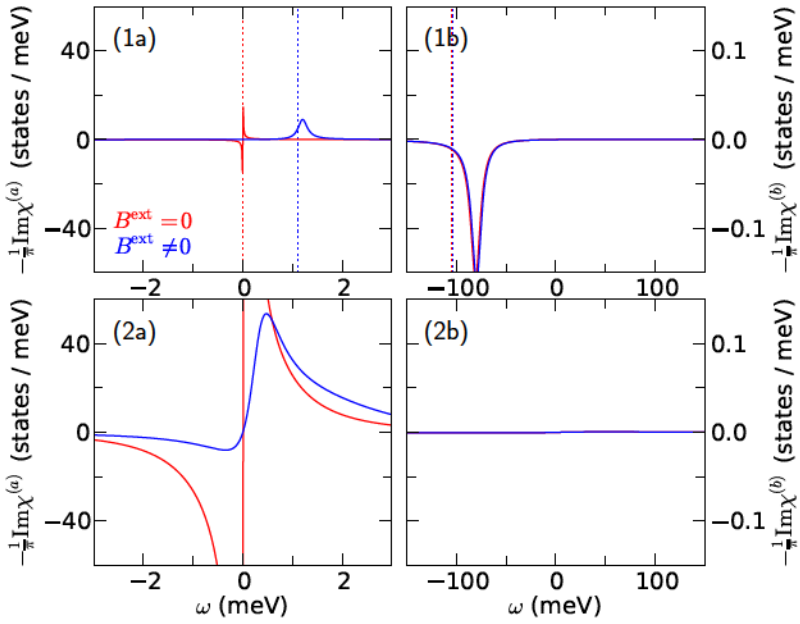

Figure 8.4.: The eigenmodes of the magnetic excitation spectra for the Mn I dimer are shown. Cases (1a) and (1b) represent first and second eigenmode of the system for a FM alignment of the magnetic moments. The AFM alignment results in the two eigenmodes as shown in cases (2a) and (2b). Each mode is shown for zero (red curves) and finite (blue curves) applied magnetic field. Eigenmode (1b) shows a negative resonance frequency due to the AFM coupling of the two atoms. The dotted vertical lines indicate the resonance positions obtained from the adiabatic approach, see caption of Fig. 8.2. Also note the different scaling on the axes compared to Fig. 8.2.

of the external magnetic field, *i.e.*, the z-axis, which represents a metastable state of the system.

In Fig. 8.4(1b) the second eigenmode of the system for a parallel alignment of the magnetic moments is shown, without and with applied magnetic field (red and blue curves, respectively). In contrast to the Fe I dimer, this eigenmode shows a negative resonance frequency, even when no magnetic field is applied ($B^{\text{ext}} = 0$). This is in accordance with the expected resonance frequency when the LLG model is utilized, see Eq. (8.12), where $\gamma = 2$ and $\eta = 0$ are assumed and J and m_d are as given in Table 8.1. In Fig. 8.5(1b) the precession of the two moments are depicted. A comparison to the analogue solution for positive J (see Fig. 8.3(1b)) reveals that the precession direction (indicated by the direction of the green arrows) is opposite, *i.e.*, the system exhibits a resonance for a

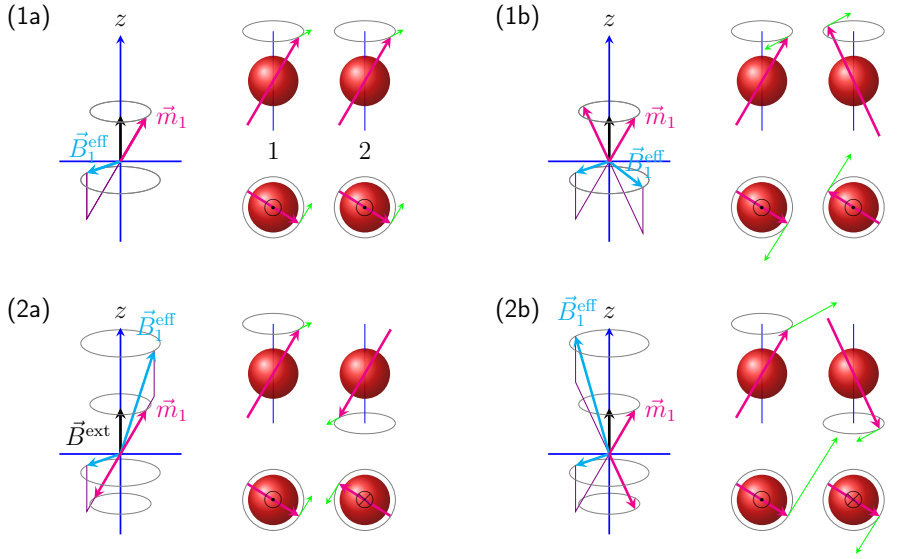

Figure 8.5.: For a dimer of identical atoms with an antiferromagnetic coupling ($J < 0$) this figure illustrates four different cases which are in accordance to the four cases shown in Fig. 8.3. The effective magnetic fields $\vec{B}_1^{\text{eff}}$ and $\vec{B}_2^{\text{eff}}$ are given via Eqs. (8.9) and (8.10). One distinguishes $m_{2,z} = m_{1,z}$ (case (1)) and $m_{2,z} = -m_{1,z}$ (case (2)), as well as a collinear alignment of the magnetic moment (cases (a)) and the same configuration with a phase shift of π (cases (b)). Whereas all cases (a) represent acoustic modes, only the case (1b) is an optical mode of the system. The rotational sense in case (2b) is opposite (see clockwise and anticlockwise orientation of green arrows, which indicate the time-derivatives of the magnetic moments) and therefore no eigenstate of the system.

negative frequency which is in line with the eigenspectrum as shown in Fig. 8.4(1b).

The lower row in Fig. 8.4 shows the two eigenmodes for the Mn I dimer when the moments are aligned antiparallel to each other, representing the ground state of the system. In case (2a) the mode exhibits a resonance at zero frequency when no field is applied. Therefore this mode can be identified with the acoustic mode as shown in Fig. 8.5(2a).

Finally the case (2b) represents the optical mode of the AFM aligned dimer. Similar to the corresponding mode for the Fe I dimer (see Fig. 8.2(2b)) there is no observable resonance, *i.e.*, the mode is strongly damped. Also here, this can be understood by use of the LLG model, see Fig. 8.5(2b): The two magnetic moments precess in opposite directions and therefore they do not represent an eigenmode of the system.

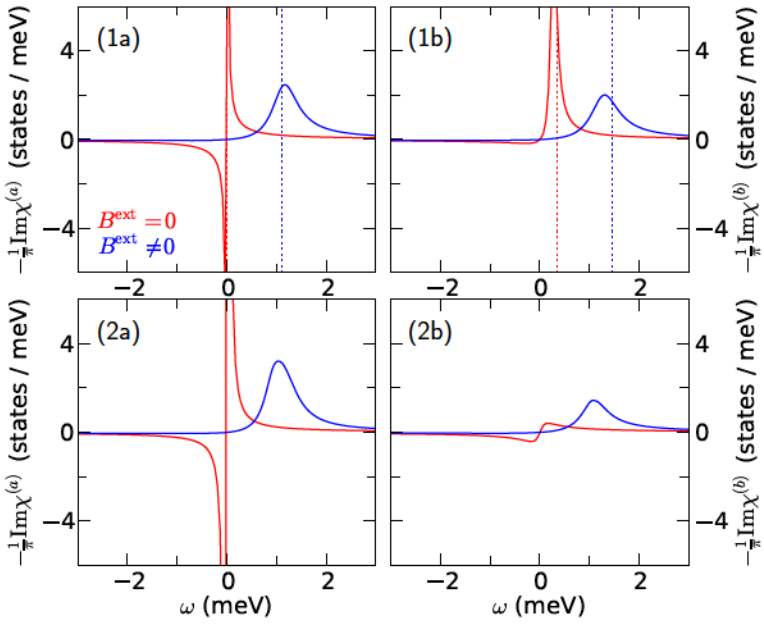

Figure 8.6.: The eigenmodes of the magnetic excitation spectra are shown for the Fe *II* dimer. The separation into four cases is in accordance to Fig. 8.2. Note that the second mode in case (1b) shows a resonance only slightly above the resonance in case (1a) and that the spectra for a FM and an AFM alignment of the magnetic moments are quite similar (compare top row to bottom row). Dotted vertical lines indicate the resonance positions as obtained via the adiabatic approach, see caption of Fig. 8.2.

8.1.2. Weak coupling

Next, we discuss spin-excitation spectra for Fe *II* and Fe *III* dimers, *i.e.*, dimers where the Fe adatoms are further apart from each other, compared to the nearest-neighbor arrangement (see Fig. 8.1 for a comparison). Naturally, the increased distance results in a weaker coupling of the two magnetic moments. As a direct consequence, possible optical resonances are in the order of magnitude as the applied magnetic field along the z-axis, *i.e.*, in the range of a few meV's. Thus, the resonance shift due to a small applied field should be visible for both eigenmodes, the acoustic as well as the optical mode.

In Fig. 8.6 the eigenmodes of the intrinsic magnetic excitation spectra for the Fe *II* dimer are presented. As it was done in the previous section, a distinction is made between the FM alignment (cases (1a) and (1b)) and the AFM alignment (cases (2a) and (2b)) of the magnetic moments. Compared to the Fe *I* dimer the coupling constant J is very small

(see Table 8.1). In fact, the J of an AFM alignment is different in sign compared to the value for a FM alignment. As a direct consequence, the resonance in the optical mode of a FM alignment of the moments (case (1b)) is found just slightly above the one of the acoustic mode (case (1a)). Experimentally a distinction of these two modes is difficult. When applying an external magnetic field (blue curves) one sees that the shift of the two resonances show the same shift in frequency. For this setup one can clearly see that the acoustic and the optical resonances shift in the same way with the external applied field.

For the AFM alignment (see Figs. 8.6(2a) and 8.6(2b)) an interesting observation can be made: In contrast to the previously discussed dimers, the optical mode (2b) shows an enhanced response that is in the same order of magnitude as the resonance of the acoustic eigenmode (2a). This can be attributed to two characteristics of this dimer: First, the exchange coupling J is very small, the smallest of all investigated dimers. Thus, the coupling between the two adatoms on the surface is negligible and their excitation spectra should not deviate much from the one for a single magnetic adatom. In fact, the g values and lifetimes of a single Fe atom on the Cu(111) surface have been calculated in Ch. 6 and read $g^{\text{eff}} = 1.95$ and $\tau = 590$ fs (see Table 6.2), which is in satisfying agreement to the values of g^{eff} and $\tau^{(\alpha)}$ presented in Table 8.3. Second, the system exhibits a significant damping of the spin-excitation. Usually a strong damping indicates that the lifetime of the excitation is reduced due to a decay into Stoner excitations in the substrate. For eigenmode (2b), however, an increased damping of the system leads to the opposite behavior, *i.e.*, the mode gets enhanced. This is supported by an analysis using the LLG model for different damping strengths, see Fig. G.2.

As last example within this Section we turn to the Fe III dimer where the two Fe atoms are separated by twice the nearest-neighbor distance. In Fig. 8.7 the eigenmodes of the intrinsic magnetic excitation spectra are shown. Values that characterize the different eigenmodes are given in Table 8.3. In the same manner as performed for the previous

dimer		g^{eff}	$\omega^{(a)}$ (meV)	$\tau^{(a)}$ (fs)	$\omega^{(b)}$ (meV)	$\tau^{(b)}$ (fs)
Fe II	(FM)	2.13	1.17	533.	1.30	486.
	(AFM)	–	1.04	492.	1.08	489.
Fe III	(FM)	2.08	1.14	522.	−0.18	4190.
	(AFM)	–	0.67	308.	2.16	53.7

Table 8.3.: Spin-excitation spectra for Fe II and Fe III dimers: For each system the effective g value, $g^{\text{eff}} = \omega^{(a)}/B^{\text{ext}}$, is given. The two eigenmodes are characterized by their maxima, $\omega^{(a)}$ and $\omega^{(b)}$, as well as the corresponding lifetimes, $\tau^{(a)}$ and $\tau^{(b)}$. The lifetimes are given by $\tau = \hbar/(2\ \Gamma)$, where Γ is the full-width at half maximum. All values are obtained when applying a magnetic field $B^{\text{ext}} = 0.55\ \text{meV}/\mu_{\text{B}}$.

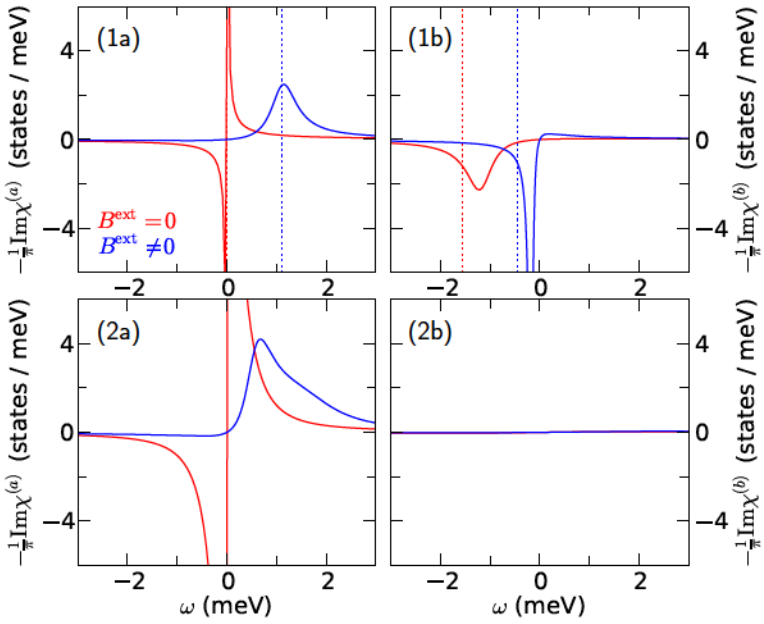

Figure 8.7.: The eigenmodes of the intrinsic magnetic excitation spectra for the Fe *III* dimer are shown. The upper row represents the two eigenmodes for a parallel alignment of the magnetic moments (cases (1a) and (1b)), whereas the lower row shows the two eigenmodes for an antiparallel alignment. Each mode is plotted twice, once without applied magnetic field (red curves) and once with with a field of strength $B^{\text{ext}} = 0.55\ \text{meV}/\mu_{\text{B}}$ (blue curves). Note that the coupling is slightly antiferromagnetic ($J < 0$) and that the applied field nearly compensates this coupling, see blue curve in case (1b). Dotted vertical lines indicate the resonance positions as obtained via the adiabatic approach, see caption of Fig. 8.2.

three dimers, we distinguish four cases: The cases (1a) and (1b) represent the two modes for the dimer with magnetic moments that are aligned parallel to each other, whereas the cases (2a) and (2b) represent the two modes for an antiparallel alignment. Similar to the Fe *II* dimer, acoustic and optical mode for cases (1a) and (1b) are found in the same energy window. Due to the fact that J is slightly negative (see Table 8.1) the optical eigenmode in case (1b) shows a negative resonance frequency. However, the applied field is almost large enough to shift the resonance to zero frequency and even further to a positive frequency value. In the framework of the LLG model, this corresponds to a modification of the scenario as shown in Fig. 8.5(1b): Increasing the applied external field in Fig. 8.5(1b) leads to a tilting of the effective magnetic fields until at some point B_i^{eff} is parallel to $\vec{m}_i$

for $i \in \{1, 2\}$. Then, the torque on the magnetic moments vanishes and no precession is observed (corresponding to a resonance frequency at zero). A further increase of the external magnetic field results in a precession rotation in the opposite direction compared to Fig. 8.5(1b), *i.e.*, the resonance is found for a positive frequency.

8.2. Trimers

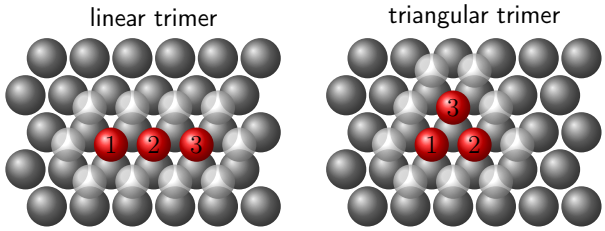

Figure 8.8.: The two different trimer structures are shown from a top view. The gray spheres represent the topmost layer of the Cu(111) surface. The red spheres represent the three impurity atoms that are aligned along a chain (left) or that form a triangle (right). The additional vacuum sites that surround the impurity cluster are indicated by semitransparent white spheres.

In this Section we analyze magnetic excitation spectra for trimers, *i.e.*, clusters that consist of three magnetic atoms. Whereas in the dimer structures (see Sec. 8.1) two eigenmodes of the system could be distinguished, one finds three eigenmodes for the trimer structure, an acoustic mode and two optical modes. A main focus is set on the comparison of two different arrangements of the three atoms, which are sketched in Fig. 8.8. In one case the atoms are positioned along a straight line (a chain) with nearest-neighbor distance among adjacent atoms. Thus, the atom in the middle shows a nearest-neighbor coupling to two neighbors, whereas the two atoms at the edge of the impurity structure exhibit only one nearest neighbor to couple to (*cf.* Fig. 8.8, left). In the other case the atoms are placed in a equilateral triangle, so that for each atom there exist two nearest-neighbor atoms (*cf.* Fig. 8.8, right). Therefore, the latter case has a higher symmetry, which is reflected in the excitation spectrum as it will become apparent later in this Section.

In the presented analysis the investigated trimer structures are built out of Fe adatoms only. Following the analysis performed for the Fe dimers (see Sec. 8.1) the nearest-neighbor Fe atoms show a strong FM coupling ($J > 0$, see Fe I dimer in Table 8.1) that allows to concentrate on a parallel alignment of the magnetic moments only, which is the appropriate ground state.

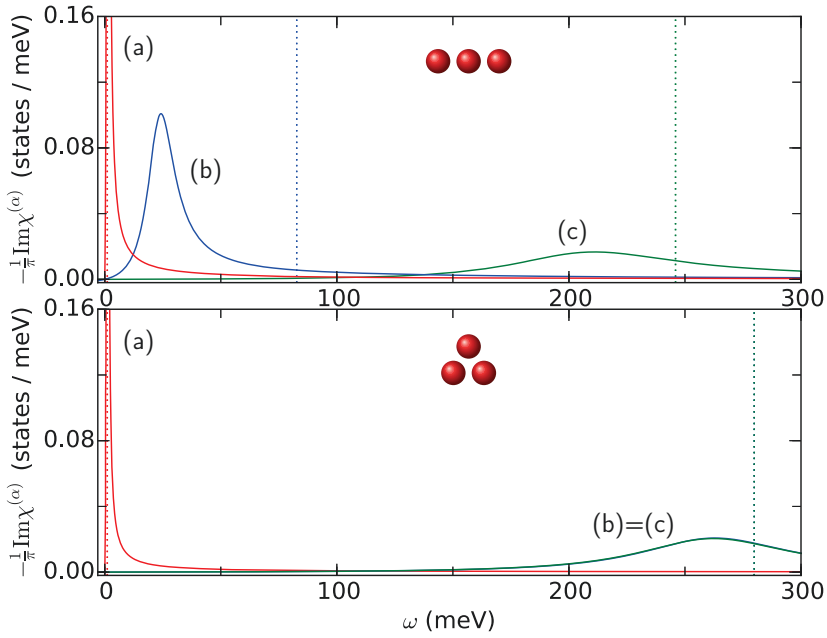

Figure 8.9.: Top figure: The three eigenmodes of the intrinsic excitation spectrum for the linear Fe trimer are shown. They show resonances at three different frequencies. Bottom figure: The eigenmodes for the triangular Fe trimer are shown. Two eigenmodes are degenerate. Dotted vertical lines indicate the resonance positions obtained by use of the adiabatic approach, using Eqs. (8.13), (8.14) and (8.15) for the linear trimer, and Eqs. (8.16) and (8.17) for the triangular trimer, where $\gamma = 2$, $\eta = 0$, $B^{\mathrm{ext}} = 0.55\ \mathrm{meV}/\mu_{\mathrm{B}}$, and parameters as given in Table 8.4.

8.2.1. Linear *vs.* triangular Fe trimer

In Fig. 8.9 the eigenmodes of the excitation spectra for Fe trimers are shown for a linear (top panel) and a triangular (bottom panel) arrangement. In both cases an external magnetic field of $B^{\mathrm{ext}} = 0.55\ \mathrm{meV}/\mu_{\mathrm{B}}$ along the z direction was applied, such that each resonance shifts by about $1.1\ \mathrm{meV}$ higher in frequency compared to the expected value without field. For each trimer Table 8.4 lists ground-state and spectral properties. Analogue to the analysis of dimers in Sec. 8.1, the obtained resonance positions in the calculated spectra for the two trimers are understandable in terms of the LLG model (see Eq. (8.8) and the trimer discussion in Appendix G), for which the resulting eigenmodes are visualized in Figs. 8.10 and 8.11. Under the assumption that no g shift and no damping is present ($\gamma = 2$, $\eta = 0$) the resonance frequencies as predicted by the adiabatic approach

are shown in Fig. 8.9 as vertical dotted lines, where the values for J and $\overline{m}_d$ are extracted from Table 8.4.

For the intrinsic excitation spectrum of the linear Fe trimer three different curves (red, blue, green) are shown. They represent the three eigenmodes of the system, each showing a resonance at different frequencies. The eigenmode with the resonance lowest in frequency is labeled (a) and is the acoustic mode. If no applied field was present this resonance would appear at zero frequency and thus obey the Goldstone theorem. In the LLG model (see Fig. 8.10(a)) this corresponds to three magnetic moments that precess in phase and show only a small precession speed (indicated by green arrows) that is linear in the applied field,

$$\omega^{(\mathrm{a})}_{\mathrm{LLG,lin}} = \frac{\gamma}{\sqrt{1+\eta^2}} B_z^{\mathrm{ext}} \,. \tag{8.13}$$

It is zero when no external field is applied ($B_z^{\mathrm{ext}} = 0$), which is in line with the fact that then, the magnetic moments and the effective magnetic fields are aligned parallel to each other and their vector product vanishes.

The second eigenmode (b) in the top panel of Fig. 8.9 shows a resonance at higher frequency and describes the optical mode of the system that is lowest in energy. The

Fe trimer	$m_{d,1}$ $m_{d,2}$ $m_{d,3}$ $\}$ (μ_{B})	J_{12} J_{23} J_{13} $\}$ $\left(\frac{\mathrm{meV}}{\mu_{\mathrm{B}}^2}\right)$	g^{eff}	$\omega^{(a)}$ $\omega^{(b)}$ $\omega^{(c)}$ $\}$ (meV)	$\tau^{(a)}$ $\tau^{(b)}$ $\tau^{(c)}$ $\}$ (fs)
	2.76	14.9	2.30	1.27	753.
linear	2.72	14.9		24.2	22.7
	2.76	−4.82		211.	3.60
	2.74	17.0	1.97	1.08	1810.
triangular	2.74	16.9		263.	4.22
	2.75	16.9		263.	4.13

Table 8.4.: Ground state and spectral properties of the linear and the triangular Fe trimer: For the three Fe adatoms (labeled 1, 2, and 3) the spin magnetic moments $m_{d,i}$, $i \in \{1,2,3\}$, the coupling constants J_{12}, J_{23}, and J_{13}, that are connected to the calculated Kohn-Sam susceptibility at zero frequency via Eq. (8.4), the effective g value, $g^{\mathrm{eff}} = \omega^{(a)}/B^{\mathrm{ext}}$, as well as the resonance frequencies $\omega^{(\alpha)}$ and corresponding lifetimes $\tau^{(\alpha)} = \hbar/(2\,\Gamma^{(\alpha)})$ for the eigenmodes $(\alpha) \in \{(a),(b),(c)\}$ are listed. $B^{\mathrm{ext}} = 0.55\ \mathrm{meV}/\mu_{\mathrm{B}}$ is the applied magnetic field, where $\Gamma^{(\alpha)}$ denotes the full-width at half-maximum. Note that J_{13} describes the nearest-neighbor coupling for the triangular trimer while for the linear trimer the distance between atoms 1 and 3 is twice as large.

resonance appears much broader and exhibits a shorter lifetime (see Table 8.4). In terms of the LLG model this mode describes three magnetic moments of which the outer ones precess with a phase shift of π while the inner atom shows no movement at all (see Fig. 8.10(b)). This has an interesting consequence: The onsite excitation spectrum for the inner atom should not contain a response to the eigenmode (b). Indeed this is the case, as will be shown in the subsequent Sec. 8.3. As discussed in Appendix G, the resonance position of mode (b) is given by

$$\omega_{\mathrm{LLG,lin}}^{(\mathrm{b})} = \frac{\gamma}{\sqrt{1+\eta^2}} \left(B_z^{\mathrm{ext}} + J\overline{m}_d \right) \ , \tag{8.14}$$

where J is the nearest-neighbor exchange coupling and $\overline{m}_d = \frac{1}{3}\left(m_{d,1} + m_{d,2} + m_{d,3}\right)$ is the averaged magnetic moment.

Eigenmode (c) represents the optical mode of the system that is highest in energy and exhibits the shortest lifetime. Utilizing the LLG model one finds the resonance position at

$$\omega_{\mathrm{LLG,lin}}^{(\mathrm{c})} = \frac{\gamma}{\sqrt{1+\eta^2}} \left(B_z^{\mathrm{ext}} + 3J\overline{m}_d \right) \ . \tag{8.15}$$

In this eigenmode the outer magnetic moments exhibit an in-phase precession while the inner atom rotates with a phase shift of π and twice the amplitude compared to the other two moments (see Fig. 8.10(c)).

Next, we proceed to the discussion of the Fe trimer in a triangular arrangement. It was stated earlier that such a structure exhibits a higher symmetry compared to the linear trimer, which is reflected in the position of the resonance frequencies at which the three eigenmodes of the intrinsic excitation spectra reach their maxima. The eigenmode with label (a) (red curve in Fig. 8.9, lower panel) represents the acoustic mode of the system and obeys the Goldstone theorem, *i.e.*, its frequency is located at zero when $B^{\mathrm{ext}} = 0$ (analogue to eigenmode (a) of the linear trimer). This mode is visualized in Fig. 8.11(a), where all magnetic moments precess in phase. The corresponding resonance frequency reads

$$\omega_{\mathrm{LLG,tri}}^{(\mathrm{a})} = \frac{\gamma}{\sqrt{1+\eta^2}} B_z^{\mathrm{ext}} \ . \tag{8.16}$$

which is identical to Eq. (8.13), the resonance frequency for the acoustic eigenmode of the linear Fe trimer. In Table 8.4 one realizes a small difference between the resonance positions of the acoustic modes for both trimer structures (reflected in two different effective g values, $g_{\mathrm{lin}}^{\mathrm{eff}} = 2.3$ and $g_{\mathrm{tri}}^{\mathrm{eff}} = 2.0$). A possible explanation for this is that the precession of a magnetic moment is affected by both, the external magnetic field along the z-direction as well as the coupling to adjacent precessing magnetic moments. The stronger the coupling among the atoms of the cluster, the more the cluster's excited eigenstate can be stabilized against external fields, such that for the triangular trimer arrangement a longer lifetime at a lower resonance frequency can be achieved, when compared to the linear trimer.

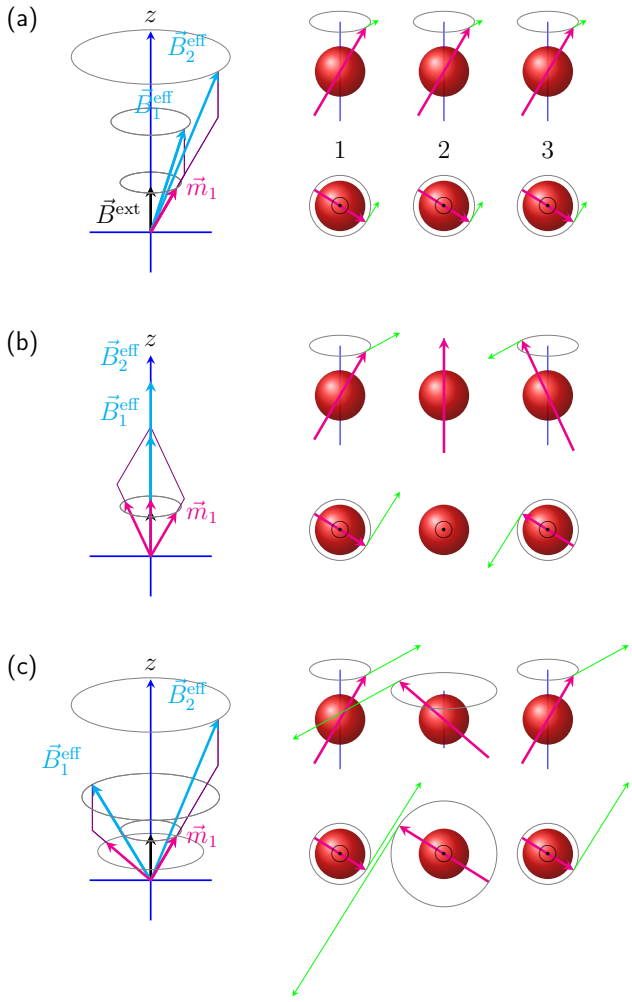

Figure 8.10.: The three different eigenmodes for a linear trimer of identical atoms with a ferromagnetic nearest-neighbor coupling $J > 0$ are shown. The external magnetic field $\vec{B}^{\text{ext}}$ points along the z axis and the effective magnetic fields are given by $\vec{B}_1^{\text{eff}} = \vec{B}_3^{\text{eff}} = J\vec{m}_2 + \vec{B}^{\text{ext}}$ and $\vec{B}_2^{\text{eff}} = J\left(\vec{m}_1 + \vec{m}_3\right) + \vec{B}^{\text{ext}}$ (*cf.* Eqs. (G.47) and (G.48)). Lowest in energy is the acoustic mode (a) in which all atoms point in the same direction and show a precession around the z axis. The first optical mode (b) shows a phase shift of π between the two edge atoms, while the center atom remains still. The second optical mode (c) shows edge atoms that rotate in phase, while now the center atom experiences a phase shift of π and twice the amplitude. The increase of energy manifests in a higher rotation frequency, see green arrows.

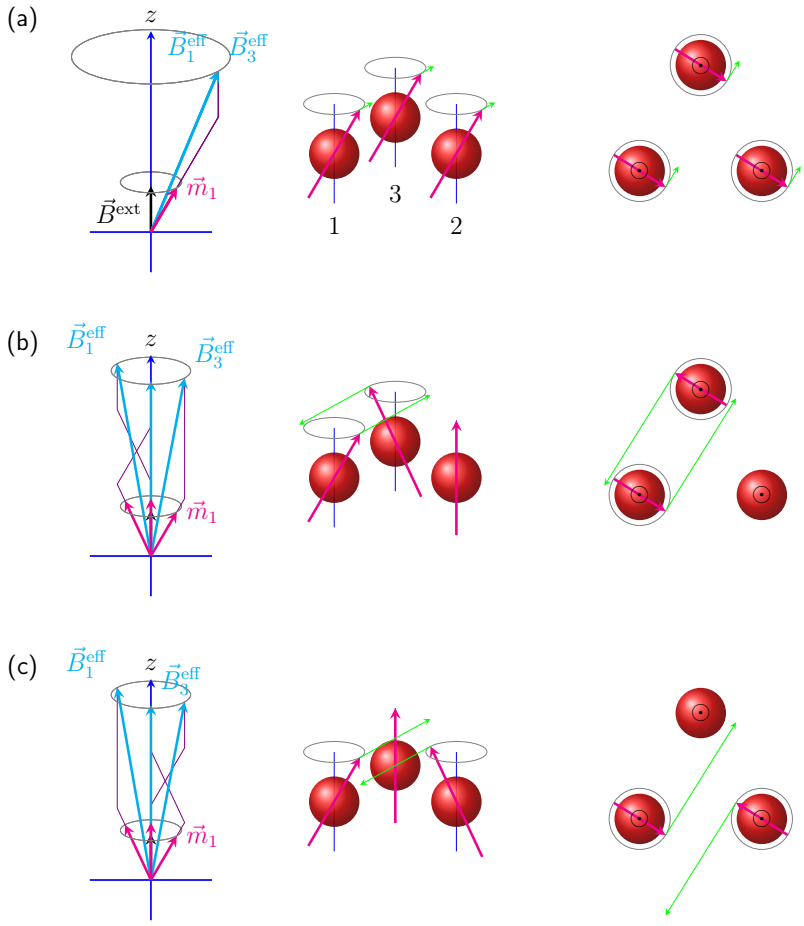

Figure 8.11.: For a triangular trimer of identical atoms with a ferromagnetic nearest-neighbor coupling $J > 0$ two eigenmodes are degenerate. The external magnetic field $\vec{B}^{\text{ext}}$ points along the z axis and the effective magnetic fields are given by $\vec{B}_1^{\text{eff}} = J\,(\vec{m}_2 + \vec{m}_3) + \vec{B}^{\text{ext}}$, $\vec{B}_2^{\text{eff}} = J\,(\vec{m}_1 + \vec{m}_3) + \vec{B}^{\text{ext}}$, and $\vec{B}_3^{\text{eff}} = J\,(\vec{m}_1 + \vec{m}_2) + \vec{B}^{\text{ext}}$ (*cf.* Eqs. (G.52), (G.53), and (G.54)). Lowest in energy is the acoustic mode (a) in which all atoms point in the same direction and show a precession around the z axis. The two optical modes (b) and (c) are degenerate in energy. Two atoms rotate with a relative phase shift of π while the third atom remains still. The increase of energy manifests in a higher rotation frequency, see green arrows.

The second and the third eigenmode of the triangular Fe trimer (labeled (b) and (c), blue and green curves in Fig. 8.9, lower panel) are degenerate. One arrives at the same result when solving the LLG model for this structure (see Appendix G). The corresponding resonance frequency reads

$$\omega^{(\mathrm{b})}_{\mathrm{LLG,tri}} = \omega^{(\mathrm{c})}_{\mathrm{LLG,tri}} = \frac{\gamma}{\sqrt{1+\eta^2}} \left(B_z^{\mathrm{ext}} + 3J\overline{m}_d \right) \ , \tag{8.17}$$

which is the same expression as given by Eq. (8.15). In Figs. 8.11(b) and 8.11(c) the eigenmodes are visualized. In both cases, one atom remains without motion while the other two perform a precession with a phase shift of π. Due to the symmetry of the setup their corresponding precession frequencies are identical. This is a crucial difference to the linear Fe trimer and stresses the importance of the structural arrangement of the regarded impurity structure on the surface.

A closing remark on mode (b) of the linear Fe trimer: In the top panel of Fig. 8.9, one realizes that the resonance position using the LLG model (blue dotted vertical line, see also Eq. (8.14)) overestimates the resonance position obtained from the calculated spectrum of eigenstates by a factor of about 3. The reason is that within the LLG model (*cf.* Appendix G) only the exchange-coupling constant J describing the nearest-neighbor interaction is included and J_{nnn}, the coupling between the outer two atoms, is thus neglected. It turns out, however, that, by use of Eq. (8.4), the exchange coupling between the two outer atoms is of the same order of magnitude compared to J and reads $J_{\mathrm{nnn}} = -4.82\ \mathrm{meV}/\mu_{\mathrm{B}}^2 \approx -\frac{1}{3}\,J$ (see J_{13} for the linear Fe chain in Table 8.4). Applying the formalism as given in Appendix G) on a trimer chain where the next-nearest-neighbor coupling J_{nnn} is taken into account produces exactly the same eigenstates and resonance frequencies as under the assumption $J_{\mathrm{nnn}} = 0$, except for $\omega^{(\mathrm{b})}_{\mathrm{LLG,lin}}$ which gets modified to

$$\tilde{\omega}^{(\mathrm{b})}_{\mathrm{LLG,lin}} = \frac{\gamma}{\sqrt{1+\eta^2}} \left(B_z^{\mathrm{ext}} + (J + J_{\mathrm{nnn}})\, \overline{m}_d \right) \ . \tag{8.18}$$

Compared to $\omega^{(\mathrm{b})}_{\mathrm{LLG,lin}} = 82.7\ \mathrm{meV}$, the new value $\tilde{\omega}^{(\mathrm{b})}_{\mathrm{LLG,lin}} = 32.7\ \mathrm{meV}$ shows a significant better agreement with the calculated spectral resonance position ($\omega^{(b)} = 24.2\ \mathrm{meV}$, see Table 8.4). Finally, one can also understand why such an improvement is found only for eigenmode (b), while the energy for modes (a) and (c) remain unchanged. Recalling the precession of the two outer magnetic moments for these three eigenmodes (*cf.* Fig. 8.10(a)-(c)) reveals that for eigenmodes (a) and (c) they precess in phase and remain always parallel, meaning that a coupling via J_{nnn} does not affect the corresponding excitation energies. In contrast to this, these two moments rotate in eigenmode (b) with a phase shift of π and due to the fact that in the discussed structure they prefer a AFM next-nearest neighbor coupling ($J_{\mathrm{nnn}} < 0$) the resonance frequency for that eigenmode shifts to a lower value.

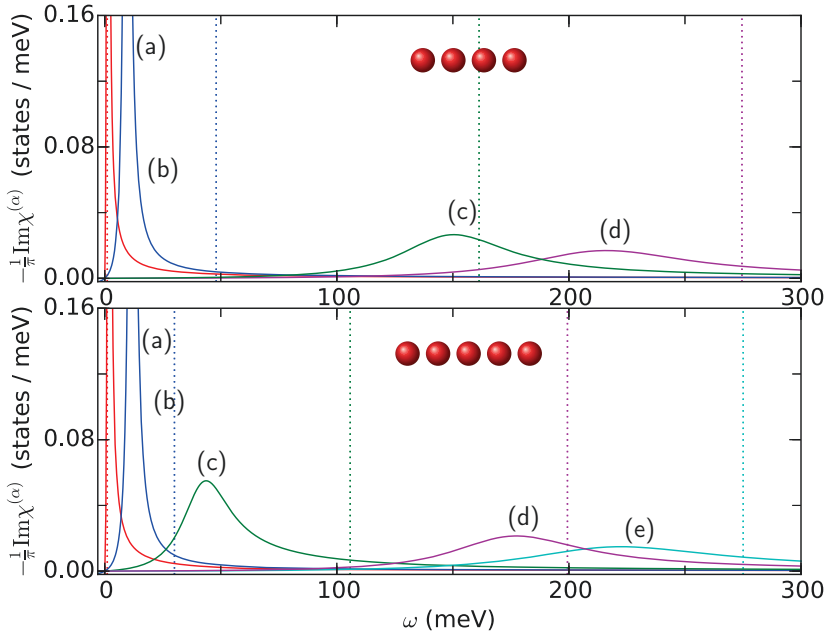

Figure 8.12.: The eigenmodes of the intrinsic excitation spectra for a linear chain of four (upper panel) and five (lower panel) Fe adatoms are shown. Dotted vertical lines indicate the resonance positions as given by the adiabatic approach, using Eqs. (8.19) and (8.20).

8.3. Building the Fe chain – atom by atom

In this Section we compare the intrinsic magnetic excitation spectra for linear Fe chains of different lengths. As it was already found in the discussion of dimers and trimers (see Secs. 8.1 and 8.2) the number of atoms in the impurity cluster is of great importance for the resulting spectrum. In Fig. 8.12 the eigenmodes of the intrinsic excitation spectra for two different chains are shown. For upper panel a chain consisting of four Fe atoms is considered. Each of the four presented eigenmodes shows a resonance. The position of the resonance is compared to the resonance frequency that is expected when solving the LLG model (see Appendix G), where one finds

$$\omega_{\mathrm{LLG}}^{(\alpha)} = \begin{cases} \frac{\gamma}{\sqrt{1+\eta^2}} B_z^{\mathrm{ext}} & , \quad (\alpha) = (a) \\ \frac{\gamma}{\sqrt{1+\eta^2}} \left(B_z^{\mathrm{ext}} + \left(2-\sqrt{2}\right) \overline{J}\overline{m}_d \right) & , \quad (\alpha) = (b) \\ \frac{\gamma}{\sqrt{1+\eta^2}} \left(B_z^{\mathrm{ext}} + 2\overline{J}\overline{m}_d \right) & , \quad (\alpha) = (c) \\ \frac{\gamma}{\sqrt{1+\eta^2}} \left(B_z^{\mathrm{ext}} + \left(2+\sqrt{2}\right) \overline{J}\overline{m}_d \right) & , \quad (\alpha) = (d) \end{cases} . \tag{8.19}$$

Furthermore, the average over magnetic moments within the chain ($\overline{m}_d = 2.76\ \mu_\mathrm{B}$) and the average over nearest-neighbor exchange couplings within the chain ($\overline{J} = 11.0\ \mathrm{meV}/\mu_\mathrm{B}^2$) are used. As already discussed for the trimer (see end of Sec. 8.2) a better agreement between calculated resonance and expected resonance when using the LLG model could be achieved when interactions beyond nearest neighbors were taken into account (this assumption is supported by the fact that also in the chain next-nearest neighbors couple antiferromagnetically).

In the lower panel of Fig. 8.12 eigenmodes of the excitation spectra for a linear chain with five Fe atoms is analyzed. Also here the eigenmodes are degenerate and five resonances at different resonance frequencies are found. The expected resonance positions when using the LLG model (see Appendix G) read

$$\omega_\mathrm{LLG}^{(\alpha)} = \begin{cases} \frac{\gamma}{\sqrt{1+\eta^2}} B_z^\mathrm{ext} & , \quad (\alpha) = (a) \\ \frac{\gamma}{\sqrt{1+\eta^2}} \left(B_z^\mathrm{ext} + \frac{1}{2}\left(3-\sqrt{5}\right)\overline{J}\overline{m}_d \right) & , \quad (\alpha) = (b) \\ \frac{\gamma}{\sqrt{1+\eta^2}} \left(B_z^\mathrm{ext} + \frac{1}{2}\left(5-\sqrt{5}\right)\overline{J}\overline{m}_d \right) & , \quad (\alpha) = (c) \\ \frac{\gamma}{\sqrt{1+\eta^2}} \left(B_z^\mathrm{ext} + \frac{1}{2}\left(3+\sqrt{5}\right)\overline{J}\overline{m}_d \right) & , \quad (\alpha) = (d) \\ \frac{\gamma}{\sqrt{1+\eta^2}} \left(B_z^\mathrm{ext} + \frac{1}{2}\left(5+\sqrt{5}\right)\overline{J}\overline{m}_d \right) & , \quad (\alpha) = (e) \end{cases} , \tag{8.20}$$

where here $\overline{m}_d = 2.72\ \mu_\mathrm{B}$ and $\overline{J} = 11.9\ \mathrm{meV}/\mu_\mathrm{B}^2$ are used. Note that the more atoms are included in the chain, the less fluctuation in these parameters is observed.

Up to this point of the Chapter only eigenmodes of the regarded systems are discussed. In Fig. 8.13 we show the onsite excitation spectra for linear Fe chains of different lengths. In the topmost figure the dimer spectrum (corresponding to the Fe I dimer in Sec. 8.1 for the FM alignment of spins) for the first atom is shown. The spectrum of the second atom is identical due to symmetry. Both eigenmodes from Fig. 8.2 contribute. For the second onsite spectrum the spectra of atoms 1 and 3 are the same while the spectrum for atom 2 is different. Especially remarkable is that the latter spectrum has no contribution from the first optical mode, which is in agreement with the expectation from the LLG model (see Fig. 8.10(b)). ISTS measurements should therefore show a different excitation spectrum, depending on whether the STM tip is placed above an edge atom or above the center atom. Increasing the number of atoms within the chain shows how the obtained spectra contain more and more excitation resonances, *i.e.*, the possible excitations of the impurity cluster increase and the resonance density grows. In the next Section we compare chain and ring structures of six and more Fe atoms and discuss how the excitation spectra evolve in the limit of $N \to \infty$, where N denotes the Fe atoms within a chain of infinite length.

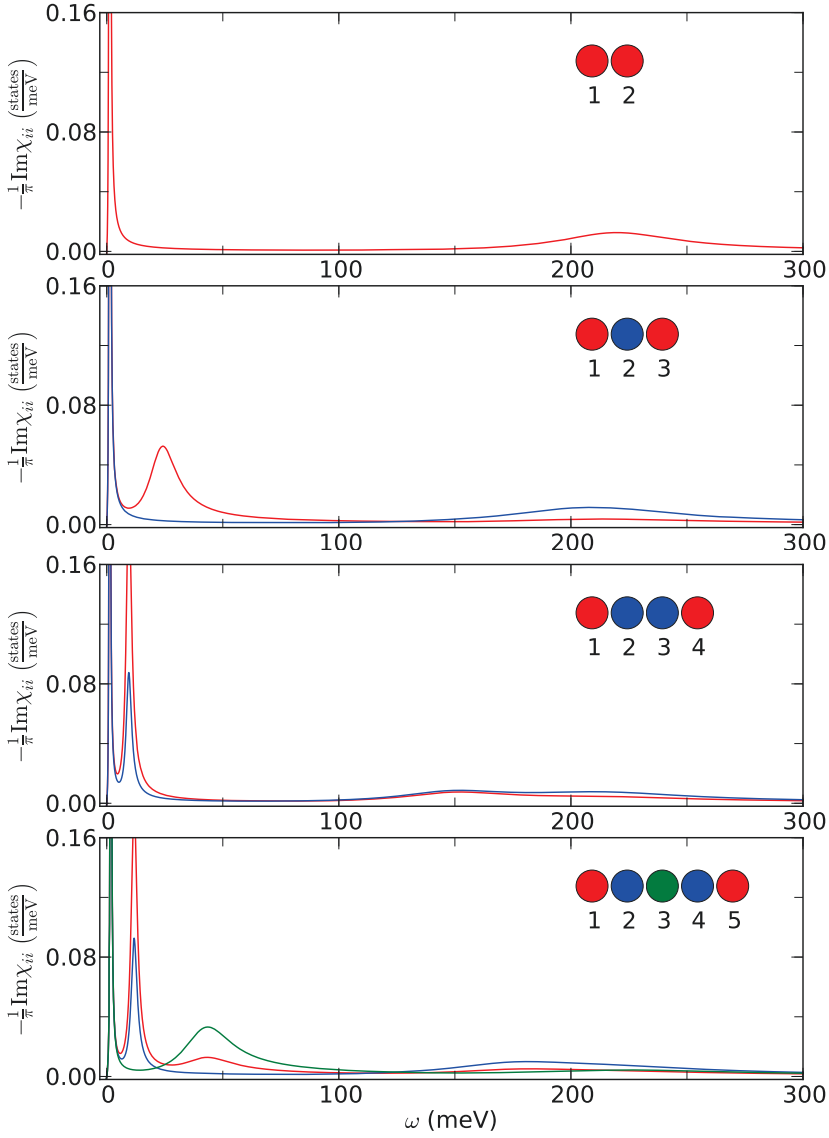

Figure 8.13.: Onsite intrinsic magnetic excitation spectra for linear Fe chains of different lengths. Due to a mirror plane in the middle of the chain, atoms at opposite positions within the chain exhibit the same excitation spectrum, indicated by the same color in the insets.

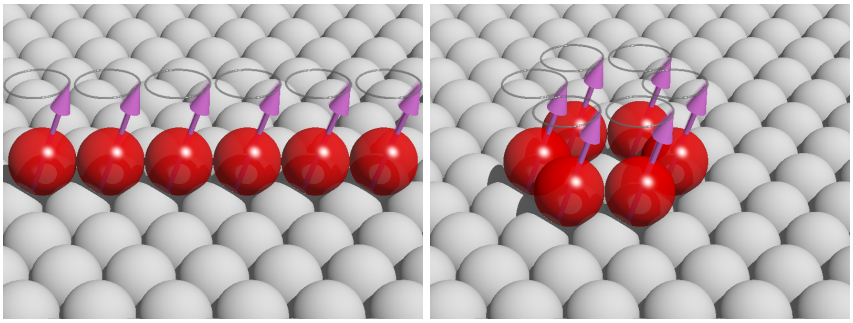

Figure 8.14.: This figure illustrates two different arrangements of six magnetic impurity atoms (red spheres) placed on the Cu(111) surface (gray spheres): a linear chain (left panel) and a ring structure (right panel). For the chain the two atoms at the edge have only one nearest neighbor while the four inner atoms have two. For the ring all six atoms have two nearest neighbors reflecting the higher symmetry of the system. For both arrangements the acoustic mode is depicted, *i.e.*, all moments precess in phase and remain parallel to each other at any time.

8.4. Chain *vs.* ring clusters – importance of boundary condition

As it was shown earlier in this Chapter, the magnetic excitation spectrum can show substantial differences for two impurity clusters that only differ in the topological arrangement of the magnetic impurity atoms. For a dimer consisting of two Fe atoms (see Sec. 8.1), a variation of the interatomic distance modifies the exchange coupling and therefore the position of the optical resonance frequency. Furthermore, it was shown in Sec. 8.2 that the excitation spectrum for a trimer of Fe atoms exhibits two degenerate optical modes when the atoms are arranged within a regular triangle, while for the same atoms aligned along a straight line two nondegenerate optical modes are found.

In this Section the aspect of degeneracy within the trimer spectra is picked up again and the analysis is extended to clusters with a higher number of atoms. For a hexamer, *i.e.*, a cluster that contains six magnetic impurity atoms, Fig. 8.14 shows two arrangements, a linear chain and a ring. The difference between a chain and a ring lies in the boundary conditions for the atoms (a ring can be seen as a bended chain with closed ends). In a ring all atoms have two nearest neighbors, whereas the chain has edge atoms with only one nearest neighbor.

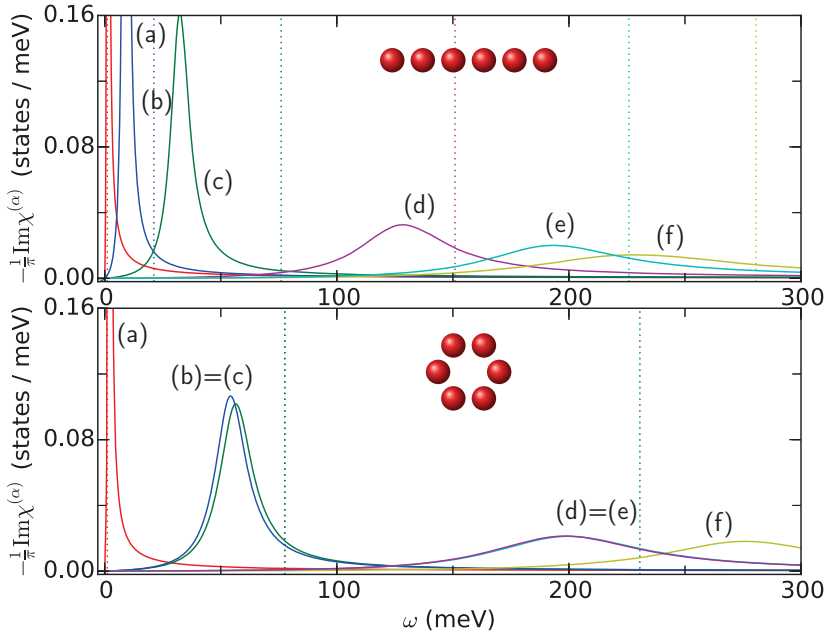

Figure 8.15.: Eigenmodes of the magnetic excitation spectra for an Fe hexamer, aligned along a straight line (upper panel) or arranged as ring (lower panel) on the Cu(111) surface, see Fig. 8.14 for a visualization. The resonance frequencies obtained from the adiabatic approach are indicated by dotted vertical lines. Although their agreement to the calculated resonance positions is limited, the LLG model predicts for the ring two pairwise degenerate eigenstate resonances, in agreement to the calculated spectra.

8.4.1. Fe chains *vs.* Fe rings

In Fig. 8.15 two Fe hexamers on the Cu(111) surface are considered and the eigenmodes of the corresponding magnetic excitation spectra are shown. The first hexamer is a chain (upper panel) and the second hexamer is a ring (lower panel), see Fig. 8.14 for a visualization on how the structures are arranged on the surface. In addition, Fig. 8.15 shows the expected resonance frequencies when applying the LLG model (see Appendix G) which are indicated by dotted vertical lines. For the hexamer chain the resonances are

given by

$$\omega_{\mathrm{LLG}}^{(\alpha)} = \begin{cases} \frac{\gamma}{\sqrt{1+\eta^2}} B_z^{\mathrm{ext}} & , \quad (\alpha) = (a) \\ \frac{\gamma}{\sqrt{1+\eta^2}} \left(B_z^{\mathrm{ext}} + \left(2-\sqrt{3}\right) \overline{J}\overline{m}_d \right) & , \quad (\alpha) = (b) \\ \frac{\gamma}{\sqrt{1+\eta^2}} \left(B_z^{\mathrm{ext}} + \overline{J}\overline{m}_d \right) & , \quad (\alpha) = (c) \\ \frac{\gamma}{\sqrt{1+\eta^2}} \left(B_z^{\mathrm{ext}} + 2\overline{J}\overline{m}_d \right) & , \quad (\alpha) = (d) \\ \frac{\gamma}{\sqrt{1+\eta^2}} \left(B_z^{\mathrm{ext}} + 3\overline{J}\overline{m}_d \right) & , \quad (\alpha) = (e) \\ \frac{\gamma}{\sqrt{1+\eta^2}} \left(B_z^{\mathrm{ext}} + \left(2+\sqrt{3}\right) \overline{J}\overline{m}_d \right) & , \quad (\alpha) = (f) \end{cases} , \tag{8.21}$$

while the hexamer ring shows two pairs of degenerate resonances frequencies for the eigenmodes,

$$\omega_{\mathrm{LLG}}^{(\alpha)} = \begin{cases} \frac{\gamma}{\sqrt{1+\eta^2}} B_z^{\mathrm{ext}} & , \quad (\alpha) = (a) \\ \frac{\gamma}{\sqrt{1+\eta^2}} \left(B_z^{\mathrm{ext}} + \overline{J}\overline{m}_d \right) & , \quad (\alpha) = (b) = (c) \\ \frac{\gamma}{\sqrt{1+\eta^2}} \left(B_z^{\mathrm{ext}} + 3\overline{J}\overline{m}_d \right) & , \quad (\alpha) = (d) = (e) \\ \frac{\gamma}{\sqrt{1+\eta^2}} \left(B_z^{\mathrm{ext}} + 4\overline{J}\overline{m}_d \right) & , \quad (\alpha) = (f) \end{cases} . \tag{8.22}$$

In order to apply these formulas, one calculates the average over all nearest-neighbor exchange coupling constants, where the value $\overline{J} = 13.6 \ \mathrm{meV}/\mu_{\mathrm{B}}^2$ was found for both, the hexamer chain and the hexamer ring, and the average over all magnetic moments, $\overline{m}_d = 2.75 \ \mu_{\mathrm{B}}$ for the chain and $\overline{m}_d = 2.82 \ \mu_{\mathrm{B}}$ for the ring. As it was already observed for the trimers (see Sec. 8.2), the structure with higher symmetry (the ring) shows degenerate eigenmodes (modes (b) and (c), as well as modes (d) and (e)), while the other system (the chain) shows resonances frequencies that are pairwise different.

The larger the number N of atoms that form a chain or a ring the less significant should be their difference in the magnetic excitation spectra, since the boundary condition becomes less important. The discussion of the LLG model in Appendix G closes with the generalization to N atoms and one finds the eigenmodes of such a structure are eigenvalues to a tridiagonal matrix which describes the susceptibility for a nearest-neighbor coupling. The corresponding eigenmodes show resonance frequencies at

$$\omega_{\mathrm{LLG}}^{(\alpha)} = \frac{\gamma}{\sqrt{1+\eta^2}} \left(B_z^{\mathrm{ext}} + 2 \left(1 - \cos \frac{k}{N+1} \pi \right) \overline{J}\overline{m}_d \right) , \tag{8.23}$$

where the different eigenvalues are labeled with $(\alpha) \in \{(a), (b), \dots\}$ and

$$k = k(\alpha) = \begin{cases} 1 & , \ (\alpha) = (a) \\ 2 & , \ (\alpha) = (b) \\ \dots \end{cases} . \tag{8.24}$$

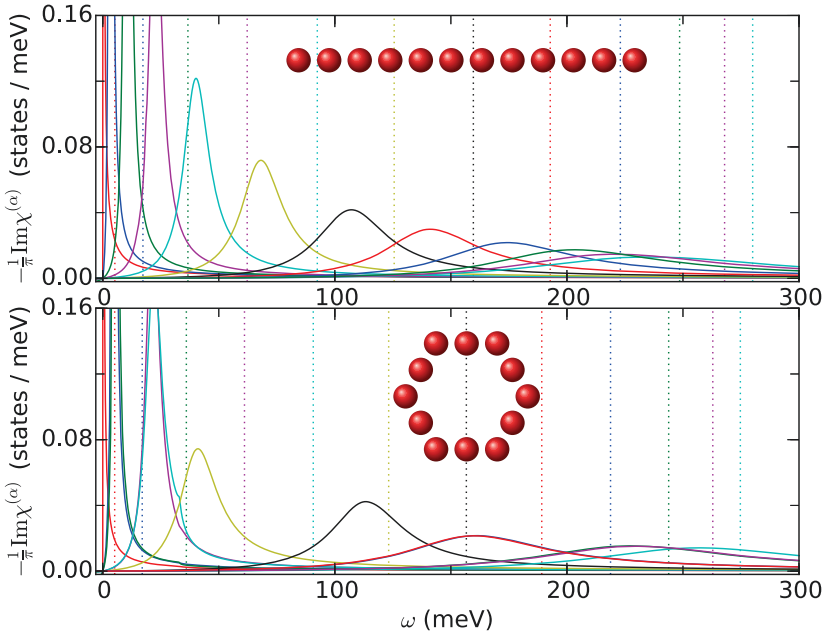

Figure 8.16.: Comparison of eigenmodes of the intrinsic magnetic excitation spectra for clusters of twelve Fe atoms on the Cu(111) surface, arranged along a linear chain (top figure) and arranged as ring (bottom figure). For the chain, twelve eigenmodes at difference resonance frequencies are found, while for the ring several modes are pairwise degenerate. For both systems dotted vertical lines indicate the expected resonance positions of each mode when applying the adiabatic approach, see Eq. (8.23).

In Fig. 8.16 the eigenmodes of the spin-excitation spectra for two twelve-atomic Fe clusters, a linear chain and a ring structure, are shown. As expected from the previous analysis, the latter structure exhibits eigenmodes that are degenerate, while for the linear chain the eigenmodes show resonances at different frequency values. Indicated by dotted vertical lines the resonance frequencies as given by Eq. (8.23) are shown for $N = 12$. In both plots, the same value for the averaged nearest-neighbor exchange coupling, $\overline{J} = 11.3\ \mathrm{meV}/\mu_\mathrm{B}^2$, and the averaged magnetic moment, $\overline{m}_d = 2.79\ \mu_\mathrm{B}$, are used. In fact, for both systems one observes a clear tendency to find an accumulation of resonances at the edges of the shown spectra and therefore reproduce a cosine-like distribution in the limes $N \to \infty$.

8.5. Summary

In this Chapter we studied magnetic excitation spectra for different transition metal clusters that are placed on the Cu(111) surface. It was shown that depending on the type of considered adatom, the number of involved atoms within the cluster, as well as the distance among the atoms the resulting spectra can be very different. By investigating and comparing impurity structures that differ only in the way a given set of adatoms is arranged on the surface we studied the impact of geometrical topology on their spin-excitations. First of all, for two or more magnetically coupled atoms different modes of the system can be excited, leading to resonances at different frequencies in the excitation spectrum. In general one finds that the lifetime of such a resonance (connected to the width of the resonance) decreases with increasing resonance frequency.

We used the Landau-Lifshitz-Gilbert (LLG) model for two or more precessing moments (see Appendix G) to analyze our results obtained from first principles. A good agreement was found in terms of the resonance positions of the different modes. For the dimer with an antiparallel alignment of the moments one finds an acoustic resonance while the optical mode does not show a resonance, in accordance to the predictions of the LLG model. For trimer it was found that an even better agreement can be achieved when including exchange interactions that go beyond the nearest neighbor interaction.

The final part of this Chapter was dedicated to the comparison of magnetic excitation spectra for linear Fe chains or Fe rings with the same number of adatoms. We observed characteristic differences in the excitation energies of the eigenmodes which is directly related to the different boundary conditions of the two structures. While for the chains the resonance positions of the eigenmodes are pairwise different, the ring structures showed degenerate eigenstates, which reflects the higher symmetry of the latter arrangement.

The summary concludes with a remark on the presented results within this Chapter: Much insight into the nature of spin-excitations in nanostructures that consist out of more than one atom could already be gained by means of the transverse dynamical magnetic susceptibility χ^{+-}. However, a future goal is the expansion of the analysis to the signature of the spin-excitation in the vacuum electronic structure above the adatom, as it was presented in Chs. 6 and 7.

9. Summary and outlook

The central aim of this thesis was the exploration of magnetic excitations in $3d$ transition-metal (TM) nanostructures deposited on metallic surfaces using a first-principles approach. Since experimentally, inelastic scanning tunneling spectroscopy (ISTS) has emerged to be the method of choice to study spin dynamics in such localized environments [18, 20], a crucial demand on the developed approach was to access the impact of the spin-excitation on the density of states in the vacuum above the magnetic impurity structure, *i.e.*, the region that is usually probed by a scanning tunneling microscope (STM) tip. Due to the strong hybridization of electronic states of the impurity structure with the itinerant electrons of the substrate, the interaction of such excitations with the electronic structure becomes important. Expanding a recently established method [37, 38], that accesses the intrinsic magnetic excitation spectra from first-principles, the developments presented within this thesis account for these interactions by means of the electron self-energy, Σ. This quantity results from combining the concept of many-body perturbation theory (MBPT), which allows to systematically study inelastic scattering processes in terms of Feynman diagrams, with time-dependent density functional theory (TDDFT) in the linear response regime. With the self-energy one gains access to the electronic structure in the vacuum above the impurity structure, being renormalized by the magnetic excitation. The resulting density of states can be related to the measured ISTS spectra by means of the Tersoff-Hamann approximation [39]. In order to accomplish a realistic comparison to measured ISTS spectra, the approach is based on the Korringa-Kohn-Rostoker (KKR) Green function method, since it provides an accurate real-space description of the regarded impurity structure in form of an embedding scheme.

With the developed method at hand a number of different systems were investigated and properties that characterize the magnetic excitations were analyzed and compared among each other and to existing experiments. Single $3d$ TM adatoms and clusters of two or more $3d$ TM adatoms on the Cu(111) surface were explored as well as single $3d$ TM adatoms on the Pt(111) surface. For the latter substrate the impact of hydrogenization on the spin dynamics of the impurity structure was studied. In the following the main results of these analyses are summarized.

In a first application, we illustrated the capabilities of the new method by investigating several $3d$ TM adatoms (Cr, Mn, Fe, and Co) placed on the Cu(111) surface with a focus on Fe adatoms. We were able to attribute differences in characterizing properties of the magnetic excitation (such as the excitation lifetime or the g shift) to differences in their respective electronic structure. We showed that the new method allows to identify

the spin-character of the excitation signatures above and below the Fermi energy. Most importantly, the calculated spin-excitation spectra showed a rich variety in the shapes of the signatures. In contrast to Heisenberg models which predict a symmetric conductance spectrum with excitation signatures in step-like forms, our first-principles methods predicts asymmetric spectra with signatures that are of step-like or peak-like shapes or reversed steps, depending on the regarded adatom. Even the extinction of the spin-excitation signature was observed. Furthermore, some renormalized electronic structures revealed nontrivial additional bound states (satellites), which in the case of Fe adatoms on Cu(111) were used to explain asymmetries in experimentally obtained ISTS spectra [20]. We stress that such satellites could be misinterpreted as being the signature of the spin excitation in measured ISTS spectra. Finally, we explored the signal of the spin-excitation in the vacuum as function of distance to the magnetic adatom and conclude that besides the intensity also the shape of the excitation signature shows a dependency on the position where the signal is measured.

As a second application, the spin dynamics of different $3d$ TM adatoms (Cr, Mn, Fe, and Co) deposited on the Pt(111) surface were investigated. Similar to the Cu(111) surface, these systems showed differences in the characteristic properties of the magnetic excitations, such as their lifetimes and g shifts, and a rich variety in the shapes of spin-excitation signatures in the renormalized electronic structure at the adatom and in the vacuum region above it. For Fe and Co adatoms we additionally analyzed the impact of hydrogenization of the surface structure (Fe and Co adatoms). With this analysis we verified the experimentally observed fact that spin-excitation spectra can be affected by the presence of hydrogen atoms in the vicinity of the impurity of interest [40].

Besides magnetic excitation spectra of single adatoms, the developed method is also capable of treating nanostructures that consist of two or more magnetic atoms (dimers, trimers, *etc.*). In a third application, we analyzed intrinsic magnetic excitation spectra for such clusters deposited on the Cu(111) surface. For these systems the magnetic atoms showed couplings of different strength and sign (described by exchange coupling constants J), *i.e.*, strong or weak ferromagnetic or antiferromagnetic coupling. We showed that our method provides access to J in the adiabatic approximation that is related to a formula extracted from infinitesimal rotation of the magnetic moments [100, 103]. Our analysis shed light on three aspects of the excitation spectra for different investigated nanostructures: First, the dimer structure showed distinct different excitation spectra when a parallel and an antiparallel alignment of the spins is considered. In the former case we observed two modes, one with an acoustic and one with an optical resonance. For the latter case, however, the optical mode showed a strongly damped curve in accordance with the expectations put forward by means of the Landau-Lifshitz-Gilbert (LLG) model. Second, the addition or removal of single adatoms massively affect the spectrum. This was demonstrated by regarding chains of Fe adatoms with different lengths. We were able to assign the resonance energies in the obtained spectra to excitation modes of the system, as expected by use of the LLG model. Third, the effect of boundary conditions was analyzed by considering two impurity structures with the same number and the same type of magnetic adatoms placed on the metallic surface, once deposited along a straight

line and once in a circular arrangement. The obtained spectra showed good agreement expectations from the LLG model in terms of the obtained degree of degeneracy in the resonance energies.

The summary concludes with a short outlook, where the focus is set on a few suggestions for further developments of the presented method and potential improvements of its implementation.

Although the present work does not include the effect of spin-orbit coupling (SOC) and in order to compare to available experimental data the SOC-induced gap in the excitation spectrum was enforced by an auxiliary applied magnetic field along the out-of-plane direction, we recently showed that the inclusion of SOC can be achieved by use of a modified sum rule [70] on the level of the intrinsic magnetic excitation spectrum. Currently, this formalism is being extended to the self-energy. The difficulty is that a distinction of the two spin channels is not possible anymore and the concept of pure spin-flip processes cannot be maintained. Once this quantity is available, it opens the gate to study spin-excitations in noncollinear nanostructures from first-principles.

Another development that is currently undertaken is the extension of the formalism to layered systems. Thus, one can compare to spin-polarized inelastic electron energy loss experiments [68], where different excitation modes are obtained for multi-layered systems.

Furthermore, it is of interest to go beyond the one-shot calculations of the electron self-energy. Since this quantity depends on the Green function, a renormalization of the latter affects the structure of the self-energy in return. This task is closely related to the request to subtract double-counting terms, *i.e.*, many-particle effects that appear in both, the effective potential within the DFT formalism and the self-energy by means of the considered Feynman diagram. Also the approximation of the exchange-correlation kernel to be local in space and frequency independent (adiabatic local-density approximation, ALDA) could be replaced by a frequency sensitive form such the calculated self-energy expression is refined.

We conclude with a suggestion for a possible contribution to a vivid field of research. The present method could contribute to the study of Majorana bound states that recently were reported to exist at the edges of an Fe chain deposited on a superconducting Pb surface [106]. Majorana states are of interest in future development in the field of quantum computing, since these objects are their own antiparticles and may play a crucial role in the realization of exotic states in qubits. Thus, the understanding of dynamical effects in such systems are of crucial importance and could be tackled by our method.

A. Rydberg atomic units

All formulas within this thesis are given in terms of Rydberg atomic units. Within this unit system one defines

$$\frac{1}{4\pi\epsilon_0} = 1 \quad \text{(Coulomb's constant)}, \tag{A.1}$$

$$\hbar = 1 \quad \text{(reduced Planck's constant)}, \tag{A.2}$$

$$a_\mathrm{B} = 1 \quad \text{(Bohr radius)}, \tag{A.3}$$

$$\text{and} \quad \mathrm{Ry} = 1 \quad \text{(Rydberg energy)}. \tag{A.4}$$

As a direct consequence one also fixes

$$m_e = \frac{1}{2}\frac{\hbar}{\mathrm{Ry}\,a_\mathrm{B}^2} = \frac{1}{2} \quad \text{(electron rest mass)}, \tag{A.5}$$

$$e = \sqrt{\frac{4\pi\epsilon_0}{m_e a_\mathrm{B}}}\hbar = \sqrt{2} \quad \text{(elementary charge)}, \tag{A.6}$$

$$\text{and} \quad \mu_\mathrm{B} = \frac{e}{2m_e}\hbar = \sqrt{2} \quad \text{(Bohr magneton)}. \tag{A.7}$$

In order to allow a better comparison to experimental results, however, the presented results within this thesis are given in more common units. Among them are the length unit Ångström (Å, where $1\ \text{Å} = 10^{-10}\ \mathrm{m}$), the energy unit electron volt (eV), the time unit second (s, or as it is more convenient in spectroscopic analyses of solids, $\mathrm{fs} = 10^{-15}\ \mathrm{s}$), and the magnetic field unit Tesla (T). Furthermore, the symbols for the Bohr magneton μ_B and the Boltzmann constant k_B are kept on all formulas for clarity. Following the chosen set of units, it is most convenient to give the latter in the form

$$k_\mathrm{B} = 8.6173324 \cdot 10^{-5}\ \frac{\mathrm{eV}}{\mathrm{K}} \quad \text{(Boltzmann constant)}, \tag{A.8}$$

where the temperature unit Kelvin (K) was used. The most important quantities and their dimension conversion from Rydberg atomic units to SI units or other more common units are presented in Table A.1.

Dimension	Rydberg atomic units			SI units or other common units
length	$1\ a_{\mathrm{B}}$		$=$	0.52917720859 Å
energy	$1\ \mathrm{Ry}$		$=$	$13.60569193\ \mathrm{eV}$
			$=$	$2.17987197 \cdot 10^{-18}\ \mathrm{J}$
time				$1\ \mathrm{fs} = 10^{-15}\ \mathrm{s}$
temperature				$1\ \mathrm{K}$
electric charge	$\frac{1}{\sqrt{2}}\ e$,	where e	$=$	$1.602176487 \cdot 10^{-19}\ \mathrm{C}$
mass	$2\ m_e$,	where m_e	$=$	$9.10938215 \cdot 10^{-31}\ \mathrm{kg}$
magnetic moment	$\frac{1}{\sqrt{2}}\ \mu_{\mathrm{B}}$,	where μ_{B}	$=$	$5.7883818066 \cdot 10^{-5}\ \mathrm{eVT^{-1}}$
			$=$	$9.27400968 \cdot 10^{-24}\ \mathrm{JT^{-1}}$

Table A.1.: For a variety of different important physical quantities this table shows a comparison of Rydberg atomic units to SI units or more commonly used units. The appearing SI units are the energy unit Joule (J), the charge unit Coulomb (C), the mass unit kilogram (kg) and those mentioned in the text.

B. Details on performed calculations for spin-excitation spectra

To gain access to the dynamical susceptibility, χ, the self-energy, Σ, and the renormalized density of states, DOS, a sequence of a few calculations using different programs is required. The procedure is visualized as flow chart in Fig. B.1 and the utilization of the programs is discussed in the following.

Host potential and host Green function via the JM KKR program

The fundamental basis of all calculations is an accurate description of the electronic structure of the host system, *i.e.*, the pure Cu(111) slab in Chs. 6 and 8 or the pure Pt(111) slab in Ch. 7. This is achieved by use of the Korringa-Kohn-Rostoker (KKR) Green function method (see Ch. 3) as implemented in the Jülich-München program (abbreviation: JM, see gray boxes in Fig. B.1) in the atomic sphere approximation (ASA) with full charge density in the local spin density approximation, as parametrized by Vosko, Wilk, and Nusair [50]. For both setups, the Cu slab and the Pt slab, a thickness of 22 layers is used. Above and underneath the slab two vacuum regions with a thickness of four bulk layers each is added. The lattice constant is set to $a_{\mathrm{Cu}} = 3.615$ Å for the Cu(111) slab and $a_{\mathrm{Pt}} = 3.924$ Å for the Pt(111) slab. Structure optimizations of the impurity layer are accounted for by a relaxation of the impurity structure towards the surface: In case of the Cu(111) surface the relaxation is 14 %, in accordance with Refs. [91, 92], and 20 % for the Pt(111) surface. The percentage values are given with respect to the bulk interlayer distance, $a_{\mathrm{Cu}}/\sqrt{3} = 2.087$ Å or $a_{\mathrm{Pt}}/\sqrt{3} = 2.266$ Å. In both setups a k-point mesh of 180×180 k-points in the whole two-dimensional Brillouin zone is used within a self-consistency loop to obtain the converged host potential.

In order to prepare for using the impurity program a real-space cluster is cut out and the corresponding host Green functions (G^{host} in Fig. B.1) are stored for further use (see Fig. 6.1). The size of the cluster always includes the regarded impurity (*i.e.*, an adatom, a dimer, a trimer, and so on) and all surrounding atom positions with nearest-neighbor distance (including vacuum scattering sites), as well as vacuum sites several layers above the adatom that represent the position of a possible tip position.

After obtaining the host Green function and the host potential (V^{host} in Fig. B.1) for

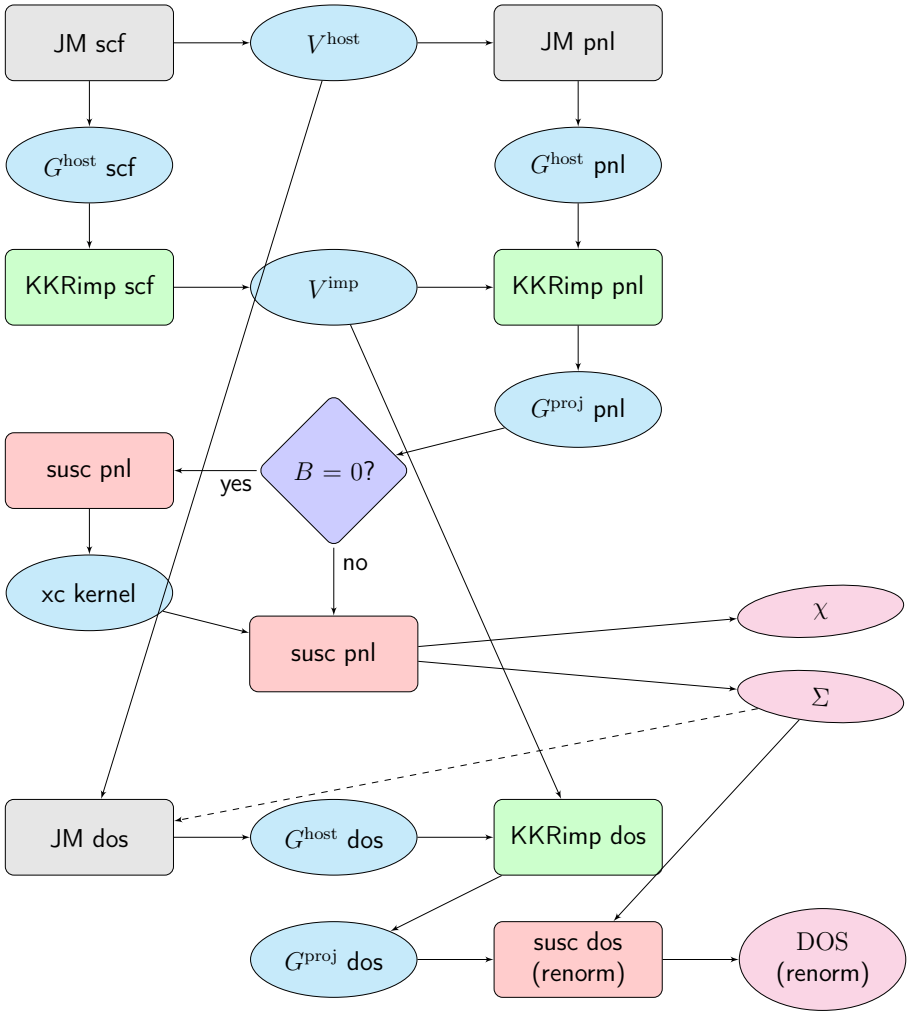

Figure B.1.: This diagram demonstrates the procedure of calculating the key quantities, the susceptibility χ, the self-energy Σ, and the renormalized density of states DOS). The dashed line indicates that the DOS contour is determined by the energy points for which the self-energy was calculated. For more information see the description within the text.

a self-consistent KKR contour (abbreviation in Fig. B.1: scf) the host Green function is determined once more within a one-shot calculation using a set of panels covering a complex energy area above the real axis and close to the Fermi energy E_{F} (see Fig. 3.3 in Sec. 3.3, abbreviation in Fig. B.1: pnl). This one-shot calculation is done with a sampling of the 2D Brillouin zone with 350×350 k-points.

Impurity potential and projected Green function via the KKR impurity program

By use of the host Green functions the impurity KKR program (see green boxes in Fig. B.1, abbreviation: KKRimp) is used to self-consistently determine the impurity potential (V^{imp} in Fig. B.1) for a desired transition-metal (TM) impurity within the impurity cluster (in this thesis: Cr, Mn, Fe, Co). Note, that this step normally has to be done at least twice: once with no applied magnetic field ($B = 0$) to determine the exchange-correlation (xc) kernel, and then for one or more nonvanishing applied B-fields along the z axis, *i.e.*, perpendicular to the (111) surface.

Together with the host Green function for the energy panels, these B-field dependent impurity potentials are used in a one-shot impurity calculation to obtain the projected form of the Green function (G^{proj} in Fig. B.1, see Sec. 3.3 for details). If not stated differently in the text the projection to a localized basis set of only d wave functions is considered, defined at E_{F}. By this procedure, the projected Green function, as well as the susceptibility and the self-energy reduce to energy dependent quantities that carry a site-dependent pair of indices. Test calculations have shown that the projection onto the d-orbital subspace is a reasonable approximation.

Access to χ and Σ via the KKRsusc program

The KKRsusc program (see light red boxes in Fig. B.1) is build upon rational fits of the projected Green functions (see Sec. 3.3 as well as Refs. [37] and [38] for further details). Depending whether an external field is applied or not the program calculates the xc kernel or the dynamical susceptibility and the self-energy via the formulas given in Chs. 4 and 5.

Access to renormalized DOS via the KKRsusc program

To obtain the renormalized DOS spectrum, *i.e.*, the impact of the spin-excitation on the electronic structure, one has to solve the Dyson equation which requires the self-energy as well as the ground state Green function for the same set of energy points. This is achieved by one-shot calculations of the JM code and the KKRimp program as sketched in the lower part of Fig. B.1, where the energy points that form the DOS contour (abbreviation in Fig. B.1: dos) are predefined by the energy values that were used for calculating

the self-energy (indicated by the dashed line in Fig. B.1). This one-shot calculation is performed using a sampling of the Brillouin zone with 350×350 k-points.

C. Important functions and identities

In the following the most important functions are listed. In addition, important related identities are given.

The Dirac δ-distribution is defined as

$$\delta(\omega) = \lim_{\eta \to 0^+} \frac{1}{\pi} \frac{\eta}{\omega^2 + \eta^2} = \begin{cases} +\infty & , \quad \omega = 0 \\ 0 & , \quad \omega \neq 0 \end{cases} , \tag{C.1}$$

such that it satisfies the integration norm condition

$$\int \mathrm{d}\omega \delta(\omega) = 1 \, . \tag{C.2}$$

The Fourier transformations read

$$\delta(\omega) = \frac{1}{2\pi} \int \mathrm{d}\tau \mathrm{e}^{\mathrm{i}\omega\tau} \quad \text{and} \quad 1 = \int \mathrm{d}\omega \mathrm{e}^{-\mathrm{i}\omega\tau} \delta(\omega) \, . \tag{C.3}$$

Suppose a function $f(\omega)$ is well-defined along the real axis. By use of the Cauchy principle value

$$\fint \mathrm{d}\omega \frac{f(\omega)}{\omega} = \lim_{\epsilon \to 0^+} \left[\int_{-\infty}^{-\epsilon} \mathrm{d}\omega \frac{f(\omega)}{\omega} + \int_{+\epsilon}^{+\infty} \mathrm{d}\omega \frac{f(\omega)}{\omega} \right] \tag{C.4}$$

one arrives at a version of the Sokhotski–Plemelj theorem for a real argument ω, the so-called Sokhatsky–Weierstrass theorem

$$\lim_{\eta \to 0^+} \int \mathrm{d}\omega \frac{f(\omega)}{\omega \pm \mathrm{i}\eta} = \fint \mathrm{d}\omega \frac{f(\omega)}{\omega} \mp \mathrm{i}\pi f(0) \, . \tag{C.5}$$

For a real number τ the Heaviside step function is defined as

$$\Theta(\tau) = -\frac{1}{2\pi\mathrm{i}} \lim_{\eta \to 0^+} \int \mathrm{d}\omega \frac{\mathrm{e}^{-\mathrm{i}\omega\tau}}{\omega + \mathrm{i}\eta} = \begin{cases} 1 & , \quad \tau > 0 \\ 0 & , \quad \tau \leq 0 \end{cases} . \tag{C.6}$$

The value $\Theta(0)$ is defined by hand and normally has no importance due to the exclusive use of the step function in integrands. In that sense the step function is used as a distribution and can be seen as integral form of the δ-distribution.

The Fermi-Dirac function is given by

$$f(E,T) = \frac{1}{\mathrm{e}^{\beta(E-\mu)}+1} \tag{C.7}$$

with $\beta = 1/k_{\mathrm{B}}T$. In the zero temperature limit the chemical potential μ turns to the Fermi energy E_{F} and one arrives at the step function (see Eq. (C.6)) with the argument $E_{\mathrm{F}} - E$,

$$f(E) = f(E, T=0) = \Theta(E_{\mathrm{F}} - E)\ . \tag{C.8}$$

D. The lowest order self-energy

This Appendix is distinctly linked to Ch. 5 and dedicated to the derivation of the lowest order self-energy within many-body perturbation theory (MBPT). First, the forms of retarded, advanced, and time-ordered Green functions in time and frequency space are discussed. Second, the lowest order self-energy as given by Eq. (5.5) in the main text is derived, where the lowest order of the Dyson equation (see Eq. (5.3) of the main text and Fig. 5.3) represents the starting point. Finally, the connection of Green function, susceptibility, and self-energy in their time-ordered and retarded forms is given, providing the link from MBPT to the Korringa-Kohn-Rostoker (KKR) formalism.

D.1. Retarded, advanced and time-ordered Green functions

The non-interacting single-particle Green function $G_0(1,2)$ is defined as solution to the equation of motion for the non-interacting Hamiltonian $\mathcal{H}_0(1)$,

$$\left(-\mathrm{i}\frac{\partial}{\partial t_1} + \mathcal{H}_0(1)\right) G_0(1,2) = -\delta(1-2)\ . \tag{D.1}$$

The arguments are combined in an index $1 = (\vec{r}_1, t_1)$ and the abbreviation $\delta(1-2) = \delta(\vec{r}_1 - \vec{r}_2)\delta(t_1 - t_2)$ is used. One distinguishes three different types of Green functions, $G_0^{[R]}(1,2)$, $G_0^{[A]}(1,2)$, and $G_0^{[t]}(1,2)$, the retarded, advanced, and time-ordered Green function, respectively. All three Green function are given at thermal equilibrium, *i.e.*, they are given with respect to the ground state wave function $|\Psi_{\mathrm{GS}}\rangle$ and take the form

$$\mathrm{i}G_0^{[R]}(1,2) = \langle\Psi_{\mathrm{GS}}|\left[\hat{\psi}(1),\hat{\psi}(2)^\dagger\right]_+|\Psi_{\mathrm{GS}}\rangle\Theta(t_1-t_2)\ , \tag{D.2}$$

$$\mathrm{i}G_0^{[A]}(1,2) = -\langle\Psi_{\mathrm{GS}}|\left[\hat{\psi}(1),\hat{\psi}(2)^\dagger\right]_+|\Psi_{\mathrm{GS}}\rangle\Theta(t_2-t_1)\ , \tag{D.3}$$

$$\text{and}\quad \mathrm{i}G_0^{[t]}(1,2) = \langle\Psi_{\mathrm{GS}}|\mathcal{T}\left[\hat{\psi}(1)\hat{\psi}(2)^\dagger\right]|\Psi_{\mathrm{GS}}\rangle\ . \tag{D.4}$$

Here, the anti-commutator $\left[\hat{\psi}(1),\hat{\psi}(2)^\dagger\right]_+ = \hat{\psi}(1)\hat{\psi}(2)^\dagger + \hat{\psi}(2)^\dagger\hat{\psi}(1)$, the Heaviside step function $\Theta(t_1-t_2)$ (see Appendix C), as well as the time-ordering operator $\mathcal{T}$ (Wick

operator)

$$\mathcal{T}\left[\hat{\psi}(1)\hat{\psi}(2)^\dagger\right] = \begin{cases} \hat{\psi}(1)\hat{\psi}(2)^\dagger & , \ t_1 > t_2 \\ -\hat{\psi}(2)^\dagger\hat{\psi}(1) & , \ t_1 < t_2 \end{cases} = \hat{\psi}(1)\hat{\psi}(2)^\dagger\Theta(t_1 - t_2) - \hat{\psi}(2)^\dagger\hat{\psi}(1)\Theta(t_2 - t_1) \tag{D.5}$$

are used. The field operator in the Heisenberg representation in second quantization and its adjoint take the forms

$$\hat{\psi}(1) = \hat{\psi}(\vec{r}_1, t_1) = \sum_n \phi_n(\vec{r}_1)\, \mathrm{e}^{-\mathrm{i}E_n t_1}\hat{c}_n \tag{D.6}$$

$$\text{and} \quad \hat{\psi}(1)^\dagger = \hat{\psi}(\vec{r}_1, t_1)^\dagger = \sum_n \phi_n^*(\vec{r}_1)\, \mathrm{e}^{+\mathrm{i}E_n t_1}\hat{c}_n^\dagger \ , \tag{D.7}$$

where the eigenfunctions for the non-interacting Hamiltonian are given by ϕ_n, E_n is the energy of the corresponding state, and $\hat{c}_n^\dagger$ ($\hat{c}_n$) is the creator (annihilator) of the state. Inserting the definition for the field operators, Eqs. (D.6) and (D.7), into the expressions of the three Green functions, *cf.* Eqs. (D.2), (D.3), and (D.4), one arrives at

$$\mathrm{i}G_0^{[R]}(1,2) = \sum_n \phi_n(\vec{r}_1)\phi_n^*(\vec{r}_2)\mathrm{e}^{-\mathrm{i}E_n(t_1-t_2)}\Theta(t_1 - t_2) \ , \tag{D.8}$$

$$\mathrm{i}G_0^{[A]}(1,2) = -\sum_n \phi_n(\vec{r}_1)\phi_n^*(\vec{r}_2)\mathrm{e}^{-\mathrm{i}E_n(t_1-t_2)}\Theta(t_2 - t_1) \ , \tag{D.9}$$

$$\text{and} \quad \mathrm{i}G_0^{[t]}(1,2) = \sum_n \phi_n(\vec{r}_1)\phi_n^*(\vec{r}_2)\mathrm{e}^{-\mathrm{i}E_n(t_1-t_2)} \cdot \begin{cases} (1 - f_n) & , \ t_1 - t_2 > 0 \\ (-f_n) & , \ t_1 - t_2 < 0 \end{cases} , \tag{D.10}$$

where $f_n = f(E_n) = (\exp(\beta(E_n - \mu)) + 1)^{-1}$ is the Fermi-Dirac function evaluated for energy E_n, $\beta = 1/k_\mathrm{B}T$, and μ the chemical potential. Here, it was assumed that the wave functions form an orthonormalized basis set and one can benefit from the simplifications

$$\langle\Psi_\mathrm{GS}|\hat{c}_m^\dagger\hat{c}_n|\Psi_\mathrm{GS}\rangle = \delta_{n,m}\langle\Psi_\mathrm{GS}|\hat{c}_n^\dagger\hat{c}_n|\Psi_\mathrm{GS}\rangle = \delta_{n,m}\, f_n \tag{D.11}$$

$$\text{and} \quad \langle\Psi_\mathrm{GS}|\hat{c}_n\hat{c}_m^\dagger|\Psi_\mathrm{GS}\rangle = \delta_{n,m}\langle\Psi_\mathrm{GS}|(1 - \hat{c}_n^\dagger\hat{c}_n)|\Psi_\mathrm{GS}\rangle = \delta_{n,m}\,(1 - f_n) \ , \tag{D.12}$$

where $\delta_{n,m}$ is the Kronecker delta.

D.1.1. Lehmann representation: Green function in Fourier space

Note, that the form of the single-particle Green functions in Eqs. (D.2), (D.3), and (D.4) only contains the difference of the two time-arguments, $t_1 - t_2$. This allows to write

$G_0(1,2) = G_0(\vec{r}_1, \vec{r}_2; t_1 - t_2)$ and one can define the Green function of Fourier space in terms of the Fourier transformation,

$$\begin{aligned} G_0(\vec{r}_1, \vec{r}_2; E) &= \int \mathrm{d}t\ \mathrm{e}^{\mathrm{i}Et} G_0(\vec{r}_1, \vec{r}_2; t) \\ &= \lim_{\eta \searrow 0} \left[\int_{-\infty}^{0} \mathrm{d}t\ \mathrm{e}^{\mathrm{i}(E - \mathrm{i}\eta)t} G_0(\vec{r}_1, \vec{r}_2; t) + \int_0^{\infty} \mathrm{d}t\ \mathrm{e}^{\mathrm{i}(E + \mathrm{i}\eta)t} G_0(\vec{r}_1, \vec{r}_2; t) \right] \\ &= \int_{-\infty}^{0} \mathrm{d}t\ \mathrm{e}^{\mathrm{i}(E - \mathrm{i}0^+)t} G_0(\vec{r}_1, \vec{r}_2; t) + \int_0^{\infty} \mathrm{d}t\ \mathrm{e}^{\mathrm{i}(E + \mathrm{i}0^+)t} G_0(\vec{r}_1, \vec{r}_2; t) \end{aligned} \quad \text{(D.13)}$$

with $t = t_1 - t_2$, the energy $E = \omega$ (in atomic units), and a small positive number η as well as the infinitesimal small positive number 0^+. The introduction of such infinitesimal small positive numbers -0^+ and $+0^+$ becomes necessary in order to ensure the convergence of the Fourier integration. For the time-ordered Green function one finds the expression

$$\begin{aligned} & G_0^{[t]}(\vec{r}_1, \vec{r}_2; E) \\ &= \int_{-\infty}^{0} \mathrm{d}t\ \mathrm{e}^{\mathrm{i}(E - \mathrm{i}0^+)t} G_0^{[t]}(\vec{r}_1, \vec{r}_2; t) + \int_0^{\infty} \mathrm{d}t\ \mathrm{e}^{\mathrm{i}(E + \mathrm{i}0^+)t} G_0^{[t]}(\vec{r}_1, \vec{r}_2; t) \\ &= -\mathrm{i} \sum_n \phi_n(\vec{r}_1) \phi_n^*(\vec{r}_2) \times \\ &\qquad \left[\frac{\mathrm{e}^{\mathrm{i}(E - E_n - \mathrm{i}0^+)t}}{\mathrm{i}(E - E_n - \mathrm{i}0^+)} \Bigg|_{t=-\infty}^{t=0} \cdot (-f_n) + \frac{\mathrm{e}^{\mathrm{i}(E - E_n + \mathrm{i}0^+)t}}{\mathrm{i}(E - E_n + \mathrm{i}0^+)} \Bigg|_{t=0}^{t=\infty} \cdot (1 - f_n) \right] . \end{aligned} \quad \text{(D.14)}$$

Due to the small infinitesimal 0^+ in the exponential function the boundary values for $t = \pm\infty$ vanish and the integration becomes well-defined. Similar expressions can be found for the retarded and the advanced Green functions. In total, the Fourier transforms of retarded, advanced, and time-ordered Green functions read

$$G_0^{[R]}(\vec{r}_1, \vec{r}_2; E) = \sum_n \phi_n(\vec{r}_1) \phi_n^*(\vec{r}_2) \frac{1}{E - E_n + \mathrm{i}0^+} , \quad \text{(D.15)}$$

$$G_0^{[A]}(\vec{r}_1, \vec{r}_2; E) = \sum_n \phi_n(\vec{r}_1) \phi_n^*(\vec{r}_2) \frac{1}{E - E_n - \mathrm{i}0^+} , \quad \text{(D.16)}$$

$$\text{and} \quad G_0^{[t]}(\vec{r}_1, \vec{r}_2; E) = \sum_n \phi_n(\vec{r}_1) \phi_n^*(\vec{r}_2) \left[\frac{f_n}{E - E_n - \mathrm{i}0^+} + \frac{1 - f_n}{E - E_n + \mathrm{i}0^+} \right] . \quad \text{(D.17)}$$

The form of the Fourier transformed Green function is called Lehmann-representation. The Green functions as defined in Eqs. (D.15), (D.16), and (D.17) can be written in terms of a complex energy argument z. The position of the poles in the complex energy plane are sketched in Fig. D.1. The poles of retarded Green functions are always below the real axis, whereas the poles of the advanced Green function are found above it (*cf.* Fig. D.1). This

reflects the nature of these two types of Green functions: Whereas the retarded Green function describes an electron (hole) that propagates forward (backward) in time, the advanced Green function describes the same for the antiparticle, *i.e.*, a hole (electron) propagation forward (backward) in time.

The time-ordered Green function has poles above and below the real axis. For the zero-temperature limit, the Fermi function f_n results in a step-function $\Theta(E_\mathrm{F} - E_n)$, where E_F is the Fermi energy. Then, the poles with E_n above and below the real axis are found below and above E_F, respectively (*cf.* Fig. D.1). The interpretation is such that depending on the energy E_n the time-ordered Green function describes an electron or a hole, propagating forward in time.

The introduction of an infinitesimal 0^+ became necessary to ensure a convergence of the expressions for the Green functions in Fourier space. By an additional Fourier transformation

$$\int \frac{\mathrm{d}E}{2\pi}\, \mathrm{e}^{-\mathrm{i}Et}\, G_0(\vec{r}_1, \vec{r}_2; E)\ , \tag{D.18}$$

where $G_0(\vec{r}_1, \vec{r}_2; E)$ is one of the Green functions as given in Eqs. (D.15), (D.16), and (D.17), one should recover the corresponding Green functions in time space (*cf.* Eqs. (D.8), (D.9), and (D.10)) and see in which way the infinitesimal 0^+ enters these expressions.

For solving Eq. (D.18) one has to distinguish the two cases $t > 0$ and $t < 0$, as will be demonstrated for the time-ordered Green function in the following. For $t > 0$ the integration of Eq. (D.18) get extended to the closed complex contour integration $\mathcal{C}_>$ (see Fig. D.1), since then $\mathrm{e}^{-\mathrm{i}zt} \xrightarrow[|z|\to\infty]{} 0$ for a complex energy z with $\mathrm{Im}z < 0$. Thus, for the time-ordered Green function Eq. (D.18) can be written

$$\begin{aligned}
&\int \frac{\mathrm{d}E}{2\pi}\, \mathrm{e}^{-\mathrm{i}Et}\, G_0^{[t]}(\vec{r}_1, \vec{r}_2; E) + \underbrace{\int_{\curvearrowleft} \frac{\mathrm{d}z}{2\pi}\, \mathrm{e}^{-\mathrm{i}zt} G_0^{[t]}(\vec{r}_1, \vec{r}_2; z)}_{=0} \\
&= \int_{\mathcal{C}_>} \frac{\mathrm{d}z}{2\pi}\, \mathrm{e}^{-\mathrm{i}zt} G_0^{[t]}(\vec{r}_1, \vec{r}_2; z) \\
&= -\mathrm{i} \sum_n \mathsf{Res}_{E_n - \mathrm{i}0^+} \left(\mathrm{e}^{-\mathrm{i}zt} G_0^{[t]}(\vec{r}_1, \vec{r}_2; , z) \right)\ ,
\end{aligned} \tag{D.19}$$

where the last step utilizes the Residue theorem and the minus sign in front of Eq. (D.19 accounts for the clockwise rotation. A similar expression is obtained for the case $t < 0$, for which the path of the complex contour integration is denoted by $\mathcal{C}_<$, *cf.* Fig. D.1. Note, that due to the anticlockwise rotation a minus sign does not appear in front of the final expression. In total one arrives at

$$G_0(\vec{r}_1, \vec{r}_2; t) \;=\; \begin{cases} -\mathrm{i} \sum_n \phi_n(\vec{r}_1) \phi_n^*(\vec{r}_2)\, \mathrm{e}^{-\mathrm{i}(E_n - \mathrm{i}0^+)t} (1 - f_n) & ,\ t > 0 \\ +\mathrm{i} \sum_n \phi_n(\vec{r}_1) \phi_n^*(\vec{r}_2)\, \mathrm{e}^{-\mathrm{i}(E_n + \mathrm{i}0^+)t} f_n & ,\ t < 0 \end{cases}\ , \tag{D.20}$$

which is the same result as obtained in Eq. (D.10), given that $t = t_1 - t_2$ and that the infinitesimal 0^+ can be dropped.

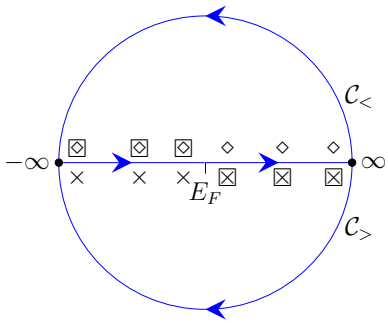

Figure D.1.: The two contour integrations $\mathcal{C}_>$ and $\mathcal{C}_<$ within the complex energy plane are shown, where the real axis schematically is indicated by a straight line from $-\infty$ to ∞. In addition the poles of the three Green functions are shown, corresponding to Eqs. (D.15), (D.16), and (D.17). The poles of the retarded Green function are indicated by crosses ($\times$) and are located underneath the real axis, whereas the advanced Green function has poles only above the real axis (diamonds, $\diamond$). For each eigenenergy E_n the time-ordered Green function has poles above and below the real axis, which in the zero-temperature limit reduces to poles above (below) it for $E_n < E_\mathrm{F}$ ($E_n > E_\mathrm{F}$), in the figure indicated by squares ($\square$).

D.2. The lowest order Dyson equation in Fourier space

In this Section the approach to the lowest order self-energy is given. For this derivation we omit the spin label for brevity and use for the time-ordered Green function the abbreviation $G^0_{1,2}(t_1 - t_2) = G_0(1,2) = G_0(\vec{r}_1, \vec{r}_2; t_1 - t_2)$. In addition, we assume that the interaction term is local in time and thus takes the form $U(\vec{r}_1, \vec{r}_2; t_1 - t_2) = U_{1,2}\delta(t_1 - t_2) = U_{2,1}\delta(t_2 - t_1)$. After performing a Fourier transformation for the time difference $t = t_1 - t_2$, Eq. (5.3) of the main text becomes

$$\begin{aligned} G_{1,2}(E) &= G^0_{1,2}(E) + \int \mathrm{d}t\, \mathrm{e}^{\mathrm{i}Et} \int \mathrm{d}3 \int \mathrm{d}4 \int \mathrm{d}5 \int \mathrm{d}6\; U_{3,5}\delta(t_3 - t_5) U_{6,4}\delta(t_6 - t_4) \\ &\quad \times G^0_{1,3}(t_1 - t_3) G^0_{5,6}(t_5 - t_6) G^0_{4,2}(t_4 - t_2) G^0_{3,4}(t_3 - t_4) G^0_{6,5}(t_6 - t_5) \\ &= G^0_{1,2}(E) + \int \mathrm{d}\vec{r}_3 \int \mathrm{d}\vec{r}_4 \int \mathrm{d}\vec{r}_5 \int \mathrm{d}\vec{r}_6 U_{3,5} U_{6,4} \int \mathrm{d}t\, \mathrm{e}^{\mathrm{i}Et} \int \mathrm{d}t_3 \int \mathrm{d}t_4 \\ &\quad \times G^0_{1,3}(t_1 - t_3) G^0_{5,6}(t_3 - t_4) G^0_{4,2}(t_4 - t_2) G^0_{3,4}(t_3 - t_4) G^0_{6,5}(t_4 - t_3)\ . \end{aligned} \tag{D.21}$$

In order to simplify Eq. (D.21) we seek to formulate all Green functions with respect to an energy variable via Fourier transformation. By taking into account only the time-dependent

part of the last term in Eq. (D.21) we get

$$\begin{aligned}
&\int \mathrm{d}t\, \mathrm{e}^{\mathrm{i}Et} \int \mathrm{d}t_3 \int \mathrm{d}t_4\; G^0_{1,3}(t_1-t_3) G^0_{5,6}(t_3-t_4) G^0_{4,2}(t_4-t_2) G^0_{3,4}(t_3-t_4) G^0_{6,5}(t_4-t_3) \\
&= \int \mathrm{d}t\, \mathrm{e}^{\mathrm{i}Et} \int \mathrm{d}t_3 \int \mathrm{d}t_4 \int \frac{\mathrm{d}E_1}{2\pi} \int \frac{\mathrm{d}E_2}{2\pi} \int \frac{\mathrm{d}E_3}{2\pi} \int \frac{\mathrm{d}E_4}{2\pi} \int \frac{\mathrm{d}E_5}{2\pi} \\
&\quad \times \mathrm{e}^{-\mathrm{i}[E_1(t_1-t_3)+E_2(t_3-t_4)+E_3(t_4-t_2)+E_4(t_3-t_4)+E_5(t_4-t_3)]} \\
&\quad \times G^0_{1,3}(E_1) G^0_{5,6}(E_2) G^0_{4,2}(E_3) G^0_{3,4}(E_4) G^0_{6,5}(E_5) \\
&= \int \mathrm{d}t\, \mathrm{e}^{\mathrm{i}Et} \int \mathrm{d}t_3 \int \mathrm{d}t_4 \int \frac{\mathrm{d}E_1}{2\pi} \int \frac{\mathrm{d}E_2}{2\pi} \int \frac{\mathrm{d}E_3}{2\pi} \int \frac{\mathrm{d}E_4}{2\pi} \int \frac{\mathrm{d}E_5}{2\pi} \\
&\quad \times \mathrm{e}^{-\mathrm{i}E_1 t_1} \mathrm{e}^{\mathrm{i}E_3 t_2}\, \mathrm{e}^{\mathrm{i}(E_1-E_2-E_4+E_5)t_3}\, \mathrm{e}^{\mathrm{i}(E_2-E_3+E_4-E_5)t_4} \\
&\quad \times G^0_{1,3}(E_1) G^0_{5,6}(E_2) G^0_{4,2}(E_3) G^0_{3,4}(E_4) G^0_{6,5}(E_5)\;. \qquad \text{(D.22)}
\end{aligned}$$

Now we use the identity (see Appendix C)

$$\int \mathrm{d}t\, \mathrm{e}^{\mathrm{i}Et} = 2\pi \cdot \delta(E) \qquad \text{(D.23)}$$

for t_3 and t_4 and evaluate the resulting δ-functions by solving the integral over E_5 and then the one over E_3,

$$\begin{aligned}
&\int \mathrm{d}t\, \mathrm{e}^{\mathrm{i}Et} \int \frac{\mathrm{d}E_1}{2\pi} \int \frac{\mathrm{d}E_2}{2\pi} \int \mathrm{d}E_3 \int \frac{\mathrm{d}E_4}{2\pi} \int \mathrm{d}E_5 \\
&\quad \times \mathrm{e}^{-\mathrm{i}E_1 t_1} \mathrm{e}^{\mathrm{i}E_3 t_2} \delta(E_1-E_2-E_4+E_5) \delta(E_2-E_3+E_4-E_5) \\
&\quad \times G^0_{1,3}(E_1) G^0_{5,6}(E_2) G^0_{4,2}(E_3) G^0_{3,4}(E_4) G^0_{6,5}(E_5) \\
&= \int \mathrm{d}t\, \mathrm{e}^{\mathrm{i}Et} \int \frac{\mathrm{d}E_1}{2\pi} \int \frac{\mathrm{d}E_2}{2\pi} \int \mathrm{d}E_3 \int \frac{\mathrm{d}E_4}{2\pi} \\
&\quad \times \mathrm{e}^{-\mathrm{i}E_1 t_1} \mathrm{e}^{\mathrm{i}E_3 t_2} \underbrace{\delta(E_1-E_2-E_4+(E_2-E_3+E_4))}_{=\delta(E_1-E_3)} \\
&\quad \times G^0_{1,3}(E_1) G^0_{5,6}(E_2) G^0_{4,2}(E_3) G^0_{3,4}(E_4) G^0_{6,5}(E_2-E_3+E_4) \\
&= \int \mathrm{d}t\, \mathrm{e}^{\mathrm{i}Et} \int \frac{\mathrm{d}E_1}{2\pi} \int \frac{\mathrm{d}E_2}{2\pi} \int \frac{\mathrm{d}E_4}{2\pi}\, \mathrm{e}^{-\mathrm{i}E_1 t_1} \mathrm{e}^{\mathrm{i}E_1 t_2} \\
&\quad G^0_{1,3}(E_1) G^0_{5,6}(E_2) G^0_{4,2}(E_1) G^0_{3,4}(E_4) G^0_{6,5}(E_2-E_1+E_4) \\
&= \int \frac{\mathrm{d}E_1}{2\pi} \int \frac{\mathrm{d}E_2}{2\pi} \int \frac{\mathrm{d}E_4}{2\pi} \int \mathrm{d}t\, \mathrm{e}^{\mathrm{i}(E-E_1)t} \\
&\quad \times G^0_{1,3}(E_1) G^0_{5,6}(E_2) G^0_{4,2}(E_1) G^0_{3,4}(E_4) G^0_{6,5}(E_2-E_1+E_4)\;. \qquad \text{(D.24)}
\end{aligned}$$

In the last step we used that $t = t_1 - t_2$. Once more by using Eq. (D.23), we can replace time integral and the exponential expression by another δ-function with argument $E - E_1$

and subsequently perform the integration over E_1. Thus, we find

$$\begin{aligned}
&\int \mathrm{d}E_1 \int \frac{\mathrm{d}E_2}{2\pi} \int \frac{\mathrm{d}E_4}{2\pi} \delta(E - E_1) \\
&\times G^0_{1,3}(E_1) G^0_{5,6}(E_2) G^0_{4,2}(E_1) G^0_{3,4}(E_4) G^0_{6,5}(E_2 - E_1 + E_4) \\
= &\int \frac{\mathrm{d}E_2}{2\pi} \int \frac{\mathrm{d}E_4}{2\pi} G^0_{1,3}(E) G^0_{5,6}(E_2) G^0_{4,2}(E) G^0_{3,4}(E_4) G^0_{6,5}(E_2 - E + E_4) \\
= &\; G^0_{1,3}(E) G^0_{4,2}(E) \int \frac{\mathrm{d}E_2}{2\pi} G^0_{5,6}(E + E_2) \int \frac{\mathrm{d}E_4}{2\pi} G^0_{3,4}(E_4) G^0_{6,5}(E_2 + E_4) \; ,
\end{aligned} \tag{D.25}$$

where in the last step the substitution $E_2 \to E_2 + E$ was used. For Eq. (D.21) we get the result

$$\begin{aligned}
G_{1,2}(E) = &\; G^0_{1,2}(E) + \int \mathrm{d}\vec{r}_3 \int \mathrm{d}\vec{r}_4 G^0_{1,3}(E) G^0_{4,2}(E) \int \mathrm{d}\vec{r}_5 \int \mathrm{d}\vec{r}_6 \\
&\times U_{3,5} U_{6,4} \int \frac{\mathrm{d}E_2}{2\pi} G^0_{5,6}(E + E_2) \underbrace{\int \frac{\mathrm{d}E_4}{2\pi} G^0_{3,4}(E_4) G^0_{6,5}(E_2 + E_4)}_{\stackrel{\mathrm{def}}{=} \mathrm{i}\chi^0_{36;54}(E_2)} \; .
\end{aligned} \tag{D.26}$$

The definition of the susceptibility $\chi^0_{36;54}(E_2)$ reveals the structure of a convolution of two Green functions. An additional convolution of this quantity with another Green function points the way to the structure of the self-energy of lowest order, as given in Fig. 5.3. One defines

$$G_{1,2}(E) = G^0_{1,2}(E) + \int \mathrm{d}\vec{r}_3 \int \mathrm{d}\vec{r}_4 G^0_{1,3}(E) \Sigma^0_{3,4}(E) G^0_{4,2}(E) \; , \tag{D.27}$$

with

$$\Sigma^0_{3,4}(E) = \int \mathrm{d}\vec{r}_5 \int \mathrm{d}\vec{r}_6 U_{3,5} S^0_{53;46}(E) U_{6,4} \tag{D.28}$$

and

$$S^0_{53;46}(E) = \mathrm{i} \int \frac{\mathrm{d}E_2}{2\pi} G^0_{5,6}(E + E_2) \chi^0_{36;54}(E_2) \; . \tag{D.29}$$

The expressions for $\Sigma^0_{3,4}(E)$, $S^0_{53;46}(E)$, and $\chi^0_{36;54}(E_2)$ are those given in the main text (see Eqs. (5.5), (5.6), and (5.7)). In the following we solve the energy integrations that appear in the expressions for $\chi^0_{36;54}(E_2)$ and $\Sigma^0_{3,4}(E)$ and discuss their physical meanings.

D.2.1. The time-ordered single-particle susceptibility

Before the self-energy can be addressed we consider the term that describes the susceptibility. By use of the expression for the time-ordered Green function in Fourier space (see

Eq. (D.17)) we find

$$\begin{aligned}\chi^0_{36;54}(E_2) &= -\mathrm{i}\int\frac{\mathrm{d}E_4}{2\pi}G^0_{3,4}(E_4)G^0_{6,5}(E_2+E_4)\\ &= -\mathrm{i}\int\frac{\mathrm{d}E_4}{2\pi}\sum_{n,m}\phi_n(\vec{r}_3)\phi^*_n(\vec{r}_4)\phi_m(\vec{r}_6)\phi^*_m(\vec{r}_5)\\ &\quad\times\left[\frac{1-f_n}{E_4-E_n+\mathrm{i}0^+}+\frac{f_n}{E_4-E_n-\mathrm{i}0^+}\right]\\ &\quad\times\left[\frac{1-f_m}{E_2+E_4-E_m+\mathrm{i}0^+}+\frac{f_m}{E_2+E_4-E_m-\mathrm{i}0^+}\right]. \qquad \text{(D.30)}\end{aligned}$$

The integration over E_4 can be performed by closing the contour in the half circle above or below the real axis. By use of the Residue theorem the integrands containing residuals on just one side of the real axis do not contribute so that we are left with solving the expression

$$\begin{aligned}\chi^0_{36;54}(E_2) &= -\mathrm{i}\sum_{n,m}\phi_n(\vec{r}_3)\phi^*_n(\vec{r}_4)\phi_m(\vec{r}_6)\phi^*_m(\vec{r}_5)\\ &\quad\times\int\frac{\mathrm{d}E_4}{2\pi}\left[\frac{1-f_n}{E_4-E_n+\mathrm{i}0^+}\cdot\frac{f_m}{E_2+E_4-E_m-\mathrm{i}0^+}+\right.\\ &\qquad\left.\frac{f_n}{E_4-E_n-\mathrm{i}0^+}\cdot\frac{1-f_m}{E_2+E_4-E_m+\mathrm{i}0^+}\right]. \qquad \text{(D.31)}\end{aligned}$$

By utilizing the Residue theorem and the contour integration $\mathcal{C}_<$ from Fig. D.1 we find that

$$\begin{aligned}&\int_{-\infty}^{\infty}\frac{dE_4}{2\pi}\underbrace{\frac{1-f_n}{E_4-(E_n-\mathrm{i}0^+)}\cdot\frac{f_m}{E_4-(E_m-E_2+\mathrm{i}0^+)}}_{=g(E_4)}\\ &= \int_{-\infty}^{\infty}\frac{dE_4}{2\pi}g(E_4)+\underbrace{\int_{\curvearrowleft}\frac{dz}{2\pi}g(z)}_{=0}=\int_{\mathcal{C}_<}\frac{dz}{2\pi}g(z)\overset{!}{=}+\mathrm{i}\mathsf{Res}_{E_m-E_2+\mathrm{i}0^+}\left(g(z)\right)\\ &= +\mathrm{i}\frac{(1-f_n)f_m}{E_m-E_2+\mathrm{i}0^+-(E_n-\mathrm{i}0^+)}=-\mathrm{i}\frac{(1-f_n)f_m}{E_2-(E_m-E_n)-\mathrm{i}0^+} \qquad \text{(D.32)}\end{aligned}$$

and analogue

$$\int_{-\infty}^{\infty}\frac{dE_4}{2\pi}\frac{f_n}{E_4-(E_n+\mathrm{i}0^+)}\cdot\frac{1-f_m}{E_4-(E_m-E_2-\mathrm{i}0^+)}=+\mathrm{i}\frac{f_n(1-f_m)}{E_2-(E_m-E_n)+\mathrm{i}0^+} \qquad \text{(D.33)}$$

which allows to solve Eq. (D.31). We get

$$\begin{aligned}\chi^0_{36;54}(E_2) &= \sum_{n,m}\phi_n(\vec{r}_3)\phi^*_n(\vec{r}_4)\phi_m(\vec{r}_6)\phi^*_m(\vec{r}_5)\\ &\quad\times\left[\frac{f_n(1-f_m)}{E_2-(E_m-E_n)+\mathrm{i}0^+}-\frac{(1-f_n)f_m}{E_2-(E_m-E_n)-\mathrm{i}0^+}\right]. \qquad \text{(D.34)}\end{aligned}$$

The first term in Eq. (D.34) contains the expression $f_n(1-f_m)$ which only is non-zero for $E_n < E_\mathrm{F} < E_m$ (in the zero temperature limit). Thus, this term only contributes for an occupied n-state and an unoccupied m-state, causing $E_m - E_n$ to be a positive number. Therefore a resonance is achieved for positive E_2, a process where energy absorption takes place. On the other hand the second term only contributes when $E_m < E_\mathrm{F} < E_n$ meaning that $E_m - E_n$ becomes negative. Thus, the resulting resonance (for a negative E_2) describes a process in which energy emission takes place.

The backwards Fourier transformation from E_2 to $t_3 - t_4$ reads

$$\begin{aligned}
\chi^0_{36;54}(t_3-t_4) &= \int_{-\infty}^{\infty} \frac{dE_2}{2\pi}\, \mathrm{e}^{-\mathrm{i}E_2(t_3-t_4)} \chi^0_{36;54}(E_2) \\
&= \sum_{n,m} \phi_n(\vec{r}_3)\phi_n^*(\vec{r}_4)\phi_m(\vec{r}_6)\phi_m^*(\vec{r}_5) \int_{-\infty}^{\infty} \frac{dE_2}{2\pi}\, \mathrm{e}^{-\mathrm{i}E_2(t_3-t_4)} \\
&\quad \times \underbrace{\left[\frac{f_n(1-f_m)}{E_2 - (E_m - E_n) + \mathrm{i}0^+} - \frac{(1-f_n)f_m}{E_2 - (E_m - E_n) - \mathrm{i}0^+} \right]}_{=\tilde{g}(E_2)} . \qquad \text{(D.35)}
\end{aligned}$$

Depending on whether $t_3 - t_4$ is positive or negative we extend the integral along the real axis to a complex integral along the contour $\mathcal{C}_>$ or $\mathcal{C}_<$, respectively (see Fig. D.1). This case differentiation ensures that the added half-circle integration does not contain any non-zero contribution. Using the Residue theorem we get

$$\begin{aligned}
&\int_{-\infty}^{\infty} \frac{dE_2}{2\pi}\, \mathrm{e}^{-\mathrm{i}E_2(t_3-t_4)} \tilde{g}(E_2) \\
&= \int_{\mathcal{C}_\gtrless} \frac{dz}{2\pi}\, \mathrm{e}^{-\mathrm{i}E_2(t_3-t_4)} \tilde{g}(E_2) \overset{!}{=} \mp \mathrm{i}\mathsf{Res}_{E_m - E_n \mp \mathrm{i}0^+} \left(\mathrm{e}^{-\mathrm{i}z(t_3-t_4)} \tilde{g}(z) \right) \\
&= \begin{cases} -\mathrm{i}\, \mathrm{e}^{-\mathrm{i}(E_m - E_n - \mathrm{i}0^+)(t_3-t_4)} f_n(1-f_m) & , t_3 - t_4 > 0 \\ +\mathrm{i}\, \mathrm{e}^{-\mathrm{i}(E_m - E_n + \mathrm{i}0^+)(t_3-t_4)} (1-f_n) f_m & , t_3 - t_4 < 0 \end{cases} . \qquad \text{(D.36)}
\end{aligned}$$

Thus, the Fourier transformation of the full expression in Eq. (D.34) is given by

$$\begin{aligned}
\chi^0_{36;54}(t_3-t_4) &= -\mathrm{i} \sum_{n,m} \phi_n(\vec{r}_3)\phi_n^*(\vec{r}_4)\phi_m(\vec{r}_6)\phi_m^*(\vec{r}_5)\, \mathrm{e}^{-\mathrm{i}(E_m - E_n)(t_3-t_4)} \\
&\quad \times \begin{cases} f_n(1-f_m) & , t_3 - t_4 > 0 \\ (1-f_n) f_m & , t_3 - t_4 < 0 \end{cases} \\
&= -\mathrm{i} G_0(3,4) G_0(6,5) \delta(t_3 - t_5) \delta(t_6 - t_4) . \qquad \text{(D.37)}
\end{aligned}$$

In Fig. D.2 we show the Feynman diagram for the single-particle susceptibility and analyze the contracted situation with $\delta(\vec{r}_3 - \vec{r}_5)$ and $\delta(\vec{r}_4 - \vec{r}_6)$.

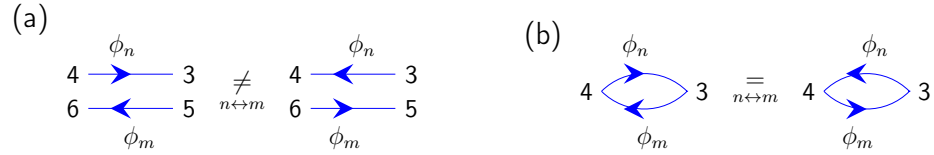

Figure D.2.: The Feynman diagram for the general single particle susceptibility is shown (a) as a four-point quantity, $\chi^0_{36;54}$, and (b) in its contracted form, $\chi^0_{34;34}$. Depending on the order of time one reads it from left to right ($t_3 > t_4$) or *vice versa*. Thus, the roles for hole and particle swap. Due to the possibility of relabeling ($n \leftrightarrow m$) we find that in the contracted form (b) the particle-hole pair does not differ from the hole-particle pair.

D.2.2. The time-ordered lowest order self-energy

Next we turn to the term that describes the lowest order self-energy (*cf.* Eq. (D.28)). Again we insert the expression for the time-ordered Green functions (see Eq. (D.17)). By use of the analogue expression for the time-ordered susceptibility (see Eq. (D.34)) the energy integral in Eq. (D.29) is given by (omitting the imaginary unit for a moment)

$$
\begin{aligned}
&\int \frac{\mathrm{d}E_2}{2\pi} G^0_{5,6}(E+E_2)\chi^0_{36;54}(E_2) \\
&= \sum_{k,n,m} \phi_k(\vec{r}_5)\phi_k^*(\vec{r}_6)\phi_n(\vec{r}_3)\phi_n^*(\vec{r}_4)\phi_m(\vec{r}_6)\phi_m^*(\vec{r}_5) \\
&\quad \times \int \frac{\mathrm{d}E_2}{2\pi} \left[\frac{1-f_k}{E_2-(E_k-E-\mathrm{i}0^+)} + \frac{f_k}{E_2-(E_k-E+\mathrm{i}0^+)} \right] \\
&\quad \times \left[\frac{f_n(1-f_m)}{E_2-(E_m-E_n-\mathrm{i}0^+)} - \frac{(1-f_n)f_m}{E_2-(E_m-E_n+\mathrm{i}0^+)} \right] \\
&= \sum_{k,n,m} \phi_k(\vec{r}_5)\phi_k^*(\vec{r}_6)\phi_n(\vec{r}_3)\phi_n^*(\vec{r}_4)\phi_m(\vec{r}_6)\phi_m^*(\vec{r}_5) \\
&\quad \times \int_{\mathcal{C}_<} \frac{dz}{2\pi} \left[-\frac{1-f_k}{z-(E_k-E-\mathrm{i}0^+)} \cdot \frac{(1-f_n)f_m}{z-(E_m-E_n+\mathrm{i}0^+)} \right. \\
&\quad \left. + \frac{f_k}{z-(E_k-E+\mathrm{i}0^+)} \cdot \frac{f_n(1-f_m)}{z-(E_m-E_n-\mathrm{i}0^+)} \right] \\
&= -\mathrm{i} \sum_{k,n,m} \phi_k(\vec{r}_5)\phi_k^*(\vec{r}_6)\phi_n(\vec{r}_3)\phi_n^*(\vec{r}_4)\phi_m(\vec{r}_6)\phi_m^*(\vec{r}_5) \\
&\quad \times \left[\frac{(1-f_k)(1-f_n)f_m}{E-(E_k-E_m+E_n)+\mathrm{i}0^+} + \frac{f_k f_n(1-f_m)}{E-(E_k-E_m+E_n)-\mathrm{i}0^+} \right] . \qquad \text{(D.38)}
\end{aligned}
$$

Similar to previous integrals the Residue theorem was used. In total the time-ordered lowest order self-energy is given by

$$\begin{aligned}\Sigma^0_{34}(E) &= \int \mathrm{d}\vec{r}_5 \int \mathrm{d}\vec{r}_6 U_{3,5} U_{6,4} \sum_{k,n,m} \phi_k(\vec{r}_5)\phi_k^*(\vec{r}_6)\phi_n(\vec{r}_3)\phi_n^*(\vec{r}_4)\phi_m(\vec{r}_6)\phi_m^*(\vec{r}_5) \\ &\quad \times \left[\frac{(1-f_k)(1-f_n)f_m}{E-(E_k-E_m+E_n)+\mathrm{i}0^+} + \frac{f_k f_n(1-f_m)}{E-(E_k-E_m+E_n)-\mathrm{i}0^+}\right] . \quad \text{(D.39)}\end{aligned}$$

D.3. Connection between time-ordered and retarded expressions

In this Section the time-ordered forms of susceptibility and self-energy (as given in the previous Section) are rewritten in terms of retarded Green functions, such that their retarded analogues can be identified. In order to distinguish time-ordered and retarded expressions, we use labels (as done in Eqs. (D.2) and (D.4)).

The time-ordered Green function in Fourier space reads (*cf.* Eq. (D.17))

$$G_{12}^{[t]0}(E) = G_0^{[t]}(\vec{r}_1,\vec{r}_2;E) = \sum_n \phi_n(\vec{r}_1)\phi_n^*(\vec{r}_2)\left[\frac{1-f_n}{E-E_n+\mathrm{i}0^+} + \frac{f_n}{E-E_n-\mathrm{i}0^+}\right] \quad \text{(D.40)}$$

By replacing $-\mathrm{i}0^+$ by $+\mathrm{i}0^+$ in the second term of Eq. (D.40) one arrives at

$$\begin{aligned}&= \sum_n \phi_n(\vec{r}_1)\phi_n^*(\vec{r}_2)\left[\frac{1-f_n}{E-E_n+\mathrm{i}0^+} + \frac{f_n}{E-E_n+\mathrm{i}0^+}\right] \\ &= \sum_n \phi_n(\vec{r}_1)\phi_n^*(\vec{r}_2)\frac{1}{E-E_n+\mathrm{i}0^+} , \quad \text{(D.41)}\end{aligned}$$

which is identical to the retarded Green function $G_0^{[R]}(\vec{r}_1,\vec{r}_2;E)$ (see Eq. (D.15)). One can define real and imaginary parts for the time-ordered and retarded Green function in the same way as defined in Ch. 3. A comparison of their energy dependent terms

$$\begin{aligned}\frac{1-f_n}{E-E_n+\mathrm{i}0^+} + \frac{f_n}{E-E_n-\mathrm{i}0^+} &= \frac{\mathcal{P}}{E-E_\mathrm{F}} - \mathrm{i}\pi\delta(E-E_n)\left[1-2f_n\right] \quad \text{(D.42)} \\ \frac{1}{E-E_n+\mathrm{i}0^+} &= \frac{\mathcal{P}}{E-E_\mathrm{F}} - \mathrm{i}\pi\delta(E-E_n) . \quad \text{(D.43)}\end{aligned}$$

leads to the useful identity

$$G_{12}^{[t]0}(E) = \mathrm{Re}G_{12}^{[R]0}(E) + \mathrm{i}\,\mathrm{sgn}(E-E_\mathrm{F})\,\mathrm{Im}G_{12}^{[R]0}(E) . \quad \text{(D.44)}$$

Due to the fact that the retarded Green function is analytic above the real axis (*i.e.*, the poles are found for $E = E_n - \mathrm{i}0^+$) we can perform a closed contour integration in the

upper half of the complex plane (*e.g.*, the contour $\mathcal{C}_>$ in Fig. D.1) and use the Residue theorem. This leads to

$$\begin{aligned} 0 \overset{!}{=} & \int \frac{\mathrm{d}E'}{2\pi} G_{12}^{[R]0}(E) G_{34}^{[R]0}(E+E') \\ = & \int \frac{\mathrm{d}E'}{2\pi} \left[\mathrm{Re}G_{12}^{[R]0}(E) \mathrm{Re}G_{34}^{[R]0}(E+E') - \mathrm{Im}G_{12}^{[R]0}(E) \mathrm{Im}G_{34}^{[R]0}(E+E') \right] \\ & + \mathrm{i} \int \frac{\mathrm{d}E'}{2\pi} \left[\mathrm{Re}G_{12}^{[R]0}(E) \mathrm{Im}G_{34}^{[R]0}(E+E') + \mathrm{Im}G_{12}^{[R]0}(E) \mathrm{Re}G_{34}^{[R]0}(E+E') \right] . \end{aligned} \tag{D.45}$$

Thus, real and imaginary part of Eq. (D.45) allow to extract two useful identities, valid for retarded Green functions,

$$\int \frac{\mathrm{d}E'}{2\pi} \mathrm{Re}G_{12}^{[R]0}(E) \mathrm{Re}G_{34}^{[R]0}(E+E') = \int \frac{\mathrm{d}E'}{2\pi} \mathrm{Im}G_{12}^{[R]0}(E) \mathrm{Im}G_{34}^{[R]0}(E+E') \tag{D.46}$$

and

$$\begin{aligned} & \int_{E_\mathrm{F}+|E|}^{\infty} \frac{\mathrm{d}E'}{2\pi} \left[\mathrm{Re}G_{12}^{[R]0}(E) \mathrm{Im}G_{34}^{[R]0}(E+E') + \mathrm{Im}G_{12}^{[R]0}(E) \mathrm{Re}G_{34}^{[R]0}(E+E') \right] \\ = & -\int_{-\infty}^{E_\mathrm{F}+|E|} \frac{\mathrm{d}E'}{2\pi} \left[\mathrm{Re}G_{12}^{[R]0}(E) \mathrm{Im}G_{34}^{[R]0}(E+E') + \mathrm{Im}G_{12}^{[R]0}(E) \mathrm{Re}G_{34}^{[R]0}(E+E') \right] . \end{aligned} \tag{D.47}$$

D.3.1. The retarded susceptibility

The time-ordered susceptibility is given as convolution of two time-ordered Green functions (see Eq. (D.31)). We are now able to reformulate this convolution in terms of the retarded Green functions,

$$\begin{aligned} \chi_{36;54}^{[t]0}(E) \quad = & \quad -\mathrm{i} \int \frac{\mathrm{d}E'}{2\pi} G_{3,4}^{[t]0}(E') G_{6,5}^{[t]0}(E+E') \\ \underset{(D.44)}{=} & \quad -\mathrm{i} \int \frac{\mathrm{d}E'}{2\pi} \left[\mathrm{Re}G_{3,4}^{[R]0}(E') + \mathrm{i}\,\mathrm{sgn}(E'-E_\mathrm{F})\,\mathrm{Im}G_{3,4}^{[R]0}(E') \right] \\ & \times \left[\mathrm{Re}G_{6,5}^{[R]0}(E+E') + \mathrm{i}\,\mathrm{sgn}(E+E'-E_\mathrm{F})\,\mathrm{Im}G_{6,5}^{[R]0}(E+E') \right] . \end{aligned} \tag{D.48}$$

To improve the readability we temporarily define $R_{\mathrm{I}} = \mathrm{Re}G^{[R]0}_{3,4}(E')$ and $I_{\mathrm{I}} = \mathrm{Im}G^{[R]0}_{3,4}(E')$, as well as $R_{\mathrm{II}} = \mathrm{Re}G^{[R]0}_{6,5}(E+E')$ and $I_{\mathrm{II}} = \mathrm{Im}G^{[R]0}_{6,5}(E+E')$. We find

$$\begin{aligned}
\chi^{[t]0}_{36;54}(E) &= \int \frac{\mathrm{d}E'}{2\pi}\Big[\,\mathrm{sgn}(E'-(E_{\mathrm{F}}-E))\,R_{\mathrm{I}}I_{\mathrm{II}} + \mathrm{sgn}(E'-E_{\mathrm{F}})\,I_{\mathrm{I}}R_{\mathrm{II}} \\
&\qquad -\mathrm{i}\Big(R_{\mathrm{I}}R_{\mathrm{II}} - \mathrm{sgn}(E'-(E_{\mathrm{F}}-E))\,\mathrm{sgn}(E'-E_{\mathrm{F}})\,I_{\mathrm{I}}I_{\mathrm{II}}\Big)\Big] \\
&\underset{(D.46)}{=} \int \frac{\mathrm{d}E'}{2\pi}\Big[\,\mathrm{sgn}(E'-(E_{\mathrm{F}}-E))\,R_{\mathrm{I}}I_{\mathrm{II}} + \mathrm{sgn}(E'-E_{\mathrm{F}})\,I_{\mathrm{I}}R_{\mathrm{II}} \\
&\qquad -\mathrm{i}\Big(1 - \mathrm{sgn}(E'-(E_{\mathrm{F}}-E))\,\mathrm{sgn}(E'-E_{\mathrm{F}})\Big)I_{\mathrm{I}}I_{\mathrm{II}}\Big] \\
&= \int_{-\infty}^{E_{\mathrm{F}}-|E|} \frac{\mathrm{d}E'}{2\pi}\Big[-R_{\mathrm{I}}I_{\mathrm{II}} - I_{\mathrm{I}}R_{\mathrm{II}}\Big] \\
&+ \int_{E_{\mathrm{F}}-|E|}^{E_{\mathrm{F}}} \frac{\mathrm{d}E'}{2\pi}\Big[\mathrm{sgn}(E)\,R_{\mathrm{I}}I_{\mathrm{II}} - I_{\mathrm{I}}R_{\mathrm{II}} - \mathrm{i}\Big(1+\mathrm{sgn}(E)\Big)I_{\mathrm{I}}I_{\mathrm{II}}\Big] \\
&+ \int_{E_{\mathrm{F}}}^{E_{\mathrm{F}}+|E|} \frac{\mathrm{d}E'}{2\pi}\Big[\mathrm{sgn}(E)\,R_{\mathrm{I}}I_{\mathrm{II}} + I_{\mathrm{I}}R_{\mathrm{II}} - \mathrm{i}\Big(1-\mathrm{sgn}(E)\Big)I_{\mathrm{I}}I_{\mathrm{II}}\Big] \\
&+ \int_{E_{\mathrm{F}}+|E|}^{\infty} \frac{\mathrm{d}E'}{2\pi}\Big[R_{\mathrm{I}}I_{\mathrm{II}} + I_{\mathrm{I}}R_{\mathrm{II}}\Big]\,. \qquad \text{(D.49)}
\end{aligned}$$

Due to the signum functions the integration has to be split into four integrals. For the two middle ones the product of two signum functions was replaced by one, which is only correct within the corresponding bounds of integration. By use of Eq. (D.47) one can incorporate the last integral into the other three. This leads to

$$\begin{aligned}
\chi^{[t]0}_{36;54}(E) &= 2\int_{-\infty}^{E_{\mathrm{F}}-|E|} \frac{\mathrm{d}E'}{2\pi}\Big[-R_{\mathrm{I}}I_{\mathrm{II}} - I_{\mathrm{I}}R_{\mathrm{II}}\Big] \\
&+ \int_{E_{\mathrm{F}}-|E|}^{E_{\mathrm{F}}} \frac{\mathrm{d}E'}{2\pi}\Big[(-1+\mathrm{sgn}(E))R_{\mathrm{I}}I_{\mathrm{II}} - 2I_{\mathrm{I}}R_{\mathrm{II}} - \mathrm{i}\Big(1+\mathrm{sgn}(E)\Big)I_{\mathrm{I}}I_{\mathrm{II}}\Big] \\
&+ \int_{E_{\mathrm{F}}}^{E_{\mathrm{F}}+|E|} \frac{\mathrm{d}E'}{2\pi}\Big[(-1+\mathrm{sgn}(E))R_{\mathrm{I}}I_{\mathrm{II}} - \mathrm{i}\Big(1-\mathrm{sgn}(E)\Big)I_{\mathrm{I}}I_{\mathrm{II}}\Big] \\
&= 2\int_{-\infty}^{E_{\mathrm{F}}} \frac{\mathrm{d}E'}{2\pi}\Big[-R_{\mathrm{I}}I_{\mathrm{II}} - I_{\mathrm{I}}R_{\mathrm{II}}\Big] \\
&+ (1+\mathrm{sgn}(E))\int_{E_{\mathrm{F}}-|E|}^{E_{\mathrm{F}}} \frac{\mathrm{d}E'}{2\pi}\Big[(R_{\mathrm{I}} - \mathrm{i}I_{\mathrm{I}})I_{\mathrm{II}}\Big] \\
&+ (1-\mathrm{sgn}(E))\int_{E_{\mathrm{F}}}^{E_{\mathrm{F}}+|E|} \frac{\mathrm{d}E'}{2\pi}\Big[(-R_{\mathrm{I}} - \mathrm{i}I_{\mathrm{I}})I_{\mathrm{II}}\Big]\,. \qquad \text{(D.50)}
\end{aligned}$$

Depending on the sign of E either the second or the third integral is multiplied by zero and does not contribute. In total we find the expression

$$\chi^{[t]0}_{36;54}(E) = -2\int_{-\infty}^{E_\mathrm{F}} \frac{\mathrm{d}E'}{2\pi}\left[R_\mathrm{I} I_\mathrm{II} + I_\mathrm{I} R_\mathrm{II}\right] + 2\int_{E_\mathrm{F}-E}^{E_\mathrm{F}} \frac{\mathrm{d}E'}{2\pi}\left(R_\mathrm{I} - \mathrm{i}\,\mathrm{sgn}(E)\, I_\mathrm{I}\right) I_\mathrm{II} \quad \text{(D.51)}$$

for the time-ordered susceptibility. Now, the remaining task is to find the expression for the retarded susceptibility and relate it to Eq. (D.51).

Similar to the Green functions one arrives at the retarded susceptibility by replacing $-\mathrm{i}0^+$ by $+\mathrm{i}0^+$ in the second term of Eq. (D.34), the definition of the time-ordered susceptibility in Fourier space. This leads to

$$\chi^{[R]0}_{36;54}(E_2) = \sum_{n,m} \phi_n(\vec{r}_3)\phi_n^*(\vec{r}_4)\phi_m(\vec{r}_6)\phi_m^*(\vec{r}_5)\frac{f_n - f_m}{E_2 - (E_m - E_n) + \mathrm{i}0^+}\,. \quad \text{(D.52)}$$

By use of the Sokhatsky–Weierstrass theorem (see Eq. (C.5)) the energy-depending part of the time-ordered susceptibility (see Eq. (D.34)) can be written as

$$\begin{aligned} &\frac{f_n(1-f_m)}{E-(E_m-E_n)+\mathrm{i}0^+} - \frac{(1-f_n)f_m}{E-(E_m-E_n)-\mathrm{i}0^+} \\ =\;& (f_n - f_m)\frac{\mathcal{P}}{E-(E_m-E_n)} - \mathrm{i}\pi\delta(E-(E_m-E_n))\,(f_n + f_m - 2f_n f_m)\,. \end{aligned} \quad \text{(D.53)}$$

Doing the same for the retarded susceptibility (see Eq. (D.52)) results in

$$\begin{aligned} &\frac{f_n - f_m}{E-(E_m-E_n)+\mathrm{i}0^+} \\ =\;& (f_n - f_m)\left(\frac{\mathcal{P}}{E-(E_m-E_n)} - \mathrm{i}\pi\delta(E-(E_m-E_n))\right)\,, \end{aligned} \quad \text{(D.54)}$$

such that the difference between time-ordered and retarded susceptibility can be cut down to the two expressions

$$f_n - f_m + 2(f_n-1)f_m = \begin{cases} 1 & ,\ E_n < E_\mathrm{F} < E_m \\ 1 & ,\ E_m < E_\mathrm{F} < E_n \\ 0 & ,\ \text{else} \end{cases} \quad \text{(D.55)}$$

and

$$f_n - f_m = \begin{cases} 1 & ,\ E_n < E_\mathrm{F} < E_m \\ -1 & ,\ E_m < E_\mathrm{F} < E_n \\ 0 & ,\ \text{else} \end{cases}\,. \quad \text{(D.56)}$$

A comparison of Eqs. (D.55) and (D.56) reveals that they are identical up to a change in sign for the case that $E_m - E_n < 0$. As a consequence, the connection between time-ordered and retarded susceptibility is given by

$$\chi^{[t]0}_{36;54}(E) = \mathrm{Re}\chi^{[R]0}_{36;54}(E) + \mathrm{i}\,\mathrm{sgn}(E)\,\mathrm{Im}\chi^{[R]0}_{36;54}(E)\ . \tag{D.57}$$

Using Eq. (D.51) we arrive at the retarded form for the susceptibility

$$\begin{aligned}
&\chi^{[R]0}_{36;54}(E) \\
&\quad = \quad -2\int_{-\infty}^{E_\mathrm{F}} \frac{\mathrm{d}E'}{2\pi}\left[\mathrm{Re}G^{[R]0}_{3,4}(E')\mathrm{Im}G^{[R]0}_{6,5}(E+E') + \mathrm{Im}G^{[R]0}_{3,4}(E')\mathrm{Re}G^{[R]0}_{6,5}(E+E')\right] \\
&\qquad +2\int_{E_\mathrm{F}-E}^{E_\mathrm{F}} \frac{\mathrm{d}E'}{2\pi}\left(\mathrm{Re}G^{[R]0}_{3,4}(E') - \mathrm{i}\mathrm{Im}G^{[R]0}_{3,4}(E')\right)\mathrm{Im}G^{[R]0}_{5,6}(E+E')\ .
\end{aligned} \tag{D.58}$$

This expression can be related to the form of the Kohn-Sham susceptibility as implemented in the KKR program, see Eq. (4.37).

D.3.2. The lowest order retarded self-energy

Analogue to the procedure of finding the expression for the retarded susceptibility we now derive a connections between time-ordered and retarded self-energy and describe the latter in terms of retarded Green functions. The convolution of the Green function and the susceptibility (see Eq. (D.29)) reads

$$\begin{aligned}
&S^{[t]0}_{53;46}(E) \\
&\quad = \qquad \mathrm{i}\int \frac{\mathrm{d}E'}{2\pi} G^{[t]0}_{5,6}(E+E')\chi^{[t]0}_{36;54}(E') \\
&\quad \underset{(D.44),(D.57)}{=} \quad \mathrm{i}\int \frac{\mathrm{d}E'}{2\pi}\left[\mathrm{Re}G^{[R]0}_{56}(E+E') + \mathrm{i}\,\mathrm{sgn}(E+E'-E_\mathrm{F})\,\mathrm{Im}G^{[R]0}_{56}(E+E')\right] \\
&\qquad\qquad \times\left[\mathrm{Re}\chi^{[R]0}_{36;54}(E') + \mathrm{i}\,\mathrm{sgn}(E')\,\mathrm{Im}\chi^{[R]0}_{36;54}(E')\right]\ .
\end{aligned} \tag{D.59}$$

Again, in order to improve the readability, we temporarily define $\tilde{R}_\mathrm{I} = \mathrm{Re}G^{[R]0}_{56}(E+E')$ and $\tilde{I}_\mathrm{I} = \mathrm{Im}G^{[R]0}_{56}(E+E')$, as well as $\tilde{R}_\mathrm{II} = \mathrm{Re}\chi^{[R]0}_{36;54}(E')$ and $\tilde{I}_\mathrm{II} = \mathrm{Im}\chi^{[R]0}_{36;54}(E')$ and

make use of identities similar to those shown in Eqs. (D.46) and (D.47). We find

$$\begin{aligned}
& S^{[t]0}_{53;46}(E) \\
= \;& \mathrm{i}\int \frac{\mathrm{d}E'}{2\pi}\Big[\tilde{R}_{\mathrm{I}}\tilde{R}_{\mathrm{II}} - \operatorname{sgn}(E'-(E_{\mathrm{F}}-E))\operatorname{sgn}(E')\,\tilde{I}_{\mathrm{I}}\tilde{I}_{\mathrm{II}} \\
& \qquad +\mathrm{i}\Big(\operatorname{sgn}(E')\,\tilde{R}_{\mathrm{I}}\tilde{I}_{\mathrm{II}} + \operatorname{sgn}(E'-(E_{\mathrm{F}}-E))\,\tilde{I}_{\mathrm{I}}\tilde{R}_{\mathrm{II}}\Big)\Big] \\
= \;& \mathrm{i}\int \frac{\mathrm{d}E'}{2\pi}\Big[(1-\operatorname{sgn}(E'-(E_{\mathrm{F}}-E))\operatorname{sgn}(E'))\,\tilde{I}_{\mathrm{I}}\tilde{I}_{\mathrm{II}} \\
& \qquad +\mathrm{i}\Big(\operatorname{sgn}(E')\,\tilde{R}_{\mathrm{I}}\tilde{I}_{\mathrm{II}} + \operatorname{sgn}(E'-(E_{\mathrm{F}}-E))\,\tilde{I}_{\mathrm{I}}\tilde{R}_{\mathrm{II}}\Big)\Big] \\
= \;& \int_{-\infty}^{-|E_{\mathrm{F}}-E|}\frac{\mathrm{d}E'}{2\pi}\Big(\tilde{R}_{\mathrm{I}}\tilde{I}_{\mathrm{II}} + \tilde{I}_{\mathrm{I}}\tilde{R}_{\mathrm{II}}\Big) \\
+ \;& \int_{-|E_{\mathrm{F}}-E|}^{0}\frac{\mathrm{d}E'}{2\pi}\Big[\mathrm{i}\,(1-\operatorname{sgn}(E_{\mathrm{F}}-E))\,\tilde{I}_{\mathrm{I}}\tilde{I}_{\mathrm{II}} + \Big(\tilde{R}_{\mathrm{I}}\tilde{I}_{\mathrm{II}} + \operatorname{sgn}(E_{\mathrm{F}}-E)\,\tilde{I}_{\mathrm{I}}\tilde{R}_{\mathrm{II}}\Big)\Big] \\
+ \;& \int_{0}^{|E_{\mathrm{F}}-E|}\frac{\mathrm{d}E'}{2\pi}\Big[\mathrm{i}\,(1+\operatorname{sgn}(E_{\mathrm{F}}-E))\,\tilde{I}_{\mathrm{I}}\tilde{I}_{\mathrm{II}} + \Big(-\tilde{R}_{\mathrm{I}}\tilde{I}_{\mathrm{II}} + \operatorname{sgn}(E_{\mathrm{F}}-E)\,\tilde{I}_{\mathrm{I}}\tilde{R}_{\mathrm{II}}\Big)\Big] \\
- \;& \int_{|E_{\mathrm{F}}-E|}^{\infty}\frac{\mathrm{d}E'}{2\pi}\Big(\tilde{R}_{\mathrm{I}}\tilde{I}_{\mathrm{II}} + \tilde{I}_{\mathrm{I}}\tilde{R}_{\mathrm{II}}\Big)\,. \qquad \text{(D.60)}
\end{aligned}$$

Due to the signum functions the integration has to be split into four integrals. For the two middle ones the product of two signum functions was replaced by one, which is only correct within the corresponding bounds of integration. We get

$$\begin{aligned}
S^{[t]0}_{53;46}(E) \;=\; & -2\int_{0}^{\infty}\frac{\mathrm{d}E'}{2\pi}\Big[\tilde{R}_{\mathrm{I}}\tilde{I}_{\mathrm{II}} - \tilde{I}_{\mathrm{I}}\tilde{R}_{\mathrm{II}}\Big] \\
& -(1-\operatorname{sgn}(E_{\mathrm{F}}-E))\int_{-|E_{\mathrm{F}}-E|}^{0}\frac{\mathrm{d}E'}{2\pi}\tilde{I}_{\mathrm{I}}(\tilde{R}_{\mathrm{II}} - \mathrm{i}\tilde{I}_{\mathrm{II}}) \\
& -(1+\operatorname{sgn}(E_{\mathrm{F}}-E))\int_{0}^{|E_{\mathrm{F}}-E|}\frac{\mathrm{d}E'}{2\pi}\tilde{I}_{\mathrm{I}}(-\tilde{R}_{\mathrm{II}} - \mathrm{i}\tilde{I}_{\mathrm{II}})\,. \qquad \text{(D.61)}
\end{aligned}$$

Depending on the sign of $E_{\mathrm{F}}-E$ either the second or the third integral does not contribute. In total we find for the time-ordered lowest order self-energy the expression

$$\begin{aligned}
\Sigma^{[t]0}_{34}(E) \;=\; & \int \mathrm{d}\vec{r}_5 \int \mathrm{d}\vec{r}_6 U_{3,5}U_{6,4} \\
& \Big[-2\int_{0}^{\infty}\frac{\mathrm{d}E'}{2\pi}\Big(\tilde{R}_{\mathrm{I}}\tilde{I}_{\mathrm{II}} + \tilde{I}_{\mathrm{I}}\tilde{R}_{\mathrm{II}}\Big) - 2\int_{E_{\mathrm{F}}-E}^{0}\frac{\mathrm{d}E'}{2\pi}\tilde{I}_{\mathrm{I}}\Big(\tilde{R}_{\mathrm{II}} - \mathrm{i}\operatorname{sgn}(E-E_{\mathrm{F}})\,\tilde{I}_{\mathrm{II}}\Big)\Big]\,. \qquad \text{(D.62)}
\end{aligned}$$

The retarded self-energy is obtained when replacing $-\mathrm{i}0^+$ by $+\mathrm{i}0^+$ in the second term of Eq. (D.39). This leads to

$$\begin{aligned}\Sigma_{34}^{[R]0}(E) &= \int \mathrm{d}\vec{r}_5 \int \mathrm{d}\vec{r}_6 U_{3,5} U_{6,4} \sum_{k,n,m} \phi_k(\vec{r}_5)\phi_k^*(\vec{r}_6)\phi_n(\vec{r}_3)\phi_n^*(\vec{r}_4)\phi_m(\vec{r}_6)\phi_m^*(\vec{r}_5) \\ &\qquad \frac{f_m - f_n f_m - f_k f_m + f_k f_n}{E - (E_k - E_m + E_n) + \mathrm{i}0^+} \,. \end{aligned} \tag{D.63}$$

A comparison of (see energy-dependent terms in Eq. (D.39))

$$\begin{aligned}&\frac{(1-f_k)(1-f_n)f_m}{E-(E_k-E_m+E_n)+\mathrm{i}0^+} + \frac{(f_k f_n(1-f_m)}{E-(E_k-E_m+E_n)-\mathrm{i}0^+} \\ =\ &\frac{\mathcal{P}}{E-(E_k-E_m+E_n)}(f_m - f_n f_m - f_k f_m + f_k f_n) \\ &-\mathrm{i}\pi\delta(E-(E_k-E_m+E_n))\left((f_m - f_n f_m - f_k f_m + f_k f_n) - 2 f_k f_n (1-f_m)\right)\end{aligned} \tag{D.64}$$

and (see energy-dependent terms in Eq. (D.39))

$$\begin{aligned}&\frac{(1-f_k)(1-f_n)f_m}{E-(E_k-E_m+E_n)+\mathrm{i}0^+} + \frac{(f_k f_n(1-f_m)}{E-(E_k-E_m+E_n)+\mathrm{i}0^+} \\ =\ &\frac{\mathcal{P}}{E-(E_k-E_m+E_n)}(f_m - f_n f_m - f_k f_m + f_k f_n) \\ &-\mathrm{i}\pi\delta(E-(E_k-E_m+E_n))\,(f_m - f_n f_m - f_k f_m + f_k f_n)\end{aligned} \tag{D.65}$$

reveals that the retarded and the time-ordered self-energy differ only when $f_k f_n(1-f_m) \neq 0$, *i.e.*, E_m is above the Fermi energy whereas E_k and E_n are below. In combination with the δ-function for the energy argument this leads to the inequation

$$E = E_k - E_m + E_n < E_\mathrm{F} - E_\mathrm{F} + E_\mathrm{F} = E_\mathrm{F} \,. \tag{D.66}$$

If this inequation is fulfilled, one finds

$$f_m - f_n f_m - f_k f_m + f_k f_n = 1 \tag{D.67}$$

and

$$f_m - f_n f_m - f_k f_m + f_k f_n - 2 f_k f_n (1-f_m) = -1 \tag{D.68}$$

In total this leads to the connection between time-ordered and retarded self-energy,

$$\Sigma_{34}^{[t]0}(E) = \mathrm{Re}\Sigma_{34}^{[R]0}(E) + \mathrm{i}\,\mathrm{sgn}(E-E_\mathrm{F})\,\mathrm{Im}\Sigma_{34}^{[R]0}(E) \,. \tag{D.69}$$

Together with Eq. (D.62) this results in the expression

$$\begin{aligned}\Sigma_{34}^{[R],0}(E) &= \int \mathrm{d}\vec{r}_5 \int \mathrm{d}\vec{r}_6 U_{3,5} U_{6,4} \\ &\left[-2\int_0^\infty \frac{\mathrm{d}E'}{2\pi}\left(\tilde{R}_\mathrm{I}\tilde{I}_\mathrm{II} + \tilde{I}_\mathrm{I}\tilde{R}_\mathrm{II}\right) - 2\int_{E_\mathrm{F}-E}^0 \frac{\mathrm{d}E'}{2\pi}\tilde{I}_\mathrm{I}\left(\tilde{R}_\mathrm{II} - \mathrm{i}\tilde{I}_\mathrm{II}\right)\right] ,\end{aligned} \tag{D.70}$$

the retarded lowest order self-energy written in terms of retarded Green functions. If we now replace $\Sigma^{[R]0}$ by $\Sigma^{[R]}$ (meaning that $\chi^{[R]0}$ is replaced by the enhanced susceptibility $\chi^{[R]}$) we arrive at

$$\begin{aligned}\Sigma^{[R]}_{34}(E) &= \int \mathrm{d}\vec{r}_5 \int \mathrm{d}\vec{r}_6 U_{3,5} U_{6,4} \\ &\left[-2 \int_0^\infty \frac{\mathrm{d}E'}{2\pi} \left(\mathrm{Re}G^{[R]0}_{56}(E+E') \mathrm{Im}\chi^{[R]}_{36;54}(E') + \mathrm{Im}G^{[R]0}_{56}(E+E') \mathrm{Re}\chi^{[R]}_{36;54}(E') \right) \right. \\ &\left. -2 \int_{E_\mathrm{F}-E}^0 \frac{\mathrm{d}E'}{2\pi} \mathrm{Im}G^{[R]0}_{56}(E+E') \left(\mathrm{Re}\chi^{[R]}_{36;54}(E') - \mathrm{i}\mathrm{Im}\chi^{[R]}_{36;54}(E') \right) \right] . \end{aligned} \tag{D.71}$$

In addition we assume the Coulomb interaction to act locally in space, $U_{3,5} = U_3 \delta(\vec{r}_3 - \vec{r}_5)$ and $U_{6,4} = U_4 \delta(\vec{r}_6 - \vec{r}_4)$. Thus, we have

$$\begin{aligned}\Sigma^{[R]}_{34}(E) &= -\frac{U_3 U_4}{\pi} \left[\int_0^\infty \mathrm{d}E' \ \mathrm{Im} \left[G^{[R]0}_{34}(E+E') \chi^{[R]}_{34;34}(E') \right] \right. \\ &\left. + \int_{E_\mathrm{F}-E}^0 \mathrm{d}E' \ \mathrm{Im}G^{[R]0}_{34}(E+E') \chi^{[R]}_{34;34}(E')^* \right] . \end{aligned} \tag{D.72}$$

We now identify

$$\begin{aligned} G^{[R]0}_{34}(\Omega+E) &\longrightarrow G^{\sigma,0}_{ij}(\vec{r},\vec{r}\,';\Omega+E) \\ U_3 &\longrightarrow U_i(\vec{r}) \\ U_4 &\longrightarrow U_j(\vec{r}\,') \\ \chi^{[R]}_{34;34}(\Omega) &\longrightarrow \chi^{\sigma\overline{\sigma}}_{i;j}(\vec{r},\vec{r}\,';\Omega+\mathrm{i}0^+) \\ \Sigma^{[R]}_{34}(E) &\longrightarrow \Sigma^{\sigma}_{i;j}(\vec{r},\vec{r}\,';E) \end{aligned} \tag{D.73}$$

and find

$$\begin{aligned}&\Sigma^{\sigma}_{ij}(\vec{r},\vec{r}\,';E) \\ &= -\frac{U_i(\vec{r}) U_j(\vec{r}\,')}{\pi} \left[\int_0^\infty \mathrm{d}\Omega \ \mathrm{Im} \left[G^{\sigma,0}_{iL;jL'}(\vec{r},\vec{r}\,';\Omega+E) \overline{\chi}^{\sigma\overline{\sigma}}_{ij}(\vec{r}\,\vec{r}\,';\Omega) \right] \right. \\ &\left. - \int_0^{-V} \mathrm{d}\Omega \ \mathrm{Im} \left[G^{\sigma,0}_{iL;jL'}(\vec{r},\vec{r}\,';\Omega+E) \right] \overline{\chi}^{\sigma\overline{\sigma}}_{ji}(\vec{r}\,',\vec{r};\Omega)^* \right] , \end{aligned} \tag{D.74}$$

where

$$\overline{\chi}^{\sigma\overline{\sigma}}_{ij}(\vec{r},\vec{r}\,';\Omega) = \sum_{L,L'} \chi^{\sigma\overline{\sigma}}_{iL;jL'}(\vec{r},\vec{r}\,';\Omega) . \tag{D.75}$$

This expression is of the same structure as the one implemented in the KKR program. A derivation within the Matsubara formalism is presented in Appendix E.

E. The derivation within the Matsubara formalism

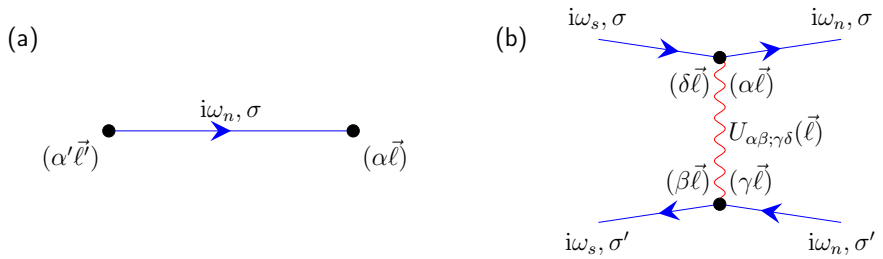

Figure E.1.: (a) The basic one electron Green function $G^{0(\sigma)}_{\alpha\alpha'}(\vec{\ell}\vec{\ell}';i\omega_n)$ as it appears in the shown Feynman diagrams. (b) The Feynman diagram that describes the Coulomb interaction $U_{\alpha\beta;\gamma\delta}(\vec{\ell})$ and how Green functions connect to it. The energy transfer is given by $i(\omega_s - \omega_n)$.

(This survey follows notes that were written by D. Mills.)

Let $G^{(\sigma)}_{\alpha\alpha'}(\vec{\ell},\vec{\ell}';i\omega_n)$ be the one electron Green function which describes a creation of an electron of energy $i\omega_n$ and of spin σ in orbital α' at site $\vec{\ell}'$ and its subsequent propagation to site $\vec{\ell}$, where it is destroyed in orbital α. The Dyson equation then reads

$$\begin{aligned} G^{(\sigma)}_{\alpha\alpha'}(\vec{\ell},\vec{\ell}';i\omega_n) &= G^{0(\sigma)}_{\alpha\alpha'}(\vec{\ell},\vec{\ell}';i\omega_n) \\ &+ \sum_{\vec{\ell}''\vec{\ell}''';\alpha''\alpha'''} G^{0(\sigma)}_{\alpha\alpha''}(\vec{\ell},\vec{\ell}'';i\omega_n)\Sigma^{(\sigma)}_{\alpha''\alpha'''}(\vec{\ell}'',\vec{\ell}''';i\omega_n)G^{(\sigma)}_{\alpha'''\alpha'}(\vec{\ell}''',\vec{\ell}';i\omega_n)\ , \end{aligned} \tag{E.1}$$

where $G^{0(\sigma)}_{\alpha\alpha'}(\vec{\ell},\vec{\ell}';i\omega_n)$ is the basic one electron Green function from which the diagrams are build, see Fig. E.1(a). The Coulomb interaction has the form

$$V_C = \frac{1}{2}\sum_{\sigma\sigma'}\sum_{\alpha\beta\gamma\delta} U_{\alpha\beta;\gamma\delta}(\vec{\ell})\hat{c}_{\alpha\sigma}(\vec{\ell})^\dagger \hat{c}_{\beta\sigma'}(\vec{\ell})^\dagger \hat{c}_{\gamma\sigma'}(\vec{\ell})\hat{c}_{\delta\sigma}(\vec{\ell})\ , \tag{E.2}$$

where the corresponding basic Coulomb scattering vertex $U_{\alpha\beta;\gamma\delta}(\vec{\ell})$ is shown in Fig. E.1(b).

In the following we want to examine the diagrammatic structure of $\Sigma^{(\sigma)}_{\alpha\alpha'}(\vec{\ell},\vec{\ell}';i\omega_n)$. Fig. E.2 shows a Feynman diagram which will lead us into the spin wave feature. We define the

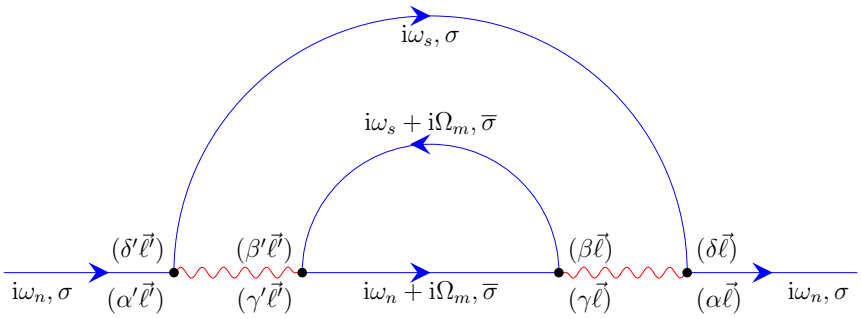

Figure E.2.: The Feynman diagram for the self-energy as given in Eq. (E.3).

shown element as $\Sigma^{0(\sigma)}_{\alpha\alpha'}(\vec{\ell},\vec{\ell}';\mathrm{i}\omega_n)$. It can be seen as the lowest order contribution to the proper self-energy. If we write this out we have

$$\Sigma^{0(\sigma)}_{\alpha\alpha'}(\vec{\ell},\vec{\ell}';\mathrm{i}\omega_n) = \sum_{\beta\beta'\gamma\gamma'\delta\delta'} U_{\alpha\beta;\gamma\delta}(\vec{\ell}) S^{0(\sigma)}_{\gamma\delta\beta';\beta\delta'\gamma'}(\mathrm{i}\omega_n) U_{\delta'\gamma';\beta'\alpha'}(\vec{\ell}') \;, \tag{E.3}$$

where

$$S^{0(\sigma)}_{\gamma\delta\beta';\beta\delta'\gamma'}(\mathrm{i}\omega_n) = \frac{1}{\beta}\sum_{\mathrm{i}\Omega_m} G^{0(\bar{\sigma})}_{\gamma\gamma'}(\vec{\ell},\vec{\ell}';\mathrm{i}\omega_n + \mathrm{i}\Omega_m)\Gamma^{0(\sigma\bar{\sigma})}_{\delta\beta';\beta\delta'}(\vec{\ell},\vec{\ell}';\mathrm{i}\Omega_m) \tag{E.4}$$

and

$$\Gamma^{0(\sigma\bar{\sigma})}_{\delta\beta';\beta\delta'}(\vec{\ell},\vec{\ell}';\mathrm{i}\Omega_m) = -\frac{1}{\beta}\sum_{\mathrm{i}\omega_s} G^{0(\sigma)}_{\delta\delta'}(\vec{\ell},\vec{\ell}';\mathrm{i}\omega_s) G^{0(\bar{\sigma})}_{\beta'\beta}(\vec{\ell}',\vec{\ell};\mathrm{i}\omega_s + \mathrm{i}\Omega_m) \;. \tag{E.5}$$

The factor of -1 in the latter equation accounts for the fermion closed loop.

In a second step we account for the random-phase approximation (RPA, see Fig. E.3) and in Eq. (E.3) replace $\Gamma^{0(\sigma\bar{\sigma})}$ by $\Gamma^{(\sigma\bar{\sigma})}$. This is possible because the analytic properties of $\Gamma^{0(\sigma\bar{\sigma})}$ and $\Gamma^{(\sigma\bar{\sigma})}$ are the same. We analyze the structure of $\Gamma^{0(\sigma\bar{\sigma})}$, and then the one of the self-energy. We wish to perform the sum over $\mathrm{i}\omega_s$ in $\Gamma^{0(\sigma\bar{\sigma})}$ first.

Figure E.3.: (a) Feynman representation of $\Gamma^{0(\sigma\bar{\sigma})}$. This term appears in Eq. (E.3). (b) In the RPA $\Gamma^{0(\sigma\bar{\sigma})}$ is defined as an infinite sum over two Green functions that interact via the Coulomb interaction.

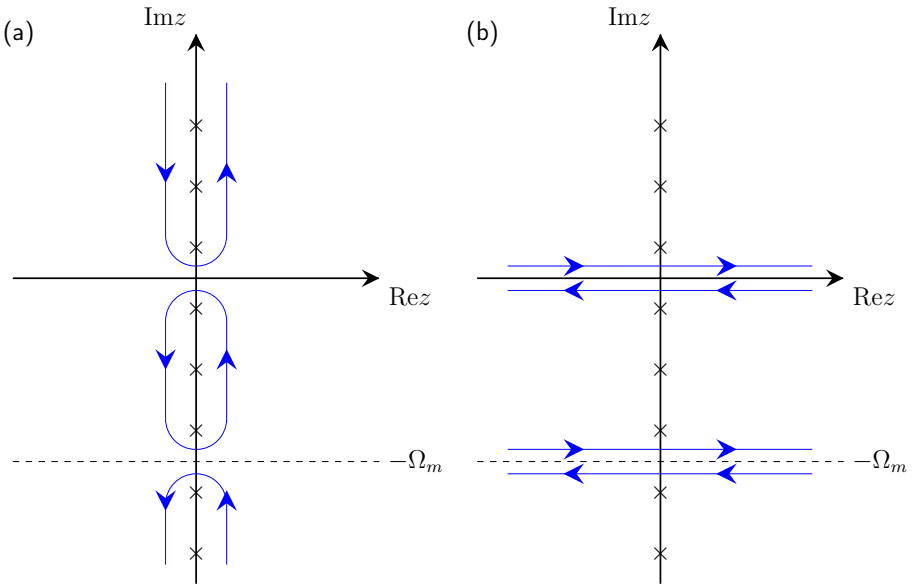

Figure E.4.: (a) Contour $\mathcal{C}$ in complex energy plane as used in Eq. (E.7) for Γ. The Matsubara points $\mathrm{i}\omega_s$ are indicated by $\times$'s. (b) Distorted contour.

E.1. The Structure of $\Gamma^{0(\sigma\overline{\sigma})}$

We suppress all indices and site labels, and write

$$\Gamma^{0(\sigma\overline{\sigma})}(\mathrm{i}\Omega_m) = -\frac{1}{\beta}\sum_{\mathrm{i}\omega_s} G^{0(\sigma)}(\mathrm{i}\omega_s)G^{0(\overline{\sigma})}(\mathrm{i}\omega_s + \mathrm{i}\Omega_m) \tag{E.6}$$

where $\mathrm{i}\omega_s = \mathrm{i}\frac{2\pi}{\beta}(s+\frac{1}{2})$ and $\mathrm{i}\Omega_m = \mathrm{i}\frac{2\pi}{\beta}m$. Now $f(z) = \left(\mathrm{e}^{\beta z}+1\right)^{-1}$ has poles at $z = -\mathrm{i}\omega_s$ with residue $-1/\beta$. Thus, we can write

$$\Gamma^{0(\sigma\overline{\sigma})}(\mathrm{i}\Omega_m) = -\frac{1}{2\pi\mathrm{i}}\oint_{\mathcal{C}} \mathrm{d}z f(z)G^{0(\sigma)}(z)G^{0(\overline{\sigma})}(z+\mathrm{i}\Omega_m) \tag{E.7}$$

with a complex energy contour $\mathcal{C}$ as shown in Fig. E.4(a). Note that the Green function $G^{0(\sigma)}(z)$ has a branch cut along $\mathrm{Im}z = 0$, so that the contour integration is chosen such that it does not cross those branches. In order to solve the complex contour integration we distort $\mathcal{C}$ so that it becomes as given in Fig. E.4(b). Thus, for a sufficiently small number

$\eta > 0$, the integration can be represented by two integrals with real argument ϵ:

$$\begin{aligned}
&\Gamma^{0(\sigma\overline{\sigma})}(\mathrm{i}\Omega_m) \\
&\quad = -\frac{1}{2\pi\mathrm{i}}\Bigg[\int_{-\infty}^{\infty}\mathrm{d}\epsilon f(\epsilon)\left(G^{0(\sigma)}(\epsilon+\mathrm{i}\eta)-G^{0(\sigma)}(\epsilon-\mathrm{i}\eta)\right)G^{0(\overline{\sigma})}(\epsilon+\mathrm{i}\Omega_m) \\
&\qquad\quad +\int_{-\infty}^{\infty}\mathrm{d}\epsilon f(\epsilon-\mathrm{i}\Omega_m)G^{0(\sigma)}(\epsilon-\mathrm{i}\Omega_m)\left(G^{0(\overline{\sigma})}(\epsilon+\mathrm{i}\eta)-G^{0(\overline{\sigma})}(\epsilon-\mathrm{i}\eta)\right)\Bigg] \\
&\quad = \int_{-\infty}^{\infty}\mathrm{d}\epsilon f(\epsilon)\left[\rho^{0(\sigma)}(\epsilon)G^{0(\overline{\sigma})}(\epsilon+\mathrm{i}\Omega_m)+G^{0(\sigma)}(\epsilon-\mathrm{i}\Omega_m)\rho^{0(\overline{\sigma})}(\epsilon)\right], \qquad \text{(E.8)}
\end{aligned}$$

where $f(\epsilon-\mathrm{i}\Omega_m)=f(\epsilon)$ was used and the spectral density

$$\rho^{0(\sigma)}(\epsilon)=-\frac{1}{2\pi\mathrm{i}}\left(G^{0(\sigma)}(\epsilon+\mathrm{i}\eta)-G^{0(\sigma)}(\epsilon-\mathrm{i}\eta)\right) \qquad \text{(E.9)}$$

for the basic one electron Green function was defined.

Now we restore the subscripts and suppose that

$$G^{0(\sigma)}_{\delta\delta'}(\vec{\ell},\vec{\ell}';z)=\sum_{\lambda}\frac{\hat{\psi}^{(\sigma)}_{\delta,\lambda}(\vec{\ell})\hat{\psi}^{(\sigma)}_{\delta',\lambda}(\vec{\ell}')^*}{z-\epsilon^{(\sigma)}_{\lambda}}\,. \qquad \text{(E.10)}$$

This leads to

$$\begin{aligned}
\rho^{0(\sigma)}_{\delta\delta'}(\vec{\ell},\vec{\ell}';\epsilon) &= -\frac{1}{2\pi\mathrm{i}}\left(G^{0(\sigma)}_{\delta\delta'}(\vec{\ell},\vec{\ell}';\epsilon+\mathrm{i}\eta)-G^{0(\sigma)}_{\delta\delta'}(\vec{\ell},\vec{\ell}';\epsilon-\mathrm{i}\eta)\right) \\
&= \sum_{\lambda}\hat{\psi}^{(\sigma)}_{\delta,\lambda}(\vec{\ell})\hat{\psi}^{(\sigma)}_{\delta',\lambda}(\vec{\ell}')^*\delta\left(\epsilon-\epsilon^{(\sigma)}_{\lambda}\right) \qquad \text{(E.11)}
\end{aligned}$$

and thus

$$\begin{aligned}
&\Gamma^{0(\sigma\overline{\sigma})}_{\delta\beta';\beta\delta'}(\vec{\ell},\vec{\ell}';\mathrm{i}\Omega_m) \\
&\quad = \int\mathrm{d}\epsilon f(\epsilon)\left[\rho^{0(\sigma)}_{\delta\delta'}(\vec{\ell},\vec{\ell}';\epsilon)G^{0(\overline{\sigma})}_{\beta'\beta}(\vec{\ell}',\vec{\ell};\epsilon+\mathrm{i}\Omega_m)+G^{0(\sigma)}_{\delta\delta'}(\vec{\ell},\vec{\ell}';\epsilon-\mathrm{i}\Omega_m)\rho^{0(\overline{\sigma})}_{\beta'\beta}(\vec{\ell}',\vec{\ell};\epsilon)\right] \\
&\quad = \sum_{\lambda\lambda'}\int\mathrm{d}\epsilon f(\epsilon)\Bigg[\hat{\psi}^{(\sigma)}_{\delta,\lambda}(\vec{\ell})\hat{\psi}^{(\sigma)}_{\delta',\lambda}(\vec{\ell}')^*\delta\left(\epsilon-\epsilon^{(\sigma)}_{\lambda}\right)\frac{\hat{\psi}^{(\overline{\sigma})}_{\beta',\lambda'}(\vec{\ell}')\hat{\psi}^{(\overline{\sigma})}_{\beta,\lambda'}(\vec{\ell})^*}{\epsilon+\mathrm{i}\Omega_m-\epsilon^{(\overline{\sigma})}_{\lambda'}} \\
&\qquad\qquad +\frac{\hat{\psi}^{(\sigma)}_{\delta,\lambda}(\vec{\ell})\hat{\psi}^{(\sigma)}_{\delta',\lambda}(\vec{\ell}')^*}{\epsilon-\mathrm{i}\Omega_m-\epsilon^{(\sigma)}_{\lambda}}\hat{\psi}^{(\overline{\sigma})}_{\beta',\lambda'}(\vec{\ell}')\hat{\psi}^{(\overline{\sigma})}_{\beta,\lambda'}(\vec{\ell})^*\delta\left(\epsilon-\epsilon^{(\overline{\sigma})}_{\lambda'}\right)\Bigg] \\
&\quad = \sum_{\lambda\lambda'}\hat{\psi}^{(\sigma)}_{\delta,\lambda}(\vec{\ell})\hat{\psi}^{(\overline{\sigma})}_{\beta',\lambda'}(\vec{\ell}')\frac{f\left(\epsilon^{(\sigma)}_{\lambda}\right)-f\left(\epsilon^{(\overline{\sigma})}_{\lambda'}\right)}{\epsilon^{(\sigma)}_{\lambda}-\epsilon^{(\overline{\sigma})}_{\lambda'}+\mathrm{i}\Omega_m}\hat{\psi}^{(\overline{\sigma})}_{\beta,\lambda'}(\vec{\ell})^*\hat{\psi}^{(\sigma)}_{\delta',\lambda}(\vec{\ell}')^* \qquad \text{(E.12)}
\end{aligned}$$

This is the structure of the electron hole propagator for finite temperatures. The numerator of each summand in Eq. (E.12) contains a difference of two Fermi functions, which

accounts for a probability to have an electron-hole excitation in eigenstates λ and λ'. The denominator of each summand shows a resonance for eigenstate energy differences that match the real part of the argument, $\mathrm{i}\Omega_m$. The structure of Eq. (E.12) is comparable to the general structure of the zero order two particle Green function, as given for example by Tang *et al.* in Eq. (2.23) of Ref. [107].

Note that numerically it is more convenient to write the spectral density in terms of the Green function on the same side of the branch cut. Because of the identity

$$G^{0(\sigma)}_{\delta\delta'}(\vec{\ell},\vec{\ell}';z^*) = G^{0(\sigma)}_{\delta'\delta}(\vec{\ell}',\vec{\ell};z)^* \tag{E.13}$$

(can be shown by use of Eq. (E.10)) the spectral density can be written as

$$\rho^{0(\sigma)}_{\delta\delta'}(\vec{\ell},\vec{\ell}';\epsilon) = -\frac{1}{2\pi\mathrm{i}}\left(G^{0(\sigma)}_{\delta\delta'}(\vec{\ell},\vec{\ell}';\epsilon+\mathrm{i}\eta) - G^{0(\sigma)}_{\delta'\delta}(\vec{\ell}',\vec{\ell};\epsilon+\mathrm{i}\eta)^*\right) . \tag{E.14}$$

E.2. The Sum Over $\mathrm{i}\Omega_m$ in the Proper Self-Energy

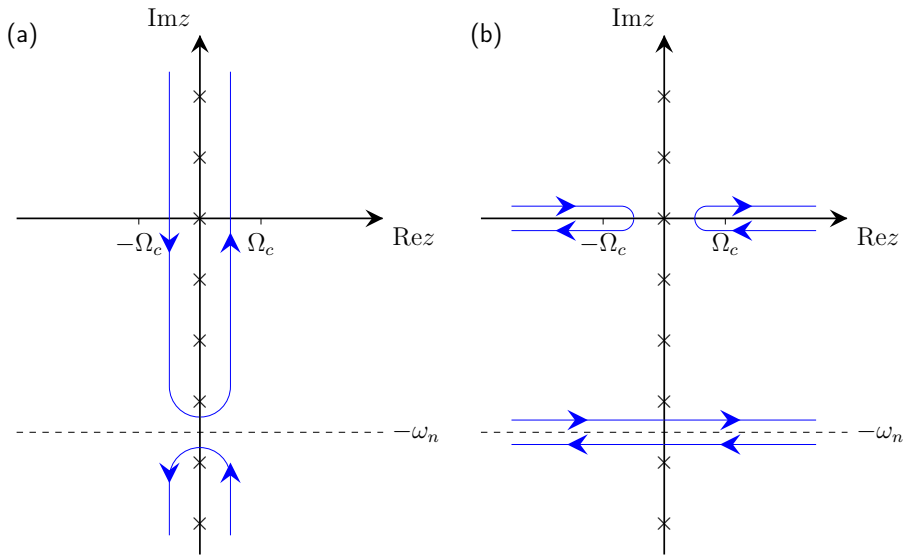

Figure E.5.: (a) Contour $\mathcal{C}$ in complex energy plane as used in Eq. (E.16) for S. The Matsubara points $\mathrm{i}\Omega_m$ are indicated by $\times$'s. (b) Distorted contour.

Suppress indices and site labels again. One has to consider

$$S^{(\sigma)}(\mathrm{i}\omega_n) = \frac{1}{\beta}\sum_{\mathrm{i}\Omega_m} G^{0(\overline{\sigma})}(\mathrm{i}\omega_n + \mathrm{i}\Omega_m)\Gamma^{(\sigma\overline{\sigma})}(\mathrm{i}\Omega_m) \tag{E.15}$$

where $\Gamma^{0(\sigma\overline{\sigma})}(\mathrm{i}\Omega_m)$ is replaced by the full propagator $\Gamma^{(\sigma\overline{\sigma})}(\mathrm{i}\Omega_m)$. As noted earlier, the analytic structure of Γ and Γ^0 are the same, and we give the prescription for calculating Γ below.

Now $\Gamma^{(\sigma\overline{\sigma})}(z)$ has a branch cut along the real axis. On what follows, suppose the branch cut extends from $+\Omega_c$ to ∞, and from $-\Omega_c$ to $-\infty$, where Ω_c is very small. We perform the limes $\Omega_c \to 0$ at the end.

Now the function $\left(1-\mathrm{e}^{-\beta z}\right)^{-1}$ has poles at $z = \mathrm{i}\Omega_m$ with residue $+\frac{1}{\beta}$. Hence we can write

$$S^{(\sigma)}(\mathrm{i}\omega_n) = -\frac{1}{2\pi\mathrm{i}} \oint_{\mathcal{C}} \mathrm{d}z\, [1+n(z)]\, G^{0(\overline{\sigma})}(z+\mathrm{i}\omega_n)\Gamma^{(\sigma\overline{\sigma})}(z) \tag{E.16}$$

where $n(z) = \left(\mathrm{e}^{\beta z}-1\right)^{-1}$ and $1+n(z) = \left(1-\mathrm{e}^{-\beta z}\right)^{-1}$. Here $\mathcal{C}$ is the contour of Fig. E.5(a). The contour can be distorted to the one shown in Fig. E.5(b), so that

$$\begin{aligned} & S^{(\sigma)}(\mathrm{i}\omega_n) \\ &= -\frac{1}{2\pi\mathrm{i}}\Bigg[\int' \mathrm{d}\Omega\, [1+n(\Omega)]\, G^{0(\overline{\sigma})}(\Omega+\mathrm{i}\omega_n) \left(\Gamma^{(\sigma\overline{\sigma})}(\Omega+\mathrm{i}\eta) - \Gamma^{(\sigma\overline{\sigma})}(\Omega-\mathrm{i}\eta)\right) \\ &\quad + \int_{-\infty}^{\infty} \mathrm{d}\epsilon\, [1+n(\epsilon-\mathrm{i}\omega_n)] \left(G^{0(\overline{\sigma})}(\epsilon+\mathrm{i}\eta) - G^{0(\overline{\sigma})}(\epsilon-\mathrm{i}\eta)\right) \Gamma^{(\sigma\overline{\sigma})}(\epsilon-\mathrm{i}\omega_n)\Bigg] . \end{aligned} \tag{E.17}$$

By $\int'$ we indicate that the region from $-\Omega_c$ to $+\Omega_c$ is excluded. With the identity

$$1+n(\epsilon-\mathrm{i}\omega_n) = \frac{1}{1-\mathrm{e}^{-\beta\epsilon}\mathrm{e}^{\mathrm{i}\beta\omega_n}} = \frac{1}{1+\mathrm{e}^{-\beta\epsilon}} = 1-f(\epsilon)\,, \tag{E.18}$$

where $f(\epsilon) = \left(\mathrm{e}^{\beta\epsilon}+1\right)^{-1}$ is the Fermi function, one arrives at

$$\begin{aligned} S^{(\sigma)}(\mathrm{i}\omega_n) &= \int' \mathrm{d}\Omega\, [1+n(\Omega)]\, G^{0(\overline{\sigma})}(\Omega+\mathrm{i}\omega_n)\rho^{\Gamma(\sigma\overline{\sigma})}(\Omega) \\ &\quad + \int_{-\infty}^{\infty} \mathrm{d}\epsilon\, [1-f(\epsilon)]\, \rho^{0(\overline{\sigma})}(\epsilon)\Gamma^{(\sigma\overline{\sigma})}(\epsilon-\mathrm{i}\omega_n)\,, \end{aligned} \tag{E.19}$$

where

$$\rho^{\Gamma(\sigma\overline{\sigma})}(\Omega) = -\frac{1}{2\pi\mathrm{i}}\left(\Gamma^{(\sigma\overline{\sigma})}(\Omega+\mathrm{i}\eta) - \Gamma^{(\sigma\overline{\sigma})}(\Omega-\mathrm{i}\eta)\right) \tag{E.20}$$

was defined. If subscripts and site indices are restored, one uses the identity

$$\Gamma^{(\sigma\overline{\sigma})}_{\delta\beta';\beta\delta'}(\vec{\ell},\vec{\ell}';z^*) = \Gamma^{(\sigma\overline{\sigma})}_{\delta'\beta;\beta'\delta}(\vec{\ell}',\vec{\ell};z)^*\,. \tag{E.21}$$

(can be shown by use of Eq. (E.12)) to find the result for the proper self-energy:

$$\Sigma^{(\sigma)}_{\alpha\alpha'}(\vec{\ell},\vec{\ell}';\mathrm{i}\omega_n) = \sum_{\beta\beta'\gamma\gamma'\delta\delta'} U_{\alpha\beta;\gamma\delta}(\vec{\ell}) S^{(\sigma)}_{\gamma\delta\beta';\beta\delta'\gamma'}(\vec{\ell},\vec{\ell}';\mathrm{i}\omega_n) U_{\delta'\gamma';\beta'\alpha'}(\vec{\ell}')\,, \tag{E.22}$$

where

$$S^{(\sigma)}_{\gamma\delta\beta';\beta\delta'\gamma'}(\vec{\ell},\vec{\ell}';\mathrm{i}\omega_n) = \int' \mathrm{d}\Omega\,[1+n(\Omega)]\,G^{0(\bar{\sigma})}_{\gamma\gamma'}(\vec{\ell},\vec{\ell}';\Omega+\mathrm{i}\omega_n)\rho^{\Gamma(\sigma\bar{\sigma})}_{\delta\beta';\beta\delta'}(\vec{\ell},\vec{\ell}';\Omega) + \int_{-\infty}^{\infty}\mathrm{d}\epsilon\,[1-f(\epsilon)]\,\rho^{0(\bar{\sigma})}_{\gamma\gamma'}(\vec{\ell},\vec{\ell}';\epsilon)\Gamma^{(\sigma\bar{\sigma})}_{\delta\beta';\beta\delta'}(\vec{\ell},\vec{\ell}';\epsilon-\mathrm{i}\omega_n) \quad \text{(E.23)}$$

and

$$\rho^{\Gamma(\sigma\bar{\sigma})}_{\delta\beta';\beta\delta'}(\vec{\ell},\vec{\ell}';\Omega) = -\frac{1}{2\pi\mathrm{i}}\left(\Gamma^{(\sigma\bar{\sigma})}_{\delta\beta';\beta\delta'}(\vec{\ell},\vec{\ell}';\Omega+\mathrm{i}\eta) - \Gamma^{(\sigma\bar{\sigma})}_{\delta'\beta;\beta'\delta}(\vec{\ell}',\vec{\ell};\Omega+\mathrm{i}\eta)^*\right) . \quad \text{(E.24)}$$

E.3. Connection to the expressions used in the KKRsusc code

In the zero temperature limit $T\to 0$ (i.e. $\beta\to\infty$) one has

$$\lim_{T\to 0}[1+n(\Omega)] = \Theta(\Omega) = \begin{cases} 1\,, & \Omega>0 \\ 0\,, & \Omega<0 \end{cases} \quad \text{(E.25)}$$

and

$$\lim_{T\to 0}[1-f(\epsilon)] = \Theta(\epsilon-E_F) = \begin{cases} 1\,, & \epsilon>E_F \\ 0\,, & \epsilon<E_F \end{cases} \quad \text{(E.26)}$$

Thus, we find for Eq. (E.22), the proper self-energy, the expression

$$\Sigma^{(\sigma)}_{\alpha\alpha'}(\vec{\ell},\vec{\ell}';\omega+\mathrm{i}\eta) = \sum_{\beta\beta'\gamma\gamma'\delta\delta'} U_{\alpha\beta;\gamma\delta}(\vec{\ell})\left[\int_0^{\infty}\mathrm{d}\Omega G^{0(\bar{\sigma})}_{\gamma\gamma'}(\vec{\ell},\vec{\ell}';\Omega+\omega+\mathrm{i}\eta)\rho^{\Gamma(\sigma\bar{\sigma})}_{\delta\beta';\beta\delta'}(\vec{\ell},\vec{\ell}';\Omega) + \int_{E_F}^{\infty}\mathrm{d}\epsilon\rho^{0(\bar{\sigma})}_{\gamma\gamma'}(\vec{\ell},\vec{\ell}';\epsilon)\Gamma^{(\sigma\bar{\sigma})}_{\delta\beta';\beta\delta'}(\vec{\ell},\vec{\ell}';\epsilon-\omega-\mathrm{i}\eta)\right]U_{\delta'\gamma';\beta'\alpha'}(\vec{\ell}') \; . \quad \text{(E.27)}$$

Here, the analytic continuation procedure for the argument was done, $\mathrm{i}\omega_n\to\omega+\mathrm{i}\eta$.

Again, let us drop the indices (including the sum over orbitals) and site labels. For the second integral in Eq. (E.27) we substitute ϵ by $\Omega+\omega$ and arrive at

$$\begin{aligned}
&\Sigma^{(\sigma)}(\omega+\mathrm{i}\eta) \\
&= U(\vec{\ell})\left[\int_0^{\infty}\mathrm{d}\Omega G^{0(\bar{\sigma})}(\Omega+\omega+\mathrm{i}\eta)\rho^{\Gamma(\sigma\bar{\sigma})}(\Omega) + \int_{E_F-\omega}^{\infty}\mathrm{d}\Omega\;\rho^{0(\bar{\sigma})}(\Omega+\omega)\Gamma^{(\sigma\bar{\sigma})}(\Omega-\mathrm{i}\eta)\right]U(\vec{\ell}') \\
&= U(\vec{\ell})\left[\int_0^{\infty}\mathrm{d}\Omega\left(G^{0(\bar{\sigma})}(\Omega+\omega+\mathrm{i}\eta)\rho^{\Gamma(\sigma\bar{\sigma})}(\Omega)+\rho^{0(\bar{\sigma})}(\Omega+\omega)\Gamma^{(\sigma\bar{\sigma})}(\Omega-\mathrm{i}\eta)\right) - \int_0^{E_F-\omega}\mathrm{d}\Omega\;\rho^{0(\bar{\sigma})}(\Omega+\omega)\Gamma^{(\sigma\bar{\sigma})}(\Omega-\mathrm{i}\eta)\right]U(\vec{\ell}') \; . \quad \text{(E.28)}
\end{aligned}$$

Since

$$\begin{aligned} & G^{0(\overline{\sigma})}(\Omega+\omega+\mathrm{i}\eta)\rho^{\Gamma(\sigma\overline{\sigma})}(\Omega) \\ = & -\frac{1}{2\pi\mathrm{i}}G^{0(\overline{\sigma})}(\Omega+\omega+\mathrm{i}\eta)\left(\Gamma^{(\sigma\overline{\sigma})}(\Omega+\mathrm{i}\eta)-\Gamma^{(\sigma\overline{\sigma})}(\Omega-\mathrm{i}\eta)\right) \end{aligned} \tag{E.29}$$

and

$$\begin{aligned} & \rho^{0(\overline{\sigma})}(\Omega+\omega)\Gamma^{(\sigma\overline{\sigma})}(\Omega-\mathrm{i}\eta) \\ = & -\frac{1}{2\pi\mathrm{i}}\left(G^{0(\overline{\sigma})}(\Omega+\omega+\mathrm{i}\eta)-G^{0(\overline{\sigma})}(\Omega+\omega-\mathrm{i}\eta)\right)\Gamma^{(\sigma\overline{\sigma})}(\Omega-\mathrm{i}\eta) \end{aligned} \tag{E.30}$$

we have for their sum

$$\begin{aligned} & G^{0(\overline{\sigma})}(\Omega+\omega+\mathrm{i}\eta)\rho^{\Gamma(\sigma\overline{\sigma})}(\Omega)+\rho^{0(\overline{\sigma})}(\Omega+\omega)\Gamma^{(\sigma\overline{\sigma})}(\Omega-\mathrm{i}\eta) \\ = & -\frac{1}{2\pi\mathrm{i}}\left(G^{0(\overline{\sigma})}(\Omega+\omega+\mathrm{i}\eta)\Gamma^{(\sigma\overline{\sigma})}(\Omega+\mathrm{i}\eta)-G^{0(\overline{\sigma})}(\Omega+\omega-\mathrm{i}\eta)\Gamma^{(\sigma\overline{\sigma})}(\Omega-\mathrm{i}\eta)\right) \end{aligned} \tag{E.31}$$

Restoring the indices and site labels, we find the solution

$$\Sigma^{(\sigma)}_{\alpha\alpha'}(\vec{\ell},\vec{\ell}';\omega+\mathrm{i}\eta)=\mathcal{I}^{(\sigma)}_{1,\alpha\alpha'}(\vec{\ell},\vec{\ell}';\omega+\mathrm{i}\eta)+\mathcal{I}^{(\sigma)}_{2,\alpha\alpha'}(\vec{\ell},\vec{\ell}';\omega+\mathrm{i}\eta) \tag{E.32}$$

with

$$\begin{aligned} & \mathcal{I}^{(\sigma)}_{1,\alpha\alpha'}(\vec{\ell},\vec{\ell}';\omega+\mathrm{i}\eta) \\ & = -\frac{1}{\pi}\sum_{\beta\beta'\gamma\gamma'\delta\delta'}U_{\alpha\beta;\gamma\delta}(\vec{\ell})U_{\delta'\gamma';\beta'\alpha'}(\vec{\ell}') \\ & \qquad \times\int_0^\infty \mathrm{d}\Omega\ \mathrm{Im}\left[G^{0(\overline{\sigma})}_{\gamma\gamma'}(\vec{\ell},\vec{\ell}';\Omega+\omega+\mathrm{i}\eta)\Gamma^{(\sigma\overline{\sigma})}_{\delta\beta';\beta\delta'}(\vec{\ell},\vec{\ell}';\Omega+\mathrm{i}\eta)\right] \end{aligned} \tag{E.33}$$

and

$$\begin{aligned} & \mathcal{I}^{(\sigma)}_{2,\alpha\alpha'}(\vec{\ell},\vec{\ell}';\omega+\mathrm{i}\eta) \\ & = +\frac{1}{\pi}\sum_{\beta\beta'\gamma\gamma'\delta\delta'}U_{\alpha\beta;\gamma\delta}(\vec{\ell})U_{\delta'\gamma';\beta'\alpha'}(\vec{\ell}') \\ & \qquad \times\int_0^{E_F-\omega} \mathrm{d}\Omega\ \mathrm{Im}\left[G^{0(\overline{\sigma})}_{\gamma\gamma'}(\vec{\ell},\vec{\ell}';\Omega+\omega+\mathrm{i}\eta)\right]\Gamma^{(\sigma\overline{\sigma})}_{\delta'\beta;\beta'\delta}(\vec{\ell}',\vec{\ell};\Omega+\mathrm{i}\eta)^*\,. \end{aligned} \tag{E.34}$$

Here we used the identity

$$\begin{aligned} \mathrm{Im}\left[G^{0(\overline{\sigma})}_{\gamma\gamma'}(\vec{\ell},\vec{\ell}';z)\right] &= \frac{1}{2\mathrm{i}}\left[G^{0(\overline{\sigma})}_{\gamma\gamma'}(\vec{\ell},\vec{\ell}';z)-G^{0(\overline{\sigma})}_{\gamma\gamma'}(\vec{\ell},\vec{\ell}';z^*)\right] \\ &= \frac{1}{2\mathrm{i}}\left[G^{0(\overline{\sigma})}_{\gamma\gamma'}(\vec{\ell},\vec{\ell}';z)-G^{0(\overline{\sigma})}_{\gamma'\gamma}(\vec{\ell}',\vec{\ell};z)^*\right] \end{aligned} \tag{E.35}$$

and a similar identity for the product of Green function and electron hole propagator.

Assuming the Lowde and Windsor form of the effective Coulomb interaction matrix elements,

$$U_{\alpha\beta;\gamma\delta}(\vec{\ell}) = U(\vec{\ell})\delta_{\alpha\gamma}\delta_{\beta\delta} \ , \tag{E.36}$$

we have

$$\begin{aligned}
&\mathcal{I}^{(\sigma)}_{1,\alpha\alpha'}(\vec{\ell},\vec{\ell}';\omega+\mathrm{i}\eta) \\
&\quad = \ -\frac{U(\vec{\ell})U(\vec{\ell}')}{\pi}\int_0^{\infty}\mathrm{d}\Omega\ \mathrm{Im}\Big[G^{0(\overline{\sigma})}_{\alpha\alpha'}(\vec{\ell},\vec{\ell}';\Omega+\omega+\mathrm{i}\eta)\overline{\Gamma}^{(\sigma\overline{\sigma})}(\vec{\ell},\vec{\ell}';\Omega+\mathrm{i}\eta)\Big]
\end{aligned} \tag{E.37}$$

and

$$\begin{aligned}
&\mathcal{I}^{(\sigma)}_{2,\alpha\alpha'}(\vec{\ell},\vec{\ell}';\omega+\mathrm{i}\eta) \\
&\quad = \ +\frac{U(\vec{\ell})U(\vec{\ell}')}{\pi}\int_0^{E_F-\omega}\mathrm{d}\Omega\ \mathrm{Im}\Big[G^{0(\overline{\sigma})}_{\alpha\alpha'}(\vec{\ell},\vec{\ell}';\Omega+\omega+\mathrm{i}\eta)\Big]\overline{\Gamma}^{(\sigma\overline{\sigma})}(\vec{\ell}',\vec{\ell};\Omega+\mathrm{i}\eta)^* \ ,
\end{aligned} \tag{E.38}$$

where we defined

$$\overline{\Gamma}^{(\sigma\overline{\sigma})}(\vec{\ell},\vec{\ell}';z) = \sum_{\beta\beta'}\Gamma^{(\sigma\overline{\sigma})}_{\beta\beta';\beta\beta'}(\vec{\ell},\vec{\ell}';z) \ . \tag{E.39}$$

If we now define $V = \omega - E_F$, the bias voltage, and identify

$$\begin{array}{ccc}
G^{0(\sigma)}_{\alpha\alpha'}(\vec{\ell},\vec{\ell}';V+\Omega+E_F+\mathrm{i}\eta) & \longrightarrow & \mathcal{G}^{0(\sigma)}_{iL;jL'}(\vec{\mathrm{r}},\vec{\mathrm{r}}';V+\Omega+E_F+\mathrm{i}0^+) \\
U(\vec{\ell}) & \longrightarrow & U_i(\vec{\mathrm{r}}) \\
\Gamma^{(\sigma\overline{\sigma})}_{\beta\beta';\beta\beta'}(\vec{\ell},\vec{\ell}';\Omega+\mathrm{i}\eta) & \longrightarrow & \chi^{(\sigma\overline{\sigma})}_{kL''lL''';lL'''kL''}(\vec{\mathrm{r}},\vec{\mathrm{r}}';\Omega+\mathrm{i}0^+) \\
\Sigma^{(\sigma)}_{\alpha\alpha'}(\vec{\ell},\vec{\ell}';V+E_F+\mathrm{i}\eta) & \longrightarrow & \Sigma^{(\sigma)}_{iL;jL'}(\vec{\mathrm{r}},\vec{\mathrm{r}}';V+\mathrm{i}0^+)
\end{array} \tag{E.40}$$

we arrive at the expressions implemented into the KKRsusc program,

$$\Sigma^{(\sigma)}_{iL;jL'}(\vec{\mathrm{r}},\vec{\mathrm{r}}';V+\mathrm{i}0^+) = \mathcal{I}^{(\sigma)}_{1,iL;jL'}(\vec{\mathrm{r}},\vec{\mathrm{r}}';V+\mathrm{i}0^+) + \mathcal{I}^{(\sigma)}_{2,iL;jL'}(\vec{\mathrm{r}},\vec{\mathrm{r}}';V+\mathrm{i}0^+) \tag{E.41}$$

with

$$\begin{aligned}
&\mathcal{I}^{(\sigma)}_{1,iL;jL'}(\vec{\mathrm{r}},\vec{\mathrm{r}}';V+\mathrm{i}0^+) \\
&\quad = \ -\frac{U_i(\vec{\mathrm{r}})U_j(\vec{\mathrm{r}}')}{\pi}\int_0^{\infty}\mathrm{d}\Omega\ \mathrm{Im}\Big[\mathcal{G}^{0(\overline{\sigma})}_{iL;jL'}(\vec{\mathrm{r}},\vec{\mathrm{r}}';V+\Omega+E_F+\mathrm{i}0^+)\overline{\chi}^{(\sigma\overline{\sigma})}(\vec{\mathrm{r}},\vec{\mathrm{r}}';\Omega+\mathrm{i}0^+)\Big]
\end{aligned} \tag{E.42}$$

and

$$\begin{aligned}
&\mathcal{I}^{(\sigma)}_{2,iL;jL'}(\vec{\mathrm{r}},\vec{\mathrm{r}}';V+\mathrm{i}0^+) \\
&\quad = \ +\frac{U_i(\vec{\mathrm{r}})U_j(\vec{\mathrm{r}}')}{\pi}\int_0^{-V}\mathrm{d}\Omega\ \mathrm{Im}\Big[\mathcal{G}^{0(\overline{\sigma})}_{iL;jL'}(\vec{\mathrm{r}},\vec{\mathrm{r}}';V+\Omega+E_F+\mathrm{i}0^+)\Big]\overline{\chi}^{(\sigma\overline{\sigma})}(\vec{\mathrm{r}}',\vec{\mathrm{r}};\Omega+\mathrm{i}0^+)^* \ ,
\end{aligned} \tag{E.43}$$

where we defined

$$\overline{\chi}^{(\sigma\overline{\sigma})}(\vec{\mathrm{r}},\vec{\mathrm{r}}';z) = \sum_{L''L''';kl} \chi^{(\sigma\overline{\sigma})}_{kL''lL''';lL'''kL''}(\vec{\mathrm{r}},\vec{\mathrm{r}}';z)\ . \tag{E.44}$$

Note that for the self-energy the argument now has the Fermi energy as offset.

F. Susceptibility within a simple model

In this Appendix we present an approach to the dynamical magnetic susceptibility via a simple model. This model is build upon two Green functions, accounting for the two spin channels, spin up (↑) and spin down (↓). Their density of states (DOS) show Cauchy–Lorentz resonances centered at $E_0^{\uparrow}$ and $E_0^{\downarrow} > E_0^{\uparrow}$ with corresponding widths $\Gamma^{\uparrow}$ and $\Gamma^{\downarrow}$, respectively. Additionally an external magnetic field B^{ext} is assumed, that points along the z-axis and leads to slightly shifted resonances $E^{\uparrow}$ and $E^{\downarrow}$. Within this model the susceptibility can be expressed in an analytical form. We analyze the form of the susceptibility in the linear regime, *i.e.*, for sufficiently small frequencies, which leads to expressions for the resonance position, the full-width at half maximum, and other properties of the spin excitation that are also utilized in the main text. For this we investigate the expansion of the susceptibility within a Taylor or a Padé series up to first order.

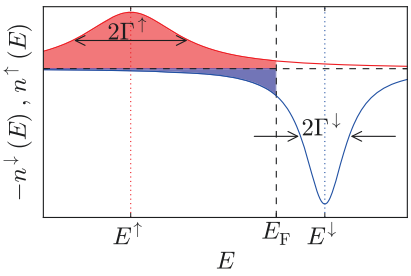

Figure F.1.: The density of states for the two spin channels as given by Eq. (F.2). The resonance positions are given by $E^{\uparrow}$ and $E^{\downarrow}$, the full-width at half maximum is twice the value of $\Gamma^{\uparrow}$ and $\Gamma^{\downarrow}$.

F.1. The simple-model Green function

We start by defining the Green functions

$$\mathcal{G}^{\uparrow}(E) = \frac{1}{E - E^{\uparrow} + \mathrm{i}\Gamma^{\uparrow}} \quad \text{and} \quad \mathcal{G}^{\downarrow}(E) = \frac{1}{E - E^{\downarrow} + \mathrm{i}\Gamma^{\downarrow}}\,, \tag{F.1}$$

where $E^{\uparrow} = E_0^{\uparrow} - B^{\mathrm{ext}}$, $E^{\downarrow} = E_0^{\downarrow} + B^{\mathrm{ext}}$, and $\Gamma^{\uparrow}, \Gamma^{\downarrow} > 0$. Note that this type of Green function is also obtained in the Anderson impurity model [108]. The density of states (DOS) as function of the energy is given by

$$n^{\sigma}(E) = -\frac{1}{\pi}\mathrm{Im}\left[\mathcal{G}^{\sigma}(E)\right] = \frac{1}{\pi}\frac{\Gamma^{\sigma}}{\left(E - E^{\sigma}\right)^2 + \left(\Gamma^{\sigma}\right)^2}\,, \tag{F.2}$$

with $\sigma \in \{\uparrow,\downarrow\}$. The spin-resolved charge is given as integral over the energy,

$$N^\sigma = \int_{-\infty}^{\infty} \mathrm{d}E\, f(E) n^\sigma(E) = \int_{-\infty}^{E_\mathrm{F}} \mathrm{d}E\, n^\sigma(E) = \frac{1}{\pi} \arctan \frac{E_\mathrm{F} - E^\sigma}{\Gamma^\sigma} + \frac{1}{2}\,. \tag{F.3}$$

where the Fermi-Dirac distribution $f(E)$ (see Appendix C) is evaluated for zero temperature. Then, the total charge, N, and the magnetization, M, are given by

$$N = N^\uparrow + N^\downarrow \quad , \quad M = N^\uparrow - N^\downarrow\,. \tag{F.4}$$

For the following analysis it is also useful to define the magnetization of the system in absence of an external magnetic field ($B^\mathrm{ext} = 0$),

$$\begin{aligned} M_0 = N_0^\uparrow - N_0^\downarrow &= \int_{-\infty}^{E_\mathrm{F}} \mathrm{d}E \left(n_0^\uparrow(E) - n_0^\downarrow(E) \right) \\ &= \frac{1}{\pi} \left(\arctan \frac{E_\mathrm{F} - E_0^\uparrow}{\Gamma^\uparrow} - \arctan \frac{E_\mathrm{F} - E_0^\downarrow}{\Gamma^\downarrow} \right)\,, \end{aligned} \tag{F.5}$$

where $n_0^\sigma(E)$ and N_0^σ are given by Eqs. (F.2) and (F.3) with $B^\mathrm{ext} = 0$.

F.2. The simple-model susceptibility

The dynamical response function is given by

$$\chi(\omega) = \frac{\chi_0(\omega)}{1 - U \cdot \chi_0(\omega)} = \left((\chi_0(\omega))^{-1} - U \right)^{-1}\,, \tag{F.6}$$

where

$$U = \left(\chi_0(0)\right)^{-1}\big|_{B^\mathrm{ext}=0} \tag{F.7}$$

is called u-parameter and ensures that χ obeys the Goldstone theorem by construction.[1] The second quantity that appears in Eq. (F.6) is the (transverse) noninteracting susceptibility. It is given by

$$\begin{aligned} \chi_0(\omega) &= -\frac{1}{\pi} \int_{-\infty}^{E_\mathrm{F}} \mathrm{d}E \Big[\mathcal{G}^\downarrow(E+\omega) \mathrm{Im}\left[\mathcal{G}^\uparrow(E)\right] - \mathrm{Im}\left[\mathcal{G}^\downarrow(E)^*\right] \mathcal{G}^\uparrow(E-\omega)^* \Big] \\ &= -\frac{1}{2\pi \mathrm{i}} \Bigg[\int_{-\infty}^{E_\mathrm{F}} \mathrm{d}E \mathcal{G}^\downarrow(E+\omega) \Big(\mathcal{G}^\uparrow(E) - \mathcal{G}^\uparrow(E)^* \Big) \\ &\qquad - \int_{-\infty}^{E_\mathrm{F}} \mathrm{d}E \Big(\mathcal{G}^\downarrow(E)^* - \mathcal{G}^\downarrow(E) \Big) \mathcal{G}^\uparrow(E-\omega)^* \Bigg]\,, \end{aligned} \tag{F.8}$$

[1] The u-parameter corresponds to the so-called exchange-correlation kernel from DFT or Stoner onsite-term in other models.

where $\mathrm{Im}\left[\mathcal{G}\right] = \frac{1}{2\mathrm{i}}\left(\mathcal{G} - \mathcal{G}^*\right)$ was used and $\mathcal{G}^*$ is the conjugate complex of $\mathcal{G}$. For zero frequency the noninteracting susceptibility reduces to a real number and takes the form

$$\chi_0(0) = -\frac{1}{\pi}\int_{-\infty}^{E_\mathrm{F}} \mathrm{d}E \mathrm{Im}\left[G^\downarrow(E)G^\uparrow(E)\right] \ . \tag{F.9}$$

In order to solve the integrals over four products of two different Green functions in Eq. (F.8) we use the identities

$$\mathcal{G}^\downarrow(E+\omega) = \frac{\mathcal{G}^\uparrow(E)}{1-(\Delta-\omega+\mathrm{i}\Lambda)\mathcal{G}^\uparrow(E)} = \frac{\mathcal{G}^\uparrow(E)^*}{1-(\Delta-\omega-2\mathrm{i}\Gamma)\mathcal{G}^\uparrow(E)^*} \ , \tag{F.10}$$

$$\mathcal{G}^\uparrow(E-\omega)^* = \frac{\mathcal{G}^\downarrow(E)^*}{1+(\Delta-\omega-\mathrm{i}\Lambda)\mathcal{G}^\downarrow(E)^*} = \frac{\mathcal{G}^\downarrow(E)}{1+(\Delta-\omega-2\mathrm{i}\Gamma)\mathcal{G}^\downarrow(E)} \ , \tag{F.11}$$

where $\Delta = E^\downarrow - E^\uparrow$, $\Lambda = -(\Gamma^\downarrow - \Gamma^\uparrow)$, and $\Gamma = \frac{1}{2}\left(\Gamma^\downarrow + \Gamma^\uparrow\right)$. By taking into account that $\mathcal{G}^2\mathrm{d}E = -\mathrm{d}\mathcal{G}$, the expression in Eq. (F.8) becomes

$$\begin{aligned}\chi_0(\omega) = +\frac{1}{2\pi\mathrm{i}}\Bigg[&\int_{\mathcal{G}^\uparrow(-\infty)=0}^{\mathcal{G}^\uparrow(E_\mathrm{F})} \frac{\mathrm{d}\mathcal{G}}{1-(\Delta-\omega+\mathrm{i}\Lambda)\mathcal{G}} - \int_0^{\mathcal{G}^\uparrow(E_\mathrm{F})^*} \frac{\mathrm{d}\mathcal{G}}{1-(\Delta-\omega-2\mathrm{i}\Gamma)\mathcal{G}} \\ &- \int_0^{\mathcal{G}^\downarrow(E_\mathrm{F})^*} \frac{\mathrm{d}\mathcal{G}}{1+(\Delta-\omega-\mathrm{i}\Lambda)\mathcal{G}} + \int_0^{\mathcal{G}^\downarrow(E_\mathrm{F})} \frac{\mathrm{d}\mathcal{G}}{1+(\Delta-\omega-2\mathrm{i}\Gamma)\mathcal{G}}\Bigg]\end{aligned} \tag{F.12}$$

F.2.1. Case $\Lambda = 0$: Equal resonance widths

Let us assume that both spin resonances have the same width $\Gamma = \Gamma^\uparrow = \Gamma^\downarrow$, so that $\Lambda = 0$. At first, the case $\omega \neq \Delta$ is considered (the discussion of the limit $\omega \to \Delta$ comes subsequently). Thus, the integration paths in Eq. (F.12) do not cross the negative real axis[2] and each integral is well-defined. We find

$$\begin{aligned}\chi_0(\omega) &= \frac{1}{2\pi\mathrm{i}}\Bigg[-\frac{\ln\left(1-(\Delta-\omega)\mathcal{G}^\uparrow(E_\mathrm{F})\right)}{\Delta-\omega} + \frac{\ln\left(1-(\Delta-\omega-2\mathrm{i}\Gamma)\mathcal{G}^\uparrow(E_\mathrm{F})^*\right)}{\Delta-\omega-2\mathrm{i}\Gamma} \\ &\quad - \frac{\ln\left(1+(\Delta-\omega)\mathcal{G}^\downarrow(E_\mathrm{F})^*\right)}{\Delta-\omega} + \frac{\ln\left(1+(\Delta-\omega-2\mathrm{i}\Gamma)\mathcal{G}^\downarrow(E_\mathrm{F})\right)}{\Delta-\omega-2\mathrm{i}\Gamma}\Bigg] \\ &\underset{(F.10),(F.11)}{=} \frac{1}{2\pi\mathrm{i}}\left[-\frac{\ln\frac{\mathcal{G}^\uparrow(E_\mathrm{F})}{\mathcal{G}^\downarrow(E_\mathrm{F}+\omega)} + \ln\frac{\mathcal{G}^\downarrow(E_\mathrm{F})^*}{\mathcal{G}^\uparrow(E_\mathrm{F}-\omega)^*}}{\Delta-\omega} + \frac{\ln\frac{\mathcal{G}^\uparrow(E_\mathrm{F})^*}{\mathcal{G}^\downarrow(E_\mathrm{F}+\omega)} + \ln\frac{\mathcal{G}^\downarrow(E_\mathrm{F})}{\mathcal{G}^\uparrow(E_\mathrm{F}-\omega)^*}}{\Delta-\omega-2\mathrm{i}\Gamma}\right] \ .\end{aligned} \tag{F.13}$$

For the special case that $\omega = \Delta$, one needs to integrate terms of the form

$$\pm\int_0^{\mathcal{G}^{\uparrow,\downarrow}(E_\mathrm{F})^{(*)}} \mathrm{d}\mathcal{G}\frac{1}{1\mp(\omega-\Delta)\mathcal{G}} = \pm\int_0^{\mathcal{G}^{\uparrow,\downarrow}(E_\mathrm{F})^{(*)}} \mathrm{d}\mathcal{G} = \pm\mathcal{G}^{\uparrow,\downarrow}(E_\mathrm{F})^{(*)} \ . \tag{F.14}$$

[2]The imaginary part of $\mathcal{G}^{-1}$ is fixed whereas its real part is varied during the integration, so that $\mathcal{G}^{-1}$ does not cross the branch cut, the negative real axis. This instance remains true for its inverse, $\mathcal{G}$.

This is also the result when taking the limits

$$\lim_{\omega\to\Delta}\left(-\frac{\ln\left(1\mp(\Delta-\omega)\mathcal{G}^{\uparrow,\downarrow}(E_{\mathrm{F}})^{(*)}\right)}{\Delta-\omega}\right)=\pm\mathcal{G}^{\uparrow,\downarrow}(E_{\mathrm{F}})^{(*)}\,, \tag{F.15}$$

which means that for $\omega=\Delta$ the function can be analytically continued.

Next, we will determine the value of $\chi_0(\omega)$ and its derivative with respect to ω at $\omega=0$. Because of

$$\ln\frac{\mathcal{G}^{\downarrow}(E_{\mathrm{F}})}{\mathcal{G}^{\uparrow}(E_{\mathrm{F}}-\omega)^*}=-\ln\frac{\mathcal{G}^{\uparrow}(E_{\mathrm{F}}-\omega)^*}{\mathcal{G}^{\downarrow}(E_{\mathrm{F}})}\,, \tag{F.16}$$

the second term in Eq. (F.13) vanishes for $\omega=0$, so that we have

$$\chi_0(0)=-\frac{1}{2\pi\mathrm{i}}\frac{\ln\frac{\mathcal{G}^{\uparrow}(E_{\mathrm{F}})}{\mathcal{G}^{\downarrow}(E_{\mathrm{F}})}-\ln\frac{\mathcal{G}^{\uparrow}(E_{\mathrm{F}})^*}{\mathcal{G}^{\downarrow}(E_{\mathrm{F}})^*}}{\Delta}=-\frac{1}{\pi\Delta}\mathrm{Im}\left[\ln\frac{\mathcal{G}^{\uparrow}(E_{\mathrm{F}})}{\mathcal{G}^{\downarrow}(E_{\mathrm{F}})}\right]\,. \tag{F.17}$$

Using Eq. (F.8) directly with $\Lambda=0$ leads to

$$\begin{aligned}\chi_0(0) &= -\frac{1}{2\mathrm{i}\pi}\int_{-\infty}^{E_{\mathrm{F}}}\mathrm{d}E\Big[\underbrace{\mathcal{G}^{\downarrow}(E)\mathcal{G}^{\uparrow}(E)}_{=\frac{1}{\Delta}\left(\mathcal{G}^{\downarrow}(E)-\mathcal{G}^{\uparrow}(E)\right)}-\underbrace{\mathcal{G}^{\downarrow}(E)^*\mathcal{G}^{\uparrow}(E)^*}_{=\frac{1}{\Delta}\left(\mathcal{G}^{\downarrow}(E)^*-\mathcal{G}^{\uparrow}(E)^*\right)}\Big]\\ &= -\frac{1}{\pi\Delta}\int_{-\infty}^{E_{\mathrm{F}}}\mathrm{d}E\Big[\mathrm{Im}\left[\mathcal{G}^{\downarrow}(E)\right]-\mathrm{Im}\left[\mathcal{G}^{\uparrow}(E)\right]\Big]\\ &= -\frac{1}{\Delta}\underbrace{\left(N^{\uparrow}-N^{\downarrow}\right)}_{=M}\,.\end{aligned} \tag{F.18}$$

A comparison of Eqs. (F.17) and (F.18) allows to identify

$$M=\frac{1}{\pi}\mathrm{Im}\left[\ln\frac{\mathcal{G}^{\uparrow}(E_{\mathrm{F}})}{\mathcal{G}^{\downarrow}(E_{\mathrm{F}})}\right]\,. \tag{F.19}$$

By use of Eq. (F.18) we can also determine the u-parameter

$$U=\left(\chi_0(0)\right)^{-1}\big|_{B^{\mathrm{ext}}=0}=-\frac{\Delta_0}{M_0}<0\,, \tag{F.20}$$

with $\Delta_0=E_0^{\downarrow}-E_0^{\uparrow}$ and M_0 as given in Eq. (F.5). Because of $\frac{1}{1+x}\approx 1-x$ for $|x|\ll 1$ one obtains for $B^{\mathrm{ext}}\ll\Delta_0$ an expression that shows that, in first order, the value for the susceptibility at zero frequency shifts linearly with the applied field,

$$\begin{aligned}\chi_0(0) &= -\frac{M}{\Delta_0+2B^{\mathrm{ext}}}=-\frac{M}{\Delta_0}\,\frac{1}{1+\frac{2B^{\mathrm{ext}}}{\Delta_0}}\\ &\approx -\frac{M}{\Delta_0}\left(1-\frac{2B^{\mathrm{ext}}}{\Delta_0}\right)=\frac{1}{U}+\frac{2B^{\mathrm{ext}}}{U^2M}\,.\end{aligned} \tag{F.21}$$

The derivative of $\chi_0(\omega)$ with respect to ω reads

$$\begin{aligned}\left.\frac{\partial\chi_0(\omega)}{\partial\omega}\right|_{\omega=0} &= \frac{1}{2\pi\mathrm{i}}\left(\frac{1}{\Delta^2}(-2\pi\mathrm{i}M)\right)\\ &\quad+\frac{1}{2\pi\mathrm{i}}\left(\frac{1}{\Delta}-\frac{1}{\Delta-2\mathrm{i}\Gamma}\right)\cdot\left(\mathcal{G}^{\uparrow}(E_\mathrm{F})^*-\mathcal{G}^{\downarrow}(E_\mathrm{F})\right)\\ &= -\frac{M}{\Delta^2}+\frac{\Gamma}{\pi\Delta(\Delta-2\mathrm{i}\Gamma)}\underbrace{\left(\mathcal{G}^{\uparrow}(E_\mathrm{F})^*-\mathcal{G}^{\downarrow}(E_\mathrm{F})\right)}_{=(\Delta-2\mathrm{i}\Gamma)\mathcal{G}^{\downarrow}(E_\mathrm{F})\mathcal{G}^{\uparrow}(E_\mathrm{F})^*}\\ &= -\frac{M}{\Delta^2}+\frac{\Gamma}{\pi\Delta}\mathcal{G}^{\downarrow}(E_\mathrm{F})\mathcal{G}^{\uparrow}(E_\mathrm{F})^*\,. \end{aligned}\tag{F.22}$$

Finally we can simplify the imaginary part

$$\begin{aligned}\mathrm{Im}\left[\left.\frac{\partial\chi_0(\omega)}{\partial\omega}\right|_{\omega=0}\right] &= \frac{\Gamma}{\pi\Delta}\mathrm{Im}\left[\mathcal{G}^{\downarrow}(E_\mathrm{F})\mathcal{G}^{\uparrow}(E_\mathrm{F})^*\right]\\ &= \frac{\Gamma}{\pi\Delta}\mathrm{Im}\left[\frac{E_\mathrm{F}-E^{\downarrow}-\mathrm{i}\Gamma}{(E_\mathrm{F}-E^{\downarrow})^2+\Gamma^2}\frac{E_\mathrm{F}-E^{\uparrow}-\mathrm{i}\Gamma}{(E_\mathrm{F}-E^{\uparrow})^2+\Gamma^2}\right]\\ &= \frac{\Gamma}{\pi\Delta}\frac{-\Gamma\Delta}{(E_\mathrm{F}-E^{\downarrow})^2+\Gamma^2)\left((E_\mathrm{F}-E^{\uparrow})^2+\Gamma^2\right)}\\ &= -\pi\underbrace{\left(-\frac{1}{\pi}\mathrm{Im}\left[\mathcal{G}^{\downarrow}(E_\mathrm{F})\right]\right)}_{=n^{\downarrow}(E_\mathrm{F})}\underbrace{\left(-\frac{1}{\pi}\mathrm{Im}\left[\mathcal{G}^{\uparrow}(E_\mathrm{F})\right]\right)}_{=n^{\uparrow}(E_\mathrm{F})}, \end{aligned}\tag{F.23}$$

i.e., the slope of the imaginary part of the susceptibility is proportional to the product of density of states at the Fermi energy.

F.2.2. Case $\Lambda \neq 0$: Different resonance widths

For the case that $\Lambda \neq 0$ the noninteracting susceptibility reads

$$\begin{aligned}\chi_0(\omega) = \frac{1}{2\pi\mathrm{i}}\Bigg[&-\frac{\ln\left(1-(\Delta-\omega+\mathrm{i}\Lambda)\mathcal{G}^{\uparrow}(E_\mathrm{F})\right)}{\Delta-\omega+\mathrm{i}\Lambda}+\frac{\ln\left(1-(\Delta-\omega-2\mathrm{i}\Gamma)\mathcal{G}^{\uparrow}(E_\mathrm{F})^*\right)}{\Delta-\omega-2\mathrm{i}\Gamma}\\ &-\frac{\ln\left(1+(\Delta-\omega-\mathrm{i}\Lambda)\mathcal{G}^{\downarrow}(E_\mathrm{F})^*\right)}{\Delta-\omega-\mathrm{i}\Lambda}+\frac{\ln\left(1+(\Delta-\omega-2\mathrm{i}\Gamma)\mathcal{G}^{\downarrow}(E_\mathrm{F})\right)}{\Delta-\omega-2\mathrm{i}\Gamma}\Bigg]\\ \underset{(F.10),(F.11)}{=}\frac{1}{2\pi\mathrm{i}}&\left[-\frac{\ln\frac{\mathcal{G}^{\uparrow}(E_\mathrm{F})}{\mathcal{G}^{\downarrow}(E_\mathrm{F}+\omega)}}{\Delta-\omega+\mathrm{i}\Lambda}-\frac{\ln\frac{\mathcal{G}^{\downarrow}(E_\mathrm{F})^*}{\mathcal{G}^{\uparrow}(E_\mathrm{F}-\omega)^*}}{\Delta-\omega-\mathrm{i}\Lambda}+\frac{\ln\frac{\mathcal{G}^{\uparrow}(E_\mathrm{F})^*}{\mathcal{G}^{\downarrow}(E_\mathrm{F}+\omega)}+\ln\frac{\mathcal{G}^{\downarrow}(E_\mathrm{F})}{\mathcal{G}^{\uparrow}(E_\mathrm{F}-\omega)^*}}{\Delta-\omega-2\mathrm{i}\Gamma}\right], \end{aligned}\tag{F.24}$$

The u-parameter is given by

$$U=\left(\chi_0(0)\right)^{-1}\big|_{B^{\mathrm{ext}}=0}=-\frac{\Delta_0^2+\Lambda^2}{\Delta_0 M_0+\frac{\Lambda}{2\pi}\ln\frac{(E_\mathrm{F}-E_0^{\uparrow})^2+(\Gamma^{\uparrow})^2}{(E_\mathrm{F}-E_0^{\downarrow})^2+(\Gamma^{\downarrow})^2}}\,.\tag{F.25}$$

At $\omega = 0$, the noninteracting susceptibility is given by

$$\begin{aligned}\chi_0(0) &= -\frac{1}{2\pi \mathrm{i}}\left[\frac{\ln\frac{\mathcal{G}^{\uparrow}(E_\mathrm{F})}{\mathcal{G}^{\downarrow}(E_\mathrm{F})}}{\Delta+\mathrm{i}\Lambda}+\frac{\ln\frac{\mathcal{G}^{\downarrow}(E_\mathrm{F})^*}{\mathcal{G}^{\uparrow}(E_\mathrm{F})^*}}{\Delta-\mathrm{i}\Lambda}\right] \\ &= -\frac{1}{\pi(\Delta^2+\Lambda^2)}\mathrm{Im}\left[(\Delta-\mathrm{i}\Lambda)\ln\frac{\mathcal{G}^{\uparrow}(E_\mathrm{F})}{\mathcal{G}^{\downarrow}(E_\mathrm{F})}\right] , \end{aligned} \tag{F.26}$$

and its derivative takes the form

$$\begin{aligned}\left.\frac{\partial\chi_0(\omega)}{\partial\omega}\right|_{\omega=0} &= \frac{1}{2\pi\mathrm{i}}\left(-\frac{\mathcal{G}^{\downarrow}(E_\mathrm{F})}{\Delta+\mathrm{i}\Lambda}+\frac{\mathcal{G}^{\uparrow}(E_\mathrm{F})^*}{\Delta-\mathrm{i}\Lambda}+\frac{\mathcal{G}^{\downarrow}(E_\mathrm{F})-\mathcal{G}^{\uparrow}(E_\mathrm{F})^*}{\Delta-2\mathrm{i}\Gamma}\right. \\ &\quad \left.-\frac{\ln\frac{\mathcal{G}^{\uparrow}(E_\mathrm{F})}{\mathcal{G}^{\downarrow}(E_\mathrm{F})}}{\Delta+\mathrm{i}\Lambda}-\frac{\ln\frac{\mathcal{G}^{\downarrow}(E_\mathrm{F})^*}{\mathcal{G}^{\uparrow}(E_\mathrm{F})^*}}{\Delta-\mathrm{i}\Lambda}\right) \\ &= \frac{1}{2\pi\mathrm{i}}\left(-\frac{\mathcal{G}^{\downarrow}(E_\mathrm{F})}{\Delta+\mathrm{i}\Lambda}+\frac{\mathcal{G}^{\uparrow}(E_\mathrm{F})^*}{\Delta-\mathrm{i}\Lambda}-\mathcal{G}^{\downarrow}(E_\mathrm{F})\cdot\mathcal{G}^{\uparrow}(E_\mathrm{F})^*\right) \\ &\quad -\frac{1}{\pi}\frac{\mathrm{Im}\left[(\Delta-\mathrm{i}\Lambda)^2\ln\frac{\mathcal{G}^{\uparrow}(E_\mathrm{F})}{\mathcal{G}^{\downarrow}(E_\mathrm{F})}\right]}{(\Delta^2+\Lambda^2)^2} . \end{aligned} \tag{F.27}$$

F.3. Small frequencies: Linear expansion of response function

Within the present simple model an analytical expression for the noninteracting susceptibility and, thus, for the enhanced susceptibility becomes accessible, *cf.* Eqs. (F.24) and (F.6). Nevertheless, a systematical study of, *e.g.*, the resonance position or its width is difficult to perform for these expressions. Therefore, it can be advantageous to consider an Padé expansion of the susceptibility with respect to frequency at $\omega = 0$ instead. In first order such an expansion takes the form

$$\chi_0^{M,N}(\omega) = \frac{\sum_{k=0}^{M} a_k\omega^k}{1+\sum_{k=1}^{N} b_k\omega^k} \quad , \quad M+N=1 . \tag{F.28}$$

Note that $\sum_{k=1}^{0} c_k \stackrel{def}{=} 0$ and that $\chi_0^{1,0}(\omega)$ is identical to the Taylor-series up to the linear term. Let us define

$$\begin{aligned}\chi_0^T(\omega) \stackrel{def}{=} \chi_0^{1,0}(\omega) &= \gamma+(\alpha+\mathrm{i}\beta)\omega = \gamma\left(1+\frac{\alpha+\mathrm{i}\beta}{\gamma}\omega\right) \\ &= \underbrace{\gamma+\alpha\omega}_{=\mathrm{Re}\left[\chi_0^T(\omega)\right]} + \mathrm{i}\ \underbrace{\beta\omega}_{=\mathrm{Im}\left[\chi_0^T(\omega)\right]} \end{aligned} \tag{F.29}$$

and

$$\begin{aligned}\chi_0^P(\omega) \stackrel{def}{=} \chi_0^{0,1}(\omega) &= \frac{\gamma}{1-\frac{\alpha+\mathrm{i}\beta}{\gamma}\omega} = \gamma\left(1-\frac{\alpha+\mathrm{i}\beta}{\gamma}\omega\right)^{-1} \\ &= \underbrace{\frac{\gamma-\alpha\omega}{\left(1-\frac{\alpha\omega}{\gamma}\right)^2+\left(\frac{\beta\omega}{\gamma}\right)^2}}_{=\mathrm{Re}\left[\chi_0^P(\omega)\right]} + \mathrm{i}\underbrace{\frac{\beta\omega}{\left(1-\frac{\alpha\omega}{\gamma}\right)^2+\left(\frac{\beta\omega}{\gamma}\right)^2}}_{=\mathrm{Im}\left[\chi_0^P(\omega)\right]}, \end{aligned} \tag{F.30}$$

where

$$\gamma = \chi_0(0) \quad , \quad \alpha = \mathrm{Re}\left[\left.\frac{\partial\chi_0(\omega)}{\partial\omega}\right|_{\omega=0}\right] \quad \text{, and} \quad \beta = \mathrm{Im}\left[\left.\frac{\partial\chi_0(\omega)}{\partial\omega}\right|_{\omega=0}\right] \tag{F.31}$$

are real numbers, since $\chi_0(0)$ is real (*cf.* Eqs. (F.18) and (F.26)). Using Eqs. (F.29) and (F.30) we can now determine the dynamical response function via Eq. (F.6), the Dyson-like equation. The resulting expressions read

$$\begin{aligned}\chi^T(\omega) &= \frac{\gamma+(\alpha+\mathrm{i}\beta)\omega}{1-U(\gamma+(\alpha+\mathrm{i}\beta)\omega)} \\ &= \frac{1}{U^2}\frac{(1-2U\gamma)\,\alpha\omega+\gamma\,(1-U\gamma)-U\,(\alpha^2+\beta^2)\,\omega^2}{\left(\alpha\omega-\frac{1}{U}\,(1-U\gamma)\right)^2+(\beta\omega)^2} \\ &\quad +\mathrm{i}\frac{1}{U^2}\frac{\beta\omega}{\left(\alpha\omega-\frac{1}{U}\,(1-U\gamma)\right)^2+(\beta\omega)^2}\end{aligned} \tag{F.32}$$

and

$$\begin{aligned}\chi^P(\omega) &= \left(\frac{1}{\gamma}\left(1-\frac{\alpha+\mathrm{i}\beta}{\gamma}\omega\right)-U\right)^{-1} \\ &= -\gamma^2\frac{\alpha\omega-\gamma\,(1-U\gamma)}{(\alpha\omega-\gamma\,(1-U\gamma))^2+(\beta\omega)^2}+\mathrm{i}\gamma^2\frac{\beta\omega}{(\alpha\omega-\gamma\,(1-U\gamma))^2+(\beta\omega)^2}\,.\end{aligned} \tag{F.33}$$

Note the similarities in the imaginary parts of $\chi^T(\omega)$ and $\chi^P(\omega)$. The imaginary part of the susceptibility describes the density of the excited magnetic states. Therefore it is interesting to calculate the resulting extrema of $\mathrm{Im}\left[\chi^T(\omega)\right]$ and $\mathrm{Im}\left[\chi^P(\omega)\right]$ and the corresponding linewidths, given by the full-width at half maximum, FWHM^T and FWHM^P, which represent the inverse of the lifetime of the excited state. Taking the derivative with respect to the frequency and setting it to zero leads to

$$\begin{aligned}\left.\frac{\partial\mathrm{Im}\left[\chi^T(\omega)\right]}{\partial\omega}\right|_{\omega=\omega_{\mathrm{res}}^T} &\stackrel{!}{=} 0 \quad \underset{\beta\neq 0}{\Leftrightarrow} \quad (1-U\gamma)^2-U^2(\alpha^2+\beta^2)(\omega_{\mathrm{res}}^T)^2=0 \\ &\Rightarrow \omega_{\mathrm{res}}^T \quad \in \quad \{\pm\frac{1}{\sqrt{\alpha^2+\beta^2}}\frac{1-U\gamma}{U}\}\end{aligned} \tag{F.34}$$

and

$$\left.\frac{\partial \mathrm{Im}\chi^P(\omega)}{\partial\omega}\right|_{\omega=\omega^P_{\mathrm{res}}} \stackrel{!}{=} 0 \quad \underset{\beta\neq 0}{\Leftrightarrow} \quad (1-U\gamma)^2 - \frac{\alpha^2+\beta^2}{\gamma^2}(\omega^P_{\mathrm{res}})^2 = 0$$
$$\Rightarrow \omega^P_{\mathrm{res}} \quad \in \quad \{\pm\frac{1}{\sqrt{\alpha^2+\beta^2}}\gamma(1-U\gamma)\}\,. \tag{F.35}$$

Thus, for both functions, $\chi^T(\omega)$ and $\chi^P(\omega)$, the imaginary part exhibits two extrema, out of which we are interested in the one leading to the resonance, *i.e.*, $\alpha\omega^T_{\mathrm{res}} - \frac{1}{U}(1-U\gamma) = 0$ and $\alpha\omega^P_{\mathrm{res}} - \gamma(1-U\gamma) = 0$. These conditions are fulfilled when we identify (use $-\alpha\left(\alpha^2+\beta^2\right)^{-\frac{1}{2}} = 1 + \mathcal{O}\left(\frac{\beta}{\alpha}\right)$)

$$\omega^T_{\mathrm{res}} = -\frac{1}{\sqrt{\alpha^2+\beta^2}}\frac{1-U\gamma}{U} \quad \text{and} \quad \omega^P_{\mathrm{res}} = -\frac{1}{\sqrt{\alpha^2+\beta^2}}\gamma(1-U\gamma)\,. \tag{F.36}$$

The corresponding two values for the full-width at half maximum, FWHM^T and FWHM^P are given by

$$\mathrm{FWHM}^T = |\omega^T_+ - \omega^T_-| \quad \text{and} \quad \mathrm{FWHM}^P = |\omega^P_+ - \omega^P_-|\,, \tag{F.37}$$

where $\omega^T_\pm$ and $\omega^P_\pm$ are solutions to the equations

$$\mathrm{Im}\chi\left(\omega^T_\pm\right) = \frac{1}{2}\mathrm{Im}\chi^T\left(\omega^T_{\mathrm{res}}\right) \quad \text{and} \quad \mathrm{Im}\chi\left(\omega^P_\pm\right) = \frac{1}{2}\mathrm{Im}\chi^P\left(\omega^P_{\mathrm{res}}\right)\,. \tag{F.38}$$

A straightforward calculation shows that

$$\frac{\omega^T_\pm}{\omega^T_{\mathrm{res}}} = \frac{\omega^P_\pm}{\omega^P_{\mathrm{res}}} = \left(\left(2+\frac{\alpha}{\sqrt{\alpha^2+\beta^2}}\right) \pm \sqrt{\left(2+\frac{\alpha}{\sqrt{\alpha^2+\beta^2}}\right)^2 - 1}\right) \tag{F.39}$$

and

$$\frac{\mathrm{FWHM}^T}{|\omega^T_{\mathrm{res}}|} = \frac{\mathrm{FWHM}^P}{|\omega^P_{\mathrm{res}}|} = 2\sqrt{\left(2+\frac{\alpha}{\sqrt{\alpha^2+\beta^2}}\right)^2 - 1}\,. \tag{F.40}$$

Thus, the resonance width increases linearly with the resonance position for both, a Taylor and a Padé expansion. This important result concludes the analysis of the susceptibility in terms of a simple model.

G. The Landau-Lifshitz-Gilbert model

In order to analyze the dynamics of magnetic moments in a ferromagnet, a widely used phenomenological approach is the Landau-Lifshitz-Gilbert (LLG) model [93, 94]. Its central equation describes the precessional motion of a magnetic moment exposed to an effective magnetic field and can be seen as a classical analogue to the equation of motion for the quantum-mechanical spin operator in the Heisenberg picture, $\frac{\mathrm{d}}{\mathrm{d}t}\vec{\mathcal{S}} = \mathrm{i}\left[\vec{\mathcal{S}}, \mathcal{H}\right]$.

G.1. Landau-Lifshitz-Gilbert model for a single magnetic atom

In this Section we address the problem of a single magnetic moment $\vec{m}(t)$ in the presence of a time-dependent external magnetic field $\vec{B}^{\mathrm{ext}}(t)$ (see Sec. G.2 for an extension to more than one atom). The potential energy as function of the magnetic moment reads

$$E(\vec{m}) = -\vec{B}^{\mathrm{ext}}(t) \cdot \vec{m} \,. \tag{G.1}$$

Then, the LLG equation takes the form (see Fig. G.1 for a visualization)

$$\frac{\mathrm{d}\vec{m}}{\mathrm{d}t} = -\gamma \vec{m} \times \vec{B}^{\mathrm{eff}} + \eta \frac{\vec{m}}{m} \times \frac{\mathrm{d}\vec{m}}{\mathrm{d}t} \,, \tag{G.2}$$

where $m = |\vec{m}|$ and the effective field coincides with the external field,

$$\vec{B}^{\mathrm{eff}} = -\frac{\partial E}{\partial \vec{m}} = \vec{B}^{\mathrm{ext}} \,. \tag{G.3}$$

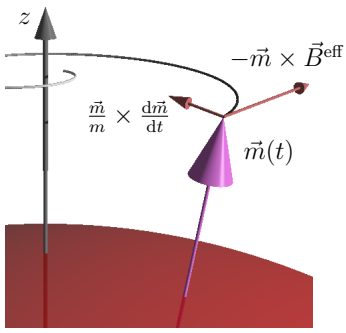

Figure G.1.: This figure illustrates the spiral trajectory as described by the LLG equation of motion, see Eq. (G.2), for the case that $\vec{B}^{\mathrm{eff}}$ points along the z direction.

Furthermore, $\gamma = |\gamma_e| = g\mu_{\mathrm{B}} > 0$ and an empirical damping parameter η have been introduced, where γ_e is the gyromagnetic ratio for an electron spin and g is called g-factor.

For a free electron, angular and magnetic moment originate from the electron spin, resulting in a g-factor of exactly 2. In metallic systems, however, the value of g can differ from 2 [21] which is a result of the system's electronic structure nearby the Fermi energy [71]. In the following we linearize the LLG equation (G.2) and map the results obtained from the performed calculations into this equation by taking an effective γ and an effective damping η into account.

Say, the external magnetic field consists of a dominant time-independent term along the positive z axis and a small transverse time-dependent part,

$$\vec{B}^{\mathrm{ext}}(t) = \begin{pmatrix} 0 \\ 0 \\ B_z^{\mathrm{ext}} \end{pmatrix} + \begin{pmatrix} B_x^{\mathrm{ext}}(t) \\ B_y^{\mathrm{ext}}(t) \\ 0 \end{pmatrix} , \tag{G.4}$$

where $B_z^{\mathrm{ext}} \gg B_x^{\mathrm{ext}}(t), B_y^{\mathrm{ext}}(t)$ at all times t. Assuming that this results in a small induced transverse magnetization, perpendicular to the dominant initial moment along the z axis,

$$\vec{m}(t) = \begin{pmatrix} 0 \\ 0 \\ m_z \end{pmatrix} + \begin{pmatrix} m_x(t) \\ m_y(t) \\ 0 \end{pmatrix} , \tag{G.5}$$

where $m_z \gg m_x(t), m_y(t)$ for all times t, one can restrict the analysis of the LLG equation to the x and the y components,

$$\begin{aligned} \frac{\mathrm{d}m_x}{\mathrm{d}t} &= -\gamma \left(m_y B_z^{\mathrm{eff}} - m_z B_y^{\mathrm{eff}} \right) + \eta \left(\frac{m_y}{m} \underbrace{\frac{\mathrm{d}m_z}{\mathrm{d}t}}_{=0} - \underbrace{\frac{m_z}{m}}_{\approx 1} \frac{\mathrm{d}m_y}{\mathrm{d}t} \right) \\ &= -\gamma \left(m_y B_z^{\mathrm{eff}} - m_z B_y^{\mathrm{eff}} \right) - \eta \frac{\mathrm{d}m_y}{\mathrm{d}t} \end{aligned} \tag{G.6}$$

and

$$\begin{aligned} \frac{\mathrm{d}m_y}{\mathrm{d}t} &= -\gamma \left(m_z B_x^{\mathrm{eff}} - m_x B_z^{\mathrm{eff}} \right) + \eta \left(\underbrace{\frac{m_z}{m}}_{\approx 1} \frac{\mathrm{d}m_x}{\mathrm{d}t} - \frac{m_x}{m} \underbrace{\frac{\mathrm{d}m_z}{\mathrm{d}t}}_{=0} \right) \\ &= -\gamma \left(m_z B_x^{\mathrm{eff}} - m_x B_z^{\mathrm{eff}} \right) + \eta \frac{\mathrm{d}m_x}{\mathrm{d}t} . \end{aligned} \tag{G.7}$$

After a variable substitution $m_\pm = m_x \pm \mathrm{i} m_y$ these two equations decouple into

$$\begin{aligned} \frac{\mathrm{d}m_\pm}{\mathrm{d}t} &= \pm \mathrm{i}\gamma \left(m_\pm B_z^{\mathrm{eff}} - m_z B_\pm^{\mathrm{eff}} \right) \pm \mathrm{i}\eta \frac{\mathrm{d}m_\pm}{\mathrm{d}t} \\ &= \pm \mathrm{i} \frac{\gamma}{1 \mp \mathrm{i}\eta} \left(m_\pm B_z^{\mathrm{eff}} - m_z B_\pm^{\mathrm{eff}} \right) \\ &= \gamma_\pm B_z^{\mathrm{eff}} m_\pm - \gamma_\pm m_z B_\pm^{\mathrm{eff}} , \end{aligned} \tag{G.8}$$

where $B^{\text{eff}}_{i,\pm} = B^{\text{eff}}_{i,x} \pm \mathrm{i} B^{\text{eff}}_{i,y}$ and $\gamma_\pm = \pm\mathrm{i}\frac{\gamma}{1\mp\mathrm{i}\eta} = \frac{-\eta\pm\mathrm{i}}{1+\eta^2}\gamma$. Eq. (G.8) is a differential equation of the form $\dot{x} = \alpha x(t) + \beta(t)$, where $\alpha \neq 0$ and $\beta(t)$ are complex numbers. Its general solution reads $x(t) = \left(x(0) + \int_0^t \mathrm{d}t' \frac{\beta(t')}{\mathrm{e}^{\alpha t'}}\right)\mathrm{e}^{\alpha t}$. Thus, we have

$$m_\pm(t) = \left(m_\pm(0) - \gamma_\pm m_z \int_0^t \mathrm{d}t' \frac{B^{\text{eff}}_\pm(t')}{\mathrm{e}^{\gamma_\pm B^{\text{eff}}_z t'}}\right)\mathrm{e}^{\gamma_\pm B^{\text{eff}}_z t} \,. \tag{G.9}$$

As long as $\eta > 0$, one finds $\mathrm{Re}\left[\gamma_\pm B^{\text{eff}}_z\right] = \frac{-\eta}{1+\eta^2}\gamma B^{\text{eff}}_z < 0$ and the exponential terms in Eq. (G.9) always contain a damping factor. If, for example, the transverse magnetic external field is switched off at a time t_0 (*i.e.*, $B^{\text{eff}}_\pm(t) = B^{\text{ext}}_\pm(t) = 0\ \forall t \geq t_0 > 0$) this damping contribution leads to the limit $m_\pm(t) \xrightarrow{t\to\infty} 0$. This implies $\vec{m}(t) \xrightarrow{t\to\infty} m_z\,\hat{\mathrm{e}}_z$, *i.e.*, the magnetic moment precesses along a spiral trajectory towards the z axis, as indicated in Fig. G.1. For the case that no damping is present ($\eta = 0$), however, the real part of $\gamma_\pm$ vanishes and for $t > t_0$ the system remains in a state $m_\pm(t) = m_\pm(t_0)\mathrm{e}^{\pm\mathrm{i}\gamma B^{\text{eff}}_z t}$, *i.e.*, it describes a precession without damping, *i.e.*, without relaxation towards its initial state.

As a next step, the form of χ^{LLG}, the response function within the LLG model, is derived. For this, the frequency domain is used and the Fourier transformation of the transverse time-dependent part of magnetic moment and magnetic field read

$$m_\pm(t) = \int \frac{\mathrm{d}\omega}{2\pi}\mathrm{e}^{-\mathrm{i}\omega t}\tilde{m}_\pm(\omega) \quad \text{and} \quad B^{\text{ext}}_\pm(t) = \int \frac{\mathrm{d}\omega}{2\pi}\mathrm{e}^{-\mathrm{i}\omega t}\tilde{B}^{\text{ext}}_\pm(\omega) \,. \tag{G.10}$$

In Fourier space Eq. (G.8) takes the form

$$\begin{aligned} -\mathrm{i}\omega\tilde{m}_\pm(\omega) &= \gamma_\pm B^{\text{eff}}_z \tilde{m}_\pm(\omega) - \gamma_\pm m_z \tilde{B}^{\text{eff}}_\pm(\omega) \\ \Leftrightarrow \quad A_\pm(\omega)\tilde{m}_\pm(\omega) &= \tilde{B}^{\text{eff}}_\pm(\omega) \,, \end{aligned} \tag{G.11}$$

where

$$\begin{aligned} A_\pm(\omega) &= \frac{1}{\gamma_\pm m_z}\left(\mathrm{i}\omega + \gamma_\pm B^{\text{eff}}_z\right) \\ &= \frac{1}{m_z}\left(\pm\frac{1\mp\mathrm{i}\eta}{\gamma}\omega + B^{\text{eff}}_z\right) \,. \end{aligned} \tag{G.12}$$

The inverse of $A_\pm$ yields the transverse LLG response function

$$\begin{aligned} \chi^{\text{LLG}}_\pm(\omega) = (A_\pm(\omega))^{-1} &= m_z \frac{1}{\pm\frac{1\mp\mathrm{i}\eta}{\gamma}\omega + B^{\text{eff}}_z} = \gamma m_z \frac{\pm\omega + \gamma B^{\text{eff}}_z + \mathrm{i}\eta\omega}{\left(\pm\omega + \gamma B^{\text{eff}}_z\right)^2 + (\eta\omega)^2} \\ &= \frac{m_z\omega_0}{B^{\text{eff}}_z}\,\frac{\pm\omega + (1+\eta^2)\,\omega_0 + \mathrm{i}\eta\omega}{(\omega \pm \omega_0)^2 + (\eta\omega_0)^2} \,, \end{aligned} \tag{G.13}$$

with $\omega_0 = \gamma B^{\text{eff}}_z / (1+\eta^2)$. The imaginary part of $\chi^{\text{LLG}}_\pm(\omega)$ describes the response spectrum of the magnetic moment and reaches a maximum when the condition

$$\frac{\mathrm{d}}{\mathrm{d}\omega}\mathrm{Im}\,\chi^{\text{LLG}}_\pm(\omega) \stackrel{!}{=} 0 \quad \Rightarrow \quad \omega_{\text{res}} = \sqrt{1+\eta^2}\omega_0 = \frac{\gamma B^{\text{eff}}_z}{\sqrt{1+\eta^2}} \tag{G.14}$$

is fulfilled. Thus, for the case of small damping ($\eta \approx 0$) and a small g shift ($\gamma \approx 2$) the resonance position is at about twice the value of the effective magnetic field along the x axis.

G.2. The Landau-Lifshitz-Gilbert model for more than one magnetic atom

In this Section we turn to the more intricate case where the regarded system contains two or more magnetic atoms. The goal here is to extend the formalism such that the LLG response function incorporates interatomic magnetic interactions, mediated by a Heisenberg-type exchange coupling among magnetic atoms.

For a system of N different magnetic atoms at sites $\{\vec{R}_i\}$, $1 \leq i \leq N$, the potential energy as function of their respective magnetic moments $\{\vec{m}_i\}$ is given by (*cf.* Eq. (8.1) in the main text)

$$E(\{\vec{m}_i\}) = -\frac{1}{2} \sum_{i,j|i\neq j} J_{ij} \vec{m}_i \cdot \vec{m}_j - \vec{B}^{\text{ext}} \cdot \sum_i \vec{m}_i \,, \tag{G.15}$$

where J_{ij} is the coupling constant between the magnetic moments located at sites $\vec{R}_i$ and $\vec{R}_j$. Since spin-orbit coupling is set aside in the present study, the coupling constant is symmetric in i and j. Furthermore, $\vec{B}^{\text{ext}} = \vec{B}^{\text{ext}}(t)$ is a time-dependent external magnetic field that shows the same strength at all sites i. One can then define an effective magnetic field acting on moment $\vec{m}_i$ as

$$\vec{B}_i^{\text{eff}} = -\frac{\partial E}{\partial \vec{m}_i} = \sum_{j|j\neq i} J_{ij} \vec{m}_j + \vec{B}^{\text{ext}} \,. \tag{G.16}$$

Then, the LLG equation for the magnetic moment with label i reads

$$\frac{\mathrm{d}\vec{m}_i}{\mathrm{d}t} = -\gamma_i \vec{m}_i \times \vec{B}_i^{\text{eff}} + \eta_i \frac{\vec{m}_i}{m_i} \times \frac{\mathrm{d}\vec{m}_i}{\mathrm{d}t} \,, \tag{G.17}$$

where $m_i = |\vec{m}_i|$ and the atom-dependent electron gyromagnetic ratio γ_i as well as an atom-dependent phenomenological damping parameter $\eta_i \geq 0$ were introduced.

Analogue to the previous Sec. G.1 it is assumed that the external magnetic field has a large time-independent component pointing along the positive z axis and small time-dependent x and y components, which induce a small time-dependent transverse part for each magnetic moment on top of the time-independent part along the positive or negative z axis,

$$\vec{B}^{\text{ext}}(t) = \begin{pmatrix} 0 \\ 0 \\ B_z^{\text{ext}} \end{pmatrix} + \begin{pmatrix} B_x^{\text{ext}}(t) \\ B_y^{\text{ext}}(t) \\ 0 \end{pmatrix} \quad \text{and} \quad \vec{m}_i(t) = \begin{pmatrix} 0 \\ 0 \\ m_{i,z} \end{pmatrix} + \begin{pmatrix} m_{i,x}(t) \\ m_{i,y}(t) \\ 0 \end{pmatrix} \,, \tag{G.18}$$

where $B_z^{\text{ext}} \gg B_x^{\text{ext}}, B_y^{\text{ext}}$ and $|m_{i,z}| \gg m_{i,x}, m_{i,y}\ \forall\ i$. Note that a ferromagnetic (FM) coupling (*i.e.*, $J_{ij} > 0$) implies that the state with lowest energy fulfills $m_{i,z} > 0\ \forall\, i$. In systems with a negative exchange or antiferromagnetic (AFM) coupling ($J_{ij} < 0$), however, it can be energetically favorable to have $m_{i,z} < 0$ for some atoms i. This is the case when the corresponding effective magnetic field (see Eq. (G.16)) has a negative z component, *i.e.*, when the coupling term due to neighboring magnetic moments overcompensates $B_z^{\text{ext}} > 0$.

Solving the LLG equation (G.17) for the x and y components of the magnetic moment $\vec{m}_i$ yields

$$\begin{aligned}\frac{\mathrm{d}m_{i,x}}{\mathrm{d}t} &= -\gamma_i \left(m_{i,y}B_{i,z}^{\text{eff}} - m_{i,z}B_{i,y}^{\text{eff}}\right) + \eta_i \left(\frac{m_{i,y}}{m_i}\underbrace{\frac{\mathrm{d}m_{i,z}}{\mathrm{d}t}}_{=0} - \frac{m_{i,z}}{m_i}\frac{\mathrm{d}m_{i,y}}{\mathrm{d}t}\right) \\ &= -\gamma_i \left(m_{i,y}B_{i,z}^{\text{eff}} - m_{i,z}B_{i,y}^{\text{eff}}\right) - \overline{\eta}_i \frac{\mathrm{d}m_{i,y}}{\mathrm{d}t} \end{aligned} \tag{G.19}$$

and

$$\begin{aligned}\frac{\mathrm{d}m_{i,y}}{\mathrm{d}t} &= -\gamma_i \left(m_{i,z}B_{i,x}^{\text{eff}} - m_{i,x}B_{i,z}^{\text{eff}}\right) + \eta_i \left(\frac{m_{i,z}}{m_i}\frac{\mathrm{d}m_{i,x}}{\mathrm{d}t} - \frac{m_{i,x}}{m_i}\underbrace{\frac{\mathrm{d}m_{i,z}}{\mathrm{d}t}}_{=0}\right) \\ &= -\gamma_i \left(m_{i,z}B_{i,x}^{\text{eff}} - m_{i,x}B_{i,z}^{\text{eff}}\right) + \overline{\eta}_i \frac{\mathrm{d}m_{i,x}}{\mathrm{d}t}\ , \end{aligned} \tag{G.20}$$

where $\overline{\eta}_i = \eta_i \frac{m_{i,z}}{m_i}$ and $\frac{m_{i,z}}{m_i} \approx +1$ or $\frac{m_{i,z}}{m_i} \approx -1$, depending on whether the magnetic moment's z component points along positive or negative z axis. After the variable substitution $m_{i,\pm} = m_{i,x} \pm \mathrm{i}m_{i,y}$ and a Fourier transformation to frequency space (see Eq. (G.10)) one arrives at the expression

$$\frac{1}{m_{i,z}}\left(\pm\frac{1 \mp \mathrm{i}\overline{\eta}_i}{\gamma_i}\omega + B_{i,z}^{\text{eff}}\right)\tilde{m}_{i,\pm}(\omega) = \tilde{B}_{i,\pm}^{\text{eff}}(\omega)\ . \tag{G.21}$$

Inserting the expression for the effective magnetic field as given in Eq. (G.16) into Eq. (G.21) we find

$$\frac{1}{m_{i,z}}\left(\pm\frac{1 \mp \mathrm{i}\overline{\eta}_i}{\gamma_i}\omega + \sum_{j|j\neq i} J_{ij}m_{j,z} + B_z^{\text{ext}}\right)\tilde{m}_{i,\pm}(\omega) - \sum_{j|j\neq i} J_{ij}\tilde{m}_{j,\pm}(\omega) = \tilde{B}_{\pm}^{\text{ext}}(\omega) \tag{G.22}$$

or in matrix notation

$$\sum_j A_{ij,\pm}\tilde{m}_{j;\pm} = \tilde{B}_{\pm}^{\text{ext}} \tag{G.23}$$

with

$$A_{ij,\pm} = \frac{1}{m_{i,z}} \left[\pm \frac{1 \mp \mathrm{i}\overline{\eta}_i}{\gamma_i} \omega + \sum_{k|k\neq i} J_{ik} m_{k,z} + B_z^{\mathrm{ext}} \right] \cdot \delta_{ij} - J_{ij} \cdot (1 - \delta_{ij}) \ . \tag{G.24}$$

In the following we drop the tilde symbol for Fourier space quantities.

The inverse of the matrix $A_\pm(\omega)$ yields the transverse LLG response function $\chi_\pm^{\mathrm{LLG}}(\omega)$, which describes how the magnetic moments $\{m_{i,\pm}\}$ respond to an external magnetic perturbation $B_\pm^{\mathrm{ext}}$,

$$m_{i;\pm} = \sum_j \chi_{ij,\pm}^{\mathrm{LLG}} B_\pm^{\mathrm{ext}} \ . \tag{G.25}$$

When the eigenstates and eigenfunctions of the matrix $A_\pm$ are known, one gets access to the eigenmodes and eigenfunctions of the susceptibility. Whereas the eigenfunctions are identical, the eigenmodes of $\chi_\pm^{\mathrm{LLG}}$ are the inverse of those of $A_\pm$. Thus, a resonance in the response function appears always when

$$\frac{\mathrm{d}}{\mathrm{d}\omega} \mathrm{Im}\left[1/\lambda^{(\alpha)}(\omega)\right] \stackrel{!}{=} 0 \ . \tag{G.26}$$

Finally, a comparison with the susceptibility as defined in the KKR formalism yields the identity $\chi_-^{\mathrm{LLG}}(\omega) = -2\chi^{+-}(\omega)$. The difference steps from the fact that in the KKR formalism the susceptibility is introduced as spin-spin-correlation function, while in this Appendix the response is given in terms of an induced magnetic moment. This gives a tool of fetching the values of J_{ij}, as explained in the main text.

G.2.1. LLG model for dimers

For a dimer Eq. (G.15), the potential energy as function of the magnetic moments, takes the form

$$E(\vec{m}_1, \vec{m}_2) = -J\vec{m}_1 \cdot \vec{m}_2 - \vec{B}^{\mathrm{ext}} \cdot (\vec{m}_1 + \vec{m}_2) \ , \tag{G.27}$$

where $J = J_{12} = J_{21}$. Then, the corresponding site-dependent effective magnetic fields take the forms

$$\vec{B}_1^{\mathrm{eff}} = J\vec{m}_2 + \vec{B}^{\mathrm{ext}} \tag{G.28}$$

$$\text{and} \quad \vec{B}_2^{\mathrm{eff}} = J\vec{m}_1 + \vec{B}^{\mathrm{ext}} \ , \tag{G.29}$$

which act on moments $\vec{m}_1$ and $\vec{m}_2$, respectively. Following Eq. (G.24) we have to determine eigenvalues and eigenfunctions of the matrix

$$A = \begin{pmatrix} a_1 + J\frac{m_{2,z}}{m_{1,z}} & -J \\ -J & a_2 + J\frac{m_{1,z}}{m_{2,z}} \end{pmatrix} \quad \text{with} \quad \begin{cases} a_1(\omega) & = -\frac{1+\mathrm{i}\eta_1 \frac{m_{1,z}}{m_1}}{\gamma_1 m_{1,z}}\omega + \frac{B_z^{\mathrm{ext}}}{m_{1,z}} \\ a_2(\omega) & = -\frac{1+\mathrm{i}\eta_2 \frac{m_{2,z}}{m_2}}{\gamma_2 m_{2,z}}\omega + \frac{B_z^{\mathrm{ext}}}{m_{2,z}} \end{cases} . \tag{G.30}$$

The eigenvalues and eigenvectors for this matrix are

$$\begin{cases} \lambda^{(a)}(\omega) = & \frac{1}{2}\left(a_1(\omega) + a_2(\omega) + J\left(\frac{m_{2,z}}{m_{1,z}} + \frac{m_{1,z}}{m_{2,z}}\right) - d(\omega)\right) \\ \lambda^{(b)}(\omega) = & \frac{1}{2}\left(a_1(\omega) + a_2(\omega) + J\left(\frac{m_{2,z}}{m_{1,z}} + \frac{m_{1,z}}{m_{2,z}}\right) + d(\omega)\right) \end{cases} \tag{G.31}$$

and

$$\begin{cases} \vec{v}^{(a)} = & \left(1\ ,\ -\frac{1}{2J}\left(a_1(\omega) - a_2(\omega) + J\left(\frac{m_{2,z}}{m_{1,z}} - \frac{m_{1,z}}{m_{2,z}}\right) - d(\omega)\right)\right)^{\mathrm{T}} \\ \vec{v}^{(b)} = & \left(1\ ,\ -\frac{1}{2J}\left(a_1(\omega) - a_2(\omega) + J\left(\frac{m_{2,z}}{m_{1,z}} - \frac{m_{1,z}}{m_{2,z}}\right) + d(\omega)\right)\right)^{\mathrm{T}} \end{cases}, \tag{G.32}$$

where

$$d(\omega) = \sqrt{\left(a_1(\omega) - a_2(\omega) + J\left(\frac{m_{2,z}}{m_{1,z}} - \frac{m_{1,z}}{m_{2,z}}\right)\right)^2 + 4J^2}\ . \tag{G.33}$$

The derived expressions get simplified when the dimer involves only atoms of the same type. Then, one can define $\gamma \equiv \gamma_1 = \gamma_2$ and $\eta \equiv \eta_1 = \eta_2$, and two cases have to be distinguished for the alignment of the z component of the magnetic moments:

Case (1): Parallel alignment ($m_z \equiv m_{1,z} = m_{2,z} > 0$)

The scenario described by this case is a setup of two magnetic moments that are aligned parallel to each other. There, one always finds two eigenmodes of the system, independent of the sign of the coupling constant J. Inserting the simplified expressions (m_z, γ, η) into Eqs. (G.30) and (G.33) leads to

$$a(\omega) = -\frac{1 + \mathrm{i}\eta}{\gamma m_z}\omega + \frac{B_z^{\mathrm{ext}}}{m_z} = a_1(\omega) = a_2(\omega) \tag{G.34}$$

and

$$d(\omega) = 2|J| = d\ . \tag{G.35}$$

With these expressions at hand one finds the eigenstates and eigenvectors of the system

$$\begin{cases} \lambda^{(a)}(\omega) = & a(\omega) + J - |J| \\ \lambda^{(b)}(\omega) = & a(\omega) + J + |J| \end{cases} \quad \text{and} \quad \begin{cases} \vec{v}^{(a)} = & \left(1, \quad +\frac{|J|}{J}\right)^{\mathrm{T}} \\ \vec{v}^{(b)} = & \left(1, \quad -\frac{|J|}{J}\right)^{\mathrm{T}} \end{cases}. \tag{G.36}$$

For the case that $J > 0$, one has $\lambda^{(a)}(\omega) = a(\omega)$ with $\vec{v}^{(a)} = (1, 1)$, which corresponds to the acoustic mode, where the two moments show a precession in phase around the z axis. By use of the condition (G.26) one finds

$$\omega_{\mathrm{res}}^{\mathrm{ac}} = \frac{\gamma}{\sqrt{1 + \eta^2}} B_z^{\mathrm{ext}}\ , \tag{G.37}$$

which means that the resonance depends linearly on the external magnetic field along z. This resonance behavior is known from the adatom case where the resonance of the response function is the Larmor frequency, see Ch. 6. Furthermore, $\lambda^{(b)}(\omega) = a(\omega) + 2J$ with $\vec{v}^{(b)} = (1, -1)$ describes another eigenstate of the system, the optical mode. Because of $\mathrm{e}^{-\mathrm{i}\pi} = -1$ the minus sign in the eigenvector indicates a phase shift by π between the two atoms on their orbital precession around the z axis. The eigenvalue $\lambda_{\pm}^{(b)}$ is by $2J$ higher (since $J > 0$) compared to $\lambda_{\pm}^{(a)}$ and the optical resonance is given by

$$\omega_{\mathrm{res}}^{\mathrm{opt}} = \frac{\gamma}{\sqrt{1+\eta^2}} \left(B_z^{\mathrm{ext}} + 2Jm_z \right) . \tag{G.38}$$

Thus, the optical resonance can be determined by the knowledge of the acoustic mode and the product of exchange interaction and the z component of the magnetic moment, Jm_z. The two eigenstates of the susceptibility within the LLG model read

$$\mathrm{Im}\left[1/\lambda^{(\alpha)}(\omega)\right] = \frac{m_z\gamma}{1+\eta^2} \frac{\eta\omega}{\left(\omega - \omega_0^{(\alpha)}\right)^2 + \left(\eta\omega_0^{(\alpha)}\right)^2} , \tag{G.39}$$

with

$$\omega_0^{(\alpha)} = \begin{cases} \frac{\gamma}{1+\eta^2} B_z^{\mathrm{ext}} & , \ (\alpha) = (a) \\ \frac{\gamma}{1+\eta^2} \left(B_z^{\mathrm{ext}} + 2Jm_z \right) & , \ (\alpha) = (b) \ . \end{cases} \tag{G.40}$$

Note, that for the case $J < 0$, the same analysis as above applies, where only the labels (a) and (b) have to be switched. Then the optical mode is lower in energy as compared to the acoustic mode. This is in line with the fact that a parallel alignment of moments that couple antiferromagnetically ($J < 0$) is energetically the most undesired state, making the optical resonance (*i.e.*, an excitation that leads to a tilting away from this AFM alignment) more favorable in energy.

Case (2): Antiparallel alignment ($m_z \equiv m_{1,z} = -m_{2,z} > 0$)

In this scenario the magnetic moment of the second atom is assumed to point antiparallel to the moment of the first atom and also antiparallel to the applied external magnetic field $\vec{B}^{\mathrm{ext}}$. In principle this leads to a break in the symmetry of the problem, since the applied field increases the value of $m_{1,z}$ while it decreases the value of $m_{2,z}$. However, as long as the applied external field remains small compared to the z component of the involved magnetic moments, the assumption $m_{1,z} = -m_{2,z}$ is reasonable.

Inserting the parameters into Eqs. (G.30) and (G.33) yields

$$a(\omega) = -\frac{1+\mathrm{i}\eta}{\gamma m_z}\omega + \frac{B_z^{\mathrm{ext}}}{m_z} = a_1(\omega) = -a_2^*(\omega) \tag{G.41}$$

and

$$d(\omega) = 2\sqrt{\left(\mathrm{Re}\left[a(\omega)\right]\right)^2 + J^2} , \tag{G.42}$$

which results in the eigenvalues

$$\begin{cases} \lambda^{(a)}(\omega) = & \mathrm{i}\,\mathrm{Im}\left[a(\omega)\right] - J - \sqrt{\left(\mathrm{Re}\left[a(\omega)\right]\right)^2 + J^2} \\ \lambda^{(b)}(\omega) = & \mathrm{i}\,\mathrm{Im}\left[a(\omega)\right] - J + \sqrt{\left(\mathrm{Re}\left[a(\omega)\right]\right)^2 + J^2} \end{cases} \tag{G.43}$$

and the corresponding eigenvectors

$$\begin{cases} \vec{v}^{(a)}(\omega) = & \left(1, \quad -\frac{\mathrm{Re}\left[a(\omega)\right] - \sqrt{\left(\mathrm{Re}\left[a(\omega)\right]\right)^2 + J^2}}{J}\right)^{\mathrm{T}} \\ \vec{v}^{(b)}(\omega) = & \left(1, \quad +\frac{\mathrm{Re}\left[a(\omega)\right] + \sqrt{\left(\mathrm{Re}\left[a(\omega)\right]\right)^2 + J^2}}{J}\right)^{\mathrm{T}} \end{cases} . \tag{G.44}$$

To determine the frequency of the resonance positions for the two eigenstates is cumbersome and a closed expressions for the frequency is difficult to find. The form of the eigenstates that describes the excitation spectra of the LLG susceptibility is given by

$$\mathrm{Im}\left[1/\lambda^{(\alpha)}(\omega)\right] = \frac{\frac{\eta\omega}{\gamma m_z}}{\left(\frac{\eta\omega}{\gamma m_z}\right)^2 + \left(J \pm \sqrt{\left(-\frac{\omega}{\gamma m_z} + \frac{B_z^{\mathrm{ext}}}{m_z}\right)^2 + J^2}\right)^2} , \tag{G.45}$$

where for $(\alpha) = (a)$ the plus sign $(+)$ and for $(\alpha) = (b)$ the minus sign $(-)$ in front of the square root is meant. Instead of regarding the derivative with respect to ω, setting the expression to zero and solving for ω we will analyze Eq. (G.45) directly:

The indication of a resonance requires the numerator in Eq. (G.45) to be minimal. For the case that $B_z^{\mathrm{ext}} = 0$ the denominator vanishes for one of the eigenmodes when $\omega = 0$, while the other eigenmode reaches the finite value $4|J|$. However, also the numerator vanishes for $\omega = 0$. By use of L'Hôpital's rule one confirms that in the former case the eigenmode diverges at $\omega = 0$. Therefore, this eigenmode represents the acoustic mode of the system that for vanishing external magnetic field leads to the Goldstone mode. Note that any positive applied field ($B_z^{\mathrm{ext}} > 0$) will prevent the denominator in Eq. (G.45) to diverge, as the frequency cannot be zero and $\gamma B_z^{\mathrm{ext}}$ at the same time. Instead, the resonance will be located somewhere in-between these two conditions, $0 < \omega_{\mathrm{res}}^{\mathrm{ac}} < \gamma B_z^{\mathrm{ext}}$.

The conclusion of this analysis is twofold: When no applied external magnetic field is present, only one resonance mode is found. It is located at $\omega = 0$ with $\vec{v} = (1, -1)$. Note that the resonance position and the corresponding eigenvector are independent of the sign of J. Due to the fact that the z components of the magnetic moments are antiparallel to each other, this eigenfunction describes two magnetic moments that precess in phase pointing always exactly antiparallel with respect to each other. When an external magnetic field is applied this mode gets strongly damped, as the condition (G.26) cannot be satisfied anymore.

In Fig. G.2 the four cases are depicted for different damping values. The parameters used here are $\gamma = 2$, $m = 1$, $J = 0.3$, and $B = 0.2$. Note that the mode (2b) gets enhanced

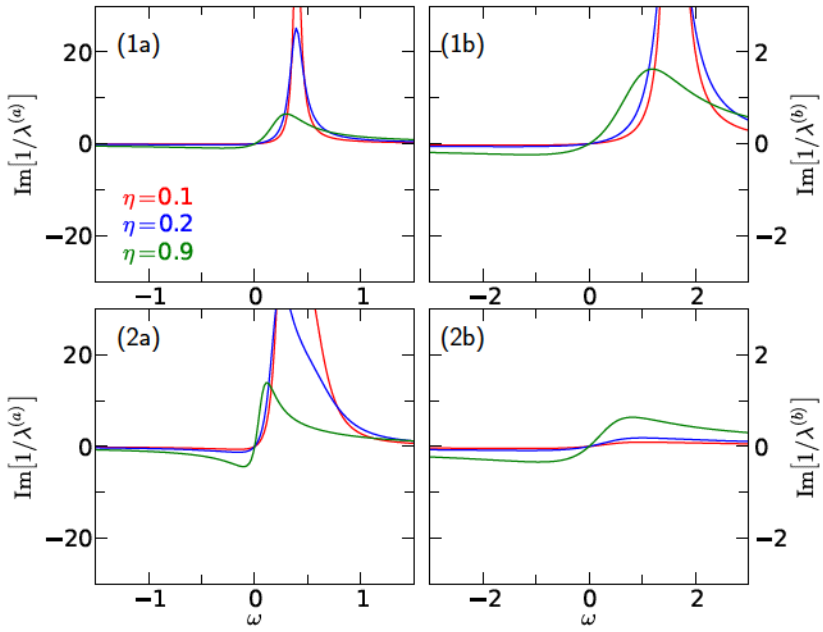

Figure G.2.: The eigenmodes of the magnetic excitation spectra for a dimer are shown. The top row presents the two eigenmodes when a FM alignment of the magnetic moments is considered (cases (1a) and (1b)), whereas in the bottom row the two modes for an AFM alignment are explored (cases (2a) and (2b)). All spectra are shown for different damping values. Note that a damping leads to a broadening in the resonances of cases (1a) and (1b), while it sharpens the resonance in case (2a) and allows a response within case (2b) in the first place.

when the value for the damping parameter η is increased, while at the same time all other modes experience a broadening and decrease in height. In the limit of $\eta \to \infty$ all modes behave like $1/\eta$.

G.2.2. LLG model for trimers

In the following we assume that the nearest-neighbor interactions are described by the exchange coupling constant J and that interactions beyond the nearest-neighbor interaction are negligible. In addition, this subsection deals with atoms of the same kind only (same magnetic moment, damping, *etc.*), which reduces the level of complexity of the involved formulas and allows to stress the impact on the resonance positions when different arrangements of the magnetic atoms are considered. For this analysis two different

arrangements are distinguished. In one case the atoms are aligned within a linear chain, in the other they form a regular triangular structure (see Fig. 8.8 in the main text). The latter has a three-fold symmetry which conveniently is already true for the (111) fcc-surface, the type of surface structure that is considered throughout this thesis.

In the case of a linear chain we find $J = J_{12} = J_{23} \neq J_{13} = 0$, *i.e.*, the exchange coupling among the edge atoms at sites 1 and 3 is neglected. The potential energy (see Eq. (G.15)) reads

$$E^{\mathrm{lin}}(\vec{m}_1, \vec{m}_2, \vec{m}_3) = J\left(\vec{m}_1 \cdot \vec{m}_2 + \vec{m}_2 \cdot \vec{m}_3\right) + \vec{B}^{\mathrm{ext}} \cdot \left(\vec{m}_1 + \vec{m}_2 + \vec{m}_3\right) \ . \tag{G.46}$$

This results in effective magnetic fields of the form

$$\vec{B}_1^{\mathrm{eff}} = \vec{B}_3^{\mathrm{eff}} = J\vec{m}_2 + \vec{B}^{\mathrm{ext}} \tag{G.47}$$

$$\text{and} \qquad \vec{B}_2^{\mathrm{eff}} = J\left(\vec{m}_1 + \vec{m}_3\right) + \vec{B}^{\mathrm{ext}} \ . \tag{G.48}$$

Following the same procedure as before the matrix from Eq. (G.24) takes the form

$$A^{\mathrm{lin}} = \begin{pmatrix} a+J & -J & 0 \\ -J & a+2J & -J \\ 0 & -J & a+J \end{pmatrix} \quad \text{with} \quad a = -\frac{1+\mathrm{i}\eta}{\gamma m_0}\omega + \frac{B_z^{\mathrm{ext}}}{m_0} \ . \tag{G.49}$$

The eigenvalues and eigenfunctions read

$$\begin{cases} \lambda^{(a)} = & a \\ \lambda^{(b)} = & a+J \\ \lambda^{(c)} = & a+3J \end{cases} \quad \text{and} \quad \begin{cases} \vec{v}^{(a)} = & (1,1,1)^{\mathrm{T}} \\ \vec{v}^{(b)} = & (1,0,-1)^{\mathrm{T}} \\ \vec{v}^{(c)} = & (1,-2,1)^{\mathrm{T}} \end{cases} \ . \tag{G.50}$$

Note that the eigenvalues are nondegenerate, $\lambda^{(a)} < \lambda^{(b)} < \lambda^{(c)}$.

For a triangular structure we have $J = J_{12} = J_{23} = J_{13}$ and the energy is given by

$$E^{\mathrm{tri}}(\vec{m}_1, \vec{m}_2, \vec{m}_3) = J\left(\vec{m}_1 \cdot \vec{m}_2 + \vec{m}_1 \cdot \vec{m}_3 + \vec{m}_2 \cdot \vec{m}_3\right) + \vec{B}^{\mathrm{ext}} \cdot \left(\vec{m}_1 + \vec{m}_2 + \vec{m}_3\right) \ . \tag{G.51}$$

This results in effective magnetic fields of the form

$$\vec{B}_1^{\mathrm{eff}} = J\left(\vec{m}_2 + \vec{m}_3\right) + \vec{B}^{\mathrm{ext}} \ , \tag{G.52}$$

$$\vec{B}_2^{\mathrm{eff}} = J\left(\vec{m}_1 + \vec{m}_3\right) + \vec{B}^{\mathrm{ext}} \ , \tag{G.53}$$

$$\text{and} \quad \vec{B}_3^{\mathrm{eff}} = J\left(\vec{m}_1 + \vec{m}_2\right) + \vec{B}^{\mathrm{ext}} \ . \tag{G.54}$$

The matrix from Eq. (G.24) takes the form

$$A^{\mathrm{tri}} = \begin{pmatrix} a+2J & -J & -J \\ -J & a+2J & -J \\ -J & -J & a+2J \end{pmatrix} \ , \tag{G.55}$$

where the definition of a is the same as in Eq. (G.49). The eigenvalues and eigenfunction of this matrix are of the form

$$\begin{cases} \lambda^{(a)} = & a \\ \lambda^{(b)} = & a+3J \\ \lambda^{(c)} = & a+3J \end{cases} \quad \text{and} \quad \begin{cases} \vec{v}^{(a)} = & (1,1,1)^{\mathrm{T}} \\ \vec{v}^{(b)} = & (1,0,-1)^{\mathrm{T}} \\ \vec{v}^{(c)} = & (1,-1,0)^{\mathrm{T}} \end{cases} . \tag{G.56}$$

Note that two eigenvalues are degenerate, $\lambda^{(a)} < \lambda^{(b)} = \lambda^{(c)}$ (assuming that $J > 0$), which reflects the higher symmetry of A^{tri} compared to the one for the linear arrangement, A^{lin} (see Eq. (G.49)).

G.2.3. LLG model for tetramers

Accounting for the LLG model for the 4-atomic linear chain the matrix structure reads

$$A = \begin{pmatrix} a+J & -J & 0 & 0 \\ -J & a+2J & -J & 0 \\ 0 & -J & a+2J & -J \\ 0 & 0 & -J & a+J \end{pmatrix} , \tag{G.57}$$

where the definition of a is the same as given in Eq. (G.49). One finds the following eigenvalues and eigenvectors

$$\begin{cases} \lambda^{(a)} = & a \\ \lambda^{(b)} = & a+(2-\sqrt{2})J \\ \lambda^{(c)} = & a+2J \\ \lambda^{(d)} = & a+(2+\sqrt{2})J \end{cases} \quad \text{and} \quad \begin{cases} \vec{v}^{(a)} = & (1,1,1,1)^{\mathrm{T}} \\ \vec{v}^{(b)} = & \left(1,\sqrt{2}-1,-(\sqrt{2}-1),-1\right)^{\mathrm{T}} \\ \vec{v}^{(c)} = & (1,-1,-1,1)^{\mathrm{T}} \\ \vec{v}^{(d)} = & \left(1,-(1+\sqrt{2}),1+\sqrt{2},-1\right)^{\mathrm{T}} \end{cases} . \tag{G.58}$$

G.2.4. LLG model for pentamers

For the linear chain of 5 atoms the matrix structure is

$$A = \begin{pmatrix} a+J & -J & 0 & 0 & 0 \\ -J & a+2J & -J & 0 & 0 \\ 0 & -J & a+2J & -J & 0 \\ 0 & 0 & -J & a+2J & -J \\ 0 & 0 & 0 & -J & a+J \end{pmatrix} , \tag{G.59}$$

and one arrives at the eigenvalues

$$\begin{cases} \lambda^{(a)} = & a \\ \lambda^{(b)} = & a + \frac{1}{2}(3-\sqrt{5})J \\ \lambda^{(c)} = & a + \frac{1}{2}(5-\sqrt{5})J \\ \lambda^{(d)} = & a + \frac{1}{2}(3+\sqrt{5})J \\ \lambda^{(e)} = & a + \frac{1}{2}(5+\sqrt{5})J \end{cases} \tag{G.60}$$

and the corresponding eigenvectors

$$\begin{cases} \vec{v}^{(a)} = & (1,1,1,1,1)^{\mathrm{T}} \\ \vec{v}^{(b)} = & \left(1, \frac{1}{2}(\sqrt{5}-1), 0, -\frac{1}{2}(\sqrt{5}-1), -1\right)^{\mathrm{T}} \\ \vec{v}^{(c)} = & \left(1, -\frac{1}{2}(3-\sqrt{5}), -(\sqrt{5}-1), -\frac{1}{2}(3-\sqrt{5}), 1\right)^{\mathrm{T}} \\ \vec{v}^{(d)} = & \left(1, -\frac{1}{2}(1+\sqrt{5}), 0, \frac{1}{2}(1+\sqrt{5}), -1\right)^{\mathrm{T}} \\ \vec{v}^{(e)} = & \left(1, -\frac{1}{2}(3+\sqrt{5}), 1+\sqrt{5}, -\frac{1}{2}(3+\sqrt{5}), 1\right)^{\mathrm{T}} \end{cases} . \tag{G.61}$$

G.2.5. LLG model for hexamers

For the six-atomic chain of equal atoms one finds the matrix

$$A = \begin{pmatrix} a+J & -J & 0 & 0 & 0 & 0 \\ -J & a+2J & -J & 0 & 0 & 0 \\ 0 & -J & a+2J & -J & 0 & 0 \\ 0 & 0 & -J & a+2J & -J & 0 \\ 0 & 0 & 0 & -J & a+2J & -J \\ 0 & 0 & 0 & 0 & -J & a+J \end{pmatrix} , \tag{G.62}$$

with the eigenvalues

$$\begin{cases} \lambda^{(a)} = & a \\ \lambda^{(b)} = & a + (2-\sqrt{3})J \\ \lambda^{(c)} = & a + J \\ \lambda^{(d)} = & a + 2J \\ \lambda^{(e)} = & a + 3J \\ \lambda^{(f)} = & a + (2+\sqrt{3})J \end{cases} \tag{G.63}$$

and corresponding eigenvectors

$$\begin{cases} \vec{v}^{(a)} = & (1,1,1,1,1,1)^{\mathrm{T}} \\ \vec{v}^{(b)} = & \left(1,\sqrt{3}-1,2-\sqrt{3},-(2-\sqrt{3}),-(\sqrt{3}-1),-1\right)^{\mathrm{T}} \\ \vec{v}^{(c)} = & (1,0,-1,-1,0,1)^{\mathrm{T}} \\ \vec{v}^{(d)} = & (1,-1,-1,1,1,-1)^{\mathrm{T}} \\ \vec{v}^{(e)} = & (1,-2,1,1,-2,1)^{\mathrm{T}} \\ \vec{v}^{(f)} = & \left(1,-(1+\sqrt{3}),2+\sqrt{3},-(2+\sqrt{3}),1+\sqrt{3},-1\right)^{\mathrm{T}} \end{cases} . \tag{G.64}$$

The six-atomic ring of equal atoms has the matrix form (note that the first and last atoms couple via the matrix elements $A_{16} = A_{61} = -J$)

$$A = \begin{pmatrix} a+2J & -J & 0 & 0 & 0 & -J \\ -J & a+2J & -J & 0 & 0 & 0 \\ 0 & -J & a+2J & -J & 0 & 0 \\ 0 & 0 & -J & a+2J & -J & 0 \\ 0 & 0 & 0 & -J & a+2J & -J \\ -J & 0 & 0 & 0 & -J & a+2J \end{pmatrix} , \tag{G.65}$$

with the eigenvalues and eigenfunctions

$$\begin{cases} \lambda^{(a)} = & a \\ \lambda^{(b)} = & a+J \\ \lambda^{(c)} = & a+J \\ \lambda^{(d)} = & a+3J \\ \lambda^{(e)} = & a+3J \\ \lambda^{(f)} = & a+4J \end{cases} \text{ and } \begin{cases} \vec{v}^{(a)} = & (1,1,1,1,1,1)^{\mathrm{T}} \\ \vec{v}^{(b)} = & (1,1,0,-1,-1,0)^{\mathrm{T}} \\ \vec{v}^{(c)} = & (1,0,-1,-1,0,1)^{\mathrm{T}} \\ \vec{v}^{(d)} = & (1,0,-1,1,0,-1)^{\mathrm{T}} \\ \vec{v}^{(e)} = & (1,-1,0,1,-1,0)^{\mathrm{T}} \\ \vec{v}^{(f)} = & (1,-1,1,-1,1,-1)^{\mathrm{T}} \end{cases} . \tag{G.66}$$

Once again, due to symmetry, we obtain energetically degenerate eigenmodes.

G.2.6. LLG model for larger ring and chain structures

Finally we discuss the resonances in the excitation spectrum of ring and chain structures for the case that the number of atoms is large, *i.e.*, $N \gg 1$. Then, the difference in the spectra of a ring and of a chain arrangement should vanish, as they only differ in the boundary conditions for atom 1 and atom N (see discussion of the trimer or the hexamer).

Thus, for both structures the matrix can be approximated by a tridiagonal matrix,

$$A = \begin{pmatrix} a+2J & -J & 0 & & & \\ -J & a+2J & -J & & 0 & \\ 0 & -J & a+2J & & & \\ & & & \ddots & & \\ & 0 & & & a+2J & -J \\ & & & & -J & a+2J \end{pmatrix} . \tag{G.67}$$

The eigenvalues for such a problem are given by

$$\lambda^{(\alpha)} = a + 2J \left(1 - \cos \left[\frac{k}{N+1} \pi \right] \right) , \tag{G.68}$$

where the different eigenvalues are labeled with $(\alpha) \in \{(a), (b), \dots\}$ and

$$k = k(\alpha) = \begin{cases} 1 & , \ (\alpha) = (a) \\ 2 & , \ (\alpha) = (b) \\ \dots \end{cases} . \tag{G.69}$$

The corresponding eigenvectors read

$$\vec{v}^{(\alpha)} = \left(1 \ , \ \frac{\sin \left[\frac{2k}{N+1} \pi \right]}{\sin \left[\frac{k}{N+1} \pi \right]} \ , \ \dots \ , \ \frac{\sin \left[\frac{Nk}{N+1} \pi \right]}{\sin \left[\frac{k}{N+1} \pi \right]} \right)^{\mathrm{T}} . \tag{G.70}$$

Because of $\sin \left[\frac{Nk}{N+1} \pi \right] = \sin \left[k\pi - \frac{k}{N+1} \pi \right] = (-1)^{k+1} \sin \left[\frac{k}{N+1} \pi \right]$ the first and the last component of the vector are the same up to a change in the sign. The same connection is given for the pairs of components 2 and $N-1$, 3 and $N-2$, and so on. As long as $k \ll N$ neighboring atoms precess with only a small relative phase shift which is reflected in the fact that the corresponding eigenvalue (see Eq. (G.68)) shows only a small contribution from the term proportional to J. If k is close to N, neighboring atoms precess with nearly a phase shift of π and the eigenvalue reflects the energetical costs by a large impact of the term proportional to J.

Bibliography

[1] R. Wood, The feasibility of magnetic recording at 1 Terabit per square inch, Magnetics, IEEE Transactions on **36**(1), 36–42 (Jan 2000).

[2] M. N. Baibich, J. M. Broto, A. Fert, F. N. Van Dau, F. Petroff, P. Etienne, G. Creuzet, A. Friederich, and J. Chazelas, Giant Magnetoresistance of (001)Fe/(001)Cr Magnetic Superlattices, Phys. Rev. Lett. **61**, 2472–2475 (Nov 1988).

[3] G. Binasch, P. Grünberg, F. Saurenbach, and W. Zinn, Enhanced magnetoresistance in layered magnetic structures with antiferromagnetic interlayer exchange, Phys. Rev. B **39**, 4828–4830 (Mar 1989).

[4] Y. Shiroishi, K. Fukuda, I. Tagawa, H. Iwasaki, S. Takenoiri, H. Tanaka, H. Mutoh, and N. Yoshikawa, Future Options for HDD Storage, Magnetics, IEEE Transactions on **45**(10), 3816–3822 (Oct 2009).

[5] M. Bode, M. Heide, K. von Bergmann, P. Ferriani, S. Heinze, G. Bihlmayer, A. Kubetzka, O. Pietzsch, S. Blügel, and R. Wiesendanger, Chiral magnetic order at surfaces driven by inversion asymmetry, Nature **447**, 190–193 (Mar 2007).

[6] B. Santos, J. M. Puerta, J. I. Cerda, R. Stumpf, K. von Bergmann, R. Wiesendanger, M. Bode, K. F. McCarty, and J. de la Figuera, Structure and magnetism of ultra-thin chromium layers on W(110), New J. Phys. **10**(1), 013005 (Jan 2008).

[7] P. Ferriani, K. von Bergmann, E. Y. Vedmedenko, S. Heinze, M. Bode, M. Heide, G. Bihlmayer, S. Blügel, and R. Wiesendanger, Atomic-Scale Spin Spiral with a Unique Rotational Sense: Mn Monolayer on W(001), Phys. Rev. Lett. **101**(2), 027201 (Jul 2008).

[8] B. Zimmermann, M. Heide, G. Bihlmayer, and S. Blügel, First-principles analysis of a homochiral cycloidal magnetic structure in a monolayer Cr on W(110), Phys. Rev. B **90**, 115427 (Sep 2014).

[9] S. Heinze, K. von Bergmann, M. Menzel, J. Brede, A. Kubetzka, R. Wiesendanger, G. Bihlmayer, and S. Blügel, Spontaneous atomic-scale magnetic skyrmion lattice in two dimensions, Nature Physics **7**, 713–718 (Jul 2011).

[10] N. Romming, C. Hanneken, M. Menzel, J. E. Bickel, B. Wolter, K. von Bergmann, A. Kubetzka, and R. Wiesendanger, Writing and Deleting Single Magnetic Skyrmions, Science **341**(6146), 636–639 (Aug 2013).

[11] P. Gambardella, S. Rusponi, M. Veronese, S. S. Dhesi, C. Grazioli, A. Dallmeyer, I. Cabria, R. Zeller, P. H. Dederichs, K. Kern, C. Carbone, and H. Brune, Giant Magnetic Anisotropy of Single Cobalt Atoms and Nanoparticles, Science **300**(5622), 1130–1133 (May 2003).

[12] C. F. Hirjibehedin, C. P. Lutz, and A. J. Heinrich, Spin Coupling in Engineered Atomic Structures, Science **312**(5776), 1021–1024 (May 2006).

[13] G. Binnig and H. Rohrer, Scanning tunneling microscopy, Surface Science **126**, 236 – 244 (Mar 1983).

[14] M. Bode, Spin-polarized scanning tunnelling microscopy, Reports on Progress in Physics **66**(4), 523 (Mar 2003).

[15] R. Wiesendanger, Spin mapping at the nanoscale and atomic scale, Rev. Mod. Phys. **81**, 1495–1550 (Nov 2009).

[16] B. C. Stipe, M. A. Rezaei, and W. Ho, Single-Molecule Vibrational Spectroscopy and Microscopy, Science **280**(5370), 1732–1735 (Jun 1998).

[17] G. Teobaldi, M. Peñalba, A. Arnau, N. Lorente, and W. A. Hofer, Including the probe tip in theoretical models of inelastic scanning tunneling spectroscopy: CO on Cu(100), Phys. Rev. B **76**, 235407 (Dec 2007).

[18] A. J. Heinrich, J. A. Gupta, C. P. Lutz, and D. M. Eigler, Single-Atom Spin-Flip Spectroscopy, Science **306**(5695), 466–469 (Oct 2004).

[19] T. Balashov, T. Schuh, A. F. Takács, A. Ernst, S. Ostanin, J. Henk, I. Mertig, P. Bruno, T. Miyamachi, S. Suga, and W. Wulfhekel, Magnetic Anisotropy and Magnetization Dynamics of Individual Atoms and Clusters of Fe and Co on Pt(111), Phys. Rev. Lett. **102**, 257203 (Jun 2009).

[20] A. A. Khajetoorians, S. Lounis, B. Chilian, A. T. Costa, L. Zhou, D. L. Mills, J. Wiebe, and R. Wiesendanger, Itinerant Nature of Atom-Magnetization Excitation by Tunneling Electrons, Phys. Rev. Lett. **106**, 037205 (Jan 2011).

[21] B. Chilian, A. A. Khajetoorians, S. Lounis, A. T. Costa, D. L. Mills, J. Wiebe, and R. Wiesendanger, Anomalously large g factor of single atoms adsorbed on a metal substrate, Phys. Rev. B **84**, 212401 (Dec 2011).

[22] B. Bryant, A. Spinelli, J. J. T. Wagenaar, M. Gerrits, and A. F. Otte, Local Control of Single Atom Magnetocrystalline Anisotropy, Phys. Rev. Lett. **111**, 127203 (Sep 2013).

[23] A. A. Khajetoorians, T. Schlenk, B. Schweflinghaus, M. dos Santos Dias, M. Steinbrecher, M. Bouhassoune, S. Lounis, J. Wiebe, and R. Wiesendanger, Spin Excitations of Individual Fe Atoms on Pt(111): Impact of the Site-Dependent Giant Substrate Polarization, Phys. Rev. Lett. **111**, 157204 (Oct 2013).

[24] L. Limot, E. Pehlke, J. Kröger, and R. Berndt, Surface-State Localization at Adatoms, Phys. Rev. Lett. **94**, 036805 (Jan 2005).

[25] J. Fransson, Spin Inelastic Electron Tunneling Spectroscopy on Local Spin Adsorbed on Surface, Nano Lett. **9**, 2414 (May 2009).

[26] N. Lorente and J.-P. Gauyacq, Efficient Spin Transitions in Inelastic Electron Tunneling Spectroscopy, Phys. Rev. Lett. **103**, 176601 (Oct 2009).

[27] J. Fernández-Rossier, Theory of Single-Spin Inelastic Tunneling Spectroscopy, Phys. Rev. Lett. **102**, 256802 (Jun 2009).

[28] M. Persson, Theory of Inelastic Electron Tunneling from a Localized Spin in the Impulsive Approximation, Phys. Rev. Lett. **103**, 050801 (Jul 2009).

[29] A. Hurley, N. Baadji, and S. Sanvito, Spin-flip inelastic electron tunneling spectroscopy in atomic chains, Phys. Rev. B **84**, 035427 (Jul 2011).

[30] A. Hurley, N. Baadji, and S. Sanvito, Bias asymmetry in the conductance profile of magnetic ions on surfaces probed by scanning tunneling microscopy, Phys. Rev. B **86**, 125411 (Sep 2012).

[31] P. Buczek, A. Ernst, and L. M. Sandratskii, Standing Spin Waves as a Basis for the Control of Terahertz Spin Dynamics: Time Dependent Density Functional Theory Study, Phys. Rev. Lett. **105**, 097205 (Aug 2010).

[32] V. P. Zhukov, E. V. Chulkov, and P. M. Echenique, Lifetimes and inelastic mean free path of low-energy excited electrons in Fe, Ni, Pt, and Au: *Ab initio* $\mathrm{GW}+\mathrm{T}$ calculations, Phys. Rev. B **73**, 125105 (Mar 2006).

[33] E. Şaşıoğlu, A. Schindlmayr, C. Friedrich, F. Freimuth, and S. Blügel, Wannier-function approach to spin excitations in solids, Phys. Rev. B **81**, 054434 (Feb 2010).

[34] M. C. T. D. Müller, Electron-Magnon Interaction in GT Approximation, Master's thesis, RWTH Aachen University, 2011.

[35] D. L. Mills and P. Lederer, Dynamical Properties of Magnetic Impurities in Transition Metals, Phys. Rev. **160**, 590 (Aug 1967).

[36] R. B. Muniz and D. L. Mills, Local Spin Dynamics of Magnetic Moments on Metal Surfaces, Phys. Rev. B **68**, 224414 (Dec 2003).

[37] S. Lounis, A. T. Costa, R. B. Muniz, and D. L. Mills, Dynamical Magnetic Excitations of Nanostructures from First Principles, Phys. Rev. Lett. **105**, 187205 (Oct 2010).

[38] S. Lounis, A. T. Costa, R. B. Muniz, and D. L. Mills, Theory of Local Dynamical Magnetic Susceptibilities from the Korringa-Kohn-Rostoker Green Function Method, Phys. Rev. B **83**, 035109 (Jan 2011).

[39] J. Tersoff and D. R. Hamann, Theory and Application for the Scanning Tunneling Microscope, Phys. Rev. Lett. **50**, 1998–2001 (Jun 1983).

[40] Q. Dubout, F. Donati, C. Wäckerlin, F. Calleja, M. Etzkorn, A. Lehnert, L. Claude, P. Gambardella, and H. Brune, Controlling the Spin of Co Atoms on Pt(111) by Hydrogen Adsorption, Phys. Rev. Lett. **114**, 106807 (Mar 2015).

[41] M. Born and R. Oppenheimer, Zur Quantentheorie der Molekeln, Annalen der Physik **389**(20), 457–484 (1927).

[42] S. Lloyd, Computational Capacity of the Universe, Phys. Rev. Lett. **88**, 237901 (May 2002).

[43] P. Hohenberg and W. Kohn, Inhomogeneous Electron Gas, Phys. Rev. **136**(3B), B864–B871 (Nov 1964).

[44] M. Levy, Universal variational functionals of electron densities, first-order density matrices, and natural spin-orbitals and solution of the v-representability problem, Proceedings of the National Academy of Sciences **76**(12), 6062–6065 (Dec 1979).

[45] W. Kohn and L. J. Sham, Self-Consistent Equations Including Exchange and Correlation Effects, Phys. Rev. **140**, A1133–A1138 (Nov 1965).

[46] R. O. Jones, *NIC Series Volume 31 Computational Nanoscience: Do It Yourself! Lecture Notes*, chapter Introduction to Density Functional Theory and Exchange-Correlation Energy Functionals, Johannes Grotendorst and Stefan Blügel and Dominik Marx, IFF, Forschungszentrum Jülich, winterschool edition, Feb 2006.

[47] C. A. Ullrich and Z.-h. Yang, A Brief Compendium of Time-Dependent Density Functional Theory, Brazilian Journal of Physics **44**(1), 154–188 (Feb 2014).

[48] P. A. M. Dirac, Note on Exchange Phenomena in the Thomas Atom, Mathematical Proceedings of the Cambridge Philosophical Society **26**(03), 376–385 (Jul 1930).

[49] G. Ortiz and P. Ballone, Correlation energy, structure factor, radial distribution function, and momentum distribution of the spin-polarized uniform electron gas, Phys. Rev. B **50**, 1391–1405 (Jul 1994).

[50] S. H. Vosko, L. Wilk, and M. Nusair, Accurate spin-dependent electron liquid correlation energies for local spin density calculations: a critical analysis, Canadian Journal of Physics **58**(8), 1200–1211 (Mar 1980).

[51] E. Runge and E. K. U. Gross, Density-Functional Theory for Time-Dependent Systems, Phys. Rev. Lett. **52**, 997–1000 (Mar 1984).

[52] R. van Leeuwen, Mapping from Densities to Potentials in Time-Dependent Density-Functional Theory, Phys. Rev. Lett. **82**, 3863–3866 (May 1999).

[53] J. Korringa, On the calculation of the energy of a Bloch wave in a metal, Physica **13**, 392 – 400 (Aug 1947).

[54] W. Kohn and N. Rostoker, Solution of the Schrödinger Equation in Periodic Lattices with an Application to Metallic Lithium, Phys. Rev. **94**, 1111–1120 (Jun 1954).

[55] T. H. Dupree, Electron scattering in a crystal lattice, Annals of Physics **15**(1), 63 – 78 (Jul 1961).

[56] N. Papanikolaou, R. Zeller, and P. H. Dederichs, Conceptual improvements of the KKR method, Journal of Physics: Condensed Matter **14**(11), 2799 (Mar 2002).

[57] J. Zabloudil, R. Hammerling, L. Szunyogh, and P. Weinberger, *Electron Scattering in Solid Matter: a theoretical and computational treatise*, Springer Science & Business Media, Mar 2006.

[58] P. Soven, Coherent-Potential Model of Substitutional Disordered Alloys, Phys. Rev. **156**, 809–813 (Apr 1967).

[59] B. Zimmermann, *Ab initio description of transverse transport due to impurity scattering in transition metals*, PhD thesis, Jülich, 2014.

[60] R. Zeller, Multiple-scattering solution of Schrodinger's equation for potentials of general shape, Journal of Physics C: Solid State Physics **20**(16), 2347 (Jun 1987).

[61] D. S. G. Bauer, *Development of a relativistic full-potential first-principles multiple scattering Green function method applied to complex magnetic textures of nano structures at surfaces*, PhD thesis, Jülich, 2013.

[62] P. Buczek, *Spin dynamics of complex itinerant magnets*, PhD thesis, International Max Planck Research School, Halle, 2009.

[63] C. G. Shull, Early development of neutron scattering, Rev. Mod. Phys. **67**, 753–757 (Oct 1995).

[64] M. Farle, Ferromagnetic resonance of ultrathin metallic layers, Reports on Progress in Physics **61**(7), 755 (Jul 1998).

[65] J. Schäfer, D. Schrupp, E. Rotenberg, K. Rossnagel, H. Koh, P. Blaha, and R. Claessen, Electronic Quasiparticle Renormalizztion on the Spin Wave Energy Scale, Phys. Rev. Lett. **92**, 097205 (Mar 2004).

[66] X. Y. Cui, K. Shimada, M. Hoesch, Y. Sakisaka, H. Kato, Y. Aiura, S. Negishi, M. Higashiguchi, Y. Miura, H. Namatame, and M. Taniguchi, High Resolution Angle-resolved Photoemission Spectroscopy of Iron: A Study of the Self-energy, J. Mag. Mat. **310**, 1617 (Mar 2007).

[67] A. Hofmann, X. Y. Cui, J. Schäfer, S. Meyer, P. Höpfner, C. Blumenstein, M. Paul, L. Patthey, E. Rotenberg, J. Bünemann, F. Gebhard, T. Ohm, W. Weber, and R. Claessen, Renormalization of Bulk Magnetic Electron States at High Binding Energies, Phys. Rev. Lett. **102**, 187204 (May 2009).

[68] H. Ibach, High resolution electron energy loss spectroscopy of spin waves in ultra-thin

film – The return of the adiabatic approximation?, Surface Science **630**(0), 301 – 310 (Dec 2014).

[69] A. L. Fetter and J. D. Walecka, *Quantum theory of many-particle systems*, AcGraw-Hill, Boston, 1971.

[70] M. dos Santos Dias, B. Schweflinghaus, S. Blügel, and S. Lounis, Relativistic dynamical spin excitations of magnetic adatoms, Phys. Rev. B **91**, 075405 (Feb 2015).

[71] S. Lounis, M. dos Santos Dias, and B. Schweflinghaus, Transverse dynamical magnetic susceptibilities from regular static density functional theory: Evaluation of damping and g shifts of spin excitations, Phys. Rev. B **91**, 104420 (Mar 2015).

[72] T. Balashov, A. F. Takács, M. Däne, A. Ernst, P. Bruno, and W. Wulfhekel, Inelastic Electron-magnon Interaction and Spin Transfer Torque, Phys. Rev. B **78**, 174404 (Nov 2008).

[73] Y.-L. Wang and D. J. Scalapino, Dynamic Susceptibility of Magnetic Ions in Metals, Phys. Rev. **175**, 734 (Nov 1968).

[74] J. A. Appelbaum and W. F. Brinkman, Electron-Magnon Effects in Ferromagnetic Junctions, Phys. Rev. **183**, 553 (Jul 1969).

[75] D. M. Edwards and J. A. Hertz, Electron-magnon interactions in itinerant ferromagnetism. I. Formal theory, Journal of Physics F: Metal Physics **3**(12), 2174 (Dec 1973).

[76] D. M. Edwards and J. A. Hertz, Electron-magnon interactions in itinerant ferromagnetism. II. Strong ferromagnetism, Journal of Physics F: Metal Physics **3**(12), 2191 (Dec 1973).

[77] M. Celasco and M. Corrias, Electron Correlations in Itinerant Strong Ferromagnetism: Effect of Electron-Magnon Interaction on the Self-Energy, Nuovo Cimento **33**, 807 (Jun 1976).

[78] J. Hong and D. L. Mills, Theory of the spin dependence of the inelastic mean free path of electrons in ferromagnetic metals: A model study, Phys. Rev. B **59**, 13840–13848 (Jun 1999).

[79] A. Liebsch, Ni d-band self-energy beyond the low-density limit, Phys. Rev. B **23**, 5203–5212 (May 1981).

[80] G. Baym and L. P. Kadanoff, Conservation Laws and Correlation Functions, Phys. Rev. **124**, 287 (Oct 1961).

[81] Kanamori, Electron Correlation and Ferromagnetism of Transition Metals, Prog. Theo. Phys. **30**, 275 (Sep 1963).

[82] W. G. Aulbur, L. Jönsson, and J. W. Wilkins, Quasiparticle Calculations in Solids, volume 54 of *Solid State Physics*, pages 1 – 218, Academic Press, 1999.

[83] P. Romaniello, F. Bechstedt, and L. Reining, Beyond the GW Approximation: Combining Correlation Channels, Phys. Rev. B **85**, 155131 (Apr 2012).

[84] V. P. Zhukov, E. V. Chulkov, and P. M. Echenique, Lifetimes of Excited Electrons In Fe And Ni: First-Principles GW and the T-Matrix Theory, Phys. Rev. Lett. **93**, 096401 (Aug 2004).

[85] K. Karlsson and F. Aryasetiawan, Exchange-correlation Kernel in Time-dependent Density Functional Theory Derived from Many-Body Theory, International J. of Mod. Phys. B **18**, 1055 (Mar 2004).

[86] U. Brandt, Modified T-matrix approximation in itinerant ferromagnets, Z. Phys. **244**(3), 217–229 (Feb 1971).

[87] A. A. Khajetoorians, J. Wiebe, B. Chilian, S. Lounis, S. Blügel, and R. Wiesendanger, Atom-by-atom engineering and magnetometry of tailored nanomagnets, Nature Phys. **8**, 497–503 (Apr 2012).

[88] A. Brodde, S. Tosch, and H. Neddermeyer, Scanning tunnelling microscopy and spectroscopy on Cu(111) and Au(111), Journal of Microscopy **152**(2), 441–448 (Nov 1988).

[89] A. A. Khajetoorians, J. Wiebe, B. Chilian, and R. Wiesendanger, Realizing All-Spin–Based Logic Operations Atom by Atom, Science **332**(6033), 1062–1064 (May 2011).

[90] C. F. Hirjibehedin, C.-Y. Lin, A. F. Otte, M. Ternes, C. P. Lutz, B. A. Jones, and A. J. Heinrich, Large Magnetic Anisotropy of a Single Atomic Spin Embedded in a Surface Molecular Network, Science **317**(5842), 1199–1203 (Aug 2007).

[91] V. S. Stepanyuk, A. N. Baranov, D. V. Tsivlin, W. Hergert, P. Bruno, N. Knorr, M. A. Schneider, and K. Kern, Quantum interference and long-range adsorbate-adsorbate interactions, Phys. Rev. B **68**, 205410 (Nov 2003).

[92] N. N. Negulyaev, V. S. Stepanyuk, W. Hergert, P. Bruno, and J. Kirschner, Atomic-scale self-organization of Fe nanostripes on stepped Cu(111) surfaces: Molecular dynamics and kinetic Monte Carlo simulations, Phys. Rev. B **77**, 085430 (Feb 2008).

[93] L. Landau and E. Lifshitz, Theory of the dispersion of magnetic permeability in ferromagnetic bodies, Phys. Z. Sowietunion **8**, 153–169 (1935).

[94] T. L. Gilbert, A phenomenological theory of damping in ferromagnetic materials, Magnetics, IEEE Transactions on Magnetics **40**(6), 3443–3449 (Nov 2004).

[95] A. F. Otte, M. Ternes, K. von Bergmann, S. Loth, H. Brune, C. P. Lutz, C. F. Hirjibehedin, and A. J. Heinrich, The Role of Magnetic Anistropy in the Kondo Effect, Nature Phys. **4**, 847 (Sep 2008).

[96] T. Jamneala, V. Madhavan, W. Chen, and M. F. Crommie, Scanning tunneling spectroscopy of transition-metal impurities at the surface of gold, Phys. Rev. B **61**, 9990–9993 (Apr 2000).

[97] S. Lounis, P. Mavropoulos, P. H. Dederichs, and S. Blügel, Surface-state scattering by adatoms on noble metals: *Ab initio* calculations using the Korringa-Kohn-Rostoker Green function method, Phys. Rev. B **73**, 195421 (May 2006).

[98] C. Etz, J. Zabloudil, P. Weinberger, and E. Y. Vedmedenko, Magnetic properties of single atoms of Fe and Co on Ir(111) and Pt(111), Phys. Rev. B **77**, 184425 (May 2008).

[99] G. Kresse and J. Hafner, *Ab initio* molecular dynamics for liquid metals, Phys. Rev. B **47**, 558–561 (Jan 1993).

[100] A. I. Liechtenstein, M. I. Katsnelson, and V. A. Gubanov, Exchange interactions and spin-wave stiffness in ferromagnetic metals, Journal of Physics F: Metal Physics **14**(7), L125 (Jul 1984).

[101] V. Antropov, The exchange coupling and spin waves in metallic magnets: removal of the long-wave approximation, Journal of Magnetism and Magnetic Materials **262**(2), L192 – L197 (Feb 2003).

[102] P. Bruno, Exchange Interaction Parameters and Adiabatic Spin-Wave Spectra of Ferromagnets: A "*Renormalized* Magnetic Force Theorem", Phys. Rev. Lett. **90**, 087205 (Feb 2003).

[103] M. I. Katsnelson and A. I. Lichtenstein, Magnetic susceptibility, exchange interactions and spin-wave spectra in the local spin density approximation, Journal of Physics: Condensed Matter **16**(41), 7439 (Oct 2004).

[104] C. Kittel, Theory of Antiferromagnetic Resonance, Phys. Rev. **82**, 565–565 (May 1951).

[105] F. Keffer and C. Kittel, Theory of Antiferromagnetic Resonance, Phys. Rev. **85**, 329–337 (Jan 1952).

[106] S. Nadj-Perge, I. K. Drozdov, J. Li, H. Chen, S. Jeon, J. Seo, A. H. MacDonald, B. A. Bernevig, and A. Yazdani, Observation of Majorana fermions in ferromagnetic atomic chains on a superconductor, Science **346**(6209), 602–607 (Oct 2014).

[107] H. Tang, M. Plihal, and D. Mills, Theory of the spin dynamics of bulk Fe and ultrathin Fe(100) films, Journal of Magnetism and Magnetic Materials **187**(1), 23 – 46 (Aug 1998).

[108] P. W. Anderson, Localized Magnetic States in Metals, Phys. Rev. **124**, 41–53 (Oct 1961).

List of publications

(S1) A. A. Khajetoorians, T. Schlenk, B. Schweflinghaus, M. dos Santos Dias, M. Steinbrecher, M. Bouhassoune, S. Lounis, J. Wiebe, and R. Wiesendanger, Spin Excitations of Individual Fe Atoms on Pt(111): Impact of the Site-Dependent Giant Substrate Polarization, Phys. Rev. Lett. **111**, 157204 (Oct 2013).

(S2) B. Schweflinghaus, M. dos Santos Dias, A. T. Costa, and S. Lounis, Renormalization of electron self-energies via their interaction with spin excitations: A first-principles investigation, Phys. Rev. B **89**, 235439 (Jun 2014).

(S3) S. Lounis, B. Schweflinghaus, M. dos Santos Dias, M. Bouhassoune, R. B. Muniz, and A. T. Costa, Theoretical probing of inelastic spin-excitations in adatoms on surfaces, Surface Science **630**, 317 – 324 (Jul 2014).

(S4) M. dos Santos Dias, B. Schweflinghaus, S. Blügel, and S. Lounis, Relativistic dynamical spin excitations of magnetic adatoms, Phys. Rev. B **91**, 075405 (Feb 2015).

(S5) S. Lounis, M. dos Santos Dias, and B. Schweflinghaus, Transverse dynamical magnetic susceptibilities from regular static density functional theory: Evaluation of damping and g shifts of spin excitations, Phys. Rev. B **91**, 104420 (Mar 2015).

(S6) D. M. Crum, M. Bouhassoune, J. Bouaziz, B. Schweflinghaus, S. Blügel, and S. Lounis, Perpendicular Reading of Single Confined Magnetic Skyrmions, Nat. Commun. **6**, 8541 (Oct 2015).

(S7) B. Schweflinghaus, M. dos Santos Dias, and S. Lounis, Observing spin excitations in $3d$ transition-metal adatoms on Pt(111) with inelastic scanning tunneling spectroscopy: A first-principles perspective, Phys. Rev. B **93**, 035451 (Jan 2016).

(S8) B. Schweflinghaus, B. Zimmermann, M. Heide, G. Bihlmayer, and S. Blügel, Role of Dzyaloshinskii-Moriya interaction for magnetism in transition-metal chains at Pt step-edges, (submitted for publication), 2015.

Acknowledgments

The present work would not have been possible without the invaluable support from various people. It is my great pleasure to acknowledge their help and assistance in the following.

I would particularly like to thank my supervisor Prof. Dr. Samir Lounis for giving me the opportunity to work in this fascinating field of research as a member of this young investigator group "Functional Nanoscale Structure and Probe Simulation Laboratory" (Funsilab). In countless vivid and stimulating discussions he shared his vast scientific knowledge in the field of spin dynamics with me. He never got tired of answering my questions with admirable serenity even those that I kept posing on and on. Most importantly, his positive attitude and his strong faith in my scientific skills encouraged me to continuously improve my expertise in any aspect related to this work.

I express my gratitude to Prof. Dr. Carsten Honerkamp who kindly agreed to examine this thesis as a second referee.

Furthermore, I am deeply indebted to Prof. Dr. Stefan Blügel for giving me the opportunity to write this thesis in his institute "Quantum Theory of Materials" at the Peter Grünberg Institut and the Institute for Advanced Simulation. It was of highest priority for him to provide support for my scientific journey by everything that is in his power. In various stimulating discussions he formed and deepened my understanding of solid state physics and taught me to focus on the relevant aspects of a given problem.

I am very grateful to Dr. Manuel dos Santos Dias who supported me from the very beginning of this work in any thinkable way. The thesis greatly benefits from his impressively wide-ranging knowledge in crucial issues related to the thesis, including his profound understanding of the theoretical background and his brilliant expertise in programming. His contribution to this work cannot be rated high enough.

Moreover, I would like to thank the further members of the Funsilab group: Dr. Mohammed Bouhassoune for introducing me to the KKR formalism, Dr. Julen Ibañez Azpiroz for supportive feedback on the program usage, Dr. Filipe Guimarães for many helpful discussions concerning the LLG model, as well as Juba Bouaziz, Flaviano José Dos Santos, and our guest Dax Crum for their curiosity in learning the KKR formalism which greatly stimulated my understanding in return.

Many more people have contributed to this work by fruitful discussions or by proofreading different thesis chapters. Especially I acknowledge support from Jeiran Jokar on the TDDFT chapter, support from Dr. Phivos Mavropoulos, Dr. Long Nguyen, Dr. Bernd

Zimmermann, and Philipp Rüßmann on the KKR chapter, as well as support from Mathias Müller on the MBPT chapter.

A special thanks is also dedicated to Mrs. Ute Winkler who supported me in any administrative issue, always fast and immediately helpful.

I would like to thank Bernd and Philipp who shared the office with me, cheered me up in moments of frustration and accompanied me in a supportive way throughout the last years.

Moreover, I appreciate the wonderful atmosphere in the whole institute and the many uplifting sporting activities such as soccer, Badminton, or tennis. Many great and funny moments I will keep in memory, moments I shared with Yuriy, Alex, David, Timo, Bernd, Long, Julen, Guillaume, and many others.

Last but not least, a very special thanks goes to my parents Elisabeth and Gregor, my sister Christina and my wife Sonat, for their everlasting irreplaceable support, for their encouragement and love, and for always believing in me and being there for me.

Band / Volume 104
Spin-reorientation transition in epitaxial Ni_xPd_{1-x} fims on Cu(001): a microscopic analysis
D. Gottlob (2015), x, 134 pp
ISBN: 978-3-95806-049-4

Band / Volume 105
Resonant Magnetic Scattering Studies using Synchrotron Radiation and Laser-Generated Extreme Ultraviolet Light
C. M. Weier (2015), vii, 143 pp
ISBN: 978-3-95806-052-4

Band / Volume 106
Neutron Scattering
Lectures of the JCNS Laboratory Course held at Forschungszentrum Jülich and at the Heinz-Maier-Leibnitz Zentrum Garching
edited by Th. Brückel, D. Richter, G. Roth, A. Wischnewski and R. Zorn (2015), ca 300 pp
ISBN: 978-3-95806-055-5

Band / Volume 107
Neutron Scattering
Experimental Manuals of the JCNS Laboratory Course held at Forschungszentrum Jülich and at the Heinz-Maier-Leibnitz Zentrum Garching
edited by Th. Brückel, D. Richter, G. Roth, A. Wischnewski and R. Zorn (2015), ca 150 pp
ISBN: 978-3-95806-056-2

Band / Volume 108
STM-based quantum transport through molecular wires
N. Fournier (2015), ix, 295 pp
ISBN: 978-3-95806-059-3

Band / Volume 109
Study on the electroforming and resistive switching behaviour of nickel oxide thin fims for non-volatile memory applications
R. Weng (2015), xxi, 159 pp
ISBN: 978-3-95806-062-3

Band / Volume 110
Microswimmers – From Single Particle Motion to Collective Behaviour
Lecture Notes of the DFG SPP Summer School 2015
edited by G. Gompper, C. Bechinger, S. Herminghaus, R. E. Isele-Holder, U.B. Kaupp, H. Löwen, H. Stark, R. G. Winkler (2015)
ISBN: 978-3-95806-083-8

Band / Volume 111
Long range order in 3D nanoparticle assemblies
E. Josten (2015), 238 pp
ISBN: 978-3-95806-087-6

Band / Volume 112
Silicon nanowire structures for neuronal cell interfacing
S. Pud (2015), 153 pp
ISBN: 978-3-95806-089-0

Band / Volume 113
Memristive Phenomena -
From Fundamental Physics to Neuromorphic Computing
Lecture Notes of the 47th IFF Spring School 2016
22 February – 04 March 2016, Jülich, Germany
ed. by R. Waser and M. Wuttig (2016), ca 1000 pp
ISBN: 978-3-95806-091-3

Band / Volume 114
Single-Cell Analysis of Microbial Production Strains
in Microfluidic Bioreactors
A. M. Grünberger (2015), XIX, 225 pp
ISBN: 978-3-95806-092-0

Band / Volume 115
Magnetic order and spin dynamics in the
extended kagome system $CaBaCo_2Fe_2O_7$
J. Reim (2015), viii, 144 pp
ISBN: 978-3-95806-097-5

Band / Volume 116
Structural and electronic investigations on homo- and hetero-organic layers involving CuPc on silver single crystal surfaces
K. M. Schönauer (2015), x, 148 pp
ISBN: 978-3-95806-112-5

Band / Volume 117
First-principles investigation of inelastic magnetic excitations
in nanostructures deposited on surfaces
B. J. Schweflinghaus (2016), v, 204 pp
ISBN: 978-3-95806-115-6

Schlüsseltechnologien /
Key Technologies
Band / Volume 117
ISBN 978-3-95806-115-6